University of Strathclyde

Department of Civil and Environmental Engineering

Engineering Geosciences and Geomechanics

*Faults and Fluid Flow Research Group*

# Textural and Structural Characteristics of the Kestanelik Epithermal Vein System, NW Turkey:
# Implications for permeability enhancement mechanisms and gold exploration in epithermal systems

A thesis presented in fulfilment of the requirements for the degree of Doctor of Philosophy

by
*Nilay Gülyüz*

September, 2017

This thesis is the result of the author's original research. It has been composed by the author and has not been previously submitted for examination which has led to the award of a degree.

The copyright of this thesis belongs to the author under the terms of the United Kingdom Copyright Acts as qualified by University of Strathclyde Regulation 3.50. Due acknowledgement must always be made of the use of any material contained in, or derived from, this thesis.

Signed:

Date: 15.08.2017

# Abstract

It has long been known that faults and fracture provide a critical role in multiphase epithermal mineralization, however the mechanisms of permeability enhancement after a conduit becomes sealed up over time has been less well studied. The research in this thesis investigates the vein-scale permeability enhancement mechanisms in epithermal gold deposits through a detailed study of geology, dimensions, geometry, textures and breccias of the well-exposed Kestanelik gold deposit (NW Turkey). New mapping of the deposit and its host rocks show that the Late Eocene mineralization is associated with regional Cenozoic calc-alkaline magmatism. Vein textures and breccia components indicate repeated sealing and subsequent brecciation of wall rock and pre-existing vein infill. Kinematic analyses together with macroscopic and petrographic analyses of vein textures characterize E-W trending veins as left lateral faults, whilst NE-SW trending veins are extensional (Mode I) fractures. Although two phases of mineralization were picked up from E-W trending veins, at least three were determined from NE-SW trending veins. Cataclasite and tectonic breccia of wall rocks and early quartz, hydrothermal crackle breccias, and cement supported chaotic breccias of pre-existing vein infill, all of which are cemented by late-stage quartz, indicate that coseismic rupturing and hydraulic fracturing are two major permeability enhancement mechanisms. Faults were reactivated along the vein footwall-wall rock contact, while extensional veins were opened along their either margin. Transient local stress variation also has the potential to enhance permeability on mis-oriented surfaces and at locations where the dip changes. Constructed 3D vein geometries show subsurface vein bends are more favorable structural locations for gold to precipitate than smooth, planar segments, and the host rock schist host the majority of gold. This study emphasizes the importance of detailed structural and textural studies for gold exploration and 3D orebody modelling.

# Dedication

To my parents Aynur and Şevket

# Acknowledgements

# Table of Contents

## List of Figures

xxiii

# List of Tables

# Chapter 1: Introduction

Epithermal deposits originate in the upper, brittle crust of regions with active magmatic and geothermal activity. Mineralisation in these deposits is dominantly hosted by veins or stockworks, confirming that brittle fault and fracture systems play major role in the circulation of hydrothermal fluids (Buchanan, 1981; Hedenquist and Lowenstern, 1994; Curewitz and Karson, 1997). The ore and gangue minerals in the veins are result of multiphase precipitation (Spurr, 1925; Hulin, 1929; Buchanan, 1981; Sibson, 1987; Hedenquist *et al*., 2000), and associated with repeated and episodic fluid flow rather than a steady-state process (Sibson, 1987; Micklethwaite and Cox, 2004; Woodcock *et al.,* 2007). The mineralogical and geochemical aspects of low sulphidation (LS) epithermal systems are well known (e.g. Buchanan, 1981; White and Hedenquist, 1990; Hedenquist and Lowenstern, 1994; White and Hedenquist, 1995; Hedenquist *et al.,* 2000; Sillitoe and Hedenquist, 2003; Simmons *et al.,* 2005). However, limited studies exist on the fluid flow and permeability enhancement mechanisms in LS epithermal veins.

Radiometric dating of some hydrothermal deposits indicates that the permeability creation and hydrothermal fluid circulation could take place over thousands to tens of thousands of years (Fournier, 1989; Lalou *et al.,* 1993) and  as long as millions of years in major porphyry systems (Sillitoe, 2010). To understand the longevity of such systems it is crucial to understand how subsequent permeability enhancement can be achieved after the deposition of minerals in fractures and faults chokes permeable pathways and restricts fluid flow.

Several precipitation mechanisms are invoked for circulating hydrothermal solutions in both high and low sulphidation epithermal systems such as boiling, oxidation, fluid mixing, adiabatic boiling, pH change etc. The most favourable precipitation mechanism in low sulphidation epithermal systems is boiling (e.g. Hedenquist *et al*., 2000). In this model, epithermal fluids rise from depth along structural pathways at high temperatures under suitable pressure to prevent boiling. When the pressure drops suddenly (e.g. through faulting or fracturing-

related dilation), boiling occurs (e.g. Buchanan, 1981). Even small magnitude earthquakes (Mw<2) can trigger a boiling event (Sanchez-Alfaro *et al.,* 2016). Changes in the fluid chemistry caused by boiling result in precipitation of base metals at deeper levels, and precious ore and gangue minerals at relatively shallower depths. This occurs until the open spaces are sealed, and fracture permeability is occluded or lost (e.g. Buchanan, 1981; Henley, 1985; Hedenquist *et al.,* 2000).

Existing studies generally focus on the role and significance of geometric and mechanical aspects of the fault-fracture systems on the epithermal deposits. Terminations of individual faults and locations of multiple fault interaction are areas of high fluid flow (Curewitz and Karson, 1997; Cox *et al.* 2001; Cox, 2005; Davatzes *et al.*, 2005). Epithermal mineralisation is often located in dilational jogs within fault systems (Sibson, 1987). Major faults can be important barriers or conduits to fluid flow (Caine *et al.,* 1996; Rowland and Sibson, 2004), while the permeability may be nonuniform along the fault depending on the relationship between the variable strike of the fault and the orientation of the local stress direction (Micklethwaite *et al,.* 2010). Permeability can also be developed or maintained along individual fault segments because interconnected fractures and subsidiary faults form in the wall rocks where damage zone occurs adjacent to a fault core (Caine *et al,.* 1996; Davatzes *et al,.* 2005). The permeable damage zone structures may also change position over geological time (Woodcock *et al.,* 2007; Burnside *et al.,* 2013). Micklethwaite and Cox (2004, 2006) argued that although the permeability of the fault where the mainshock occurs may rapidly be lost due to the precipitation of hydrothermal minerals (Byerlee, 1993; Davatzes and Hickman, 2005; Cox, 2005), enhanced fluid flow may occur along the structures where aftershock ruptures focus and the location of these structures are predictable based on stress transfer modelling. Sheldon and Micklethwaite (2007) showed that aftershock zones closely correspond to the location of known mineralization.

The main aim of this thesis is to understand the vein-scale permeability enhancement mechanisms in epithermal gold deposits by examining the geology,

dimensions, geometry, textures and breccias of a well-exposed epithermal vein system at the Kestanelik gold deposit (Lapseki, Biga Peninsula, NW Turkey). Both field and drill core data were used to understand the deformation mechanics and kinematics of the vein system linked to observations of vein textures and gold grade. The results have implications for gold exploration and 3D orebody modelling in epithermal gold deposits.

This study presents significant new microstructural evidence for reactivation along the vein-wall rock contact and associated permeability development and fluid flow after the veins were clogged. These findings support the few earlier studies into the permeability enhancement mechanisms and fluid flow in epithermal systems (e.g. Sibson, 1987; Cox *et al.*, 2001; Micklethwaite and Cox, 2004; Micklethwaite, 2009) but are also the first time that detailed studies have been made of the permeability enhancement mechanisms.

Chapter 2 presents a literature review on the general characteristics of epithermal gold deposits, and structural control, permeability enhancement and fluid flow in epithermal systems. Chapter 3 briefly outlines the geology of Turkey and the Biga Peninsula. New observations of the geology of the deposit area are presented with the main structures and paleo-stress analyses, in order to constrain the conditions of emplacement of the veins. This new geological data for the first time places the deposit into the geological context and improves understanding of tectonic, magmatic and metallogenic evolution of the Biga Peninsula. Chapter 4 presents the structural characteristics (e.g. dimensions, geometry, attitude) of the mineralized quartz veins, 3D modelling of sub-surface geometries of the major mineralized quartz veins, and links these to measured gold grades. Chapter 5 describes the textures and breccias of the individual veins based on field and drill core data and petrographical analyses. Chapter 6 discusses the results presented in the thesis and examines the new findings of the study in the light of the previous studies and implications for propect evaluation and 3D orebody modelling. Chapter 7 summarizes the findings of this study and discusses possible further work.

# Chapter 2: Overview of Low Sulphidation Epithermal Gold Deposits

In this chapter, general characteristics of epithermal gold deposits are described in section 1. Section 2 focuses on reviewing the general characteristics of low sulphidation (LS) epithermal deposits. Section 3 reviews structural controls, deformation, permeability enhancement and fluid flow in epithermal gold deposits. While mineralogical and geochemical aspects of LS epithermal systems are well known; limited studies exist on the fluid flow and permeability enhancement mechanisms in LS epithermal veins. Moreover these limited studies commonly focus on the geometric and mechanical aspects of the fault-fracture systems on the epithermal deposits rather than on permeability enhancement mechanisms.

## 2.1. General characteristics of epithermal gold deposits

"Epithermal" means "shallow heat", and was first defined by Lindgren (1922). The epithermal environment typically hosts deposits of Au, Ag and base metals according to geologic reconstructions, ore mineralogy and related textures (Lindgren, 1933). They generally form at temperatures between 160 $^{\circ}$C and 270 $^{\circ}$C based on the mineral characteristics (thermal stability) of these environments, and the recording of fluid inclusions. Boiling is common in epithermal environments (Buchanan, 1981). The maximum temperature at a given depth under hydrostatic pressure depends on the vapor pressure of boiling water, so the temperature interval of 160 to 270 $^{\circ}$C is equivalent to a depth range below the paleowater table of about 50 m and 700 m respectively, although there are a few epithermal gold deposits which have formed below 1000 m depth (Hedenquist *et al.*, 2000).

Epithermal gold deposits form at the upper parts of intrusion-related hydrothermal systems, in cells of convecting water driven by intrusions that act as a heat source. Water of largely meteoric origin circulates deeply into a volcanic/sedimentary pile, becomes heated, and dissolves metals, alkalies, chlorides and sulphur species (Buchanan, 1981). The chemistry of the fluid is based on the

interaction of the meteoric water with the host rocks, magmatic fluids and gases (White and Hedenquist, 1990). The heated fluid, which is weakly saline (<1 to ~5-15 wt% NaCl eqv.) at slightly higher temperatures (200-300 $^{\circ}$C) and at pressures less than a few hundred bars (Pirajno, 2009), moves up from depth along structural pathways. Finally, the pressure drops suddenly (through any faulting, fracture) and triggers boiling. As a result of the boiling, $CO_2$ and $H_2S$ are lost to the vapour and this leads to the saturation of the ore-bearing fluid and causes the deposition of ore and gangue minerals into any available open space (Hedenquist *et al.*, 2000).

These deposits are generally observed in vein, stockwork and disseminated forms (White and Hedenquist, 1990). However, there are other orebody forms controlled by the host rock lithology, by structure and by hydrothermal processes (Hedenquist *et al.*, 2000) (Figure 2.1).

Although the most principal mineral deposition process in the epithermal environment is boiling based on the fluid inclusion characteristics (coexisting fluid and vapour phases) (e.g. Roedder, 1984), there are other mineral precipitation mechanisms occurring such as fluid mixing (dilution) and oxidation (White and Hedenquist, 1990). Mixing of ascending fluid with meteoric water results in temperature decrease and promotes mineral precipitation. In addition, oxidation is effective in mineral deposition by decreasing the pH of the rising solution and the solubilities of the metal sulphide complexes (Robb, 2005).

Because the fluids of epithermal deposits precipitate their mineral load into any open space as vein fillings, open space filling textures such as comb, crustiform, colloform banding and cockade are common in epithermal quartz veins (Figure 2.2). In addition, since the most dominant and common mineral deposition mechanism is boiling in epithermal environment, hydrothermal breccias (results of hydraulic fracturing related to vigorous boiling event) are common and diagnostic features of epithermal gold deposits (Buchanan, 1981; White and Hedenquist, 1995; Hedenquist *et al.*, 2000).
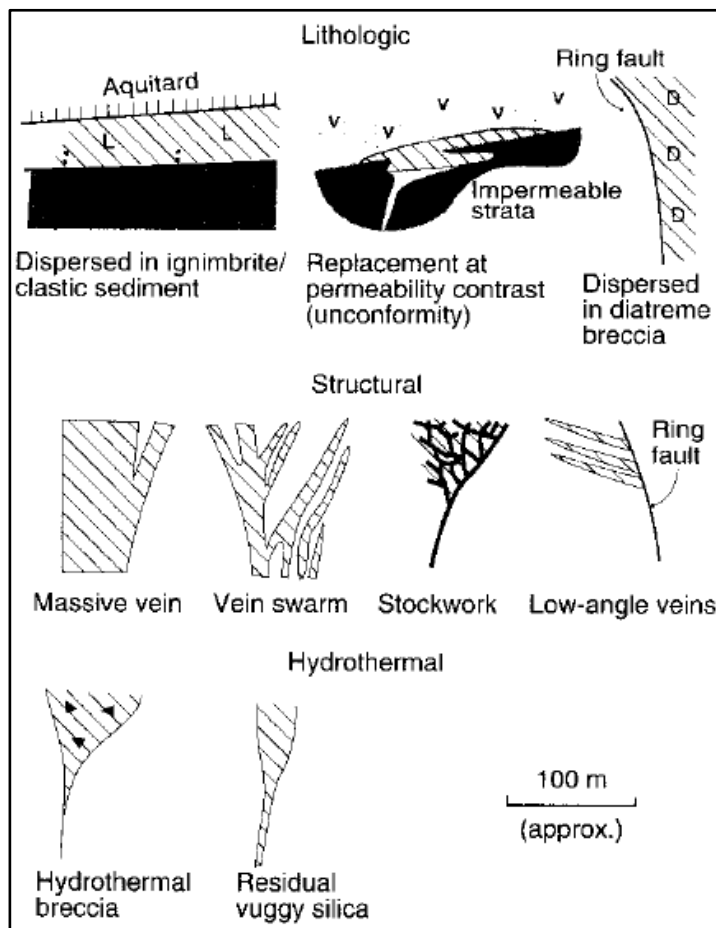
**Figure 2.1.** Examples of orebody form, controlled by the host rock lithology, structure, and hydrothermal processes. Ore shown by angled lines (from Hedenquist et al., 2000).
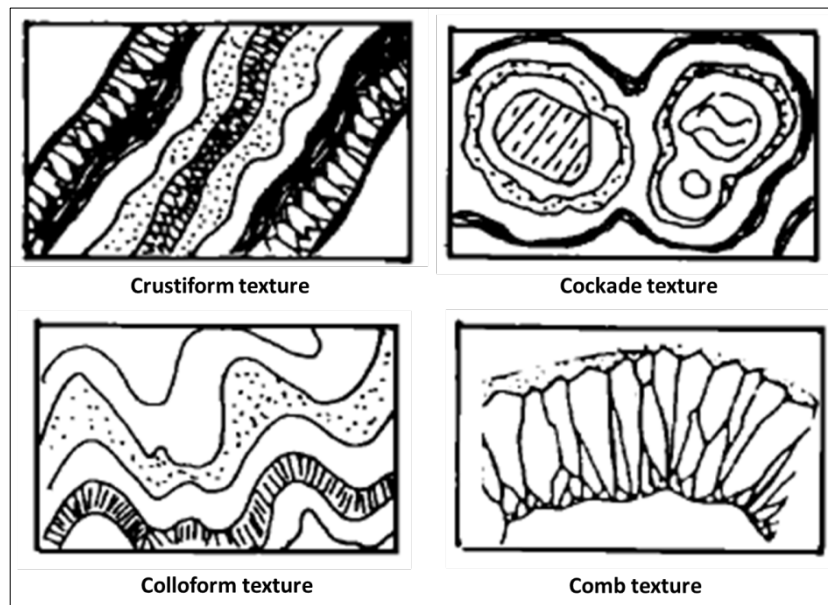


**Figure 2.2.** Common open space filling textures observed in epithermal quartz veins.

Hydrothermal alteration occurs as a result of the interaction of hot ore forming fluids with the rocks through which they circulate under evolving physico-chemical conditions (Pirajno, 2009). Understanding hydrothermal alteration is crucial in prospecting for areas of paleofluid flow and hence the zones of ore deposition (Hedenquist *et al.*, 2000). Although the alteration products depend on the chemistry of the ore-forming fluid, temperature and volume of fluid flow, type, permeability and reactivity of the host rock (White and Hedenquist, 1990), the common alteration minerals observed in the epithermal environment are given in Figure 2.3.
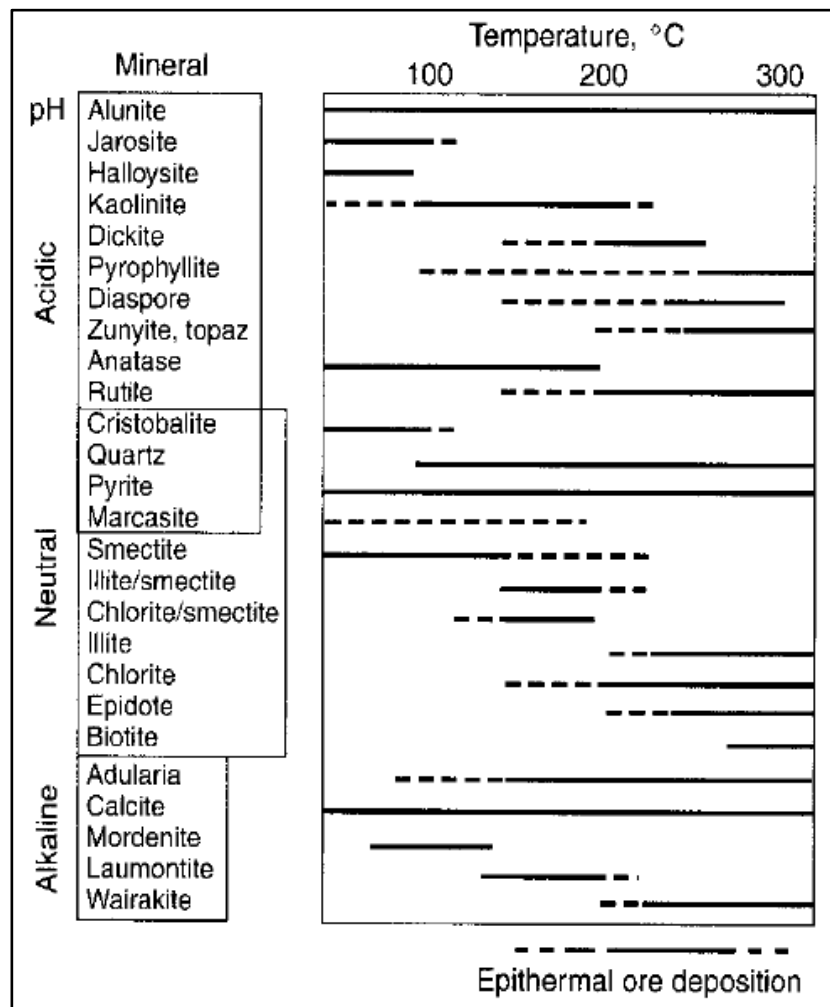


**Figure 2.3.** Thermal stability of various hydrothermal minerals observed in the epithermal environment (from Hedenquist *et al.*, 2000).

There are two principal styles of epithermal gold deposits based on fluids of contrasting chemistry (Figure 2.4). These are low sulphidation (LS) or adularia-sericite type and high sulphidation (HS) or acid-sulphate type. In addition, there is a transition type intermediate sulphidation (IS) which is defined as a subtype of the low sulphidation systems (Hedenquist *et al.*, 2000; Hedenquist and Sillitoe, 2003).

In **low-sulphidation** systems, the mineralizing fluids are those typically sourced from active geothermal systems distal from the magmatic heat source (parent intrusion) in the magmatic-hydrothermal environment (Henley and Ellis, 1983). The fluids are reduced and have near-neutral pH forming low sulphidation state sulphide minerals (Barton and Skinner, 1979). In contrast, **high-sulphidation** systems and associated high-sulphidation state minerals result from acidic and oxidized fluids formed above young volcanoes in the magmatic-hydrothermal environment (Ransome, 1907; Hedenquist *et al.*, 1994). Generalized sketches of high and low sulphidation epithermal systems are given in Figure 2.4.
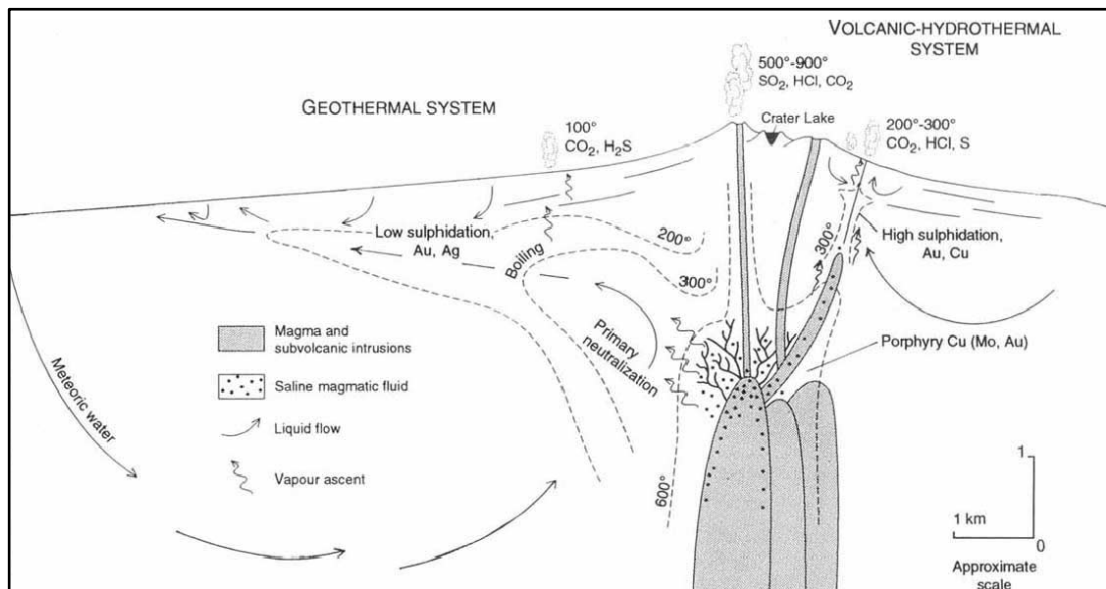


**Figure 2.4.** Schematic cross-section showing shallow, sub-volcanic intrusions, an associated stratavolcano, and the environments deduced for the formation of porphyry Cu, and high- and low-sulphidation epithermal ore deposits. Active volcanic-hydrothermal systems extend from the degassing magma to fumaroles and acidic springs, and incorporate the porphyry and/or high-sulphidation ore environments, whereas low sulphidation ore deposits form from geothermal systems characterized by neutral-pH waters that may discharge as hot springs and geysers (from Hedenquist and Lowenstern, 1994).

Most of the epithermal gold deposits occur in convergent tectonic settings (White and Hedenquist, 1990; Hedenquist and Lowenstern, 1994; White and Hedenquist, 1995), and are generally associated with post-subductional extensional regimes (Sillitoe and Hedenquist, 2003). In addition, they are abundant in intermediate to acid volcanic settings, although they may occur in bimodal volcanic settings (White and Hedenquist, 1990; Sillitoe and Hedenquist, 2003). The host rocks are generally calc-alkaline to alkaline rocks (Hedenquist *et al.*, 2000; Sillitoe and Hedenquist, 2003), and any underlying basement rocks (White and Hedenquist, 1990).

Most of the well-known epithermal gold deposits are generally of Cenozoic age, however there are a few deposits older than Tertiary (Buchanan, 1981, Simmons *et al.*, 2005).

## 2.2. Low sulphidation epithermal gold deposits

There is a variety of classifications of LS deposits in the literature. Firstly, a division exists based on the metal assemblage which consists of Au-rich LS deposits and Ag-rich LS deposits (Hedenquist and Henley, 1985). The Au-rich deposits are formed from low salinity and gas rich fluids (<1-2 wt % NaCl but up to 4 wt% gases, mainly $CO_2$ with $H_2S$) (Hedenquist and Henley, 1985), while the Ag-rich ones are associated with more saline fluids (10-15 wt% NaCl) and have economic quantities of Zn and Pb. The fluids of Au-rich LS deposits are very similar to the fluids of most active geothermal systems.

Corbett (2002) also divided LS deposits according to mineralogy related to the depth and environment of formation into two groups: ones whose mineralogies dominantly have magmatic source rocks (arc low sulphidation), and ones having mineralogies dominantly derived from circulating meteoric fluid sources (rift low sulphidation). Adularia-sericite type low-sulphidation deposits cover the rift style LS deposits. Although a variety of LS deposit types exist in the literature, general characteristics of the most common Au-rich adularia-sericite type (generally known as LS epithermal gold deposits in the literature) will be given here.

These deposits generally form distant from their magmatic heat source from the surface to as deep as 1 to 2 km, and at temperatures of 200-300$^{\circ}$C (Heald *et al.*, 1987). Intrusions located at as much as 5 to 6 km deep (Hedenquist *et al.*, 2000) act as a heat source to drive cells of convecting water causing the mineralization (Buchanan, 1981). Maximum temperature at a given depth is constrained by boiling, the most dominant process that occur in geothermal systems, and the pressures are controlled by hydrostatic conditions (Hedenquist and Henley, 1985).

Geothermal systems have deeply sourced, near-neutral pH and reduced fluids due to the fact that they have equilibrated with their host rocks during their slow ascent in a rock dominated environment. The fluids typically are of low salinity (<1 to 2 wt% NaCl equiv.), gas rich (dominantly $CO_2$ with minor $H_2S$ and $N_2$) (Giggenbach, 1992) and have low total sulphide content (usually less than 1wt. %) (White and Hedenquist, 1990). Oxygen and hydrogen stable isotope data of LS fluids indicate the dominance of meteoric water with some magmatic water and vapor components (Taylor, 1979). The meteoric-water dominance is more obvious when the magmatism has higher volumes since the larger magmatic heat source creates larger and longer lived cells of convecting meteoric water that will mask most of the evidence for magmatic water-vapor components. Any reactive, acidic and high salinity magmatic water-volatile components in the geothermal system are neutralized and reduced due to the extensive amount of interaction between thermal waters and crustal rocks occurring in this environment (Hedenquist and Lowenstern, 1994). As a result of these reactions, NaCl, $CO_2$ and most dominantly $H_2S$ occur the principal species in the ascending fluid (White and Hedenquist, 1995).

The sources of gold and other metals in the fluids of LS deposits come from low density magmatic vapour absorbed at the base of the LS environment. Any acidic gases are added into the meteoric water system by magmatic vapour and are neutralized by reaction with the host rock. This neutralization causes exchange of $H^+$ for cations, including metals, thus adds $H^+$ to the metals contributed by the vapour. Metals in the magmatic vapour may enter magmas through a variety of

pathways such as mantle melting, mass transfer from subducting slab and melting of the crust (Hedenquist and Lowenstern, 1994).

Boiling and mixing are the two principal processes in LS systems. In systems where the gold is likely to be transported as a bisulphide ($HS^-$) complex (Henley *et al.*, 1984), boiling is accepted as a critical process since boiling and its associated gas loss are the major causes of gold precipitation from bisulphide complexes (Giggenbach and Stewart, 1982). Boiling (Figure 2.5) occurs when pressure drops suddenly (e.g. through faulting or any fracturing) and the vapor pressure becomes equal to hydrostatic pressure, and the $CO_2$ and $H_2S$ are released to the vapor phase. Firstly, loss of $CO_2$ from the solution results in an increase in pH and increases the solubility of gold, but then the subsequent $H_2S$ loss decreases the solubility of gold and leads its precipitation (eqn.1; Buchanan, 1981; Henley *et al.*, 1984; Henley, 1985; Brown, 1986; Cooke and Simmons, 2000).

$$Au(HS)_2 + 0.5\ H_2 \rightarrow Au + H_2S + HS^- \quad (eqn.1)$$
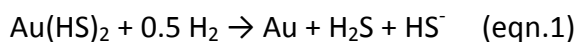
Boiling is very diagnostic in these systems and evidence that boiling occurred includes;

Alteration blankets of steam heated origin: $H_2S$ and $CO_2$ rich vapor generated during boiling event rises to the surface and condenses in the vadose zone, when $H_2S$ is oxidized to sulphate in the presence of atmospheric $O_2$; it forms steam-heated acid-sulphate water (eqn.2). The formation of steam-heated acid sulphate water results in the formation of alteration blankets at the surface of the LS system (Schoen *et al.*, 1974; Buchanan, 1981).

$$H_2S + 2O_2 = H_2SO_4 \quad (eqn.2)$$

Adularia and bladed calcite in LS veins: In LS systems and their active equivalent geothermal systems, the major controls on fluid pH are the salinity and the concentration of $CO_2$ in the solution (Henley *et al.*, 1984). Thus, boiling and associated $CO_2$ loss to the vapor results in a pH increase (eqn.3). This pH increase both causes a shift from illite to adularia stability (eqn.4) and leads to the deposition of calcite (eqn.5) (Simmons and Christenson, 1994; Hedenquist *et al.*, 2000).

$$HCO_3^- + H^- = H_2CO_3 \rightarrow CO_2 + H_2O \qquad (eqn.3)$$

$$KAlSi_3O_{10}(OH)_2 + 6SiO_2 + 2K^+ \rightarrow 3KAlSi_3O_8 + 2H^+ \qquad (eqn.4)$$

$$2HCO_3^- Ca^{2+} \rightarrow CaCO_3 + CO_2 + H_2O \quad (eqn.5)$$
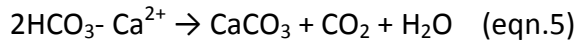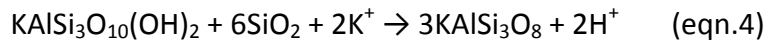
Fluid inclusion relations: During the boiling event vapor is generated; therefore, the co-existence of vapor and liquid-rich inclusions within an individual growth zone in a mineral indicates boiling at the time of trapping (Roedder and Bodnar, 1980; Roedder, 1984).

Hydrothermal breccias: Vigorous boiling event causes explosive pressure release which triggers hydraulic fracturing (Philips, 1972) and the formation of hydrothermal (crackle) breccias (Hedenquist and Henley, 1985b; Jebrak, 1997). These breccias are composed of angular clasts having no significant rotation, and show jigsaw puzzle texture (Jebrak, 1997).

While steam-heated blankets and hydrothermal breccias are also common in HS deposits, formation of adularia and bladed calcite as gangue minerals are very diagnostic (characteristics of) in LS deposits.
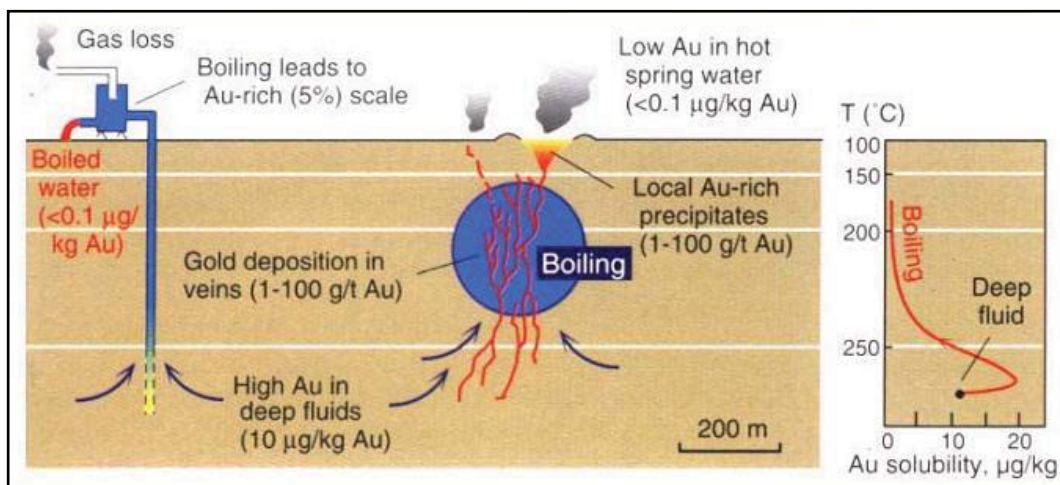


**Figure 2.5.** A sketch displaying the boiling process in the low sulphidation systems (from Cooke and Simmons, 2000).

Apart from boiling, mixing (dilution) of ascending fluids with marginal and shallow waters is the other principal process occurring in the geothermal environment. Dilution of ascending thermal waters as a result of mixing process

causes a decrease in temperature and triggers ore and gangue mineral precipitation (Giggenbach and Stewart, 1982).

The ingredients for ore and gangue minerals dissolved in the epithermal fluid rise through upflow channels. Change in fluid chemistry due to boiling first causes the base metals, then the ore and gangue minerals and finally silica sinters to deposit in a well-recognized temporal and vertical sequence (Buchanan, 1981; Hedenquist *et al.*, 2000) (Figure 2.6). The average vertical interval of LS ore mineralization zones is typically about 300 m. The boundary between the upper precious metals and lower base metals is accepted as the level of boiling (Buchanan, 1981).

Within the precious metal ore interval, the mineralogy generally consists of argentite, adularia, quartz, pyrite, electrum, calcite and ruby silvers (Buchanan, 1981). Gold ore is commonly associated with the major gangue minerals; quartz (as the most dominant), calcite and adularia (both indicating near-neutral pH conditions) and hydrothermal sericite. In the precious metal ore horizon, the quartz gangue is typically very fine grained and commonly has banded and crustified textures (Buchanan, 1981; White and Hedenquist 1995; Hedenquist *et al.*, 2000).

Deposition of the dominant gangue phase quartz is controlled by decreases in fluid temperature, pressure and salinity. These changes in fluid affect the morphology, crystal structure and chemical composition of silica and cause the formation of various quartz textures (Hayba *et al.*, 1985; Corbett and Leach, 1997). The different textures of gangue quartz forming in LS epithermal deposits and their relation to possible hydrothermal conditions will be explained in detail in Chapter 5.

Below the base of the precious metal ore interval, precious metal values gradually diminish and the content of galena, sphalerite and chalcopyrite increases. In addition, the volume of the calcite is decreased greatly while sericite and adularia are slightly to greatly diminished. Apart from these changes, quartz persists downwards from the base of the precious metal ore zone (Buchanan, 1981).
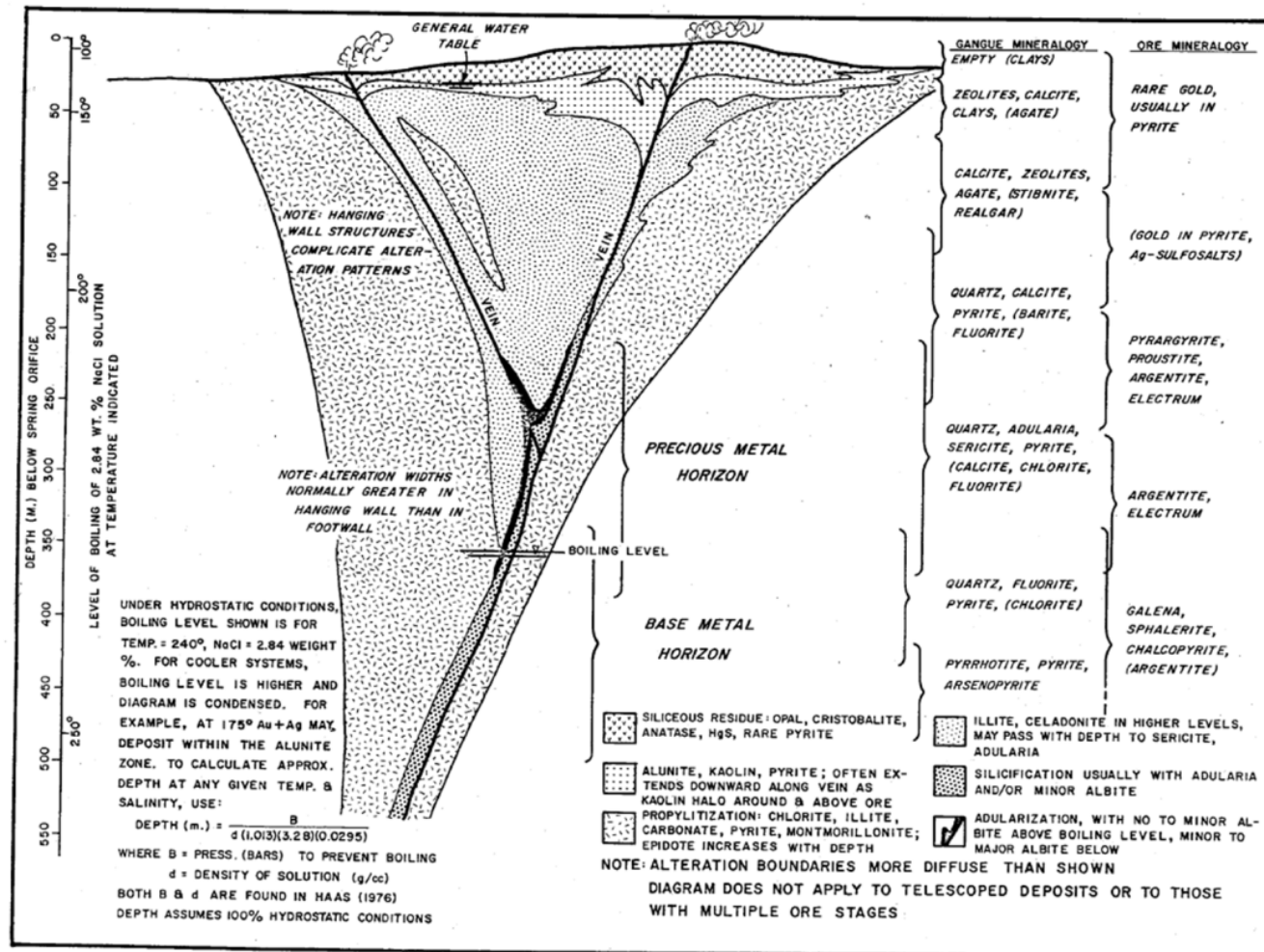
**Figure 2.6**. A generalized sketch showing the vertical and horizontal mineral zoning in a typical epithermal deposit (taken from Buchanan, 1981).

Above the precious metal ore horizon, precious metal values drop rapidly. The quartz vein filling extends above the top of the precious metal ore zone, but the width of the quartz fill in the veins gradually decreases and the quartz is deposited as agate or chalcedony above the ore shoot. Toward the vein tops, the volume of quartz and agate (or chalcedony) diminishes and calcite becomes more common (Buchanan, 1981).

At the surface of the system where the neutral pH thermal water discharges, rapid cooling of the fluid results in super-saturation and formation of silica sinters, the most distinctive paleosurface feature of LS deposits. They form finely laminated terraces of amorphous silica and may have some plant fragments (White *et al*., 1989; White and Hedenquist, 1995; Corbett and Leach, 1997; Hedenquist *et al*., 2000). The presence of silica sinter proves that the system is low sulphidation. In addition, silica sinter defines the position of the paleosurface and, most importantly, it points out the location of the principal upflow channel of boiling fluid (Hedenquist *et al*., 2000). Silica sinters may not form in areas of high relief, because the water may flow laterally a great distance before reaching the surface, mixing with ground water and thus may not be capable of precipitating silica sinter (White and Hedenquist, 1995).

Ore-associated alteration forms due to the generation of $CO_2$-rich steam-heated water on the margin of the system and extends from the base of the precious metal ore horizon to the paleosurface (Buchanan, 1981; Hedenquist *et al*., 2000). Width of alteration halos around the conduit of fluid flow depends on the primary permeability of the host rocks; structurally focused ore has narrow alteration halos while wide alteration areas form in permeable rocks (Hedenquist *et al*., 2000). Temperature decreases both with decreasing depth and with increasing distance from the conduit of fluid flow results in a clear upward and outward zonation of temperature-dependent minerals (White and Hedenquist, 1995). Argillic assemblage (dominantly kaolinite, smectite, illite) forming on the margin of the system gives way outward to propylitic assemblage (as dominantly chlorite, calcite, epidote) as the mildly acidic (pH 4-5) water is progressively neutralized by

reaction with the host rock away from the conduit (Reyes, 1990; Hedenquist, 1990; White and Hedenquist, 1995). It should be noted that interstratified illite-smectite, smectite clays and kaolinite may be found within the ore zone as supergene alteration products of hydrothermal sericite (Hedenquist *et al.*, 2000).

Steam heated acid sulphate water forming in the vadose zone results in the formation of advanced argillic (AA) alteration blankets (kaolinite, cristobalite, smectite and locally alunite and native sulphur) which typically overlie the ore system in the hanging wall. This alteration assemblage may overprint the ore zone in case of the collapse of groundwater table (Simmons and Browne, 1990; Hedenquist *et al.*, 2000). In addition, when these acid sulphate waters descend along fractures, they may cause the formation of narrow zones of higher temperature minerals such as pyrophyllite and diaspore (Reyes, 1990; Hedenquist *et al*, 2000). Care must be given to distinguishing this steam heated acid water related AA alteration from the other types of advanced argillic alteration which are hypogene AA alteration (typical of lithocaps that host HS deposits) and supergene AA alteration (Bethke, 1984; Hedenquist *et al.*, 2000). Schematic illustration showing the formation of three types of AA alteration is given in Figure 2.7.

When steam-heated water collects at the water table, aquifer controlled stratiform blankets of dense silicification (typically chalcedony) may be created up to several kilometers distant from the steam heated water generation zone (Schoen *et al.*, 1974). The horizon of silicification is generally a few meters thick but the falling or rising of the water table may increase the thickness of it. Since these waters are also Fe-rich, they may create pyrite and marcasite near the base of the horizon (Hedenquist *et al.*, 2000).

During exploration, distribution of alteration minerals enable approximate determination of paleo-isotherms which help to locate conduits of paleofluid flow and so ore mineralization, and also to determine the level of erosion (White and Hedenquist, 1995; Hedenquist *et al.*, 2000).
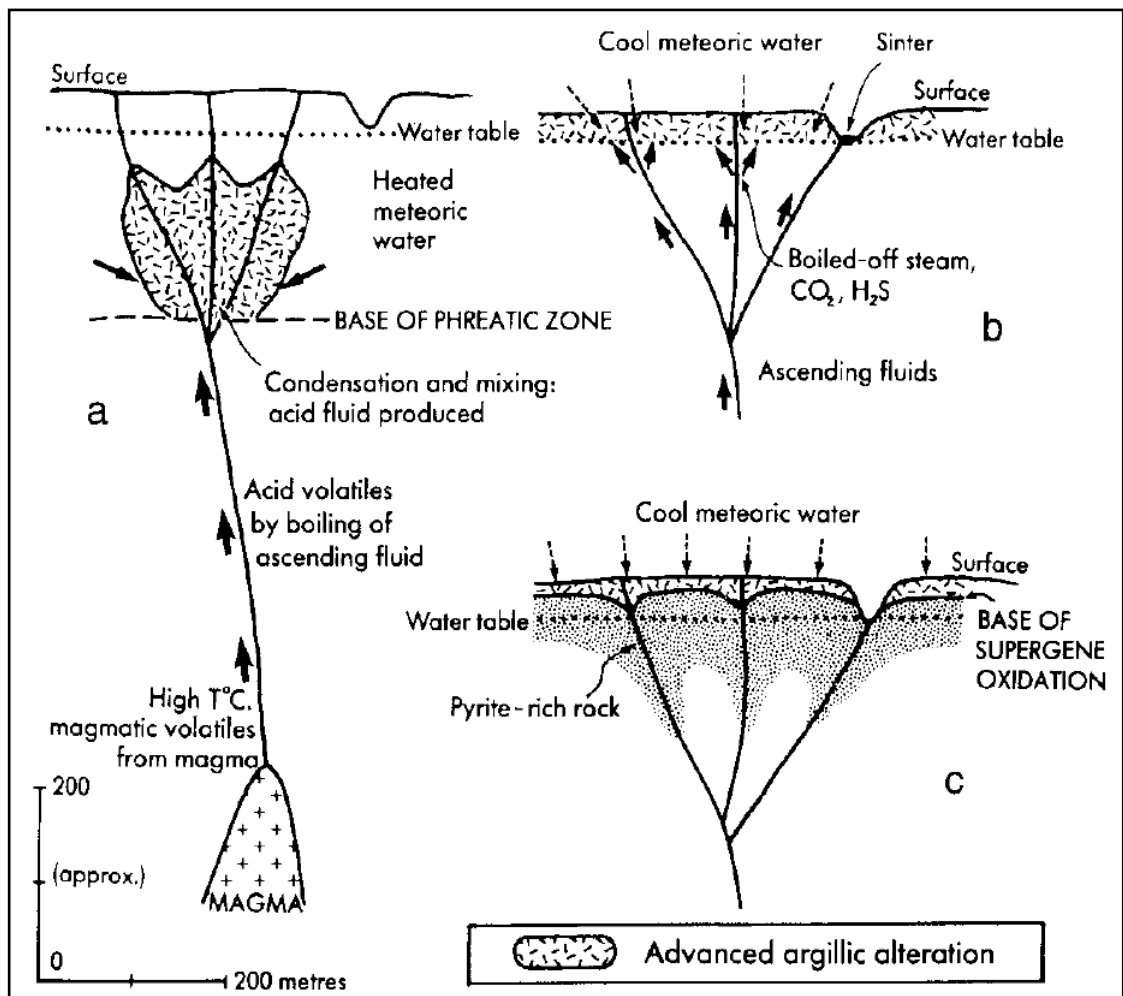
**Figure 2.7**.Schematic illustration showing the formation of three types of acid waters and advanced argillic alteration, hypogene, steam heated and supergene. In a, acidity caused by ascending and cooling HCl and $SO_2$, when the latter condenses into water, it forms sulphuric acid. In b, acidity comes from oxidation of $H_2S$ gas which condenses in the vadose zone. In c, acidity is formed when the pyrite is subjected to post hydrothermal oxidation within the vadose zone (From Sillitoe, 1993).

A schematic section showing the hypogene alteration patterns, blanket of steam-heated advanced argillic alteration and horizon of dense water table silicification in LS deposits is given in Figure 2.8.

Most low sulphidation epithermal gold deposits are associated with bimodal volcanic suites occurring in extensional tectonic settings such as continental and island-arc rifts which may form in near-, intra-, and back arc settings during the

17

subduction of oceanic crust, post-arc settings following the subduction termination, as well as post collisional settings (Figure 2.9).
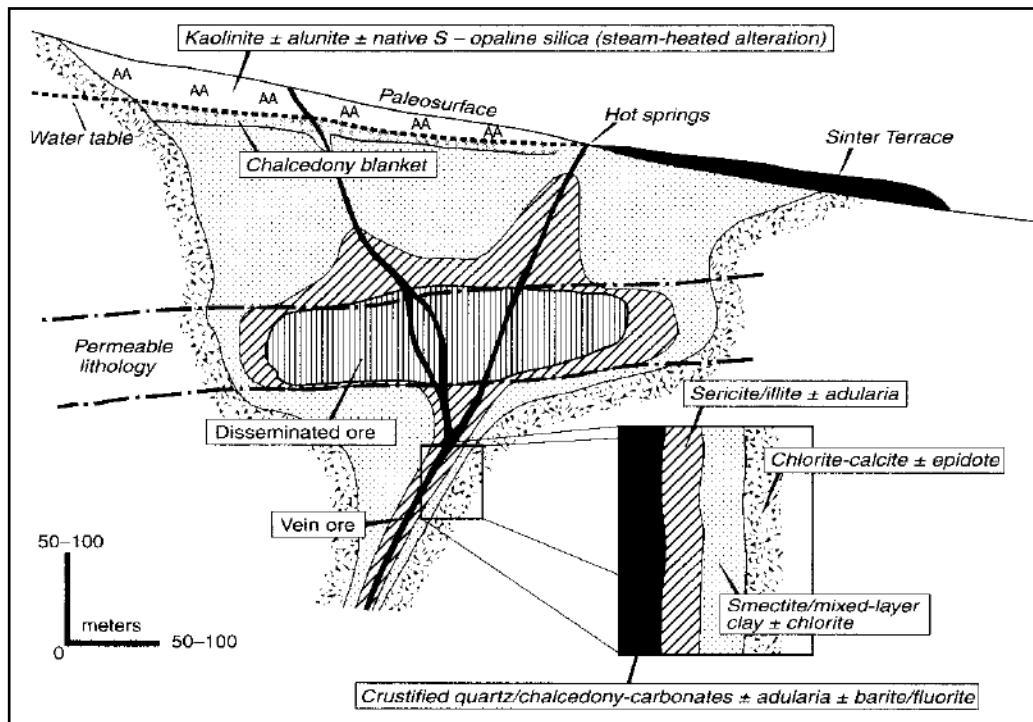


**Figure 2.8.**Schematic section that shows the generalized patterns of variable forms of hypogene alteration, steam heated advanced argillic alteration and horizon of water table silicification in a LS deposit. Note that the geologic variations may cause deviations from this generalization (from Hedenquist et al., 2000).

Bimodal volcanism related to rifting includes basalt or basaltic andesite plus rhyolite or rhyodacite of calc-alkaline and/or tholeiitic relationships with a significant lack of andesitic and dacitic rock compositions. However, there are a few deposits formed in andesitic-dacitic volcanic arcs, where regional extension is widespread (Sillitoe and Hedenquist, 2003).

LS epithermal gold deposits are generally hosted by a wide range of rock types from alkalic to calc-alkalic igneous rocks (Buchanan, 1981; Sillitoe, 1993), underlying basement rocks of any type (White and Hedenquist, 1990), and pyroclastic and sedimentary rocks (Hedenquist *et al.*, 2000).
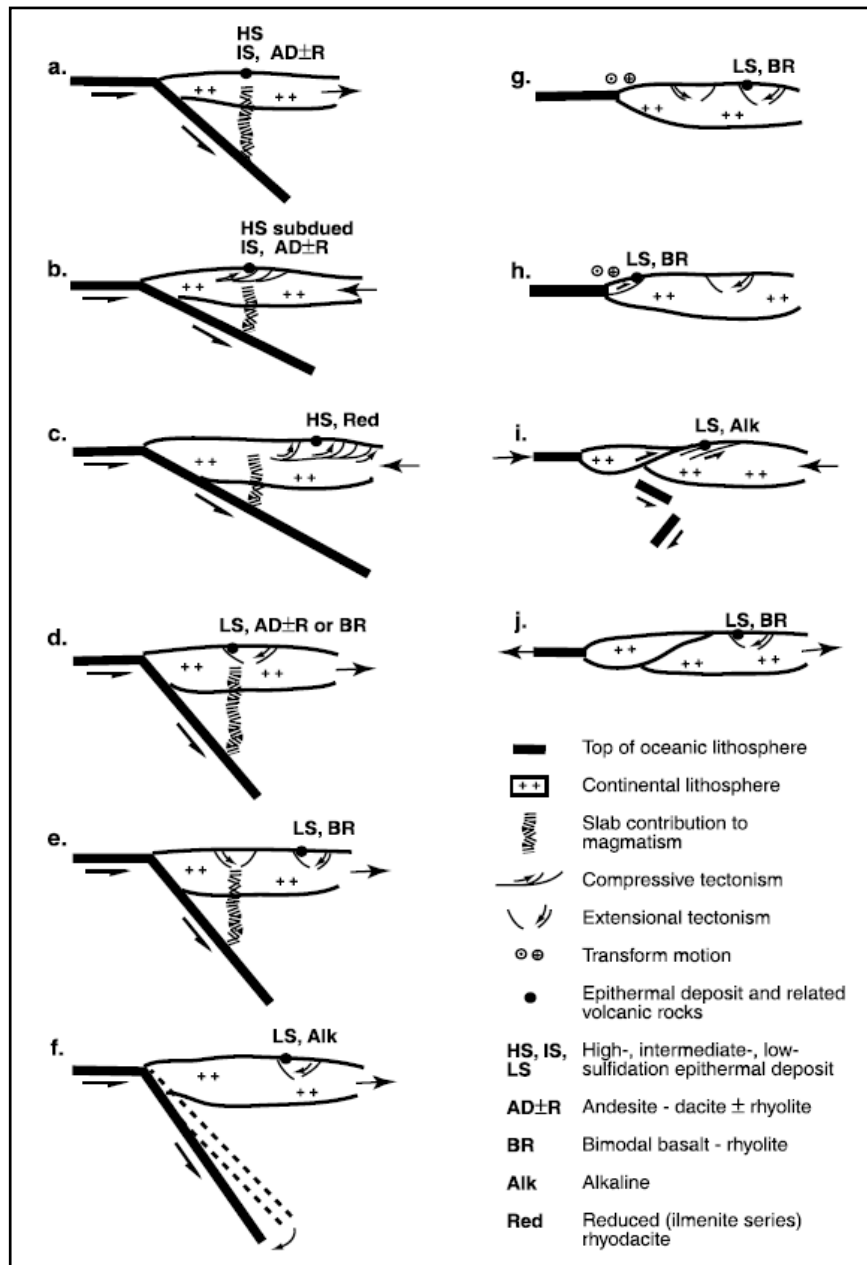
**Figure 2.9.** Schematic continental margin scale sections showing the selected volcanotectonic settings for HS, IS and LS deposits: **(a)** Neutral stress to mildly extensional arc. **(b)** Compressive back arc during arc volcanism. **(c)** Compressive arc with subdued volcanism. **(d)** Extensional arc. **(e)** Extensional back arc during arc volcanism. **(f)** Extensional back arc during transition from subduction- to rift related bimodal magmatism. **(g)** Extensional continental margin following cessation of subduction (an advent of transform faulting). **(h)** Compressive tectonism linked to transform fault boundary. **(i)** restricted postcollisional magmatism during collision-induced slab breakoff and compressive tectonism. **(j)** Extension due to tectonic collapse following continental collision (from Sillitoe and Hedenquist, 2003).

## 2.3. Structural control, deformation, permeability enhancement and fluid flow in epithermal gold deposits

Epithermal deposits originate in the upper, brittle crust of regions with active magmatic and geothermal activity. Mineralization in these deposits is dominantly hosted by veins or stockworks indicating dominant and strong structural control, although the form of these deposits may be disseminated ore that replace the host rock where lithologic control is dominant (White and Hedenquist, 1990; White and Hedenquist, 1995; Hedenquist *et al*., 2000, Cox, 2005). Brittle fault and fracture systems not only act as pathways of hydrothermal fluid circulation but also as depositional sites of epithermal ore and gangue minerals. Structures localizing these deposits are commonly pre-existing fractures, faults and fault related structures, joints, caldera structures, caldera margins and shear zones. Close to the paleosurface where structures are more complex, stockworks are more likely, passing down to veins at depth. In addition, minor structural features such as bedding and foliation planes may also host mineralization (e.g. Buchanan, 1981; Henley, 1985; White and Hedenquist, 1990; White and Hedenquist, 1995; Hedenquist *et al*., 2000; Cox *et al*. 2001; Cox, 2005). Major faults have a regional control on the localization of these deposits; however mineralization is commonly not situated on the major regional structure, but is located on a subsidiary faults and/or fracture zones (White and Hedenquist, 1990; Cox *et al*., 2001; Micklethwaite and Cox, 2004; Cox, 2005).

The most favourable mineral deposition mechanism in epithermal systems is boiling. Epithermal fluids rise from depth along structural conduits at high temperatures under suitable pressure to prevent boiling. Boiling occurs, when the pressure drops suddenly (e.g. through faulting or fracturing-related dilation) (e.g. Buchanan, 1981). Even small magnitude earthquakes (Mw<2) can trigger a boiling event (Sanchez-Alfaro *et al.,* 2016). Precipitation of ore and gangue minerals seals open spaces until structural permeability is occluded or lost (Buchanan, 1981; Henley, 1985; Hedenquist and Henley, 1985; Hedenquist *et al.,* 2000). Common

diagnostic textures in epithermal veins indicate multiple episodes of mineralization, brecciation and recementation associated with repeated and intermittent fluid flow rather than a continuous and steady-state process (Bateman, 1950; Buchanan, 1981; Sibson, 1987). Additionally, radiometric dating of some hydrothermal deposits shows that the permeability creation and hydrothermal fluid circulation could take place over thousands to tens of thousands of years (Fournier, 1989; Lalou *et al.,* 1993). This could be as long as millions of years in major porphyry systems (Sillitoe, 2010). How can permeability enhancement be achieved after the deposition of minerals in fractures and faults has choked permeable pathways and restrict fluid flow?

Boiling of the hydrothermal solution stops when the pressure increases as precipitation of minerals forms a sealed cap to the fracture system (White *et al.*, 1975). The sealing cap can be basically broken by tectonism or hydrofracturing (Buchanan, 1981) causing the creation of permeability and associated boiling and mineralization which later seals the system again. Rather than focusing on the development of fluid overpressures in the upper parts of the epithermal vein system, Hedenquist and Henley (1985b) proposes an alternative mechanism for the permeability creation in the sealed system. According to this mechanism, after the system is sealed, pressure of the fluid increases and the fluids are diverted to other channels. However, steam separated from the flowing hot water accumulates below the sealed cap and transmits the fluid pressure to the seal. Because gases continue to separate from the hot water, depth of the gas cap below the seal increases. When the seal pressure passes the lithostatic pressure, hydraulic fracturing (Philips, 1972) happens and hydrothermal eruption occurs (Figure 2.10) suggested by the presence of jigsaw puzzle textures in the vein system. Alternatively, seismicity could also cause the crushing of the seal, triggering a hydrothermal eruption without needing seal pressure higher than lithostatic (Hedenquist and Henley, 1985b).
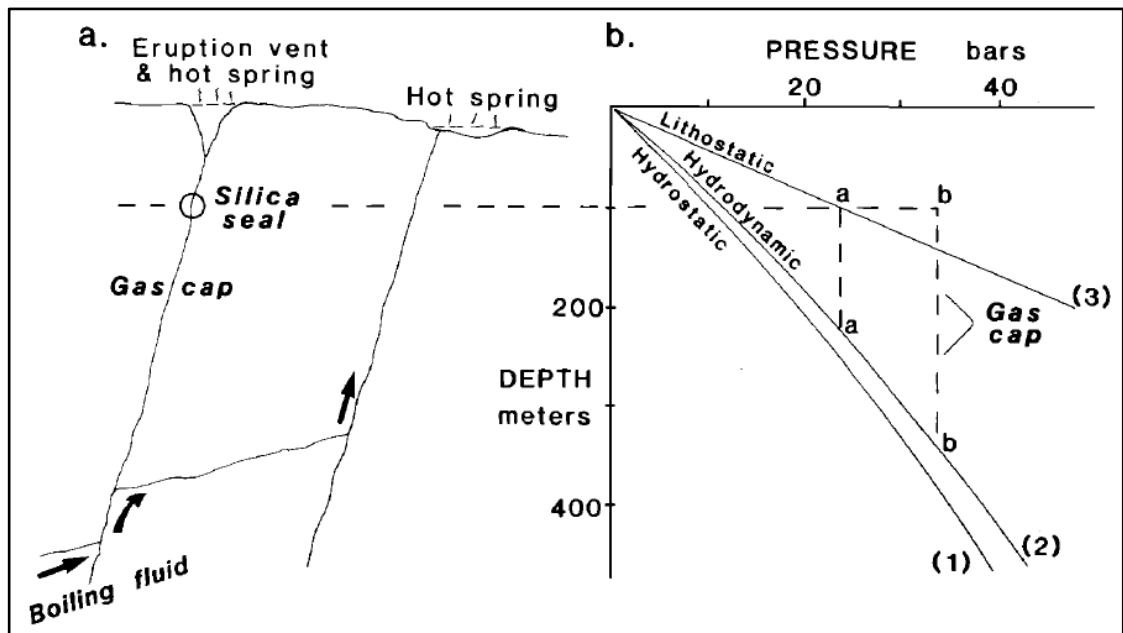
**Figure 2.10. (a)** Schematic cross section showing how local silica sealing can result in the formation of a gas cap over a boiling fluid flowing laterally, leading to hydraulic fracturing and hydrothermal eruption. **(b)** Pressure versus depth curves (1: hydrostatic; 2: hydrodynamic, 3: lithostatic) showing the extent of a gas cap necessary for pressures at a 100m deep sealed fracture to equal (profile a) or exceed (profile b) the lithostatic pressure. The pressure at the local seal is transmitted from the fluid reservoir by the compressed gas. Following sealing the gas pressure increases (aa toward bb) with time until the eruption is initiated by hydraulic fracturing or seismicity (from Hedenquist and Henley, 1985b).

Precipitation of minerals along faults causes the hydrothermal fluid to penetrate into the pore spaces of the adjacent wall rock. As the low density fluid tends to go up, the penetration zone is more widespread in the hangingwall (Philips, 1972). Increased pressure of fluid in the pore spaces of the rock above the fault plane decreases the effective principal stress of the rock and thus could trigger fault slip which in term increases permeability (Philips, 1972; Axen, 1992).

Davatzes and Hickman (2005) discuss the relationship between the deformation mechanisms controlling permeability and fluid flow, and the deformation environments controlled by the precipitated hydrothermal material in the fault/fracture system. In the shallowest zone of the geothermal system, lower pH leads to breakdown of rock forming minerals which increase the permeability of the fault zone (Davatzes and Hickman, 2005). Although exposed to the same stress

field and deformation conditions, permeability of a sealed fault can be regenerated by continued slip and associated brittle dilation (Davatzes and Hickman, 2005). Permeability may be nonuniform along the fault depending on the relationship between the variable strike of the fault and the orientation of the local stress direction (Micklethwaite *et al.*, 2010) or due to within-fault plane variability (Lunn *et al.*, 2008). Permeability can be maintained in structures dominated by calcite- and/or silica related minerals through brittle dilation associated with episodic reactivation and slip. Conversely, formation of chlorite and smectite phases due to the alteration by continued slip and fluid flow supports ductility and minimize dilatancy and permeability by inhibiting the ability of slip during shear (Davatzes and Hickman, 2005).

Permeability can be supported by the formation of new fault networks when the tectonic stress that is unfavourable for the reactivation of the sealed fault network change suddenly. However, these networks may form and propagate along unaltered rock that is more favourable with brittle failure, as the altered clay-rich rock requires large rotations in the stress field to form new fault networks (Davatzes and Hickman, 2005; Moir *et al*, 2013) because of the low frictional strength of most clays (Lockner and Beeler, 2002).

Major faults can be important barriers to or conduits to fluid flow (Caine *et al.*, 1996; Rowland and Sibson, 2004). Cataclasis causes a reduction in the grain size of the fault core that increases the deposition of minerals by increasing the area of fresh mineral surfaces and thus chemical reactions. Therefore, the core of the faults is sealed rapidly and become transient fault barriers or low permeability zones (Byerlee, 1993; Davatzes and Hickman, 2005). Despite clogging of the major faults due to mineral precipitation, permeability can be developed or maintained at the terminations of individual faults and interaction areas of multiple faults where the fracture density and connectivity is high (Curewitz and Karson, 1997; Cox *et al.*, 2001; Cox, 2005) because of the elevated stress concentration arising at these sites (Curewitz and Karson, 1997). Also, Davatzes *et al.* (2005) state that more tensile mean stress can be created by the mechanical interaction of multiple fault

segments at intersections which lead to the dilatant failure and fluid flow at these interaction areas. In addition, according to the Sibson (1987); because epithermal mineralization is often located in dilational jogs between en echelon fault segments within fault systems, arrest of earthquake ruptures at the fault tips which causes extensional fracturing and associated fluid pressure drop is responsible for triggering episodic boiling and rapid mineral deposition within dilational jogs. Moreover, following the major rupture on the main fault, precipitation in dilational jogs continues through the aftershock period (Sibson, 1987).

Permeability can also be enhanced or maintained along individual fault segments because interconnected fractures and subsidiary faults form in the adjacent wall rocks where damage zone occurs adjacent to a fault core (Caine *et al.*, 1996; Davatzes *et al.*, 2005). High permeabilities are generated in fault damage zones accompanying coseismic slip, although permeability is reduced in these zones because of the pore collapse and crack closure taking place during interseismic periods (Cox, 2005). Damage zones probably have higher bulk permeabilities than the individual fault segments owing to the more planar and structurally less complex characteristics of the individual fault segments (Cox, 2005). The damage zone structures that are permeable may also change position over geological time (Woodcock *et al.*, 2007; Burnside *et al.*, 2013). Multiple episodes of slip and the overprinting of successive brittle failure events may be observed in wide damage zones (Caine *et al.*, 1996).

Micklethwaite and Cox (2004, 2006) argue that if the event responsible for opening permeable pathways is an earthquake, although the permeability of the fault where the mainshock occurs may rapidly be lost due to the precipitation of hydrothermal minerals following the rupture events, enhanced fluid flow may occur along structures where aftershock ruptures focus. They argue that the locations of these aftershock structures are predictable based on stress transfer modelling. Using a damage mechanics formulation, Sheldon and Micklethwaite (2007) showed that aftershock zones detected by stress-transfer modelling closely correspond to the location of known mineralization. Moreover, they emphasize that the main fault

is rapidly healed after the main slip; while aftershock zone structures are exposed to the more protracted permeability and fluid flow relative to the main fault indicating enhanced mineralization potential of these zones.

# Chapter 3: Geological Setting

Kestanelik epithermal gold deposit was chosen as study area because it contains well-exposed mineralized quartz veins to study the structural controls on the veins which will shed light on the permeability enhancement processes during epithermal gold mineralization. Section 1 briefly presents the geology of Turkey. Then, section 2 outlines the geology of the Biga Peninsula according to the compiled literature data.

In section 3, the local geology of the area is defined with a geological map and a tectonostratigraphic section based on field studies conducted by the author. The main structures and paleo-stress analyses are also presented. The purpose of this section was to determine the possible age of the heat source and mineralization by linking the local geological history to the regional tectonic setting. The timing of the mineralization is a key constraint on the structural evolution of the epithermal vein-structure network.

In section 4, general characteristics of mineralization in the area are briefly described based on observations gathered during field studies and the examination of drill cores and geochemical analysis data of core samples obtained from Chesser Resources Ltd (license holder company of the Kestanelik province).

Section 5 discusses the results given in the chapter and summarizes the key highlights of the chapter.

## 3.1. Introduction to the geology of Turkey

The geological evolution of the Turkey has mainly been controlled by the relative movement of the Laurasia, Gondwana and Arabian plates during the consumption of the Paleo- and Neo-Tethys oceans. The boundaries of these plates in Turkey are represented by two main suture zones which can be considered as parts of the Alpine-Himalayan orogenic belt. The sutures are the Izmir-Ankara-Erzincan suture zone (IAESZ) (between the Pontides belonging to Laurasia and the Tauride-Anatolide block belonging to Gondwana) in the north, and the Bitlis-Zagros

suture zone (BZSZ) (between Tauride-Anatolide block and Arabian plate) in the south (Ketin, 1966) (Figure 3.1). Today's mosaic geometry of Turkey is explained by the amalgamation and/or juxtaposition of multi-rooted continental and oceanic fragments during orogenic processes.

## 3.2. Regional geology (Geology of Biga Peninsula)

Study area is located in the Biga Peninsula in NW Turkey which is characterized by juxtaposition of three tectonic terrains: Tauride-Anatolide Block (TAB) in the south, Sakarya zone of Pontides in the center and Rhodope-Strandja zone of Pontides in the north (Figure 3.1).

Cenozoic magmatic rocks together with marine and continental sedimentary rocks dominate the geology of the Biga Peninsula. Pre-Cenozoic metamorphic and ophiolitic rocks form the basement rocks of the region (Figure 3.2).
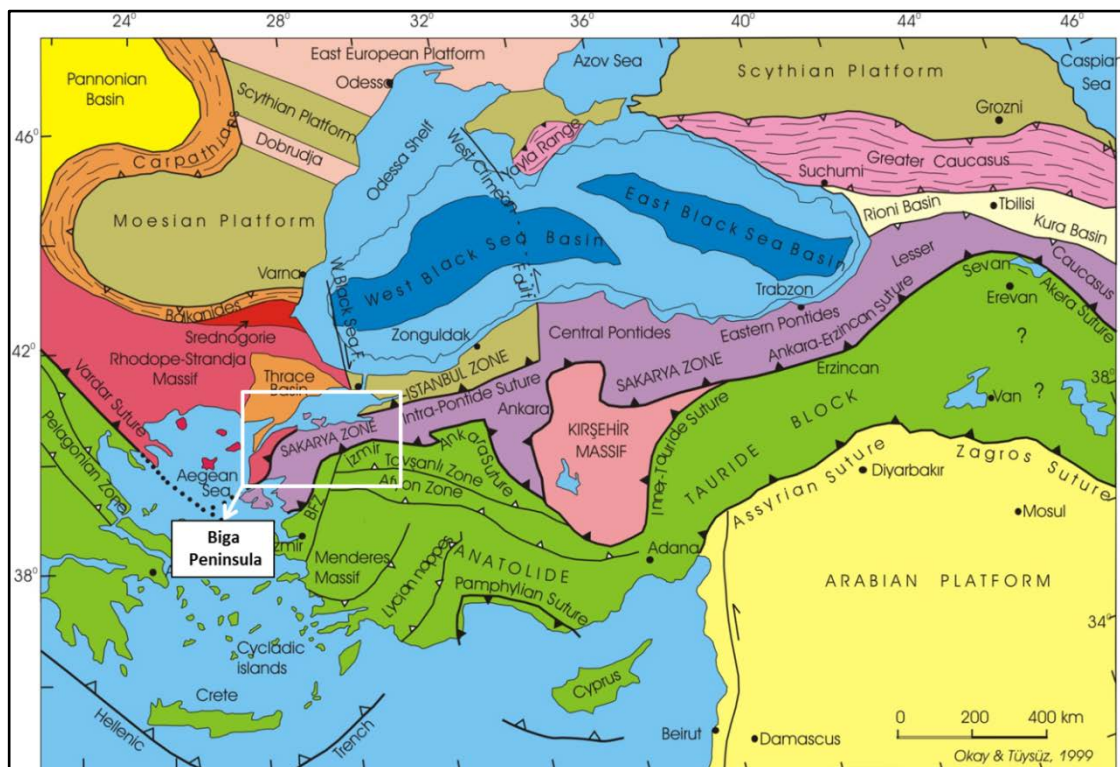


**Figure 3.1**. Paleotectonic map of Turkey (taken from Okay and Tüysüz, 1999).

### 3.2.1. Pre-Cenozoic rocks (Basement rocks)

Pre-Cenozoic basement rocks are observed as three different metamorphic complexes and slivers of NE-SW trending ophiolites or ophiolitic mélanges.

The oldest metamorphic complex is Paleozoic in age (308+/- 16 Ma, single-zircon Pb-Evaporation, Okay *et al.*, 1996) and is named as Kazdağ Massif (Bingöl *et al.*, 1973) or Kazdağ metamorphic complex (Okay and Satır, 2000). It is mainly composed of mica schist, olivine schist, amphibolite, pyroxenite, marble, metaophiolite, quartz-feldspathic gneiss, amphibolic gneiss, orthogneiss and paragneiss (Schuiling, 1959; Gümüş, 1964, Aslaner, 1965). In spite of their pre-Tertiary origin, their youngest peak metamorphism conditions were dated as Late Oligocene – Early Miocene (24-18 Ma, Okay and Satır, 2000) by Rb/Sr muscovite and biotite dating methods. An apatite fission track study of Cavazza *et al*. (2009) suggests Early to Middle Miocene (20-10 Ma) exhumation ages for the Kazdağ metamorphic complex and Cavazza *et al*. (2009) proposed that roll-back of the Hellenic trench may be the reason for the exhumation (or Miocene extension in the region). This Paleozoic basement is tectonically overlain by Permo-Triassic Karakaya complex comprising Carboniferous-Permian limestone olistoliths, blocks of Carboniferous high grade metamorphic rocks and early Permian to late Triassic low grade metamorphic rocks and pre-Jurassic intrusions (Bingöl *et al*., 1974; Aydın *et al*., 1995; Okay *et al*., 1996, 2002; Delaloye and Bingöl, 2000). These rocks are associated with the closure of the Paleo-Tethys Ocean (Şengör and Yılmaz, 1981; Okay *et al*., 1996, 1998) and are observed as thrust sheets or randomly distributed outcrops within the IAESZ. Although there is lack of information about their late stage metamorphism and/or exhumation in the literature, it is considered that they were already at the surface during the closure of the Neo-Tethys Ocean. In this respect, Tertiary evolution of these rocks can be associated with the development of an accretionary prism.  The units of the Karakaya complex together with the Kazdağ Massif are exposed at the south of the Biga Peninsula while the last metamorphic bodies of the region, which are entitled as Çamlıca metamorphics, crop out as SW-NE trending bodies in association with ophiolites along the northern

margin of the peninsula. The most common lithology of the Çamlıca metamorphics is grey, brown, greenish brown, well foliated, partly carbonitized quartz-mica schist (Okay *et al*., 1990). There is no unequivocal opinion on the tectonic setting of the Çamlıca metamorphics. Kalafatçıoğlu (1963) and Bilgin (1999) proposed that they are overlying units of the Kazdag massif. However, they have also been attributed to the closure of the one of the branches of the Neo-Tethys between Sakarya continent and Rhodope-Strandja zone (Intra-Pontide Suture Zone (IPSZ)) (Okay *et al.*, 1991: 1996: Okay and Tüysüz, 1999: Beccaletto and Jenny, 2004). Additionally, Aygül *et al*. (2012) also proposed that (i) the Çamlıca metamorphics constitute the northernmost continental margin of the former Sakarya continent (ii) they were subducted under the Rhodope-Strandja zone during the Late Cretaceous (iii) the converGençe lasted until Early Eocene and (iv) and that during Middle to Late Eocene they started to be exhumed and reached high crustal levels. Though the primary age of the Çamlıca metamorphics is not known, they are thought to be Paleozoic. Çamlıca metamorphics have probably undergone a HP–LT metamorphism based on relics of eclogites and three muscovite samples from quartz mica schists give 69 to 65 Ma Rb/Sr age intervals (Okay and Satır, 2000b). These ages indicate Maastrichtian aged regional metamorphism.

Unmetamorphosed ophiolitic bodies of the region are entitled the Çetmi ophiolitic melange and the Denizgören ophiolite (Okay *et al*., 1990). The Çetmi ophiolitic melange covers large areas to the west of Kazdağ metamorphic complex and consists of spilitised basic volcanic and pyroclastic rocks, limestone blocks, shale, and greywacke with minor serpentinite, radiolarian chert and eclogites (Okay *et al*., 1990). The Çetmi ophiolitic melange thrusts over the Çamlıca metamorphics while it has a normal faulted contact with the Kazdağ metamorphic complex. The melange is covered by Cenozoic sedimentary and volcano-sedimentary sequences (Yüzer and Tunay, 2012). The biostratigraphic ages determined from the radiolarites and limestone blocks of the melange vary between Early Triassic-Late Cretaceous time interval (Okay *et al*., 1990; Beccaletto *et al*., 2005) which indicate that the melange formation was completed by the Late Cretaceous.

The Denizgören ophiolite forms a NE-trending outcrop to the north of the town of Ezine and is largely made up of serpentinized harzburgite with minor basalt and gabbro (Okay *et al.*, 1991). The Denizgören ophiolite thrusts over Permo-Triassic aged sedimentary rocks and Çamlıca metamorphics in the west and in the east respectively (Okay *et al.*, 1991). Ar/Ar radiometric ages of amphibolites taken from the base of the ophiolite were determined as 117±1.5 and 118.3±3 Ma (Okay *et al.*, 1996), and 125±2 Ma (Beccaletto and Jenny, 2004) which constrains the probable initiation of obduction.

### 3.2.2. Cenozoic rocks

Plutonic, volcanic and volcano-sedimentary rocks which are products of Cenozoic magmatism together with marine and continental sedimentary rocks overlying the pre-Cenozoic basement rocks constitute the Cenozoic rocks of Biga Peninsula (Figure 3.2).

### 3.2.2.1. Cenozoic magmatic rocks

Extensive magmatism was prevailing in NW Turkey between the Middle Eocene and Late Miocene. Generally, Cenozoic magmatism shows calc-alkaline character between Middle Eocene and Early Miocene and alkaline character starting from the Middle Miocene (Altunkaynak and Genç, 2008). While the plutonic products of alkaline magmatism are not exposed at the surface (Akay and Erdoğan, 2004), plutonic products of calc-alkaline magmatism are widely exposed in the region. These plutons can be grouped into two with respect to the location of the Izmir Ankara Suture Zone (IASZ) separating the Sakarya zone of Pontides and the Anatolide-Tauride Block. The plutons located along and at the south of IASZ can be named as the southern group and consist of the Orhaneli, Topuk, Gürgenyayla, Göynükbelen plutons, while the ones located at the north of IASZ and at the south of Marmara Sea can be named as the northern group and include Fıstıklı, Kapıdağ, Karabiga, Kestanbol, Evciler, Eybek, Ilıca-Şamlı, Kuşcayır and Çataldağ plutons (Figure 3.2).
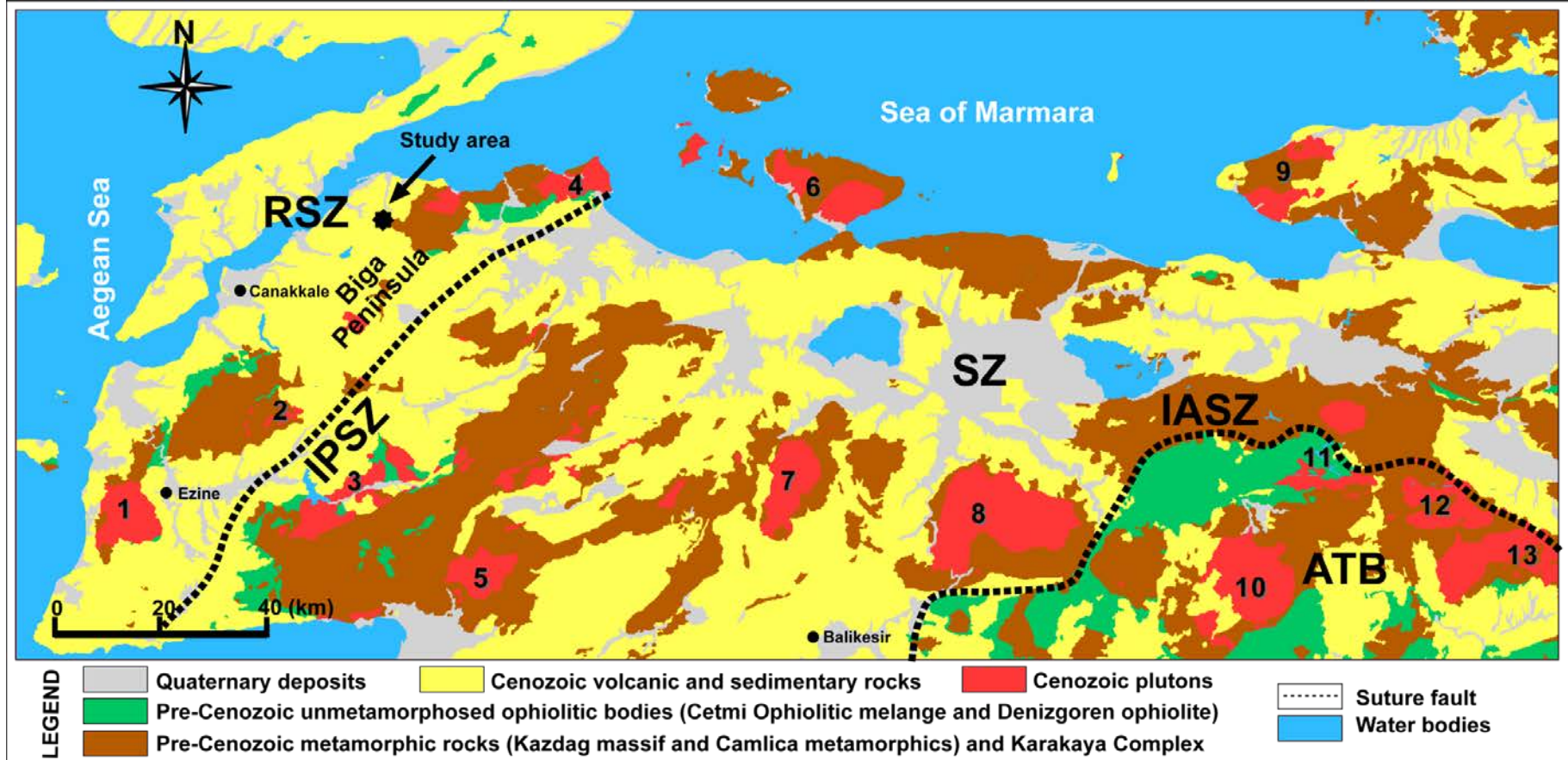
**Figure 3.2**. Simplified geological map of the Biga Peninsula (ATB: Anatolide-Tauride Block, IASZ: Izmir-Ankara Suture Zone, IPSZ: Intra-Pontide Suture Zone, RSZ: Rhodope-Strandje Zone, SZ: Sakarya Zone, 1: Kestanbol pluton, 2: Kuşçayır pluton, 3: Evciler pluton, 4: Karabiga pluton, 5: Eybek pluton, 6: Kapıdağ pluton, 7: Ilıca-Şamlı pluton, 8: Çataldağ pluton, 9: Fıstıklı pluton, 10: Orhaneli pluton, 11: Topuk pluton, 12: Göynükbelen pluton, 13: Gürgenyayla pluton) (modified from Türkecan and Yurtsever, 2002).

The Southern group plutons intrude into basement rocks of the Tauride-Anatolide Block which are overlain by ophiolitic rocks of the IAESZ (Harris *et al.*, 1994). They consist mainly of diorite, quartz diorite, granodiorite and syenite (Harris *et al.*, 1994; Altunkaynak, 2004; Dilek and Altunkaynak, 2007, Okay and Satır, 2006). Their isotopic ages range from ~53 to ~45 Ma based on Ar/Ar, Rb/Sr and U/Pb radiometric dating methods (Okay and Satır, 2006 and references therein). Their volcanic equivalents are not present in the region (Dilek and Altunkaynak, 2007).

The Northern group plutons intrude into basement rocks of the Sakarya zone and can be subdivided into two groups based on their ages and can be divided into the northern-Eocene and northern-Oligo-Miocene groups. The northern-Eocene group includes Fıstıklı, Kapıdağ and Karabiga plutons, whereas Kestanbol, Evciler, Eybek, Ilıca-Şamli, Kusçayır and Çataldağ plutons belong to the latter group.

The northern-Eocene group of plutons is mainly characterized by monzogranite, granodiorite and granites. Volcanic units associated with these plutons are pyroclastic rocks and basaltic to andesitic lavas which are intercalated with Eocene marine units (Siyako *et al.*, 1989; Genç and Yılmaz, 1997; Dilek and Altunkaynak, 2006). Their isotopic ages vary between ~48 and ~34 Ma based on Ar/Ar, K/Ar and Rb/Sr dating techniques (Delaloye and Bingöl, 2000; Okay and Satır, 2000; Köprübaşı and Aldanmaz, 2004).

The northern-Oligo-Miocene group of plutons is composed of granodiorite, granite, quartz diorite and quartz monzonite (Genç, 1998; Yücel-Öztürk *et al.*, 2005), while their volcanic counterparts consist of andesite, dacite, rhyodacite and rhyolite, together with pyroclastic rocks which are intercalated with Oligo-Miocene lacustrine sedimentary units (Bingöl *et al.*, 1994; Genç, 1998; Erkül *et al.*, 2005, Yücel-Öztürk *et al.*, 2005). Radiometric ages of these magmatic rocks and biostratigraphic ages of intercalated sedimentary units vary between ~31 and ~15 Ma (Ercan *et al.*, 1985, 1995; Genç, 1998, Erkül *et al.*, 2005).

By Middle Miocene, the geochemical character of the Cenozoic magmatism shifted from calc-alkaline to mildly-alkaline. The volcanic products of this

transitional Middle Miocene magmatism, have a short age span (around 15.2 Ma) (Ercan *et al.*, 1995; Aldanmaz *et al.*, 2000), and are mainly basaltic andesite to andesite, trachy andesite and pyroclastic rocks intercalated with mildly alkaline basaltic lavas (Akay and Erdogan, 2004; Altunkaynak and Dilek, 2006; Altunkaynak and Genç, 2008). These rocks are generally associated with NNE- trending trans-tensional fault systems (Yılmaz *et al.*, 2000; Erkül *et al.*, 2005).

Although magmatism waned for a short time between ~15-11 Ma, it was renewed in the Late Miocene. During the Late Miocene, Cenozoic magmatism in NW Turkey produced short-lived (~11 - ~8.32 Ma) OIB-type mafic alkaline lavas which classify as basalt, basanite and trachybasalt of which potassic and sodic compositions progressively increase towards the south over time (Savaşcın and Oyman, 1998; Aldanmaz *et al.*, 2000; Dilek and Altunkaynak, 2007; Altunkaynak and Genç, 2008). These Late Miocene mafic alkaline lavas are generally controlled by the structures associated with the North Anatolian Fault Zone (Kaymakcı *et al.*, 2007).

Although the Late Miocene volcanic rocks form the latest magmatic rocks of the Biga Peninsula, Cenozoic magmatic activity continued until the Quaternary in southwestern Turkey. Strongly alkaline Late Miocene to Quaternary magmatism resulted in formation of volcanic rocks which are composed of basalts, basanites and phonotephrites with potassic to ultrapotassic compositions (Richardson-Bunbury, 1996; Seyitoğlu *et al.*, 1997, Savaşcın and Oyman, 1998; Aldanmaz *et al.*, 2000; Alici *et al.*, 2002; Innocenti *et al.*, 2005; Altunkaynak and Genç, 2008). These rocks, for which ages vary between ~8.4 and ~0.13 Ma, are mainly associated with E-W-oriented major extensional fault systems (Richardson-Bunbury, 1996; Seyitoğlu *et al.*, 1997, Savaşcın and Oyman, 1998; Aldanmaz *et al.*, 2000; Alıcı *et al.*, 2002; Dilek and Altunkaynak, 2007).

Although there are a variety of recent studies about the nature of Cenozoic magmatism in western Turkey, the tectonomagmatic model behind it is controversial due to the existence of the Neo-Tethyan suture Izmir-Ankara suture zone (IASZ) in NW Turkey and still-active subduction zone along the Hellenic trench

in the south of Western Turkey (Figure 3.1). Timing of late stage subduction and collision along IASZ while still not certain, is proposed as Late Cretaceous-Early Eocene (Şengör and Yılmaz, 1981; Harris *et al.*, 1994; Okay and Tüysüz, 1999, Sherlock *et al.*, 1999; Önen and Hall, 2000, Kaymakcı *et al.*, 2009, Hinsbergen *et al.*, 2010). Commencement of north-dipping subduction along the Hellenic trench is suggested as Middle Miocene (McKenzie, 1978; LePichon and Angelier, 1979; Meulenkamp *et al.*, 1988). Therefore, tectonomagmatic models concerning the IASZ are related to post-collisional magmatism, while the one concerning the Hellenic trench are related to arc magmatism.

Delaloye and Bingöl (2000) interprets Eocene - Miocene aged intrusions as arc related intrusions due to the subduction along the Hellenic trench, while others propose a post collisional environment for the formation of the plutons exposed in northwestern Turkey through (1) slab-breakoff (Altunkaynak and Dilek, 2006; Altunkaynak, 2007; Altunkaynak and Genç, 2008) and (2) delamination of either the subducting lithosphere or the lowermost part of the lithosphere (e.g., thermal boundary layer at the base of the lithosphere) (Köprübaşı and Aldanmaz., 2004; Dilek *et al.*, 2010). In addition to these studies, a study by Okay and Satır (2006) suggests that the Eocene plutons were developed in a magmatic arc formed as a result of subduction along the WNW-ESE trending Vardar suture, although the study does not give an age for the initiation of subduction along the Vardar suture.

### 3.2.2.2. Cenozoic sedimentary rocks

Cenozoic sedimentary rocks of the Biga Peninsula consist of four different sequences separated by three major erosional unconformities: Maastrichtian-Early Eocene, Middle Eocene-Oligocene, Miocene and finally Pliocene-Quaternary sequences.

Rocks of Maastrichtian-Early Eocene age are exposed in a limited area at the east of Lapseki. Although there is no observable contact between them and the basement rocks, their northern equivalents lie on ophiolitic mélange in the Gelibolu Peninsula. In spite of having laterally and vertically transitional deeper marine to

continental sequences in the north, only continental to shallow marine deposits crop out in the south of the Biga Peninsula (Fıçıtepe formation; Sfondrini, 1961 and Siyako *et al.*, 1989).

By Middle Eocene, Maastrichtian-Early Eocene sequences are unconformably overlain by fossilliferous limestone and sandy limestone of Soğucak Formation. It is suggested that the Soğucak formation was deposited as a result of widespread transgression affecting the whole of north western Anatolia. Towards the north, it passes up to a thick Late Eocene aged turbiditic sequence composed of sandstone, shale and marl (Siyako *et al.*, 1989; Sümengen and Terlemez, 1991; Özcan *et al.*, 2010). In NW Turkey, rocks of Oligocene age indicating a marine regression are represented by coarsening upward terrigenous clastics in shale and marl; however the Biga Peninsula does not have any outcrops of this Oligocene sequence because of the lasting uplift in the region.

In the Early-Middle Miocene, fluvial conglomerate, sandstone, shale, siltstone, tuff and lignite were deposited in small, isolated, fault-bounded intra-continental basins in the southern Biga Peninsula. Commencement of this intra-continental deposition is related to the exhumation of the Kazdağ massif and they are thought to be products of a supra-detachment basin (Küçükkuyu formation; Cavazza *et al.*, 2009). In the northern Biga Peninsula, however, Miocene rocks are represented by Late Miocene aged laminated and cross bedded coastal sandstone which is in transition with a shallow marine sequence composed of limestone, conglomerate, sandstone, shale and marl towards the north and west around the Bosphorus of Canakkale and the Aegean Sea.

The Plio-Quaternary period in Biga Peninsula is represented by fluvial conglomerate, sandstone and shale together with lacustrine carbonates.

### 3.2.3. Tectonic setting of the Biga Peninsula

Tectonic evolution of the Biga Peninsula comprises two main periods: paleo-tectonic period (Pre-Neogene) and neotectonic period. Closure of Paleo- and Neo-Tethys Oceans and subsequent collision due to the progressive convergence

between these plates resulted in the amalgamation and/or juxtaposition of continental and oceanic fragments such as the Kazdağ massif, Karakaya complex, Çamlıca metamorphics, Çetmi ophiolitic melange and Denizgören ophiolite (see section 3.2.1). Although evolution of the Paleo-Tethys Ocean is controversial, it has been suggested that the closure of this ocean was completed in Late Triassic (Şengör and Yılmaz, 1981; Okay *et al.*, 1996; 1998).

Timing of late stage subduction (resulted in the closure of the northern branch of Neo-Tethys Ocean) and collision along IASZ is proposed as Late Cretaceous-Early Eocene (Şengör and Yılmaz, 1981; Harris *et al.*, 1994; Okay and Tüysüz, 1999; Sherlock *et al.*, 1999; Önen and Hall, 2000; Kaymakcı, 2009; Hinsbergen *et al.*, 2010). Middle-Late Eocene shallow marine Soğucak formation, a result of widespread transgression affecting NW Anatolia due to probable regional uplift, marks the continental collision along IASZ. Youngest peak metamorphism age of 24-18 Ma (late Oligocene-Early Miocene) obtained from the Kazdağ Massif (Okay and Satır, 2000) has been interpreted as a result of further convergence after the collision along IASZ.

Biga Peninsula neotectonics are due to: (1) dextral strike slip faulting along the North Anatolian Fault Zone (NAFZ) resulting from the westward escape of the Anatolian Block due to collision between the Arabian and Anatolian plates (McKenzie, 1972; Şengör *et al*, 1985), (2) N-S directed extension due to subduction along the Hellenic trench S of Western Turkey (McKenzie, 1972, 1978; LePichon and Angelier, 1979; Meulenkamp *et al.*, 1988) (Figure 3.3). The age of the NAFZ is proposed as Late Miocene (Kaymakcı *et al.*, 2007) and the initiation of north-dipping subduction along the Hellenic trench as Middle Miocene (McKenzie, 1978; LePichon and Angelier, 1979; Meulenkamp *et al.*, 1988). The movement along the E-W directed NAFZ with the N-S directed extension in the Biga Peninsula results in a trans-tensional regime, represented by NE-SW directed splays of NAFZ having dextral strike slip motion with normal components (Kaymakcı *et al.*, 2007).
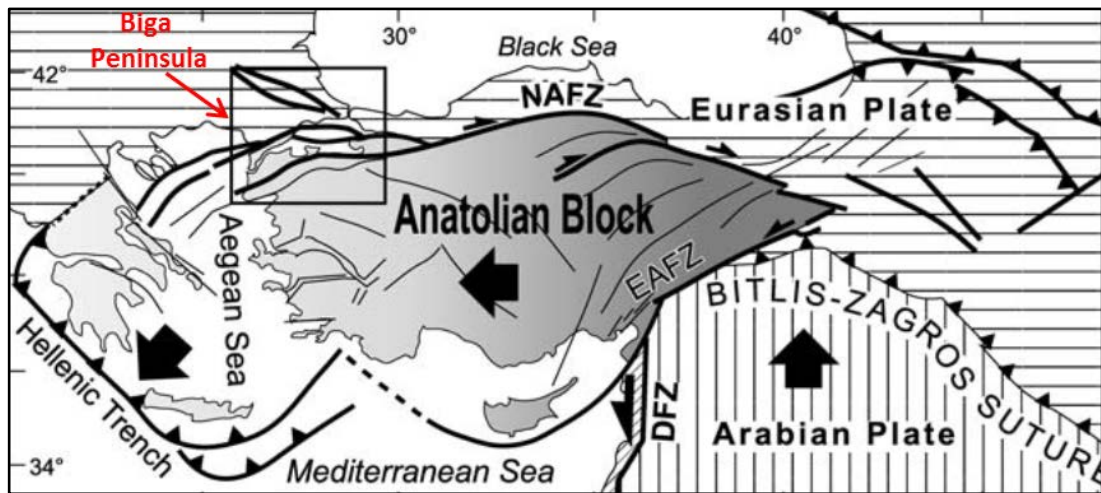
**Figure 3.3.** Map showing the major tectonic elements and plate reconstruction of Turkey. DFZ: Dead Sea Fault, EAFZ: East Anatolian Fault Zone, NAFZ: North Anatolian Fault Zone (taken from Kaymakcı *et al.*, 2007).

## 3.3. Local geology (Kestanelik deposit area geology)

Geology of the deposit area was first mapped by Tüprag (the first license holder company of the Kestanelik area) and then developed by a consultant, Simon Meldrum, on behalf of Chesser Resources Ltd. (second license holder company of the province) (Meldrum, 2009). These maps were combined by McLean (2011) in the 43-101 technical report of the Kestanelik project (Figure 3.4). In the report, there is no information on how the maps were produced, but the relationships between the intrusions, volcanic rocks and sediments are poorly understood due to paucity of critical outcrops. After two visits to the study area, it became clear that this combined map is not accurate enough for this PhD study, so I decided to re-map the geology of the area.

The deposit area is marked by two hills Kovanlık hill and Karatepe hill in the north and sits within the SE-NW valley of the Kestanelik River. Valley sides are steep and generally covered by pine trees and thorn bushes. Due to the steep geography of the area and the thick soil cover, natural outcrops are mainly on the valley floor. Multiple artificial outcrops where drill pads were sited (Figure 3.5) had not previously been incorporated into any version of the geological map and provided key constraints on the position of certain boundaries. Two weeks were spent in the

field for the purpose of geological mapping covering approximately 6 km$^2$. All accessible areas of the study area were walked and notes recorded about the rock units and the lithological boundaries. Photos were taken from key locations (well exposed part of the lithological units, lithological boundaries etc.). Strike and dip of foliations and bedding planes were measured using a Brunton geological compass. Point data (x,y,z) were collected from locations of lithological units, boundaries, strike and dip data using a Garmin GPS. These collected point data (438 points) and the top lithology of all drill holes (both diamond cut and reverse circulation (RC) holes) (397 points) (Figure 3.5) were then used to prepare the revised geological map (Figure 3.6) using GIS software Global Mapper, Google Earth and drawing software Freehand MX. A generalized tectonostratigraphic section for the area is given in Figure 3.7.
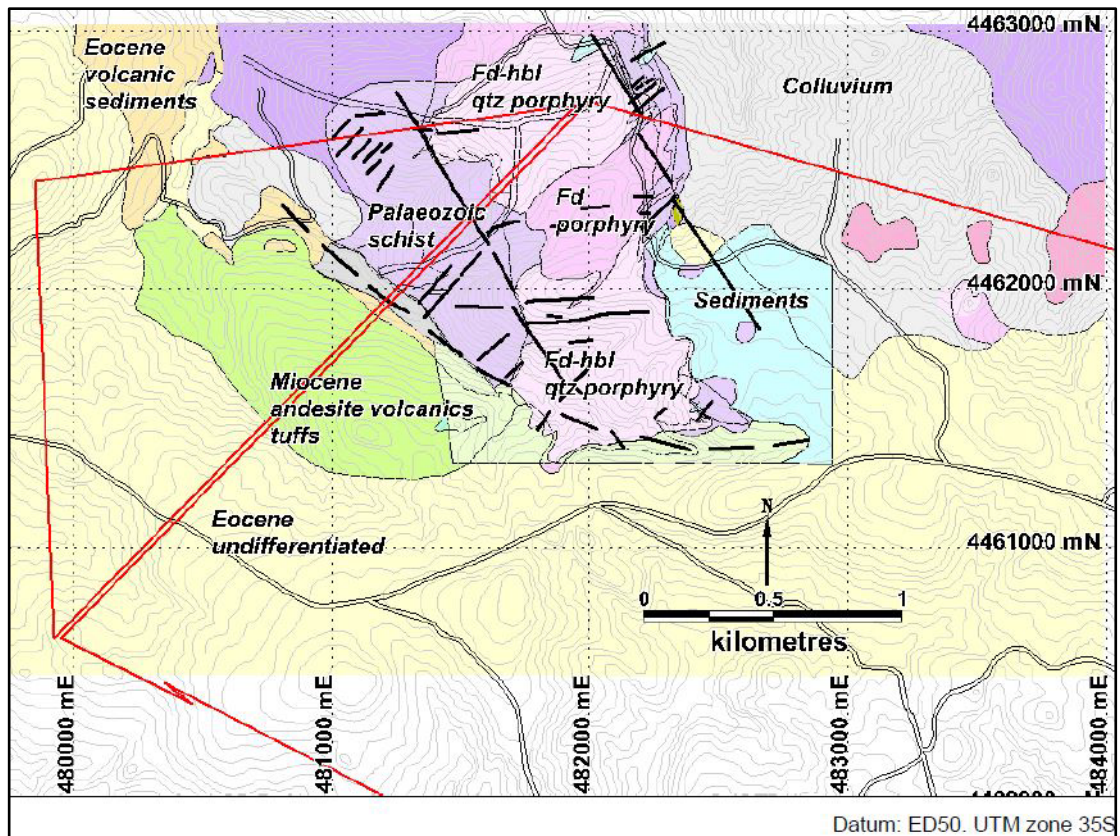


**Figure 3.4.** Detailed geology of the Kestanelik property. The license boundaries are shown as red lines. Interpreted structures are shown as black lines. (from Neil McLean, 2011).
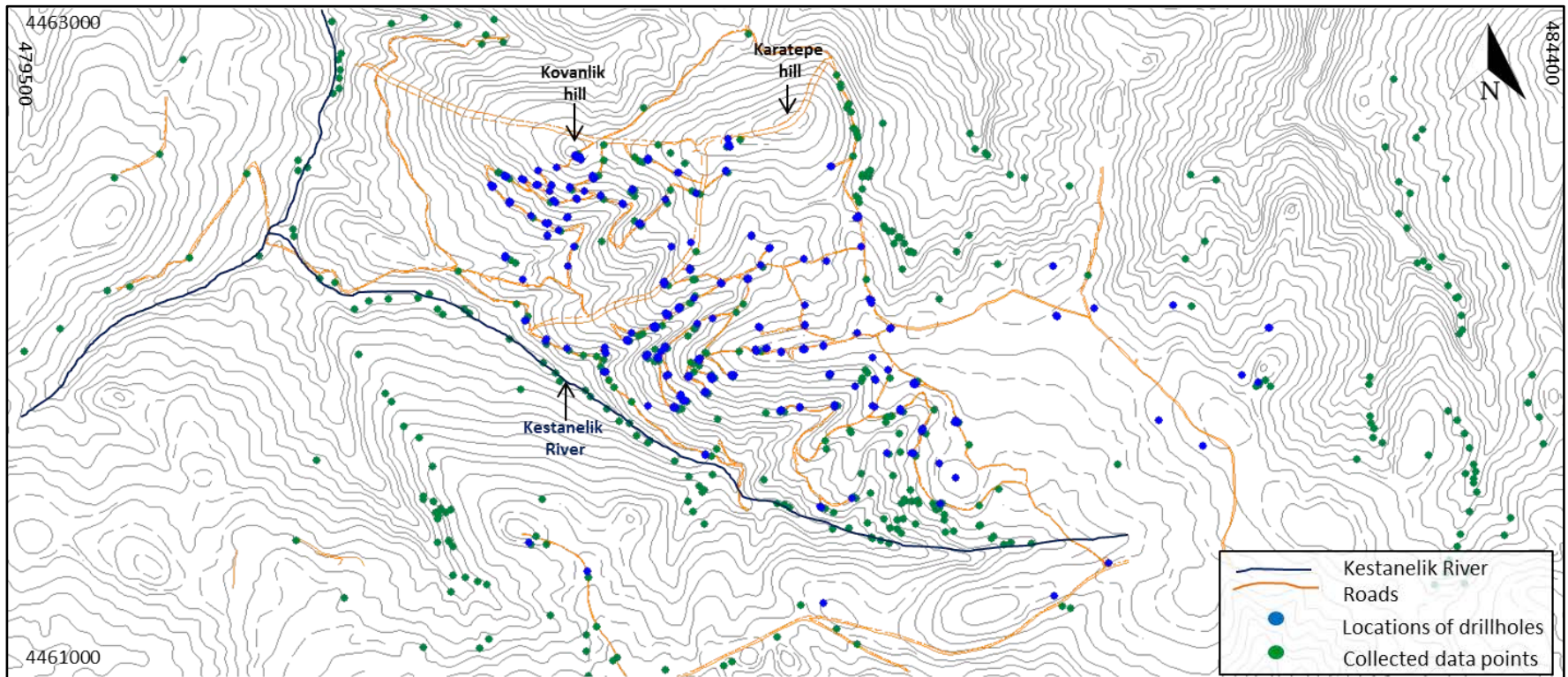
**Figure 3.5.** Topographical map of the study area with roads of drill pads and geological mapping data points (Note that the topographic contour interval is 10 m.).
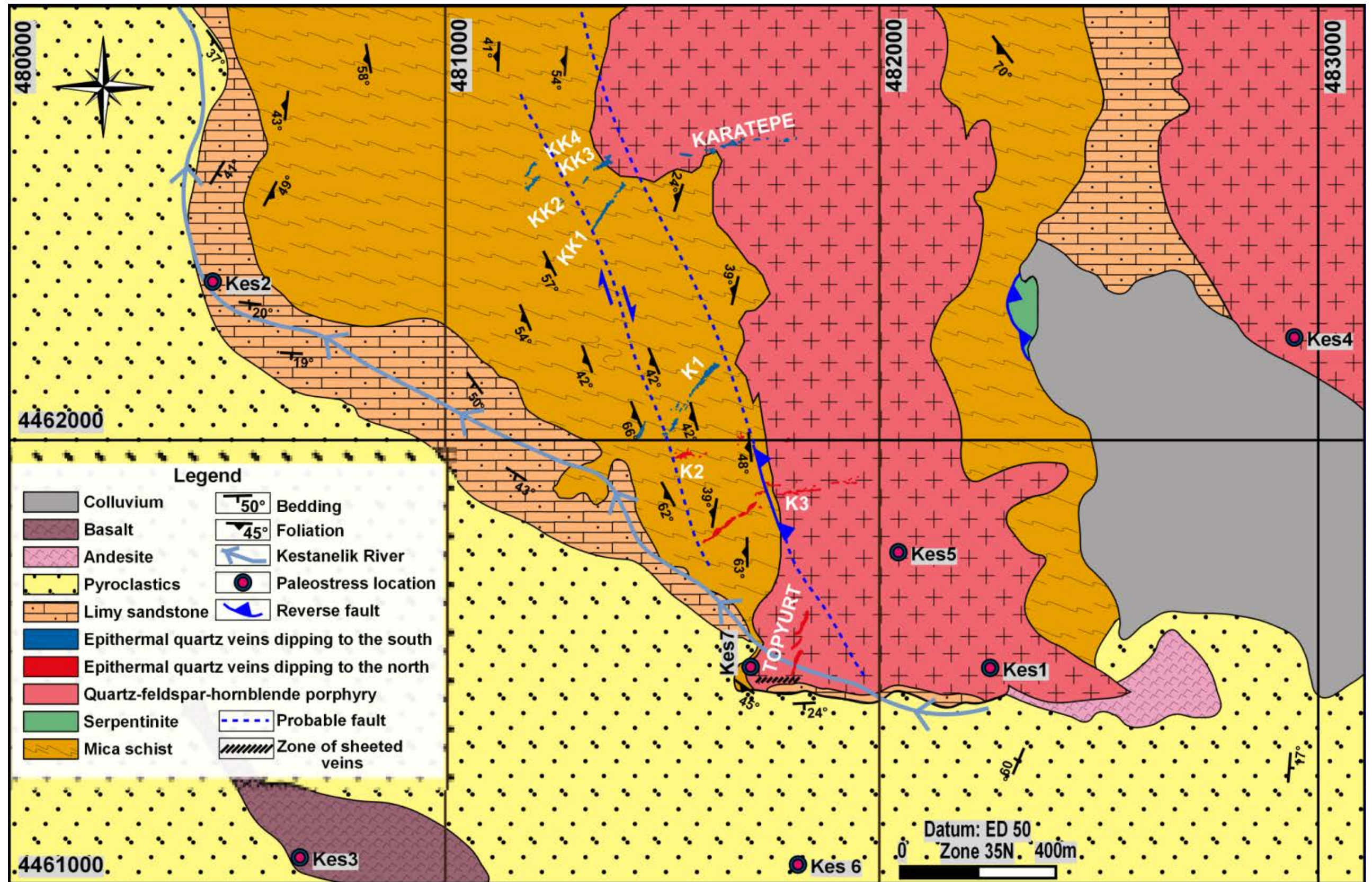
**Figure 3.6.** Geological map of the study area.

| Age | Name | Lithology | Boundary type | Explanations |
|---|---|---|---|---|
| Quaternary | Colluvium | | Unconformity | Colluvium with clasts of mica schist, meta-quartz, QFH porphyry and limy sandstone |
| Late Eocene | Sahinli Formation | | Lateral Facies Change | Coeaval basaltic dyke, andesite and andesitic to basaltic pyroclastics |
| Late Eocene | Sogucak Formation | | Nonconformity | White to pale yellow, fossilliferous limy sandstone |
| Middle Eocene | Northern Eocene Group Plutons | | Intrusive Boundary | Quartz-feldspar-hornblende (QFH) porphyry with minor biotite |
| Cretaceous | Cetmi Ophiolitic Melange | | Tectonic Boundary | Serpentinite |
| Paleozoic | Camlica Metamorphics | | | Biotite-quartz schist, and calc-schist with quartzite lenses |

**Figure 3.7.** Generalized tectonostratigraphic section of the study area.

### 3.3.1. Rock units

In total, eight rock units were defined in this study and these are, from bottom to top, mica schist, serpentine, quartz-feldspar-hornblende (QFH) porphyry, limy sandstone, pyroclastics, andesite, basalt and colluvium. Major characteristics of these units are described below.

### 3.3.1.1. Mica schist

This unit covers one-fourth of the study area and is mostly exposed in the central part. The unit belongs to Paleozoic Çamlıca metamorphics (see section 3.2.1) and forms the basement rocks of the area. The schist is biotite-dominated plus quartz and a minor amount of chlorite, so it can be defined as biotite ± quartz schist. For simplicity it will be termed as mica schist (Figure 3.8). In a very small region in the eastern part of the study area, calc-mica schist is also found (Figure 3.9). Quartzite lenses oriented are widely seen parallel to foliation (Figure 3.10). Quartzite lenses and calc-mica schist and are not mapped as separate units.
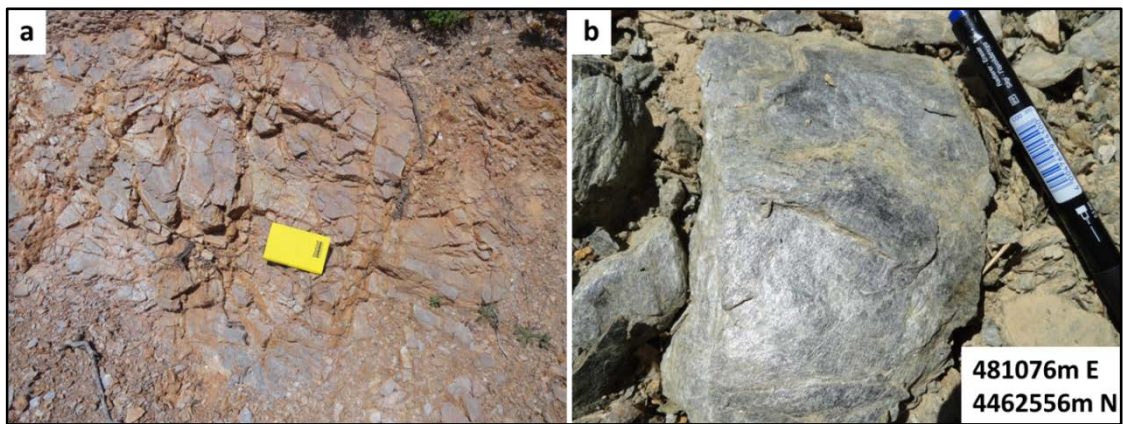


**Figure 3.8. (a)** An outcrop of biotite±quartz schist. **(b)** Close-up view of biotite±quartz schist.



**Figure 3.9. (a)** An outcrop of calc-mica schist exposed in the eastern part of the study area. **(b)** Close-up view of calc-mica schist.

**Figure 3.10.** A quartzite lens parallel to the foliation of the schist.

The unit is in contact with serpentinite (Figure 3.11) in the central part of the area but the boundary relationship is not understood. The unit is cut by QFH porphyry N of Kestanelik River (Figure 3.12) and its contact with QFH porphyry is seen in a variety of locations where the foliation of schist changes and porphyry is brecciated along the margin close to the intrusion. The unit is also unconformably overlain by pyroclastics (Figure 3.13) along most of the Kestanelik River and by Quaternary colluvium (Figure 3.11) in the central part of the area.
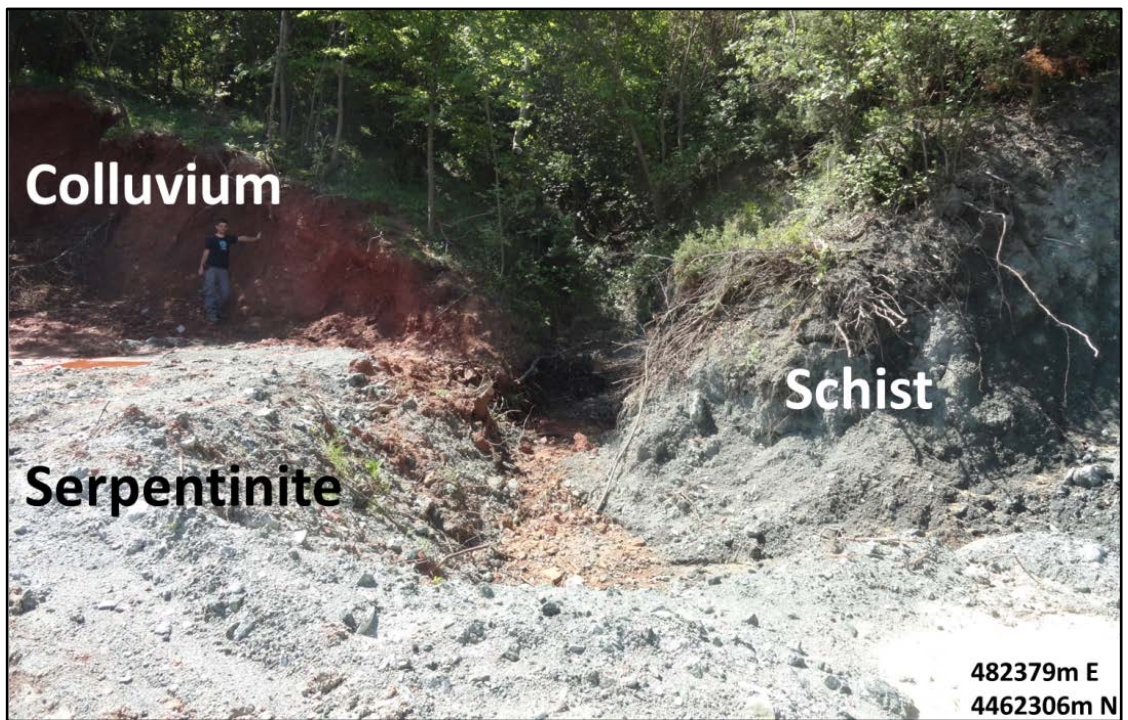
**Figure 3.11.** Contacts of mica schist with serpentinite and colluvium.
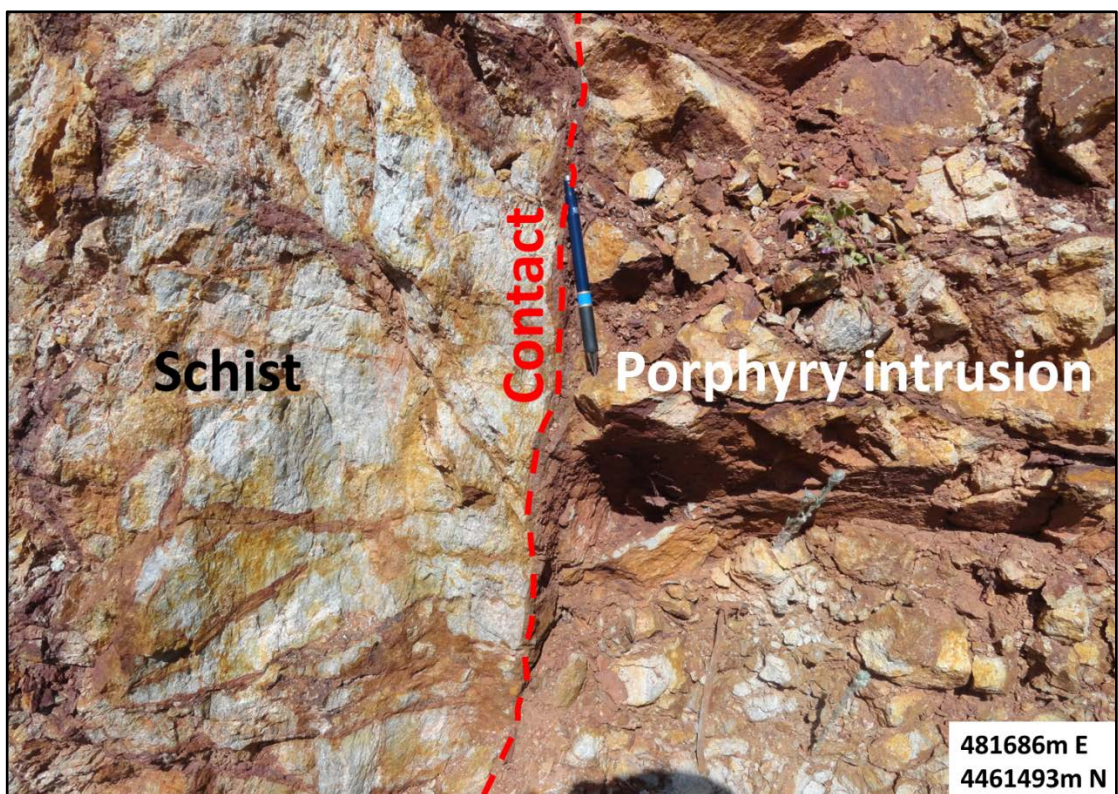


**Figure 3.12.** Contact of mica schist with QFH porphyry.
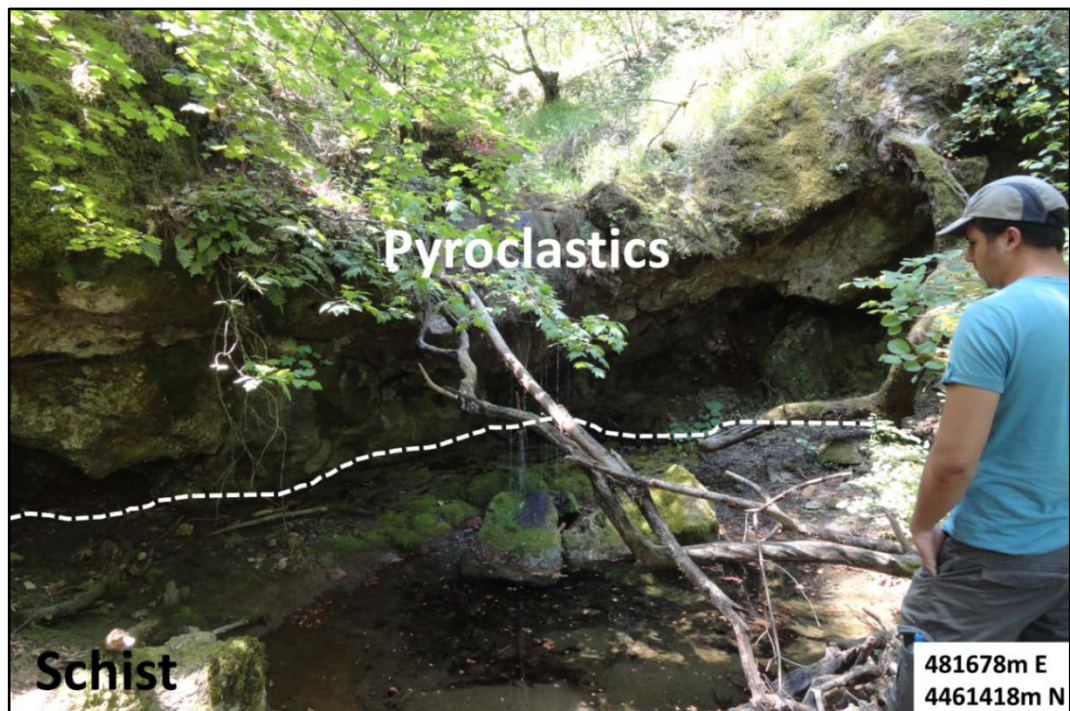
**Figure 3.13.** Contact of mica schist with pyroclastics.

### 3.3.1.2. Serpentinite

Whitish green serpentinite (Figure 3.14), represented by a small outcrop in the central part of the study area (Figure 3.6), belongs to the Çetmi ophiolitic mélange (see section 3.2.1). It is unconformably overlain by Quaternary colluvium (Figure 3.11).
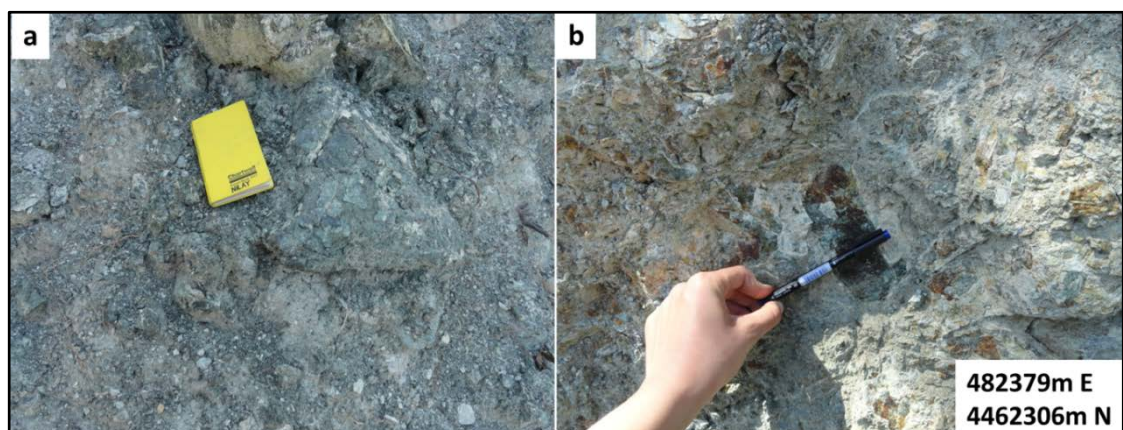


**Figure 3.14. (a)** An outcrop of serpentinite. **(b)** Close-up view of serpentinite.

### 3.3.1.3. Quartz-feldspar-hornblende porphyry

This unit is represented by two N-S elongated bodies exposed in the central and northeastern part of the study area. Since it has coarse grained quartz, feldspar and hornblende with minor biotite, it is best described as quartz-feldspar-hornblende (QFH) porphyry (Figure 3.15a-b). Where the unit cuts mica-schist it has a chilled margin (Figure 3.12). The unit is also cut by some mafic dykes which are only seen in drill core (Figure 3.15c).

In the central part of the area, it is highly altered by argillic alteration (in the form of illite) (Figure 3.16) and silicification (Figure 3.17a). The northeastern outcrop is only slightly altered and has some well-developed propylitic alteration zones (in form of chlorite with minor pyrite) (Figure 3.17b). The central outcrop is proximal to the mineralization in the area, while the eastern one is distal to it (Figure 3.6).

The unit is thought to have a genetic link with the Northern Eocene group of plutons which vary between ~48 and ~34 Ma (see section 3.2.2.1.) due to its proximity and similarity to them. Field macroscopic features, mineralogical and textural characteristics of the unit are very similar to the porphyry outcropping in the Madendağ gold deposit, which is ~35 km away from the study area (Personal communication, İlkay Kuşcu, 2016). The $^{39}Ar/^{40}Ar$ analyses of K-feldspar from the least altered part of the porphyry in the Madendağ deposit gave an age of 43.34±0.85 Ma (Ünal-İmer *et al*., 2013) which can be accepted as the probable age of QFH porphyry outcropping in the study area.

### 3.3.1.4. Limy sandstone

The limy sandstone mostly crops out along the Kestanelik River in the southern part of the study area. It also has two small outcrops in the central and SE part of the area. It is characterized by white to pale yellow, medium grained, thin to medium bedded, fossilliferous limy sandstone (Figure 3.18a). The unit is likely to be part of the Soğucak formation (section 3.2.2.2).
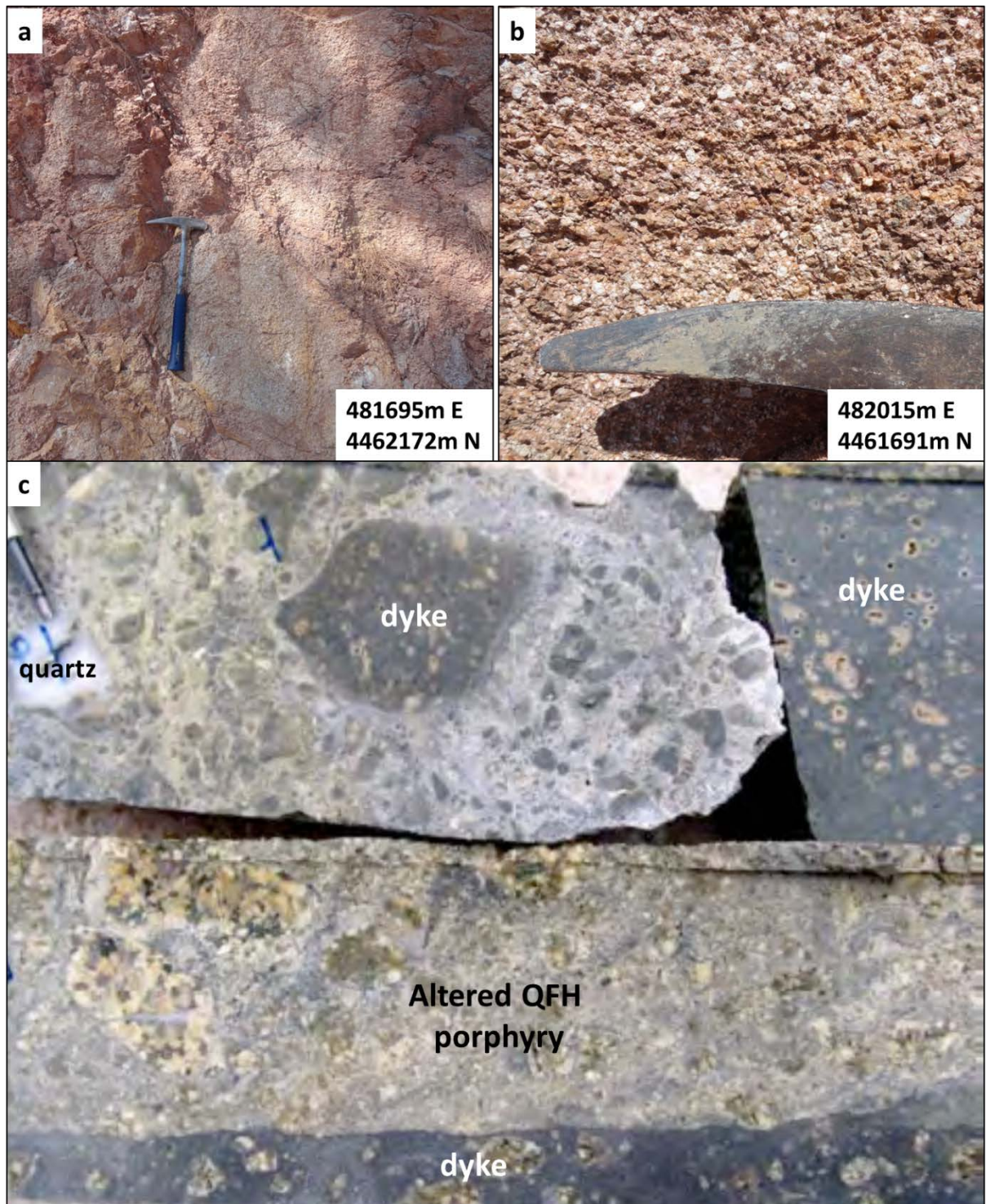
**Figure 3.15. (a)** An outcrop of QFH porphyry in the study area. **(b)** Close-up view of QFH porphyry. **(c)** A drillcore (KED-6 65.5–65.7 m) photo showing a mafic dyke (upper right) and adjacent breccia with fragments of dyke and quartz vein cemented by quartz (upper left) on the margin of altered QFH porphyry intruded by the dyke (bottom).
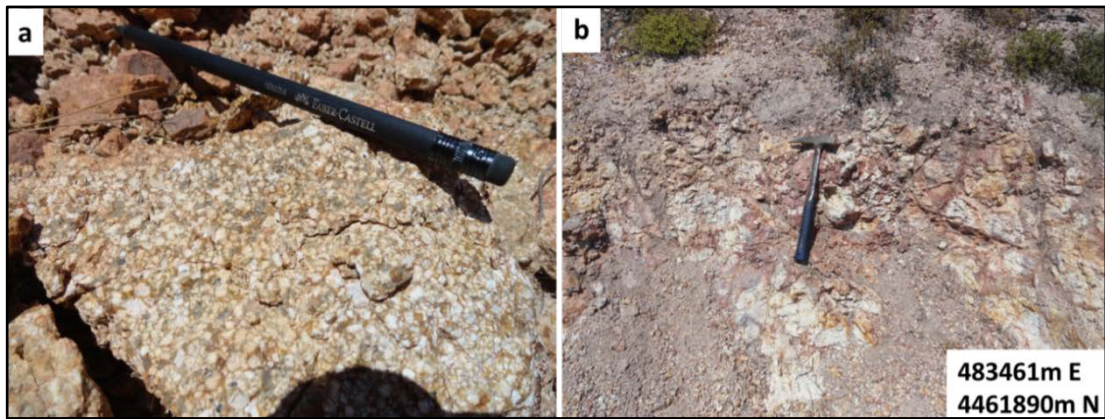
**Figure 3.16. (a)** Argillic alteration in the form of illite (replacing feldspar) in QFH porphyry. **(b)** An argilically altered outcrop of QFH porphyry.
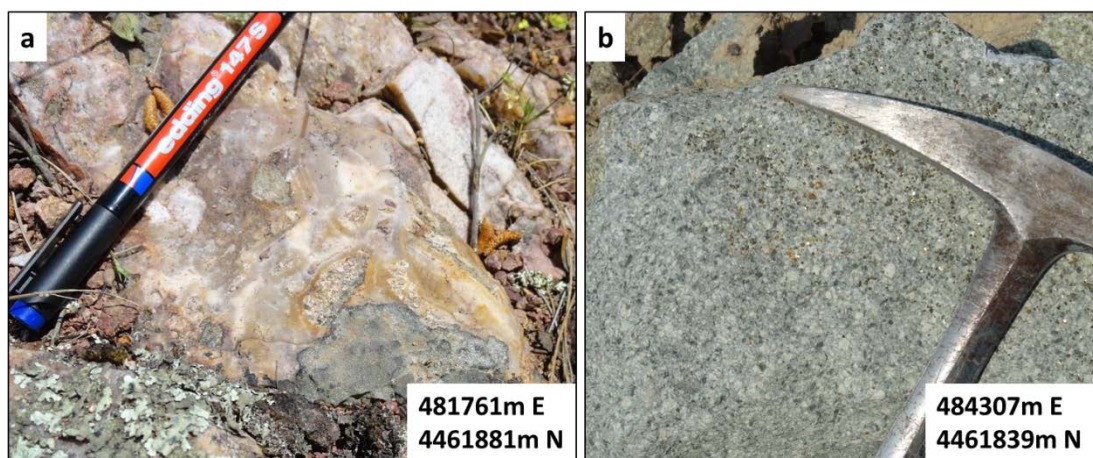


**Figure 3.17. (a)** Silicification of QFH porphyry after brecciation. **(b)** Propylitic alteration in the form of chlorite and pyrite (replacing biotite) in QFH porphyry.

Nummulite fossils (Figure 3.18b) indicate a shallow marine depositional environment, and indicate an Eocene-Oligocene age for the unit. According to a detailed study on the fossil assemblage collected from the unit, the age of the unit is suggested Priabonian (Late Eocene) (Personal communication, Ercan Ozcan, 2014).

The unit is seen to be in transition with pyroclastics at a location in the Kestanelik River (Figure 3.19 and 3.20) in the southern part of the area and a measured section for the boundary is given in Figure 3.21.
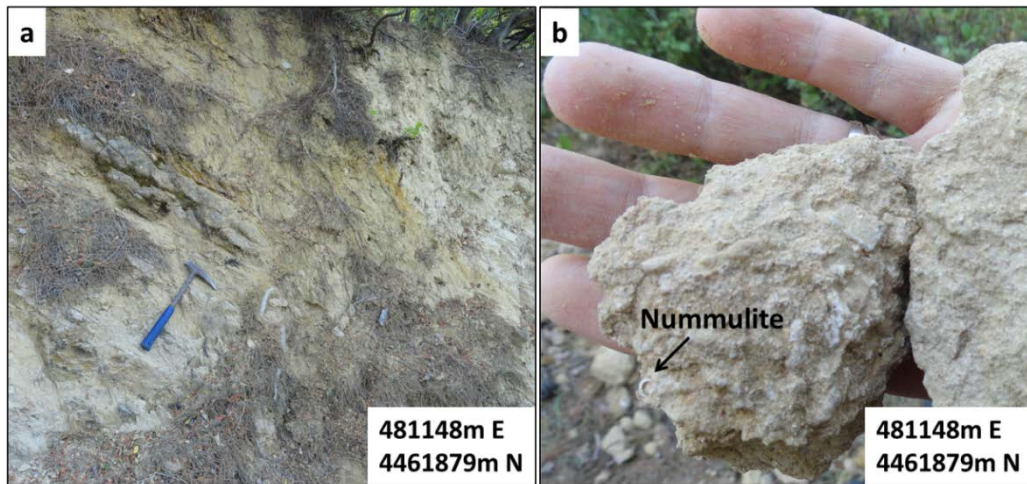
**Figure 3.18. (a)** General view of fossilliferous limy sandstone in the study area. **(b)** Nummulite fossils observed in limy sandstone.



**Figure 3.19.** A section showing the transition of fossilliferous limy sandstone with pyroclastics.
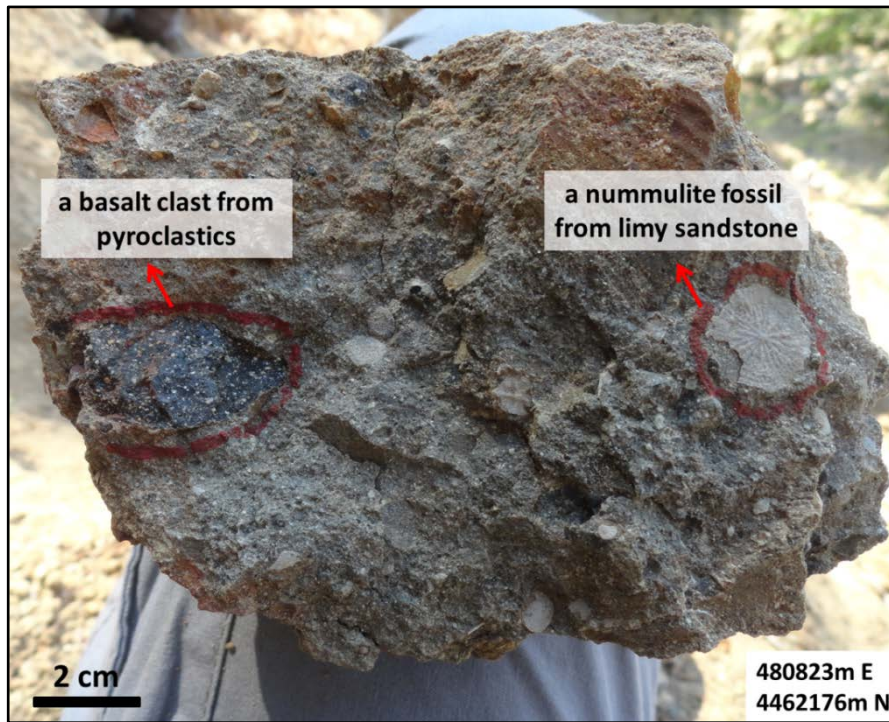
**Figure 3.20.** A grab rock sample showing the evidence of transition between limy sandstone and pyroclastics (sample taken from the section shown in Figure 3.19).
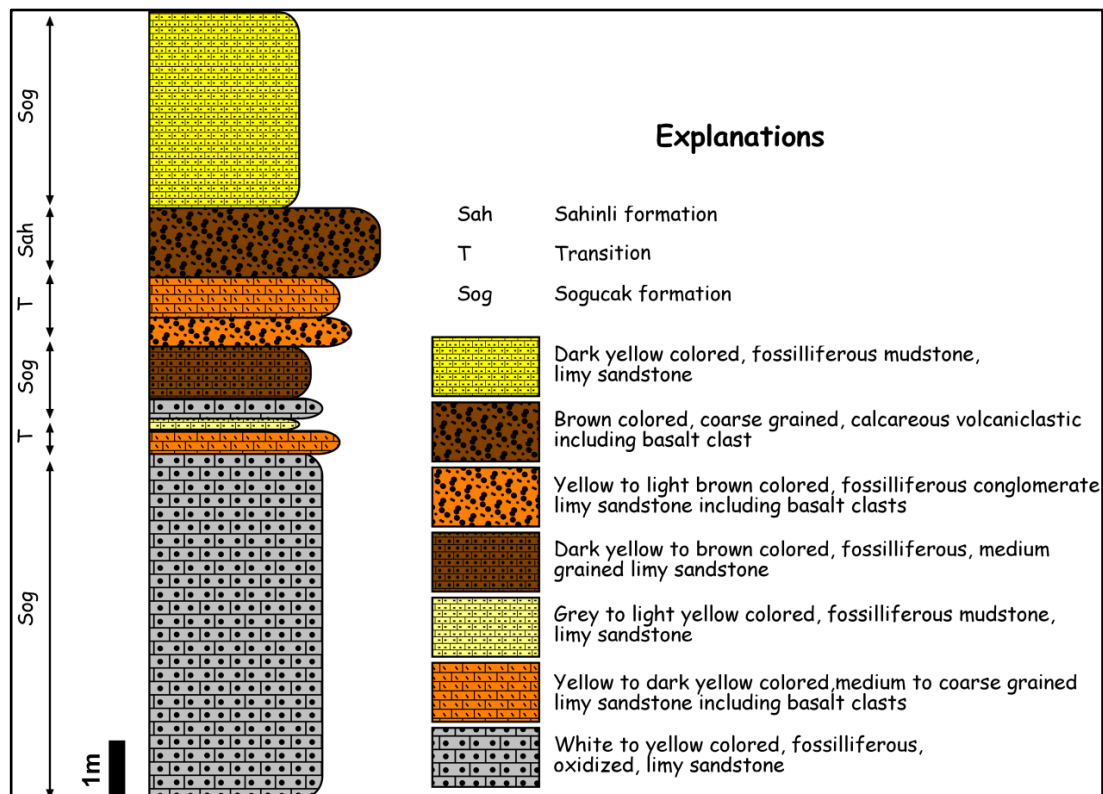


**Figure 3.21.** Measured section showing the transition of limy sandstone and pyroclastics.

50

### 3.3.1.5. Pyroclastics, andesite and basalt

Andesitic to basaltic pyroclastics, basalt and andesite are all associated and mostly crop out south of Kestanelik River in the southern part of the study area. These three units belong to Sahinli Formation (Dönmez *et al.*, 2005) for which the type locality (Şahinli Village) is 2 km from the study area.

The pyroclastics are generally grey, poorly sorted and include andesitic to basaltic clasts (Figure 3.22). In some parts of the area, they alternate with mudstones (Figure 3.23). These pyroclastics are intruded by both andesite and basalt dykes (Figure 3.6). Andesite in two small outcrops in the area is highly altered by argillisation (Figure 3.24). Basalt is exposed in the SW part of the area and is chloritized (Figure 3.25).

Considering the transitional relationship of these units with the limy sandstone, their age should be around Priabonian. This is consistent with the radiometric age (~37 Ma) obtained from the calc-alkaline volcanic rocks around Sahinli Village (Ercan *et al.*, 1998; Delaloye and Bingöl, 2000).



**Figure 3.22.** Outcrop of andesitic to basaltic pyroclastics.

**Figure 3.23.** Alternation of pyroclastics with mudstones.
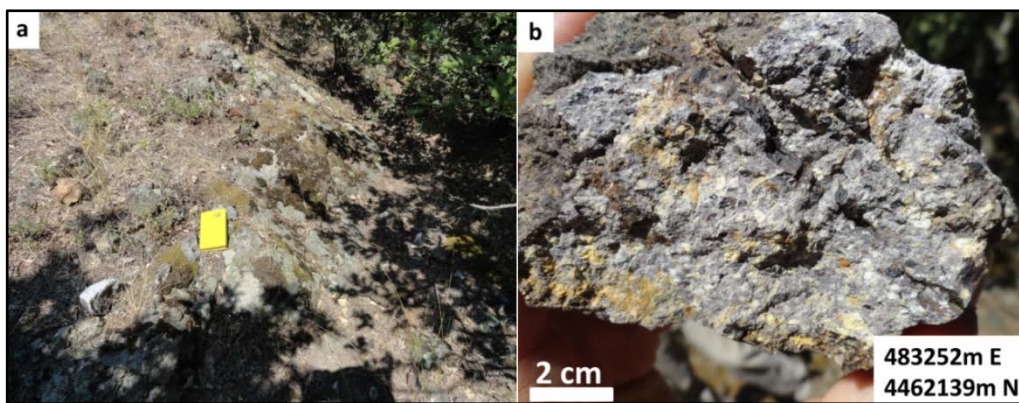


**Figure 3.24. (a)** An outcrop of altered andesite. **(b)** Argillisation in andesite.



**Figure 3.25. (a)** An outcrop of altered basalt. **(b)** Chloritization in basalt.

### 3.3.1.6. Colluvium

Quaternary colluvium is exposed in a limited part in the Kestanelik River and the eastern part of the study area. It is red, unconsolidated, matrix supported, poorly sorted (clast size ranges between 0.5 cm and 20 cm) and includes angular to rounded clasts (Figure 3.26). Clast types observed in the colluvium are mica schist, quartzite, QFH porphyry and limy sandstone (Figure 3.27). Where it has contact with serpentinite (Figure 3.11), no serpentinite clast was observed in it. Based on field observations, its maximum observable thickness is 60 m. It is the youngest unit and unconformably overlies all of the rock units in the study area.



**Figure 3.26**. General view of colluvium in the study area.
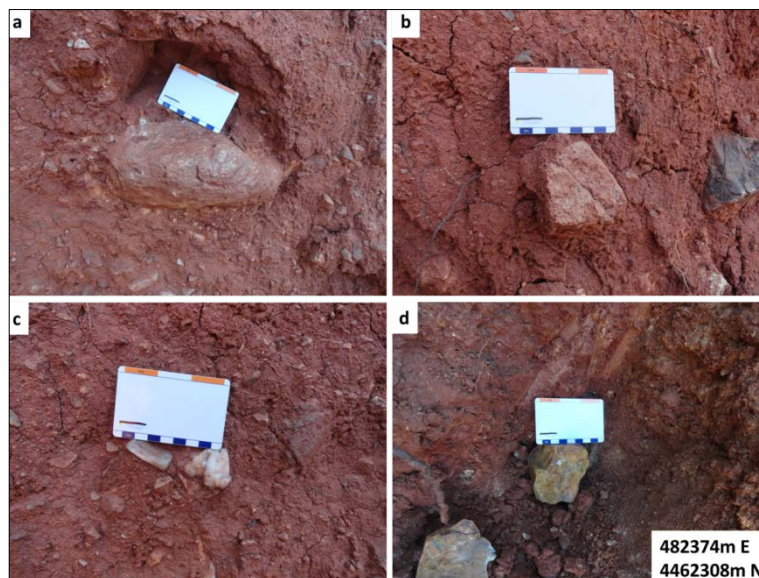


**Figure 3.27.** Clasts in the colluvium: **(a)** Mica schist. **(b)** QFH porphyry. **(c)** Quartzite. **(d)** Limy sandstone.

### 3.3.2. Structures

During geological mapping, attitude (strike and dip) measurements were taken from foliation planes of schist and bedding planes of limy sandstone and pyroclastics. These data are shown on the geological map (Figure 3.6). Attitude measurements were also collected from fault planes together with rake data.

### 3.3.2.1. Foliation

The mean strike direction of foliation planes in schist is 155° (Figure 3.28). The mean dip of the foliation planes was calculated as 43° on the software Stereonet 9.5 (Allmendinger *et al.*, 2013; Cardozo and Allmendinger, 2013).
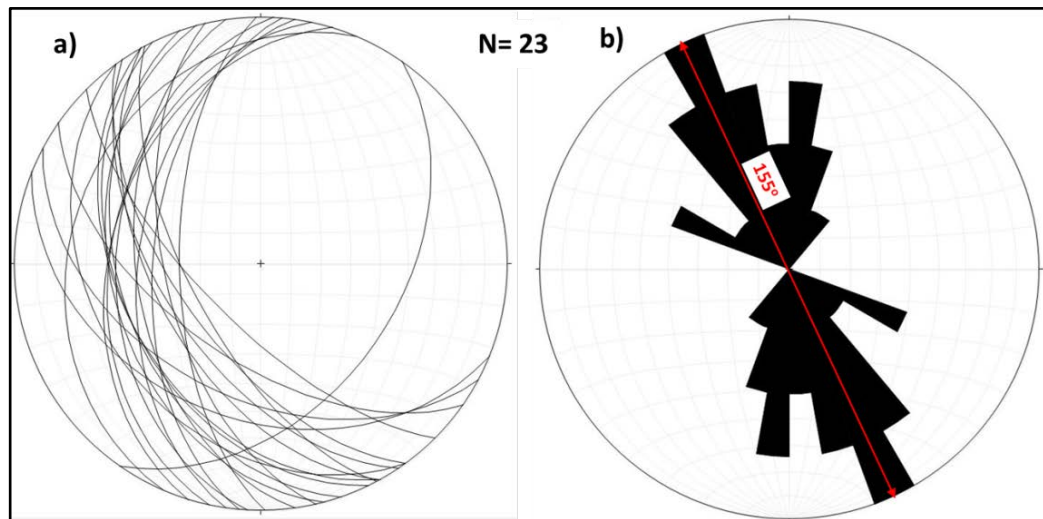


**Figure 3.28. (a)** Foliation planes of the schist plotted on an equal-area stereonet. **(b)** Rose diagram showing the strikes of foliation planes and their mean orientation.

### 3.3.2.2. Bedding

Due to limited access to the outcrops of the bedded limy sandstone and pyroclastics, only 9 attitude data were recorded (3 from pyroclastics, 6 from limy sandstone). The bedding is different in limy sandstone and the younger pyroclastics (Figure 3.29). The mean orientation of the bedding planes of the limy sandstone was calculated as 110°/29° on the Stereonet 9.5 (Allmendinger *et al.*, 2013; Cardozo and Allmendinger, 2013).
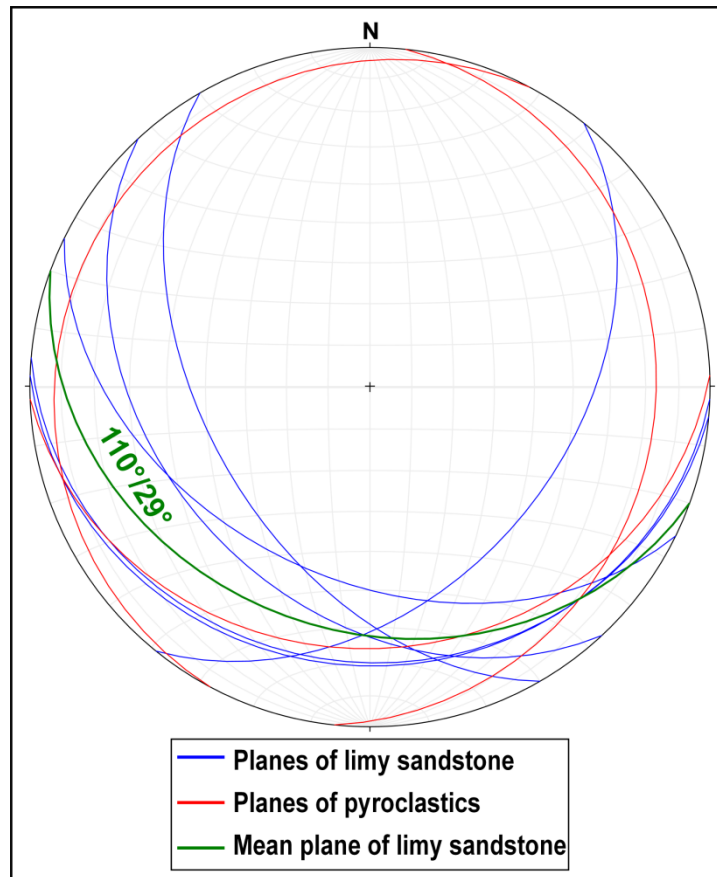
**Figure 3.29.** Bedding planes of the limy sandstone and pyroclastics, and the mean plane of the limy sandstone plotted on an equal-area stereonet.

### 3.3.2.3. Faults and paleostress analyses of fault-slip data

Attitude data, rake of slickenlines, and sense of slip (using surface geometry and/or offsets) were recorded from small–scale fault planes. In total 69 fault-slip data were collected from 7 locations (Figure 3.6) and used for paleostress analyses in order to unravel the local deformation phase(s) in the area.

The aim of paleostress analysis is to determine the stress tensor which best fits the direction of slip on the observed faults (Zalohar and Vrabec, 2007). A variety of methods have been proposed for this inverse solution (e.g. Angelier, 1979; 1984; 1989; 1994; Armijo *et al.*, 1982; Etchecopar *et al.*, 1981; Hardcastle, 1989; Orife and Lisle, 2003). All of the methods assume: (1) direction of maximum shear stress is parallel to the direction of movement on the fault plane, (2) the movement along the fault plane is independent from the movement on the other faults, (3) there is

no rotation on the block bounded by the fault planes, and (4) the stress field responsible for the movements on the fault planes is independent of the faults and homogenous. All these assumptions follow the basic hypothesis that a single stress tensor can explain the direction of slip on a set of differently oriented faults. Paleostress inverse solution was easily formulated for homogeneous fault systems (e.g. Angelier, 1979, 1989, 1994; Nemcok *et al.*, 1999). However, fault systems are generally not homogeneous and form under the effect of several different stress regimes. In this case they are called heterogeneous fault systems, and are assumed to be composed of homogenous subsystems (Angelier, 1989). Methods suggested for the analysis of heterogeneous fault slip data are mainly based on: (1) stress inversion approach that includes the best-fit tensor concept, (2) cluster analysis, and (3) Fry's (1999) sigma space concept. Zalohar and Vrabec (2007) described the Gauss method for separation of heterogeneous fault systems into the homogenous fault subsystems. This method uses the fault-slip data inversion which includes the best-fit tensor concept and defines a compatibility function as a Gaussian function. The compatibility function is dependent on the compatibility measure which takes into account both the angular misfit between the estimated and real direction of movement on the fault plane, and the ratio between the normal and shear stress on that fault plane. The compatibility function and the compatibility measure are a measure of correspondence between a trial stress tensor and fault-slip datum. The optimal stress tensor for each homogeneous fault subsystem is estimated by maximizing the summation of compatibility functions defined as object function for all fault-slip data. Topography of the object function and its global and highest local maxima represents the different stress regimes responsible from movement and activation along the fault planes.

T-TECTO 3.0 software, based on the Gauss method (Zalohar and Vrabec, 2007), was used for the paleostress analyses of the fault-slip data collected from the Kestanelik study area due to its effectiveness on separating deformation phases in heterogeneous fault systems and advantage in assigning values to separation

parameters before calculation of respective stress tensor for each stress phase. The parameters used in the calculation are defined below;

*Parameter (s):* Dispersion parameter of the distribution of angular misfits between the actual and resolved direction of slip along the fault. The limiting angle for the reliable separation of stress tensors was found as 25° during the tests of Gauss method (Zalohar and Vrabec, 2007); therefore, parameter (s) was taken as 20° for this study in order to discard possible irrelevant data.

*Parameter (d):* Represents a threshold value for compatibility measure calculated by considering the misfit angle between actual and predicted direction of movement on the fault, and also the position fault slip datum on Mohr diagram (the ratio of normal and shear stress on fault plane). The range for that parameter is suggested as >60° for highly heterogeneous stress field and >30° for less inhomogeneous stress fields by Zalohar and Vrabec (2007). In this study, this parameter was chosen as 30° due to the high possibility of having moderately heterogeneous stress field because the area is under the effects of both escape tectonics caused by the collision of Arabian and Anatolian plates in the southeastern Turkey and to the extensional tectonics caused by the subduction along the Hellenic trench in the Aegean Sea S of Western Turkey (section 3.2.3).

*Parameter q1 and q2:* (q1) roughly represents the internal friction angle of an intact rock which will be fractured whereas (q2) defines the maximum residual frictional angle for activating pre-existing fractures. In this study, (q1) and (q2) were taken as 60° and 20°. This allows the consideration of the possible re-activated fractures or intact rocks having different internal friction angles because there are different rock types hosting the faults in the study area.

The main outputs of a paleostress analysis are orientation of $\sigma_1$ (maximum), $\sigma_2$ (intermediate), and $\sigma_3$ (minimum) principal stress axes, and the shape ratio of the principal stress differences ($\Phi = (\sigma_2-\sigma_3)/(\sigma_1-\sigma_3)$). These outputs are then used for determining the basic stress regime, which is extensional where $\sigma_1$ is close to vertical, strike-slip where $\sigma_2$ is close to vertical or compressional where $\sigma_3$ is close to

vertical. In addition to these basic (pure) regimes, trans-tensional, trans-pressive, radial extensional or radial-compressional regimes also exist. In order to define these regimes, Delvaux *et al.* (1997) suggested a numeric index ($\Phi'$) calculated from ($\Phi$), where $\Phi'$ ranges from 0 to 3, as;

$\Phi'=\Phi$ where $\sigma_1$ is close to vertical

$\Phi'=2-\Phi$ where $\sigma_2$ is close to vertical

$\Phi'=2+\Phi$ where $\sigma_3$ is close to vertical

The different stress regimes with their assigned $\Phi'$ values are; radial extension ($0<\Phi'<0.25$), pure extension ($0.25<\Phi'<0.75$, trans-tension ($0.75<\Phi'<1.25$), pure strike-slip ($1.25<\Phi'<1.75$), trans-pression ($1.75<\Phi'<2.25$), pure compression ($2.25<\Phi'<2.75$) and radial compression ($2.75<\Phi'<3$).

For each location, a minimum of 4 slip data are required to be processed in a paleostress analysis. Although more is always better, in total 69 fault-slip data from 7 locations (Figure 3.6) were processed in T-TECTO 3.0 by considering the restrictions (parameters) mentioned above. The results of paleostress analyses conducted from the 7 locations are summarized in Table 3.1 and Figure 3.30.

According to the paleostress inversion solutions together with field observations and ($\Phi'$) values, three different deformation regimes were determined. The first regime is represented by 2 sites (KES2 and KES4) (Figure 3.6) and show NE-SW oriented compression with almost vertical $\sigma_3$. The second regime is represented by 4 sites (KES1, KES5, KES6 and KES7) (Figure 3.6) and indicates almost NW-SE oriented extensional with $\sigma_1$ very close to vertical. The final regime is represented by KES3 site and is determined as a pure-strike slip regime developed under ESE-WNW oriented compression and NNE-SSW oriented extension.

Although relative dating is not possible for the sites of each regime, the first two deformation regimes may belong to one deformation phase, because a NE-SW oriented compressional regime (first regime) may also cause NW-SE oriented extension (second regime).

**Table 3.1.** Results of paleostress analyses (see Figure 3.6 for localities).

| Location ID | $\sigma_1$ | $\sigma_2$ | $\sigma_3$ | Φ | Φ' | No of slip data |
|---|---|---|---|---|---|---|
| KES1 | 226/76 | 040/14 | 130/1 | 0.1 | 0.1 | 11 |
| KES2 | 211/02 | 121/12 | 310/78 | 0.8 | 2.8 | 9 |
| KES3 | 289/34 | 120/56 | 023/05 | 0.3 | 1.7 | 11 |
| KES4 | 236/02 | 145/24 | 330/66 | 0.7 | 2.7 | 9 |
| KES5 | 262/65 | 088/25 | 357/03 | 0.3 | 0.3 | 10 |
| KES6 | 219/65 | 045/25 | 314/03 | 0.4 | 0.4 | 9 |
| KES7 | 219/65 | 058/24 | 325/08 | 0.6 | 0.6 | 10 |

In this case, the pure-strike slip regime represented by KES3 site constitutes the second deformation phase in the study area. The first deformation phase indicates a NE-SW oriented compressional tectonic setting while the second deformation phase indicates pure-strike slip regime developed under an ESE-WNW oriented compressional, NNE-SSW oriented extensional tectonic setting.
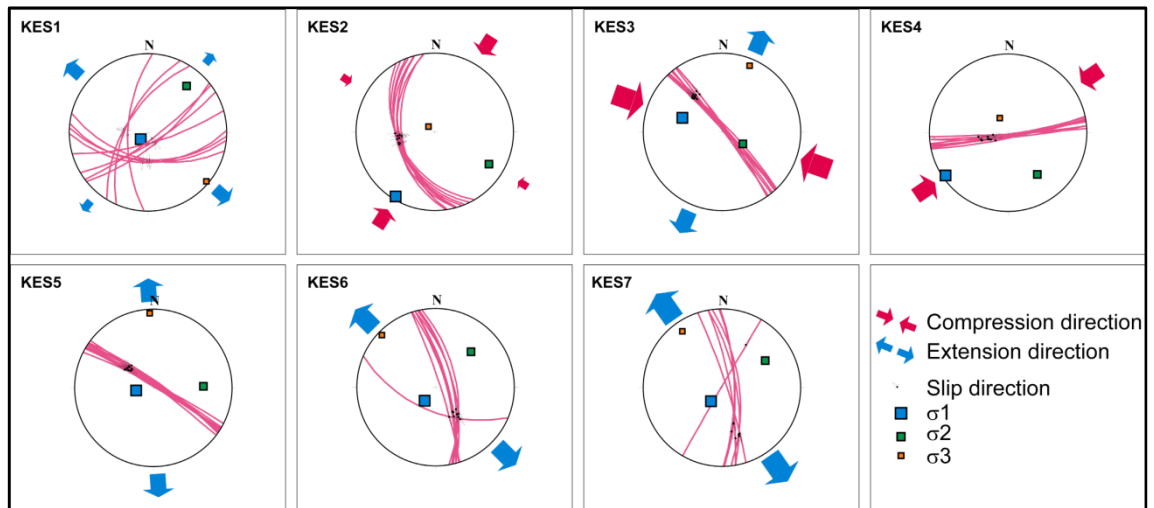


**Figure 3.30.** Cyclographic traces, slickensides and constructed paleostress configurations of fault plane measurements from the study area.

Apart from the small-scale faults used for paleostress analyses, two more faults were recognized in the central part of the area (Figure 3.6). The eastern fault was determined from the modelling of the QFH porphyry-mica schist contact by a consultant geologist Matt Houston in Micromine Software using the geological log data of available drill holes (both diamond cut and RC) (Houston, 2013). This fault is oriented NNW-SSE, dips to the NE at about 80$^{o}$ and offsets the contact up to the NE, so is interpreted as a reverse fault (Figure 3.31). The western fault is also NNW-SSE directed and interpreted from the apparent dextral movement on some of the main veins (Figure 3.6). Since there is not enough drilling around this fault, it is only seemed to be probable and still open to discussion. Due to the apparent offset of the veins and lack of mineralization in these two faults, both are regarded as post-mineralization.



**Figure 3.31**. A cross section showing the displacement of the QFH porphyry–mica schist contact across the eastern fault (from Houston, 2013).

## 3.4. Mineralization

Mineralization in the area is associated with several quartz veins, which crop out over an area of nearly 2 km$^2$. The veins have a variable thickness and locally irregular strikes and dips (Detailed information for the thickness, strike and dip amount of each vein is given in Chapter 4). The host rocks to these veins are mica schist and QFH porphyry (Figure 3.6).

Mineralization has been considered to be low-sulphidation (LS) epithermal type as evidenced by the presence of bladed quartz replacing bladed calcite, and hydrothermal breccias (Figure 3.32). Ore minerals are native gold and accessory silver. The quartz veins generally have moderate to high gold grades (Au range in 1-20 g/t) and the Au:Ag ratio is generally in the range 2:1 to 1:1. Gangue minerals are principally quartz and chalcedony with pyrite and traces of chalcopyrite, sphalerite and galena which are generally disseminated in the vein quartz. Amethystine quartz is also present in some parts of the vein system hosted by QFH porphyry.

Vein quartz textures generally show open space filling and replacement characteristics. The most striking feature of the veins is brecciation. Quartz vein breccias are generally composed of monomictic to polymictic clasts of host rocks and/or previous phase(s) cemented by iron-oxide quartz which indicate that at least two phases of mineralization occurred in the area. (Detailed descriptions of the vein textures, breccias and multiphase mineralization are given in Chapter 5).
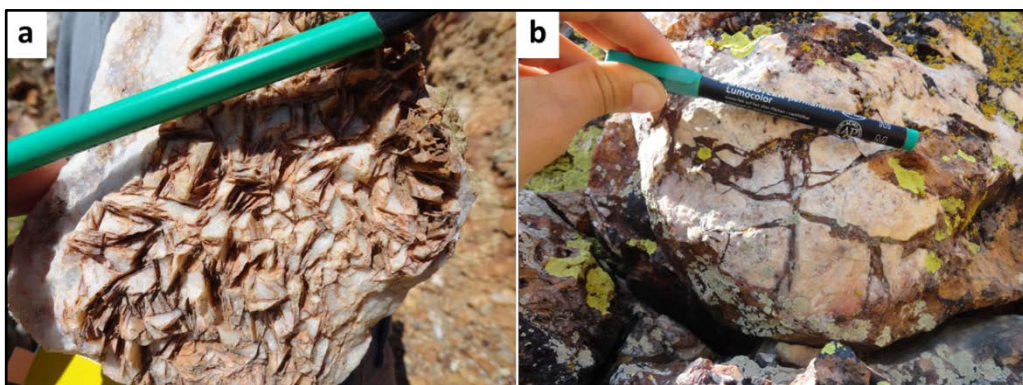


**Figure 3.32.** Evidence of boiling and LS epithermal mineralization: **(a)** Bladed quartz replacing bladed calcite. **(b)** Hydrothermal breccia with clasts of previous mineralization phases cemented by quartz-iron oxide.

The presence of hydrothermal breccias and bladed quartz replacing bladed calcite indicate that the most dominant mineral precipitation mechanism from hydrothermal solution is boiling. In addition, iron-oxide quartz cement to the hydrothermal breccias suggests that oxidation (due to mixing with surface waters) was also an effective precipitation mechanism.

Hydrothermal alteration forms an envelope around the veins and is dominantly represented by argillic alteration in the form of illite and smectite; however propylitic alteration in the form of chlorite and pyrite also exists distal to the veins (Figure 3.16 and 3.17b).

## 3.5. Discussion and summary

The study area is located within the Biga Peninsula, NW Turkey where the Paleozoic metamorphic and ophiolitic basement rocks are cut by Eocene-Miocene aged plutons and covered by Cenozoic volcanic and sedimentary units. Starting from the Middle Eocene, extensive magmatism started to prevail in NW Turkey, which shifted from calc-alkaline to alkaline in the Middle Miocene. The eight rock units defined in the study area are, from oldest to youngest, mica schist, serpentinite, QFH porphyry, limy sandstone, pyroclastics, andesite, basalt and colluvium. Basement rock mica schist belonging to the Çamlıca metamorphics is cut by QFH porphyry, obducted by serpentinites of the Çetmi Ophiolitic melange and covered by the volcanic and sedimentary units of the area. Limy sandstone of the Soğucak formation is in transition with volcaniclastics of the Sahinli formation in the area, although Yüzer and Tunay (2012) states that Soğucak formation is overlain by Şahinli formation.

The gold mineralization in the area is associated with quartz veins hosted by Paleozoic mica schist and Lutetian (43.34±0.85 Ma) QFH porphyry. The oldest unit covering the mineralized veins is Priabonian aged limy sandstone, and the youngest host rock to the veins is QFH porphyry of with an assumed age of 43.34±0.85 Ma. The age of the mineralization must therefore be Late Lutetian-Early Priabonian. The host rock QFH porphyry cannot be the heat source for the epithermal system

because the coarse grain size of the porphyry shows that it was emplaced at a greater depth and then uplifted and eroded before mineralization. There must have been a younger intrusion below the mineralized quartz vein system to provide the heat source. As the age of the mineralization is Late Lutetian-Early Priabonian, the heat source most likely has a genetic link with the Cenozoic calc-alkaline magmatism continuing around the study area.

The gold mineralization in the area is LS epithermal type as evidenced by some diagnostic features of LS epithermal deposits: bladed quartz and hydrothermal breccia. Boiling is very likely to be the dominant mineral precipitation mechanism which is evident from the common occurrence of bladed quartz replacing bladed calcite in the veins. Absence of silica sinter, the diagnostic paleosurface indicator of LS epithermal systems, implies that the epithermal system must have been subjected to erosion, and that only the subsurface parts of the vein system are presently exposed at Kestanelik.

Two main local deformation phases were determined from the paleostress analyses: a NE-SW oriented compressional regime and pure-strike slip regime developed under ESE-WNW oriented compression and NNE-SSW oriented extension. The first deformation phase may be associated with collision and further convergence after the closure of the northern branch of the Neo-Tethys Ocean along the IASZ in NW Turkey in the Late Cretaceous-Early Eocene (Şengör and Yılmaz, 1981; Harris *et al.*, 1994; Okay and Tüysüz, 1999, Sherlock *et al.*, 1999; Önen and Hall, 2000, Kaymakcı *et al.*, 2009, Hinsbergen *et al.*, 2010). The second phase is represented by the KES3 fault which cuts basalt that is the youngest unit of the area apart from colluvium. This second phase may be related to the present-day trans-tensional neotectonic regime characterized by the splays of North Anatolian Fault Zone in NW Turkey (see section 3.2.3).

# Chapter 4: Structural Geology of the Veins

Investigating the geometries, kinematics and failure mechanisms of the quartz veins in the Kestanelik study area, and the paleostress of the area during gold mineralization are keys to understand the permeability enhancement processes during epithermal gold mineralization. In this respect, section 1 gives information about the general characteristics of site-scale major mineralized quartz veins with a map showing their distribution, zoomed map of each vein and some key photos. Section 2 presents general characteristics of the sheeted mineralized quartz veins in the valley and their kinematics. In section 3, general characteristics of vein-associated structures (wall rock veins) are described together with two detailed maps.

Section 4 includes the results of 3D modeling of the sub-surface geometries of the major mineralized quartz veins together with key figures, cross sections, rose diagrams and histograms in order to be able to (1) constrain the geometry of the structures hosting the veins better and (2) investigate gold grade distribution with respect to vein geometry.

Boiling (phase separation), the most dominant gold precipitation mechanism in LS epithermal systems, occurs when pressure drops suddenly resulting in precipitation of gold (e.g. Henley, 1985; Hedenquist *et al.*, 2000). While fluid in the conduit ascends, a thickness increase sudden in time during rupture would lead to a drop in the fluid pressure causing boiling and associated gold precipitation. Therefore, it was examined whether the gold grade varies with true thickness of the vein by performing regression analyses between true thickness values and gold grades. Possible correlation was also examined between the host rock type and gold grade.

The final section discusses the results presented in the chapter and summarizes the key highlights.

## 4.1. General structural characteristics of major mineralized quartz veins

During field studies, mineralization and quartz veins were mapped using a very sensitive GPS (±0.1 cm) and attitude measurements were recorded from the places where strike and dip of the actual boundary could be measured in order to understand their structural characteristics, geometries and kinematics. Host rock contact relationships were examined for each vein in the field and in diamond cut drill cores.

Nine major mineralized quartz veins form a northwest trending corridor in the study area, from north to south: Karatepe, Karakovan 4 (KK4), Karakovan 3 (KK3), Karakovan 2 (KK2), Karakovan 1 (KK1), K1, K2, K3 and Topyurt veins (Figure 4.1). The host rocks are mica schist and quartz-feldspar-hornblende porphyry (QFH porphyry). There are two mineralized vein sets in the study area based on orientation of their strikes; first set strikes NE-SW and hosts the majority of gold mineralization while the second set trends E-W. All of the veins are continuous (not segmented) except the segmented K3 vein and Topyurt veins, however some veins have discontinuous outcrop traces due to erosion. Veins have variable thickness and locally irregular strikes and dips.

***Karatepe vein*** located at the northern part of the area is hosted entirely within the QFH porphyry. It strikes E-W, has a strike length of 350 m (Figure 4.1) and an average dip of 70° south. There is 40 m elevation difference between the tips of the vein outcrop. Width of the vein changes between 0.8 m and 8 m on the surface. Outcrop orientation data reveal that the vein has a very corrugated strike on a meter scale. Host rock QFH porphyry around the vein is highly fractured and heavily altered (Figure 4.2). Hydrothermal quartz veinlets show a large range of orientations close the vein contacts (Figure 4.3).
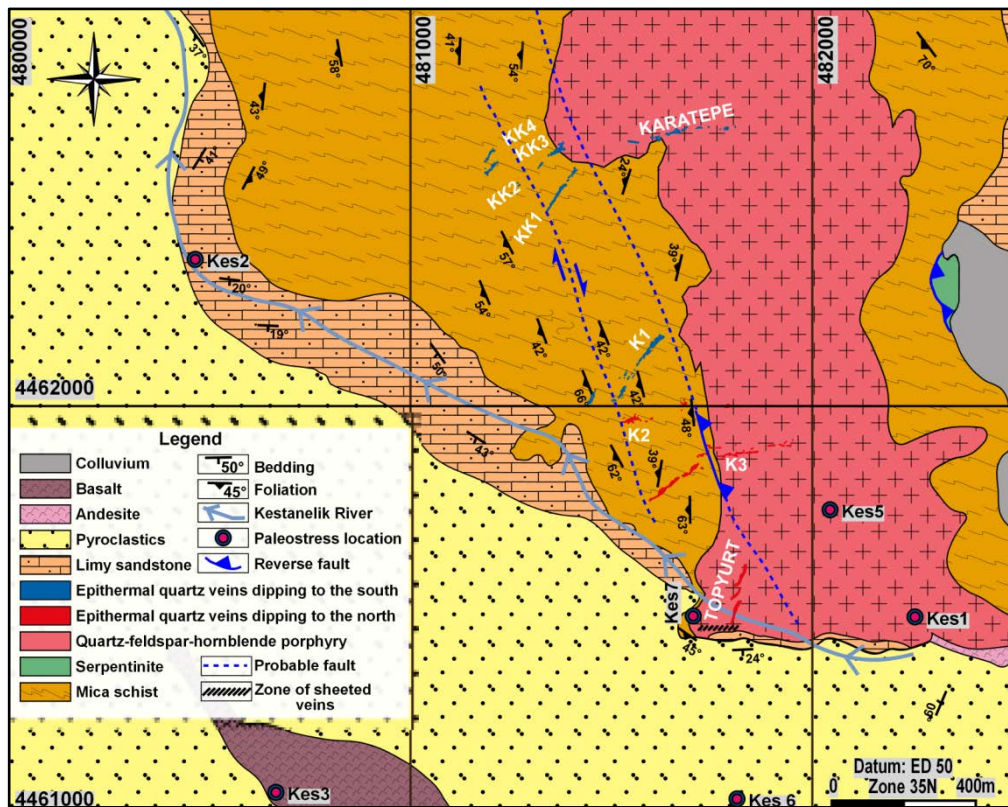
**Figure 4.1.** Geological map showing the major mineralized quartz veins and the zone sheeted quartz veins in the study area. Note that the boundary of the region where sheeted quartz veins outcrop was not mapped out so the shaded zone showing them is just indicative.
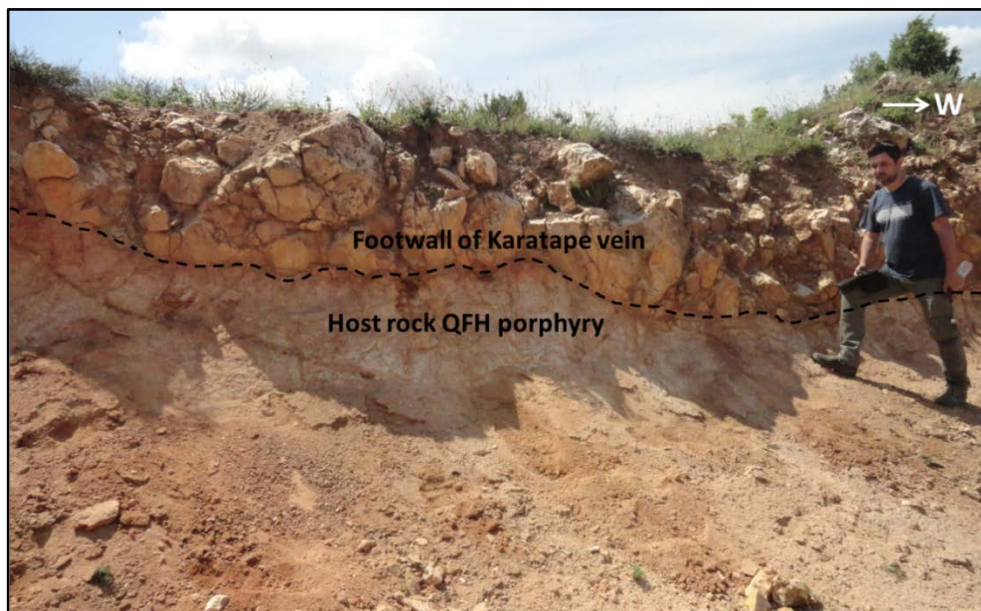


**Figure 4.2.** Heavily altered and fractured host rock QFH porphyry around the steeply dipping margin of the Karatepe vein.

66
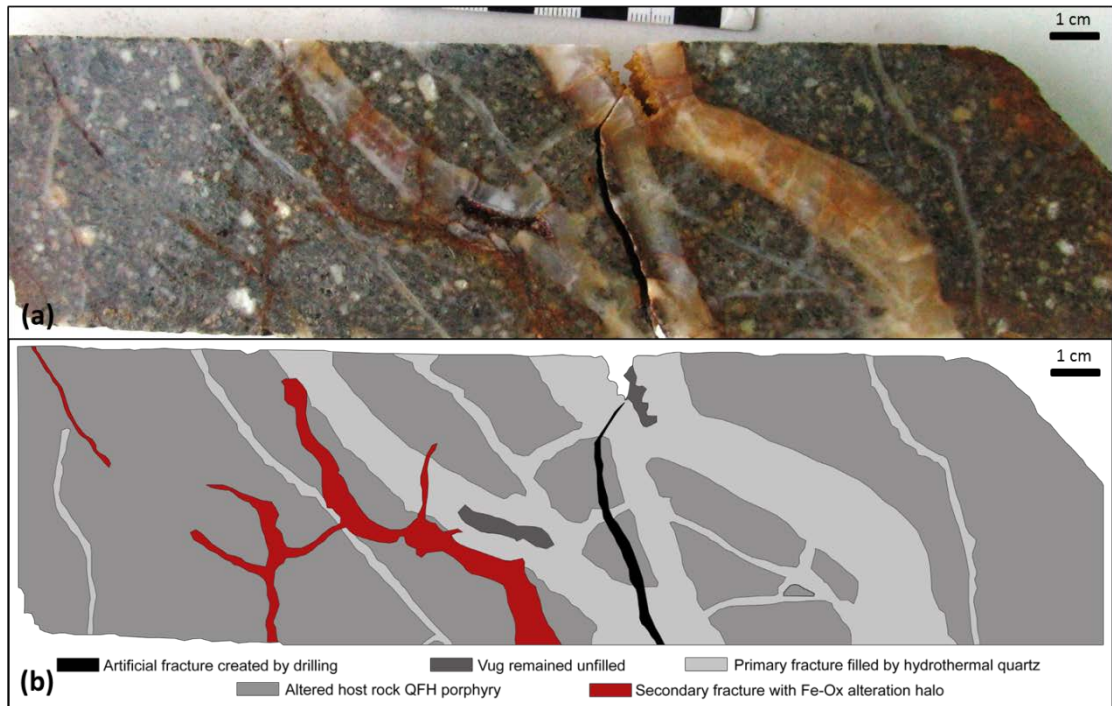
**Figure 4.3.** A core sample from KED-18 133.8-134 m showing large range of vein orientations close to the Karatepe vein-host rock contact at the footwall (FW) of the vein.

***KK3 vein and KK4 vein*** are hosted by mica schist and strike almost NE-SW (Figure 4.1). KK3 vein has 52 m strike length and its width varies between 2 m and 8.7 m. The vein dips to SE with an average dip of 70 degrees. KK4 vein has a strike length of 47 m and dips to SE with an average dip of 68 degrees. It attains thickness between 1 m and 5.8 m on the surface. The elevation differences between the tips of the KK3 and KK4 vein outcrops are 25 m and 20 m respectively.

***KK1 vein and KK2 vein*** are also hosted by mica schist and trend approximately NE-SW (Figure 4.1). KK1 vein trend extends 150 m along strike and the vein dips to SE with an average dip of 77 degrees. Vein outcrop width varies between 1.2 m and 9 m. KK2 vein has an intermittent outcrop, extends for 185 m, dips to SE with an average dip of 76 degrees and its outcrop width varies between 1 m and 8.5 m. The difference in elevation between the tips of the KK1 and KK2 vein outcrops are 45 m and 24 m respectively. These veins have sharp contacts with their host rock mica schist, foliation of the schist does not change adjacent to the veins and there is not any wall rock veins around them (Figure 4.4).

NE-SW trending *K1 vein* extends intermittently over a strike length of around 240 m and dips to the SE (Figure 4.1) with an average dip of 75 degrees. There is 35 m elevation difference between the tips of the vein outcrop. The vein pinches and swells and attains thickness between 0.9 m and 13.6 m on the surface. Around the vein, attitude of foliation planes does not change (Figure 4.5).
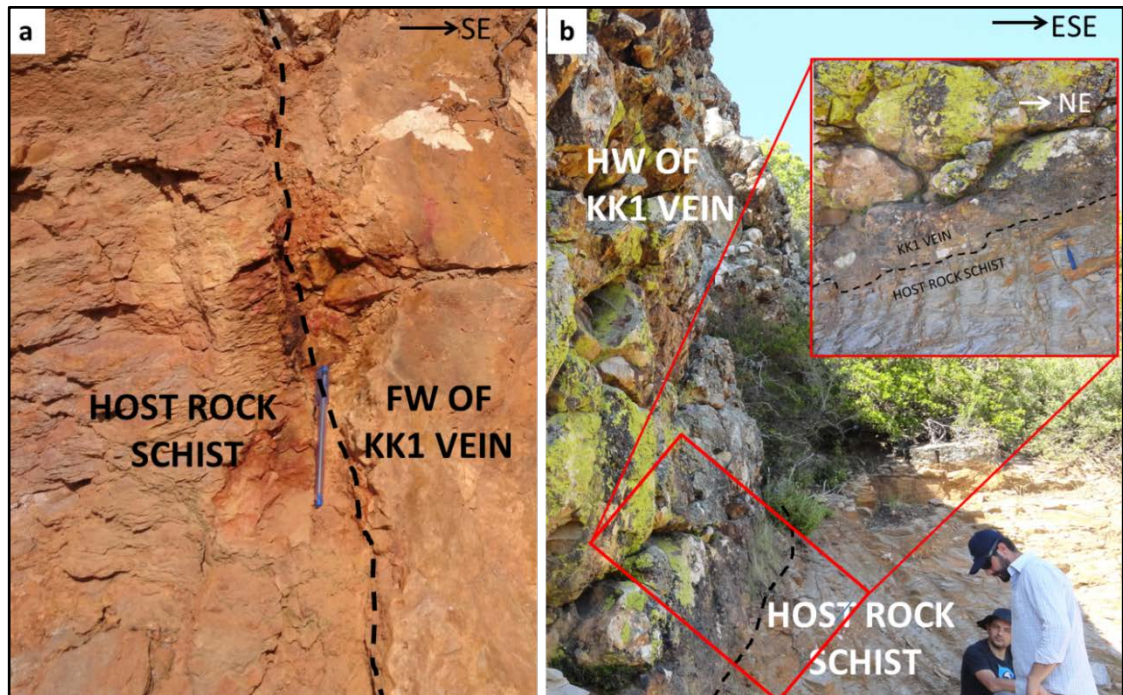


**Figure 4.4.** Photos showing the contacts of KK1 vein with its host rock mica schist: **(a)** Sharp contact between FW of KK1 vein and schist. **(b)** Sharp contact between hangingwall (HW) of KK1 vein and schist. Note that the foliation of the schist does not change adjacent to the vein.

*K2 vein* has an E-W trending intermittent strike length of 86 m and dips shallowly to north (Figure 4.1) with an average dip of 44 degrees. The vein is hosted by mica schist and attains widths between 0.6 m and 12.9 m on the surface. Schist adjacent to the vein is highly deformed and contains up to 6-7 cm wide hydrothermal quartz veins discordant to the foliation planes (Figure 4.6).

**Figure 4.5.** Photo of KED-105 74.5-82 m interval core boxes showing that the foliation of the schist does not change around the K1 vein. Note that the white veins around the K1 vein interval generally observed parallel to the foliation planes include meta-quartz (Yellow dashed lines envelopes the vein interval.).

*K3 vein system* is composed of two segments and its strike extends over 510 m (Figure 4.1). The western segment of the vein system (K3W vein) hosted by mica schist trends NE-SW with a strike length of 230 m (Figure 4.1). It dips to NW with an average angle of 62 degrees. There is 80 m elevation difference between the tips of the vein outcrop. Its outcrop width varies between 2 m and 12.5 m. Host rock schist is highly deformed around the K3W vein (Figure 4.7).

The eastern segment of the vein system (K3E vein), hosted by QFH porphyry, extends intermittently over an E-W oriented corrugated strike with a length of 280 m and dips to north (Figure 4.1) with an average angle of 71 degrees. 15 m elevation difference exists between the tips of the vein outcrop.
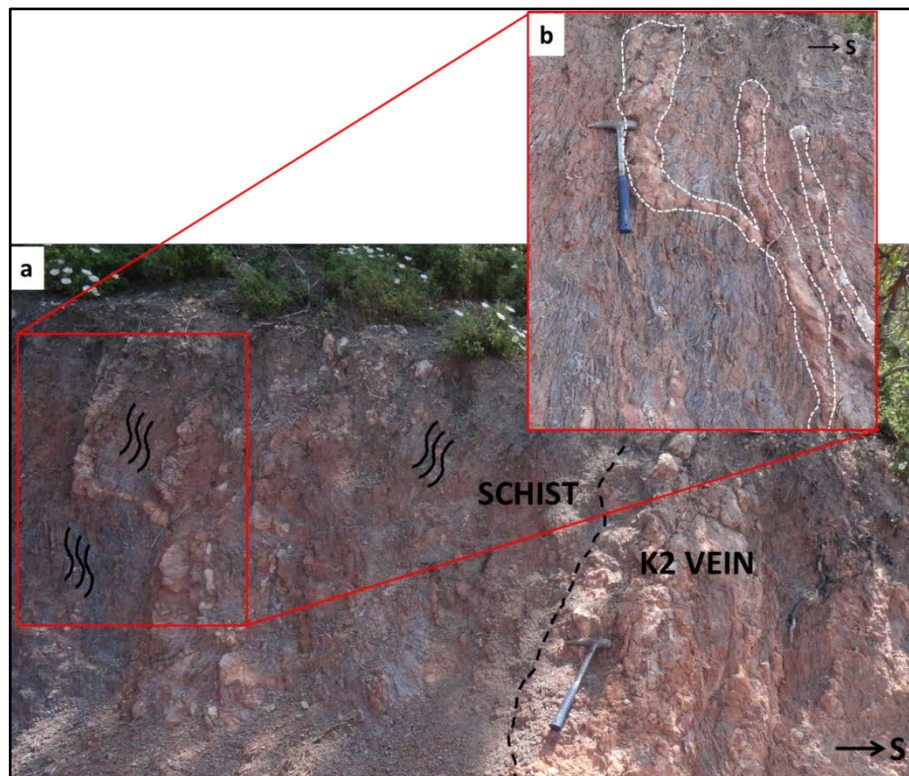
**Figure 4.6. (a)** Photo showing that the schist adjacent to the K2 vein is highly deformed and hosts hydrothermal quartz veins discordant to the foliation planes. **(b)** Closer view of discordant hydrothermal quartz veins. (Waved black lines represent the orientation of foliation surfaces; white dashed lines represent the boundaries of discordant veins.) Note that the foliation surfaces are not continuous and change their attitude.

The vein attains width between 0.6 and 7.8 m on the surface. The western segment of K3 vein is more persistent and thicker than its eastern part. Host rock porphyry is intensely deformed around the K3E vein (Figure 4.8).

**Topyurt vein system,** hosted by QFH porphyry, is located at the southern part of the study area and cuts approximately perpendicular to the Kestanelik River valley. It has 3 sub-parallel NE-SW trending veins in an N-S trending zone (Figure 4.1) with a total exposed strike length of 154 m and an average dip of 65° NW. Outcrop vein width is between 2 and 10 m. Host rock porphyry around the vein system is generally covered by trees and soil although the wall rock veins are visible (Figure 4.9).

Host rock, strike length, mean strike, mean dip angle, and minimum and maximum width of each vein are summarized in Table 4.1.

70
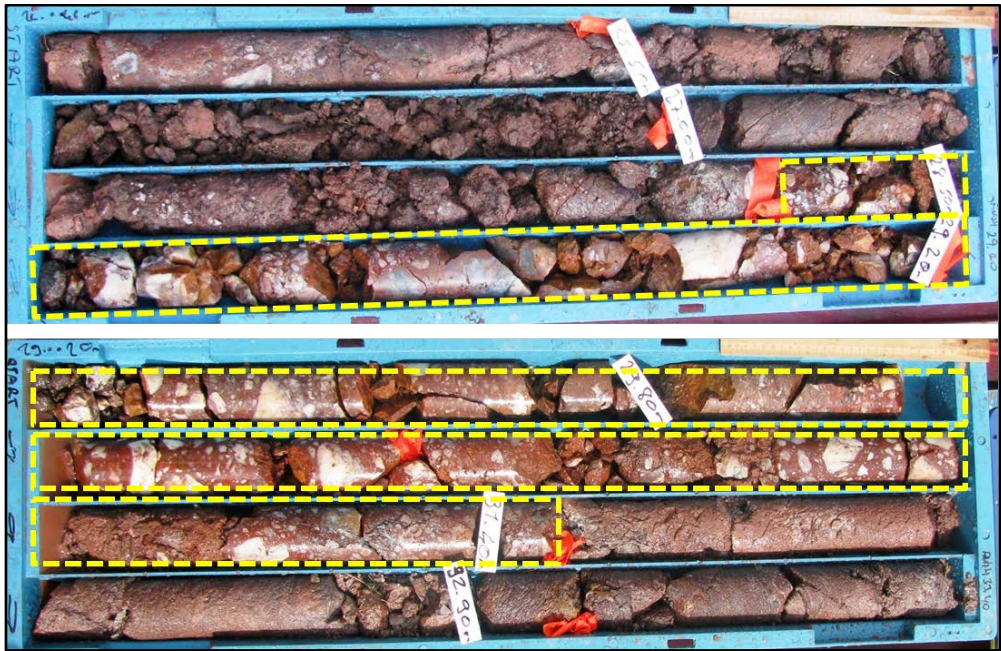
**Figure 4.7.** Photo of KED-20 24.9-33.4 m interval core boxes showing that the host rock schist is highly fractured and brecciated around the K3W vein. Note that the deformation is higher around the HW of the vein and schist includes the fragments of hydrothermal quartz veinlets around the HW of the vein (Yellow dashed lines envelopes the vein interval).



**Figure 4.8.** Photo of KED-76 78.5-86.2 m interval core boxes showing that the host rock porphyry is fractured, brecciated and veined around the K3E vein. Note that porphyry includes the fragments of hydrothermal quartz veinlets around the HW of the vein (Yellow dashed lines envelopes the vein interval).

**Figure 4.9.** Photo showing one of the wall rock veins around the Topyurt vein system. Note that the host rock porphyry is covered by soil and trees.

**Table 4.1.**General characteristics of major mineralized quartz veins.

| Vein | Host rock | No of data | Mean strike (°) | Mean dip (°) | Strike length (m) | Min. width (m) | Max. width (m) | Host rock deformation |
|---|---|---|---|---|---|---|---|---|
| Karatepe | porphyry | 23 | 084 | 70 | 350 | 0,8 | 8 | F, V |
| KK1 | schist | 11 | 047 | 77 | 150 | 1,2 | 9 | ND |
| KK2 | schist | 13 | 045 | 76 | 185 | 1 | 8,5 | ND |
| KK3 | schist | 5 | 047 | 70 | 52 | 2 | 8,7 | ND |
| KK4 | schist | 4 | 042 | 68 | 47 | 1 | 5,8 | ND |
| K1 | schist | 15 | 040 | 75 | 240 | 0,9 | 13,6 | ND |
| K2 | schist | 8 | 268 | 44 | 86 | 0,6 | 12,9 | FC, V |
| K3E | porphyry | 18 | 275 | 71 | 280 | 0,6 | 7,8 | F, B, V |
| K3W | schist | 16 | 237 | 62 | 230 | 2 | 12,5 | F, B, V |
| Topyurt | porphyry | 10 | 225 | 65 | 154 | 2 | 10 | V |

B: Brecciated, F: Fractured, FC: Foliation Changes, ND: Not Deformed, V: Veined

## 4.2. Sheeted quartz veins in the valley and their kinematics

In addition to major mineralized quartz veins, sheeted mineralized quartz veins are present along Kestanelik River in the southern part of the study area (Figure 4.1). They are oriented almost perpendicular to the river bed and sub-parallel to each other (Figure 4.10a-b). Their thicknesses vary between 0.5 cm and 15 cm; therefore they cannot be shown individually on the map, and the region where they outcrop has been indicated by shading (Figure 4.1).
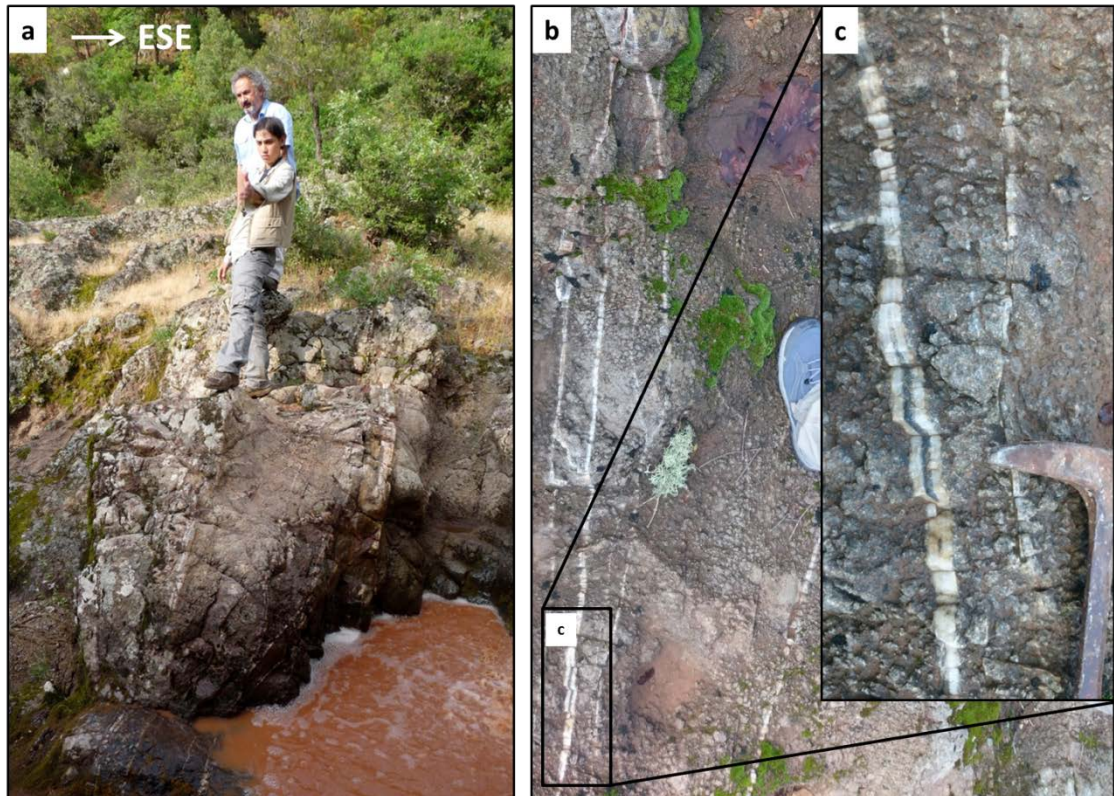


**Figure 4.10. (a)** Photo showing the sub-vertical and sub-parallel sheeted quartz veins along the Kestanelik River valley. **(b)** Photo showing some of the sheeted quartz veins. **(c)** Closer view of one of the sheeted extensional veins having comb textured well developed hydrothermal quartz crystals oriented perpendicular to the vein walls.

These veins contain well developed quartz crystals almost perpendicular to the vein walls (Figure 4.10c), and there is no evidence of shearing along the vein walls; therefore they are very likely to be extension veins. Attitude data were also recorded from them in order to make inferences on their kinematics (since

extension veins form normal to $\sigma_3$). A rose diagram of their strike values is given in Figure 4.11.
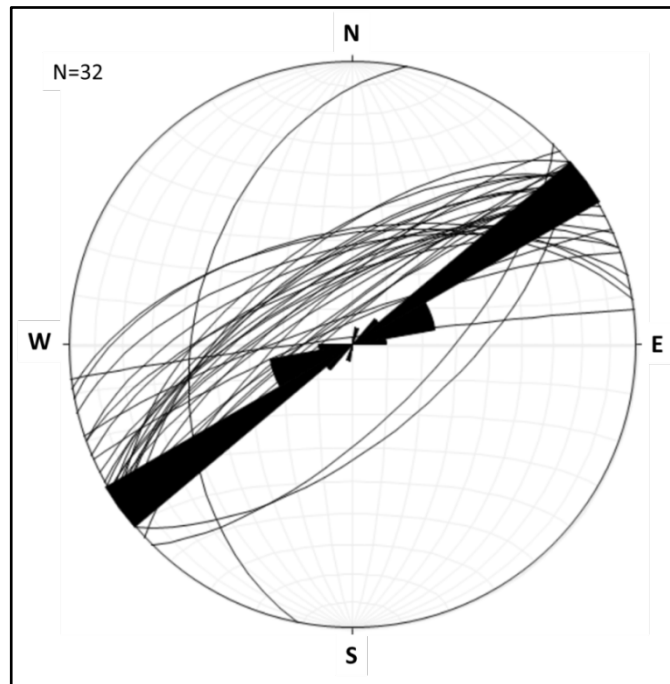


**Figure 4.11.** Planes of the sheeted extension veins plotted on an equal-area stereonet and the rose plot of their strike values.

## 4.3. Wall rock veins and their kinematics

In order to better understand the kinematics of the structures hosting the veins, detailed structural data (thickness, infill type, length, attitude, and typology) were collected from the wall rock structures surrounding the two of the major mineralized quartz veins: *Karatepe vein* and *Topyurt vein*. Dense vegetation and thick soil cover around other vein-associated structures prevented the collection of structural data.

The area surrounding the Karatepe vein is dominated by extension veins (Figure 4.12a-b-c). These veins have comb textured hydrothermal quartz crystals oriented perpendicular to the vein walls (Figure 4.12c). Their surface width changes between 4 and 26 cm. Extension veins in the HW of the vein only arise around the eastern tip (Figure 4.12a). The density of extension veins calculated parallel to the strike of the main vein is higher in the footwall (0.072 per meter) compared to the

hangingwall (0.05 per meter) (Figure 4.12a). Extension veins around the Karatepe vein have large range of orientations and rose plot of their strike values is given in Figure 4.12d.
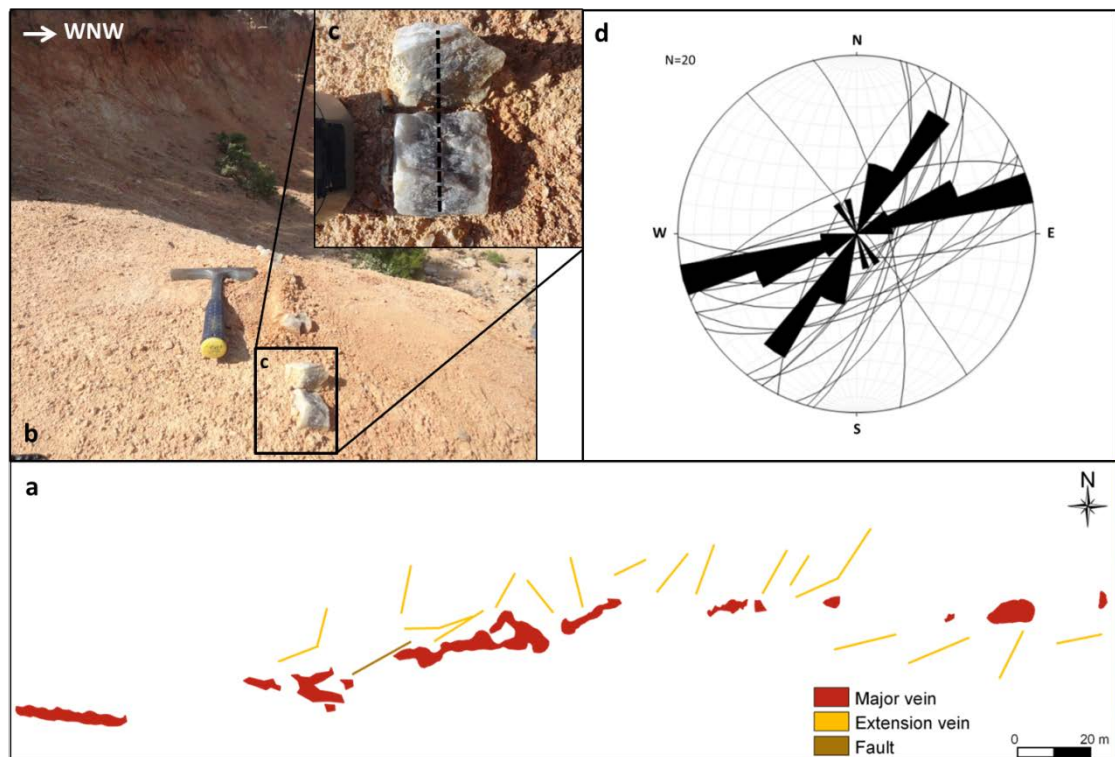


**Figure 4.12. (a)** Detailed map of the Karatepe vein and its wall rock veins. **(b)** Photo showing one of the extension veins around the Karatepe vein. **(c)** Closer view of the extension vein having comb textured hydrothermal quartz. **(d)** Planes of the extension veins around the Karatepe vein plotted on an equal-area stereonet and the rose plot of their strike values.

The area surrounding the Topyurt vein system is also dominated by extension veins (Figure 4.13a-b). These veins are only observed in the FW of the vein system (Figure 4.13a) and their width changes between 3 cm and 20 cm on the surface. The density of extension veins between the mid- and southernmost segments of the vein system (0.25 per meter) is highest (Figure 4.13a). A rose plot of their strike data is presented in Figure 4.13c. Topyurt vein geometry and associated structures seem to define right lateral en-echelon brittle shear zone (Figure 4.13a).
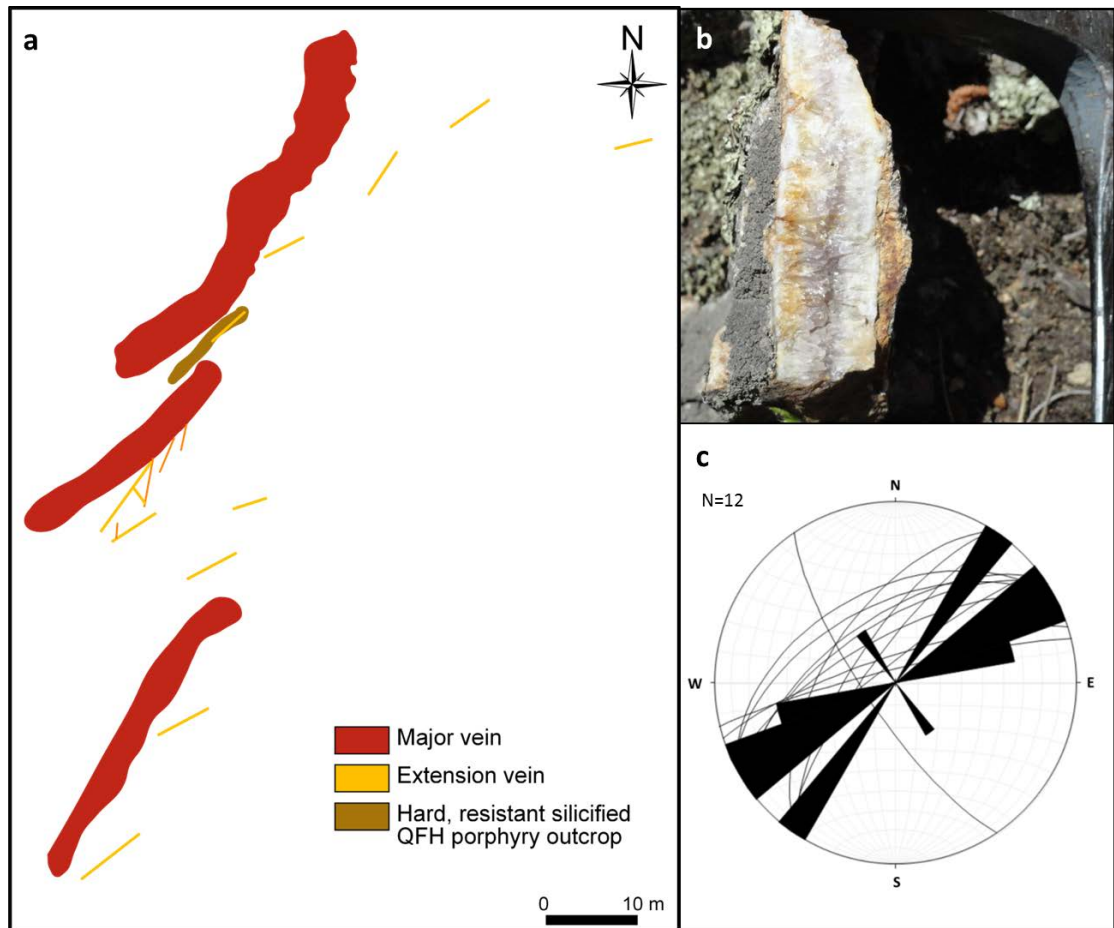
**Figure 4.13. (a)** Detailed map of the Topyurt vein and its wall rock veins. **(b)** Photo showing one of the extension veins having comb textured hydrothermal quartz around the Topyurt vein. **(c)** Planes of the extension veins around the Topyurt vein plotted on an equal-area stereonet and the rose plot of their strike values.

Hydrothermal macro-crystalline quartz was observed also in the extensional veins along the river valley similar to the ones around the Topyurt and Karatepe veins. The consistent textures and orientations of the main veins and sheeted veins suggest that all these veins are related to same hydrothermal mineralization event. Strikes of all these veins were plotted on a rose diagram (Figure 4.14) in order infer the kinematics of the hydrothermal structure-vein system. According to the rose plot (Figure 4.14), direction of horizontal component of the minimum principal stress ($\sigma_3$) is *N35°W*.
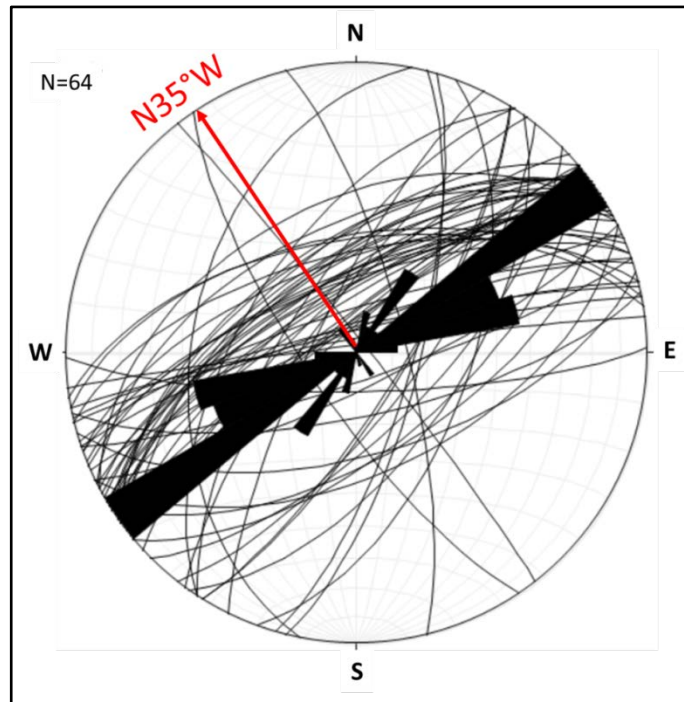
**Figure 4.14.** Planes of the all extension in the study area plotted on an equal-area stereonet and the rose plot of their strike values with an inferred horizontal component of minimum principal stress direction N35°W.

## 4.4. 3D modeling of vein geometries

Hangingwall and footwall surfaces of the major mineralized quartz veins (HW refers to the wall above a seam of ore and the FW refers to the wall below the seam) were modeled in 3D using the log data and geochemistry data from diamond cut and reverse circulation (RC) drill holes supplied by the Kestanelik gold deposit license holder company (Chesser Resources Ltd.) and the detailed mapped geometries of vein outcrops. Geochemistry data were obtained from the half core samples collected from drill core intervals with sample lengths in the range of 1 m to 1.5 m and samples collected from the RC drill holes over 1 m intervals. The surfaces were modeled using structural modeling and analysis software MOVE granted by Midland Valley's Academic Software Initiative, GIS application software Global Mapper distributed by BLUE MARBLE Geographics and GIS mapping software ArcGIS produced by ESRI.

Firstly, collar (x,y,z), survey and assay (lithological log) data of drill holes and vector data (sensitive GPS data) of the veins were imported to MOVE. Multiple quartz vein (QV) intersections were generally the case for a drill hole. In order to understand which QV intersection should be included to model the vein surfaces, firstly dip amount and dip direction of the vein measured from its outcrop were taken into account to see which intersection is likely to belong to the main vein, by assuming that the attitude of the vein does not change in the subsurface. Then, the quartz textures of the QV intervals were examined using the photos of drill cores to understand which QV interval has the general textural characteristics of the main vein, by assuming that the textural characteristics do not change as much with depth as they do laterally between main veins and wall rock veins. Finally, the geochemistry data from the drill holes were examined to look for relatively high gold and silver grades of the QV intervals by assuming that the main vein will have a higher gold grade as its textural characteristics generally indicate boiling (see chapter 2). At the end of these steps, one to seven QV intervals (varying between each drillhole) were discarded and the most appropriate QV interval was selected. After deciding the QV interval to be included), point data were created at the top and bottom of the intersection to model the HW and FW surfaces of the vein respectively. Point data where drill holes cut the vein surfaces were created using the procedure above in *MOVE*. In order to connect these subsurface points to the surface, surface points were created along the vein outcrop boundaries by applying elevations to these points from the digital elevation model (DEM) of the study area in *Global Mapper*. Surface point data created in *Global Mapper* and the subsurface point data created in *MOVE* were exported separately and imported to ArcGIS and merged there as input data to create continuous HW and FW surfaces of the vein using the natural neighbor interpolation method (Sibson, 1981) since this interpolation method works well with randomly distributed data (Watson, 1992). Natural neighbor interpolation method uses the data points to interpolate the surface values for each vertex (single point which has a 3D position) by identifying and weighting these data points using a Delanuey triangulation. Number of vertex is

determined statistically by ArcGIS prior to surface generation and depends on the number of input points and distances between the input points. Created surface passes through the input points and is smooth everywhere except at locations of the input data (Sibson, 1981).

The surfaces created in *ArcGIS* were then imported to *MOVE* in order to analyze the surface geometries in terms of strike, dip and thickness. Strike and dip data were calculated for the surfaces of each vein by creating vertex attributes. Rose plots were formed in MOVE using the vertex strike data to express the orientation data of each vein surfaces statistically. Exported vertex dip data were used to create histogram of dip amount for each vein surfaces. Thickness values were calculated by constructing lines perpendicular to the local vein dip between the vertices at the HW and FW surfaces in MOVE (Figure 4.15). Histogram of thickness data was also created for each vein.
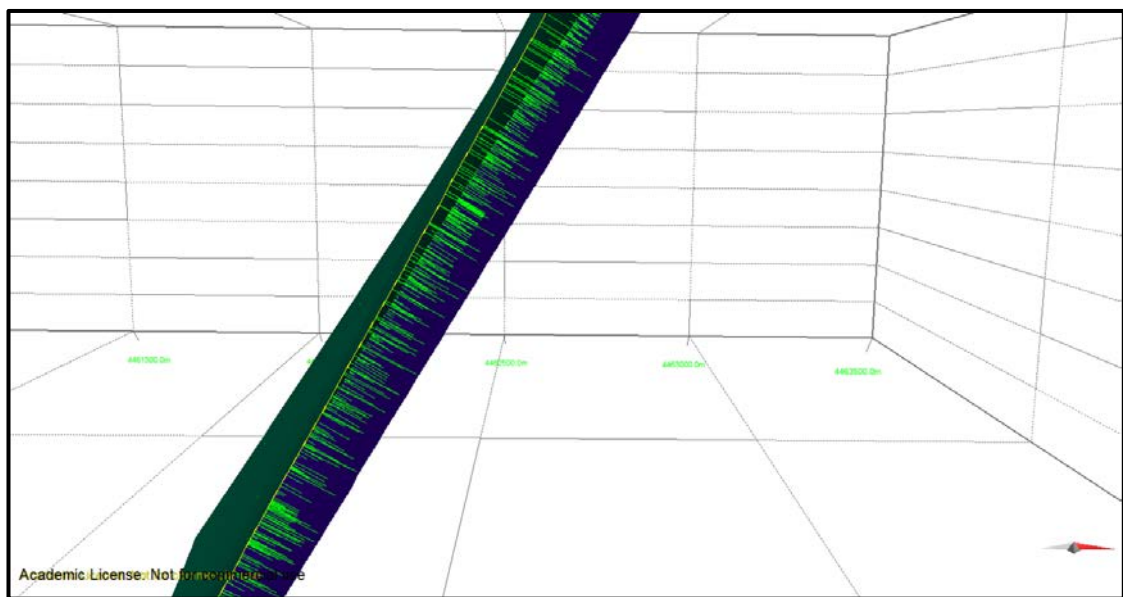


**Figure 4.15.** A MOVE image showing the constructed lines between the two surfaces of a vein used which then used for calculating the true thickness values. Note that just 2% of the lines are shown.

Univariate statistical analyses of the data obtained from 3D modeling were performed using *Microsoft Office Excel 2010 Professional*. Descriptive statistical parameters (given in Table 4.2) were calculated to provide the basic features of the

strike, dip and thickness data. Most of the strike and dip data have skewed distributions so median values of orientation (strike/dip) data are presented for each vein in the section. The median is much better than mean values to describe the central tendency of the data for skewed distributions.

I hypothesized that while fluid entering the conduit is moving up, a thickness increase sudden in time during rupture in the conduit would lead to a drop in the fluid pressure causing boiling (the most dominant gold precipitation mechanism) and associated gold precipitation (see chapter 2). In this respect, true thickness values vs. mean gold grades of each vein intersection were plotted on a scatter graph and regression analysis was performed to estimate the degree of relationship among these two variables for each vein in order to investigate if the gold grade varies with the true thickness of the vein. Moreover, p-values ($\alpha=0.01$) were calculated in regression analyses of Excel in order to decide whether there is a statistically significant relationship between the true vein thickness and gold grade. Additionally, a possible correlation was examined between the host rock type and gold grade.

To better understand the geometries of the structures hosting the veins, vertical cross sections were created in MOVE. Sections run perpendicular to the vein strikes and were constructed using the modeled vein surfaces and the DEM of the study area. 4 vertical cross sections were created in total for each vein (except K3W-12 vertical cross sections created) with equal spacing between the sections which is determined based on the strike length of each vein.

7 major veins were modeled in total: the Karatepe, KK1, KK2, KK3, KK4, K1 and K3 (K3E and K3W) veins (Figure 4.16). K2 vein could not be modeled due to the small number and low quality of the drill holes around the vein. Topyurt vein system was also not modeled since drilling activity was not permitted around the vein due to the existence of a protection area which supplies water to the nearby Şahinli Village.
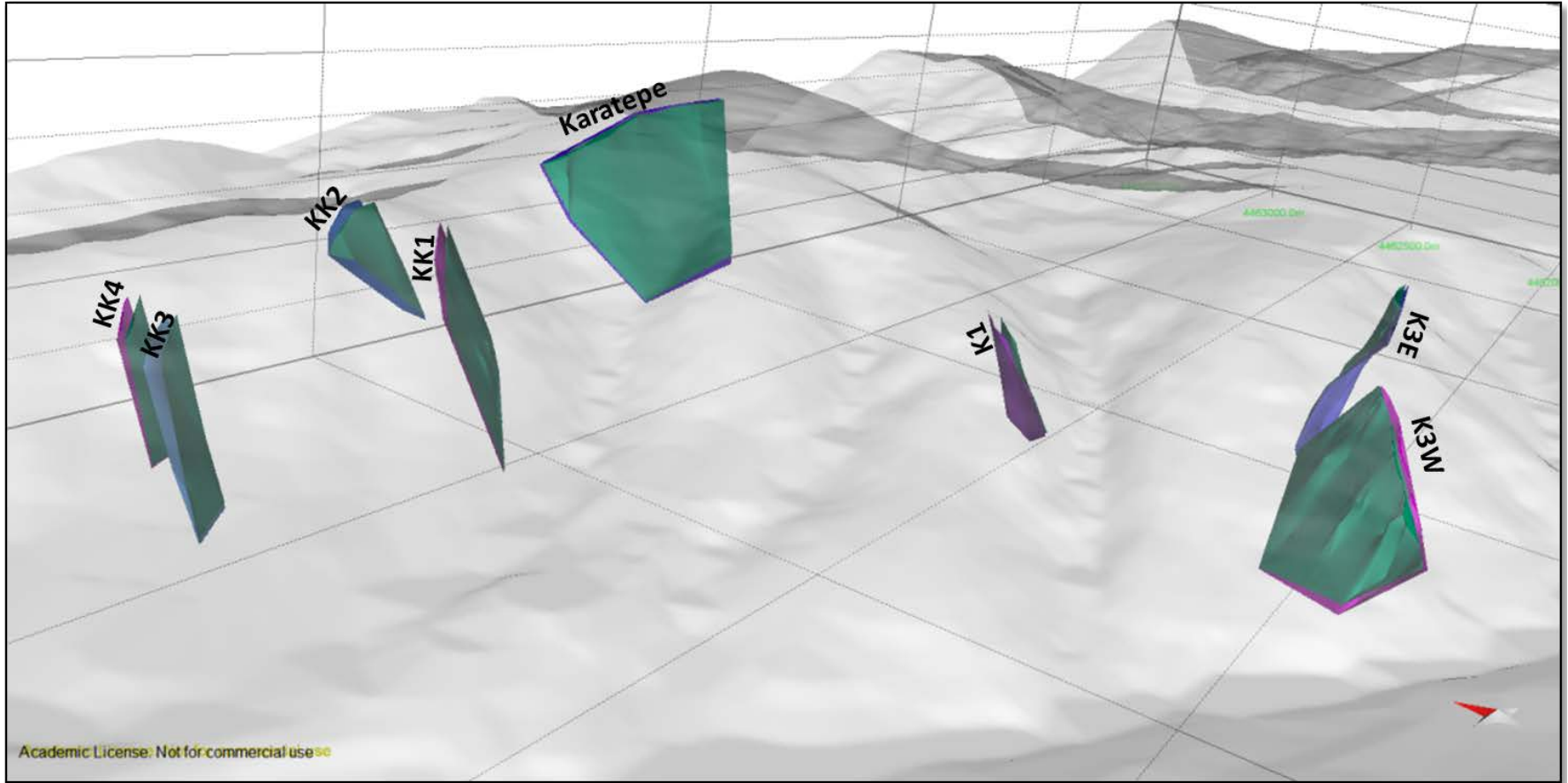
**Figure 4.16.** 3D view of modeled top and bottom surfaces of all veins with DEM.

### 4.4.1. Results of 3D Modeling

*Karatepe vein* geometry was modeled from 6 diamond cut and 3 RC drillhole data (Figure 4.17). Vein orientation undulates slightly along strike which is also evident from the strike measurements of the vein outcrop which vary between 032° and 112°. The lateral tips of the vein are plunging inwards. The median orientation of this moderately dipping structure is 085.8°/56.3° (strike/dip) at its FW surface and 085.8/57.3 at its HW surface. When this median orientation data is compared to the mean surface orientation of the vein (084°/70°), surface strike data seems representative. The mean surface dip data is higher than the subsurface dip although the center of the vein bends along dip and becomes steeper below a depth of 140 m (Figure 4.18).

A cluster of shallow dips (<50°) (Figure 4.19b-d) are due to the artificial surfaces created by the interpolation of outcrop data points (Figure 4.18). The deepest drill intersection is around 160 m below surface. From the geochemistry data of modeled drillhole intervals the gold grades are generally low and the mean Au grade of the vein is 0.458 ppm (g/t) with the highest and lowest grade results being 1.021 g/t and 0.133 g/t respectively.

Vertical cross sections created as close to perpendicular to vein strike as possible (Figure 4.20) show that the thickness of the vein increases gradually towards to the surface. The vein has almost constant dip until the depths of 140 m below surface (at the level 260 m above sea level (asl) where the center of the HW surface of the vein bends and become steeper (Figure 4.18). Steeper dips (>75°) on the histograms of dip amount data (Figure 4.19b-d) are related to this steep section.
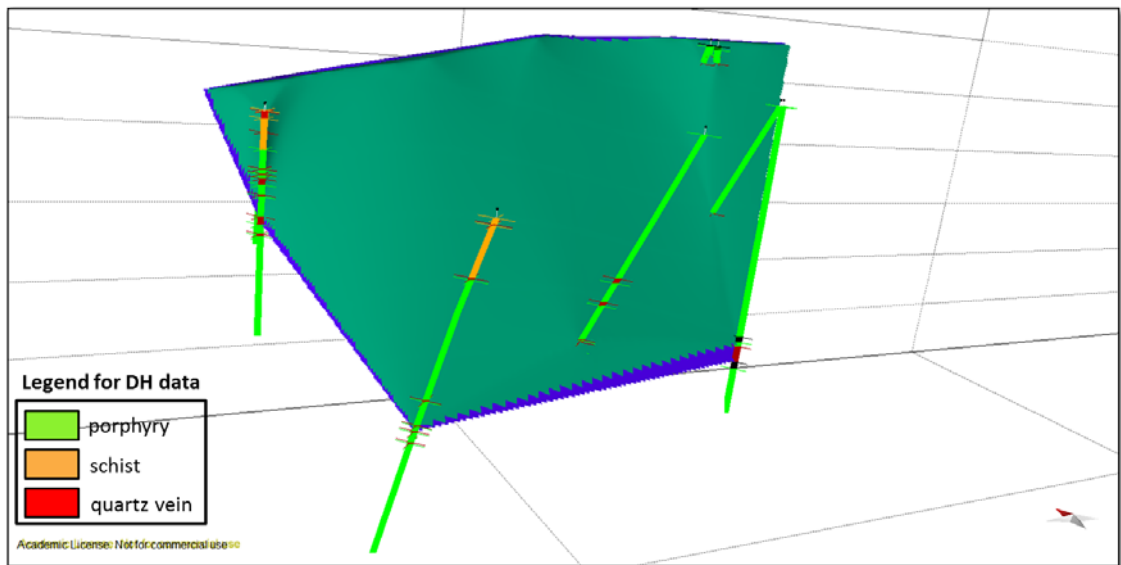
**Figure 4.17.** 3D view of modeled surfaces of Karatepe vein with used drill holes.
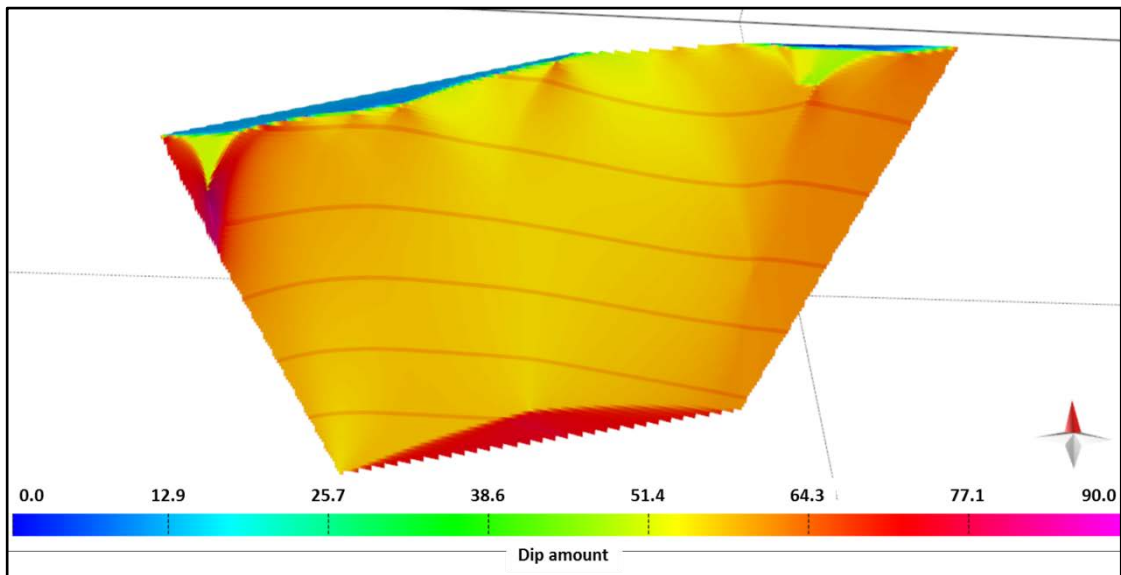


**Figure 4.18.** Colored dip amount map of Karatepe HW surface.

The average thickness of the modeled vein is 5.1 m (Figure 4.21a). The correlation coefficient of a scatter graph of thickness vs. gold grade is estimated as 0.003 (Figure 4.21b). In addition, the p-value was calculated as 0.89 (p>0.01).

*KK1 vein* geometry was modeled using 5 diamond cut and 6 RC drillhole data (Figure 4.22). Orientation of the vein is almost constant along strike and down dip, i.e. a tabular geometry. Median values of the orientation of HW and FW surfaces of

the vein are 054.9°/61.8° and 054.8°/59.1° respectively. Mean of orientation data collected from the outcrop of the vein is 047°/77°; therefore the surface data does not seem so representative although there are just three outcrop orientation measurements since surface access to the vein is limited in extent.
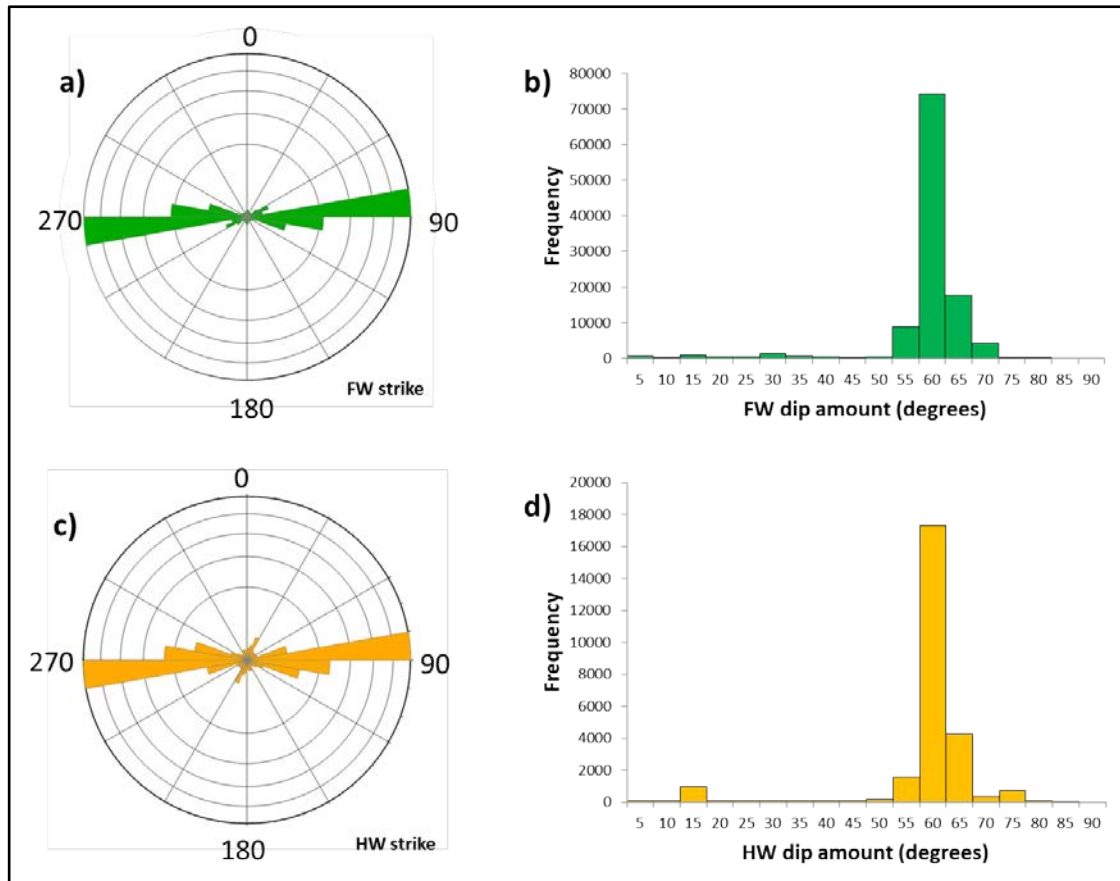


**Figure 4.19. (a)** Rose plot of strike data of modeled Karatepe vein FW surface. **(b)** Histogram of dip amount data of modeled Karatepe vein FW surface. **(c)** Rose plot of strike data of modeled Karatepe vein HW surface. **(d)** Histogram of dip amount data of modeled Karatepe vein HW surface.

Strike values of the vein surfaces are not scattered both at HW and FW (Figure 4.23a-c) which is also clearly visible on the 3D view of the vein (Figure 4.22). Small cluster of shallow dips shown on the histograms (Figure 4.23b-d) correspond to the flat-lying section in the mid of the vein (Figure 4.24) which is also shown on Section 1 and 2 (Figure 4.25b). The deepest drill intersection is around 125 m below surface.
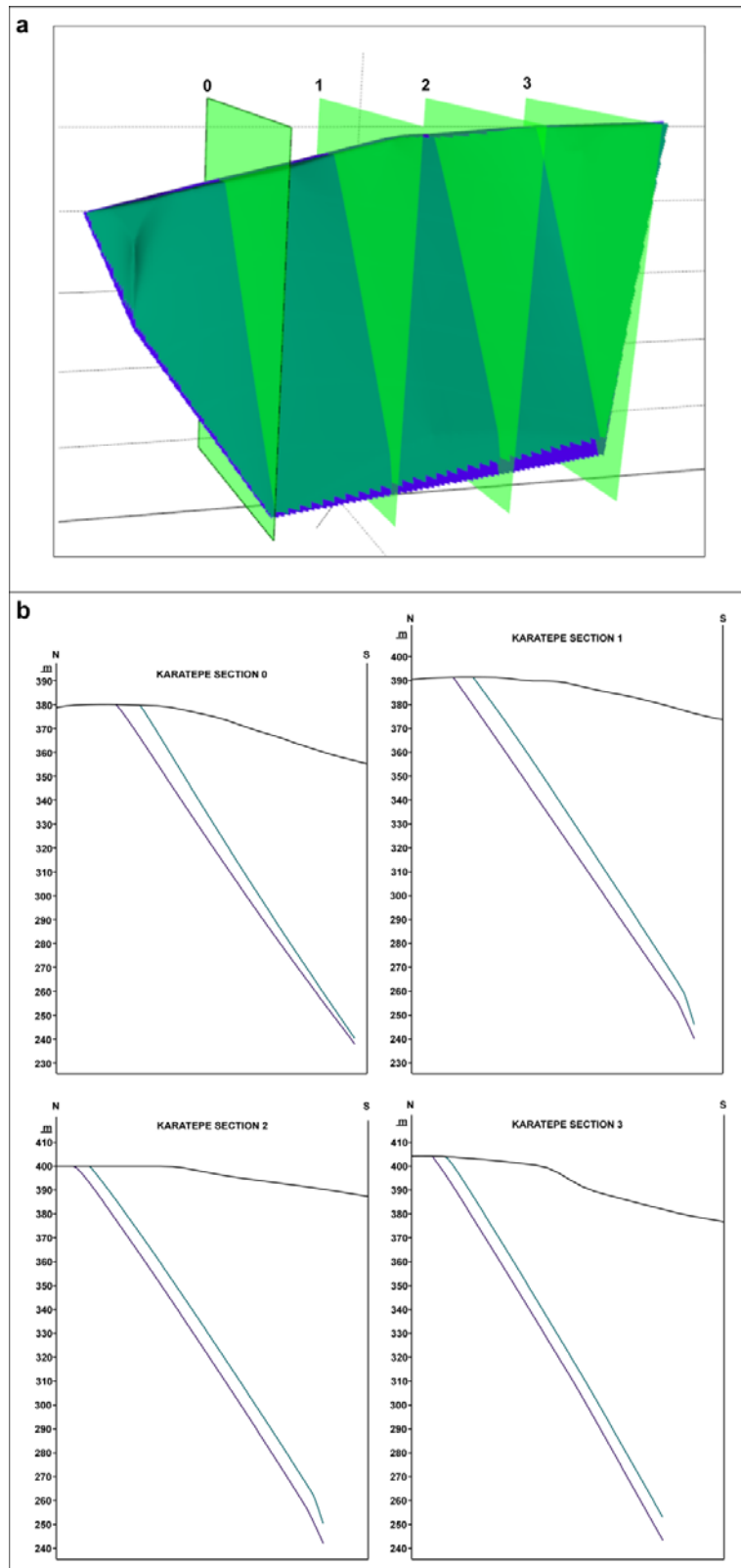
**Figure 4.20. (a)** Modeled Karatepe vein with cross-section lines. **(b)** Vertical cross sections of Karatepe vein.
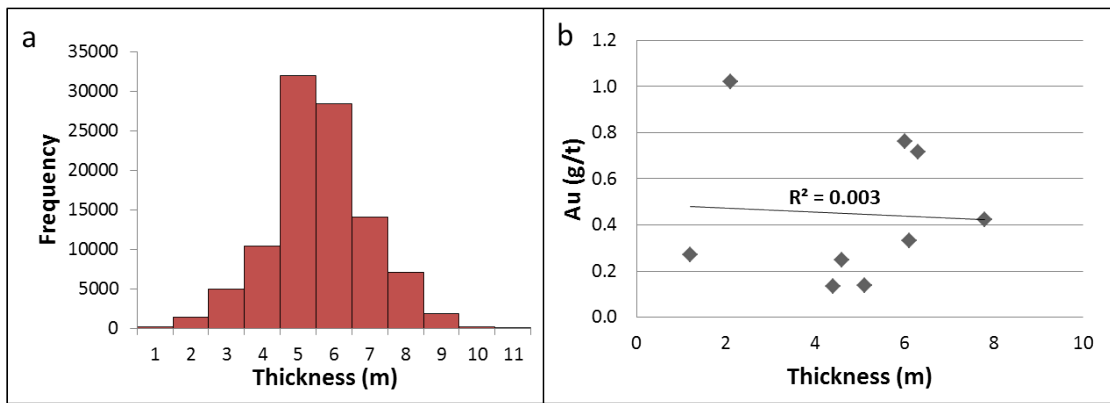
**Figure 4.21. (a)** Histogram of thickness data of Karatepe vein. **(b)** Scatter graph of thickness vs. gold grades of Karatepe vein with linear regression line and correlation coefficient value.
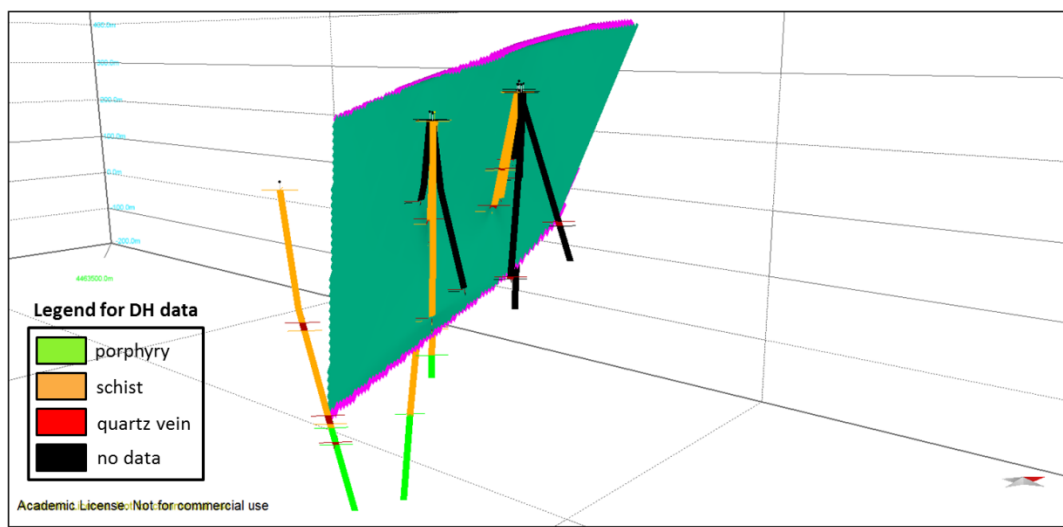


**Figure 4.22.** 3D view of modeled surfaces of KK1 vein with used drill holes.

Vertical cross sections (Figure 4.25) indicate that the thickness of the vein is almost constant till a depth of 40 m below surface (the level 265 m asl). Above 40m the thickness starts to increase gradually towards to the surface at the southwestern end of the vein. At the northern end the thickness decreases consistently with depth. Away from the tips of the vein, the vein bends at 60 m below surface (at the level 255 m asl) and gets thicker and gentler there. Below this level, the vein gets steeper and thinner (Figure 4.24 and 4.25). Average thickness of the vein is 2.4 m (Figure 4.26).

86
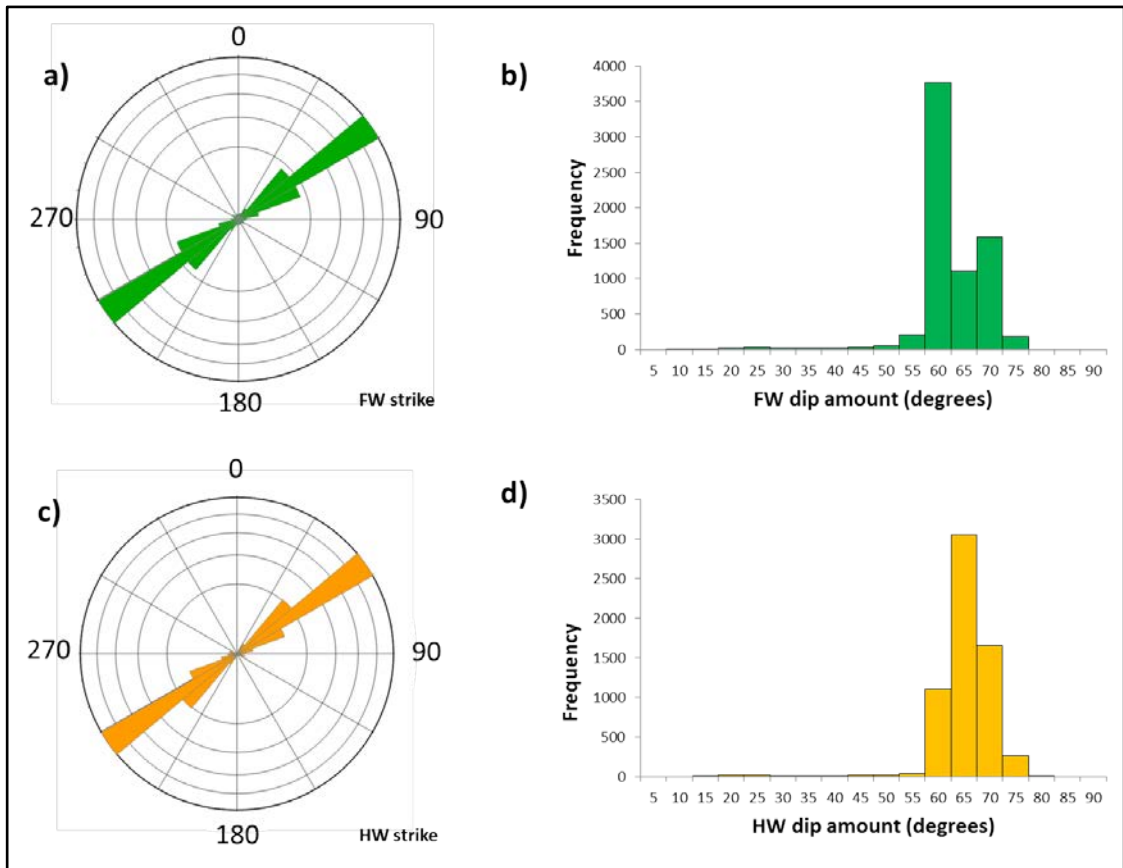
**Figure 4.23. (a)** Rose plot of strike data of modeled KK1 vein FW surface. **(b)** Histogram of dip amount data of modeled KK1 vein FW surface. **(c)** Rose plot of strike data of modeled KK1 vein HW surface. **(d)** Histogram of dip amount data of modeled KK1 vein HW surface.
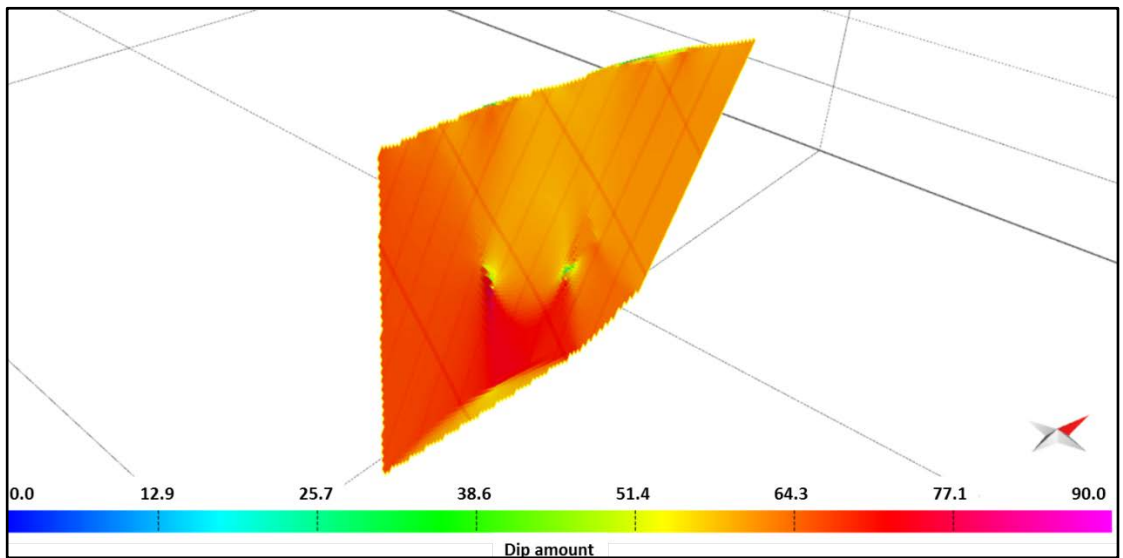


**Figure 4.24.** Colored dip amount map of KK1 HW surface.

According to the geochemical data from the modeled drillhole intervals, the mean Au grade of the vein is 3.356 g/t with the highest and lowest grade results being 8.68 g/t and 0.043 g/t respectively.  Two drill holes cut the vein where it bends along dip and the average Au grades of these vein intervals are 7.28 g/t and 8.68 g/t which are the two highest gold grades in this vein.

The correlation coefficient value calculated for the scatter graph of thickness vs. gold grade is 0.0694 (Figure 4.27a). Also, p-value was calculated as 0.67 ($p > 0.01$). Thickness vs. gold grade was plotted again to see the degree of relationship among these two variables when bend-related gold grades are taken out (Figure 4.27b) however correlation coefficient value was not calculated as there are only three points.

*KK2 vein* geometry was modeled from 4 diamond cut and 4 RC drillholes (Figure 4.28). According to the modeled geometry; the vein has almost planar geometry. Southwestern tip of the HW surface of the vein is plunging inwards (Figure 4.29). This change in geometry may be related to the artificial surface outcrop points which may have resulted from the erosion of the vein outcrop or vegetation. Median values of the direction of HW and FW surfaces of the vein are 065.8°/55.8° and 066.4°/52.1° respectively. Mean of orientation data collected from the outcrop of the vein is 045°/76°; therefore the surface data does not represent the subsurface orientation of the vein.  Cluster of dips <40° shown on the histogram of HW dip (Figure 4.30d) results from the plunging of the SW tip of the HW surface of the vein (Figure 4.29). The deepest drill intersection is around 100 m below surface.
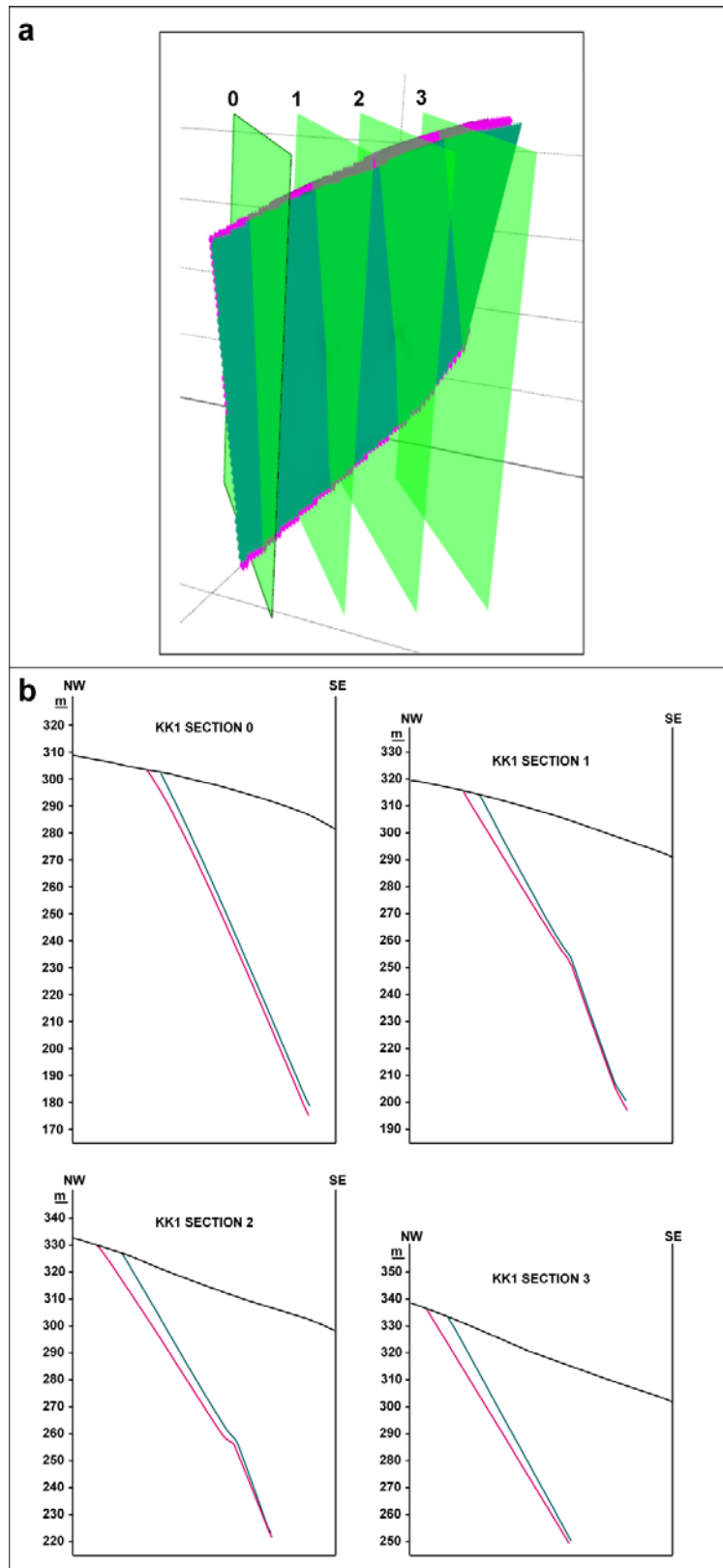
**Figure 4.25. (a)** Modeled KK1 vein with cross-section lines. **(b)** Vertical cross sections of KK1 vein.
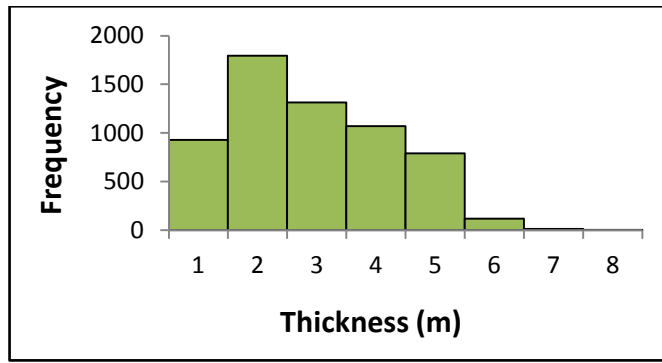
**Figure 4.26.** Histogram of thickness data of KK1 vein.
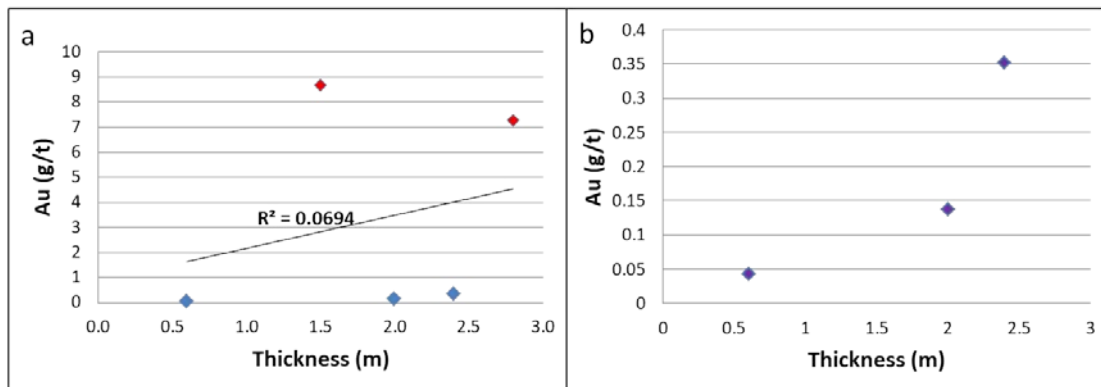


**Figure 4.27. (a)** Scatter graph of thickness vs. gold grade of KK1 vein with linear regression line and correlation coefficient value. Note that the points indicated by red color correspond to bend-related gold grades. **(b)** Scatter graph of thickness vs. gold grade of KK1 vein when bend-related gold grades are taken out.
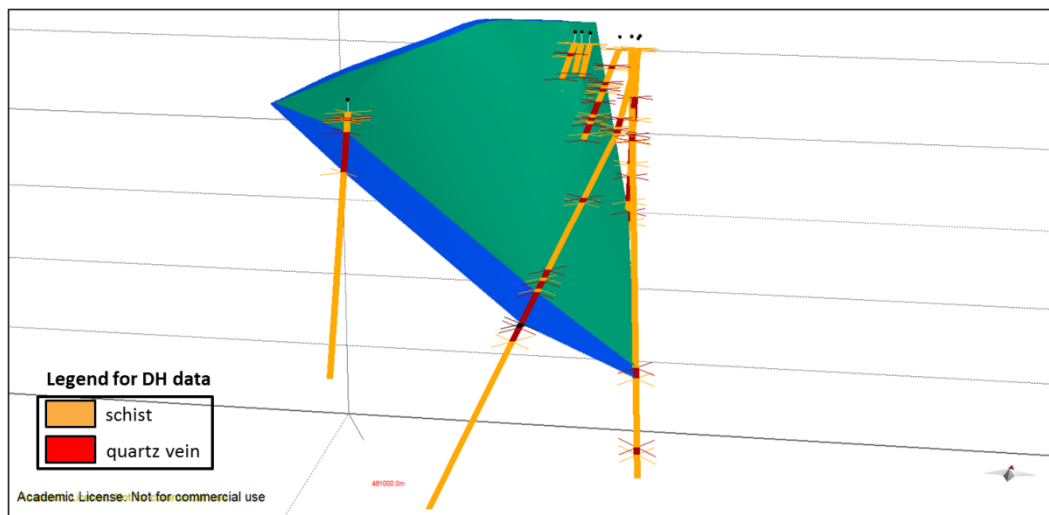


**Figure 4.28.** 3D view of modeled surfaces of KK2 vein with used drill holes.

90
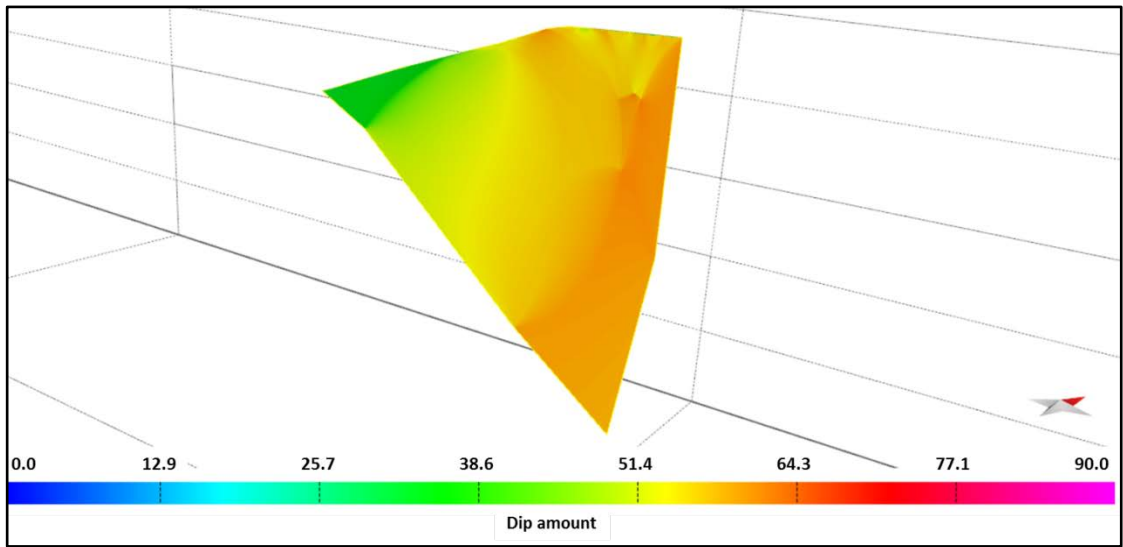
**Figure 4.29.** Colored dip amount map of KK2 HW surface.
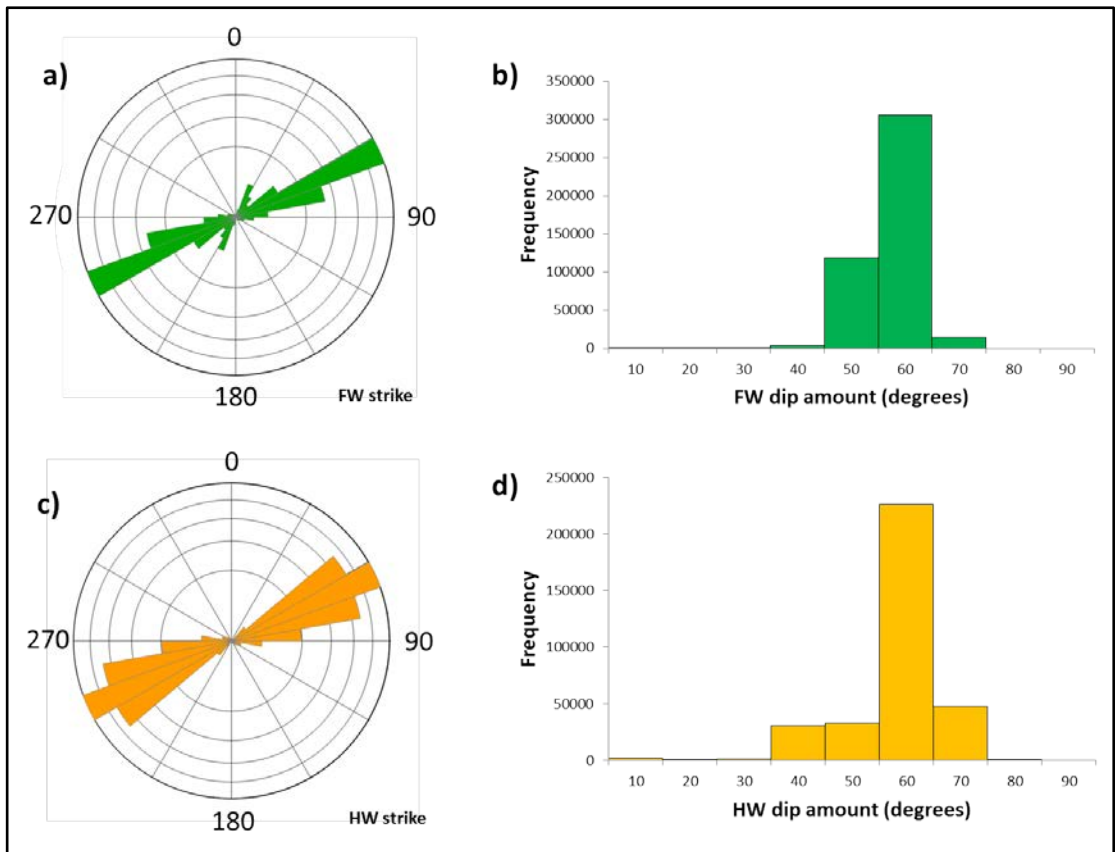


**Figure 4.30. (a)** Rose plot of strike data of modeled KK2 vein FW surface. **(b)** Histogram of dip amount data of modeled KK2 vein FW surface. **(c)** Rose plot of strike data of modeled KK2 vein HW surface. **(d)** Histogram of dip amount data of modeled KK2 vein HW surface.

Vertical cross sections constructed perpendicular to the vein strike (Figure 4.31) shows that vein gets thinner as elevation increases at its southwestern end where it plunges inwards. At its northeastern end, FW surface of the vein bends at 20 m below surface (at the level 330 m asl) (Figure 4.31b). Small cluster of strike values around 030° belonging to modeled FW surface of the vein (Figure 4.30a) is related to change in strike around the bending location of the FW surface (Figure 4.31b). Mean thickness of the vein is 5.4 m (Figure 4.32).

The mean Au grade of the vein is 2.081 g/t with the highest and lowest grade results being 3.556 g/t and 0.365 g/t respectively. Au grade values coming from the bending location intervals are 2.488 g/t and 2.86 g/t which are higher than the mean Au grade of the vein. Correlation coefficient value and p-value were estimated as 0.0503 (Figure 4.33a) and 0.59 (p>0.01) respectively. When bend-related gold grades are ignored, a negative correlation coefficient value of 0.03 is found (Figure 4.33b).

*KK3 vein* geometry was modeled from 6 diamond cut and 2 RC drillhole data (Figure 4.34). The modeled geometry shows that the vein is continuous at depth towards southwest. Median values of the orientation of HW and FW surfaces of the vein are 055.7°/66.2° and 065.3°/61.6° respectively. Mean orientation of the vein calculated from the measurements collected from the vein outcrop is 047°/70° which indicates that the dip amount of the vein does not change so much with depth while the strike of the vein is changing both at FW and HW with depth.
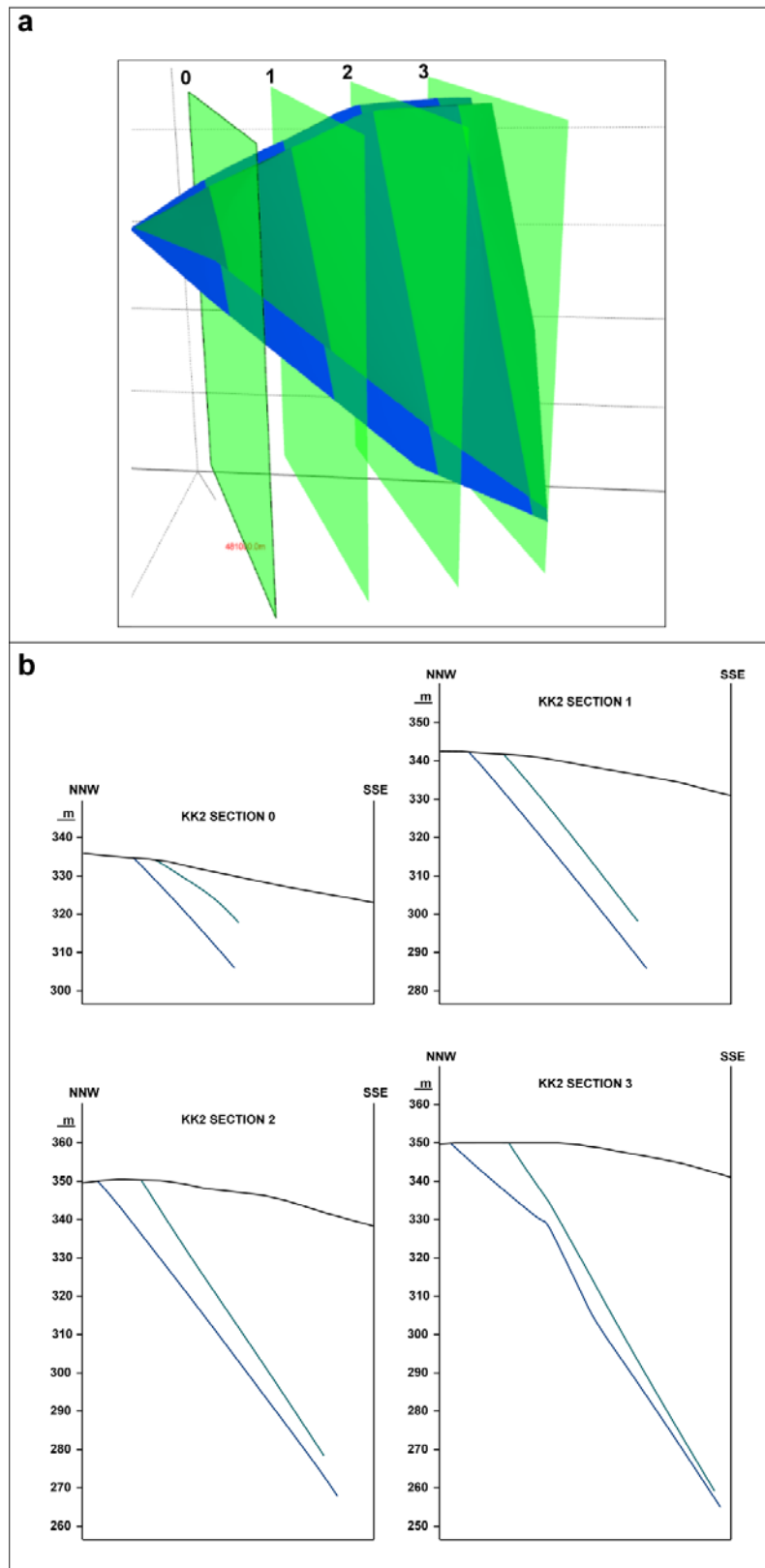
**Figure 4.31. (a)** Modeled KK2 vein with cross-section lines. **(b)** Vertical cross sections of KK2 vein.
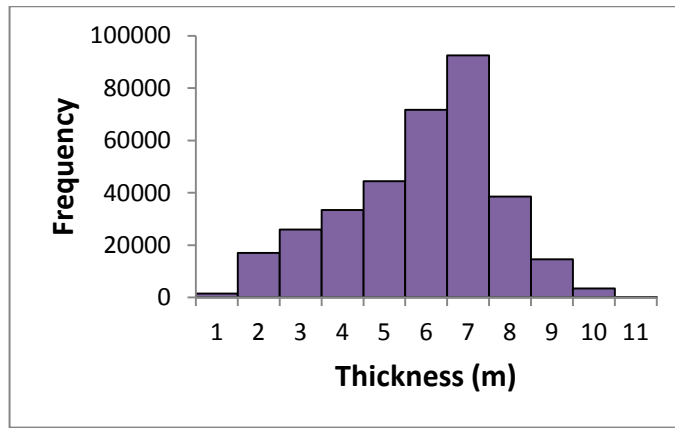
**Figure 4.32.** Histogram of thickness data of KK2 vein.
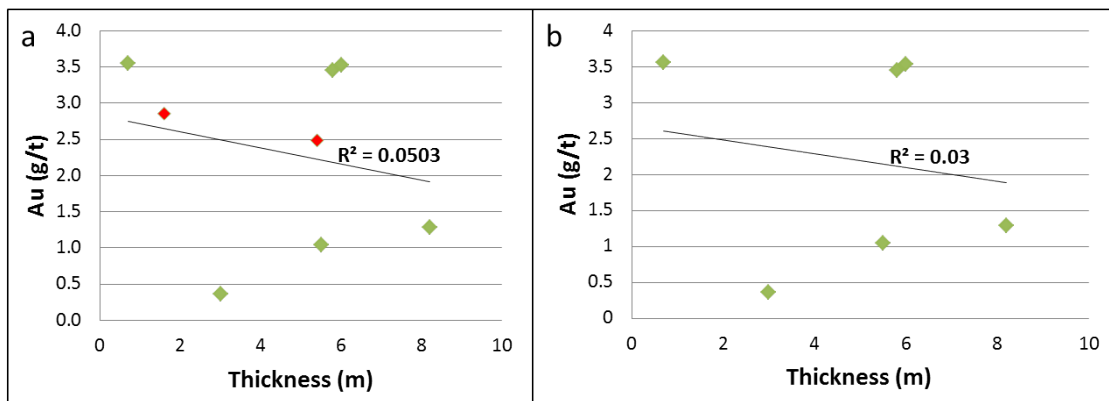


**Figure 4.33. (a)** Scatter graph of thickness vs. gold grades of KK2 vein. Note that the points indicated by red color correspond to bend-related gold grades. **(b)** Scatter graph of thickness vs. gold grades of KK2 vein when bend-related gold grades are taken out.
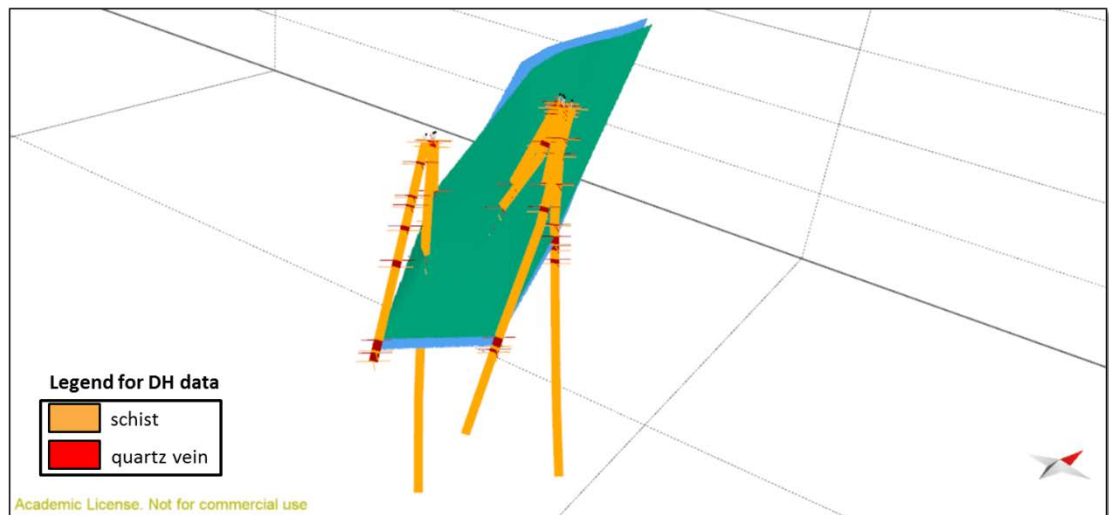


**Figure 4.34.** 3D view of modeled surfaces of KK3 vein with used drill holes.

Steeper dip amounts (>70°) at the HW surface of the vein (Figure 4.35d) are related to the steep section at the southwestern tip of the vein which does not outcrop on the surface (Figure 4.36). The deepest drill intersection is around 120 m below surface.

According to the vertical cross sections (Figure 4.37), the geometry of the vein is similar to a plane that flares upwards and its thickness increases substantially at shallower depths. The average thickness of the vein is 4.4 m (Figure 4.38a).
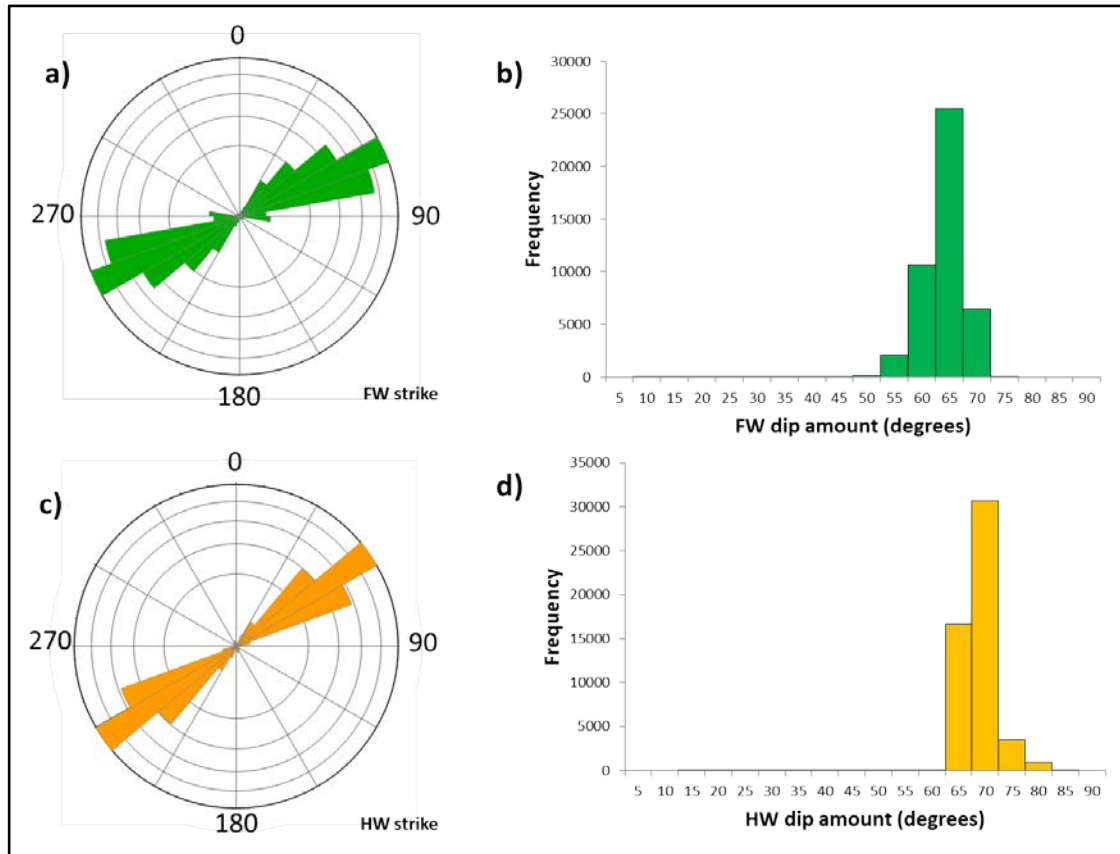


Figure 4.35. (a) Rose plot of strike data of modeled KK3 vein FW surface. (b) Histogram of dip amount data of modeled KK3 vein FW surface. (c) Rose plot of strike data of modeled KK3 vein HW surface. (d) Histogram of dip amount data of modeled KK3 vein HW surface.
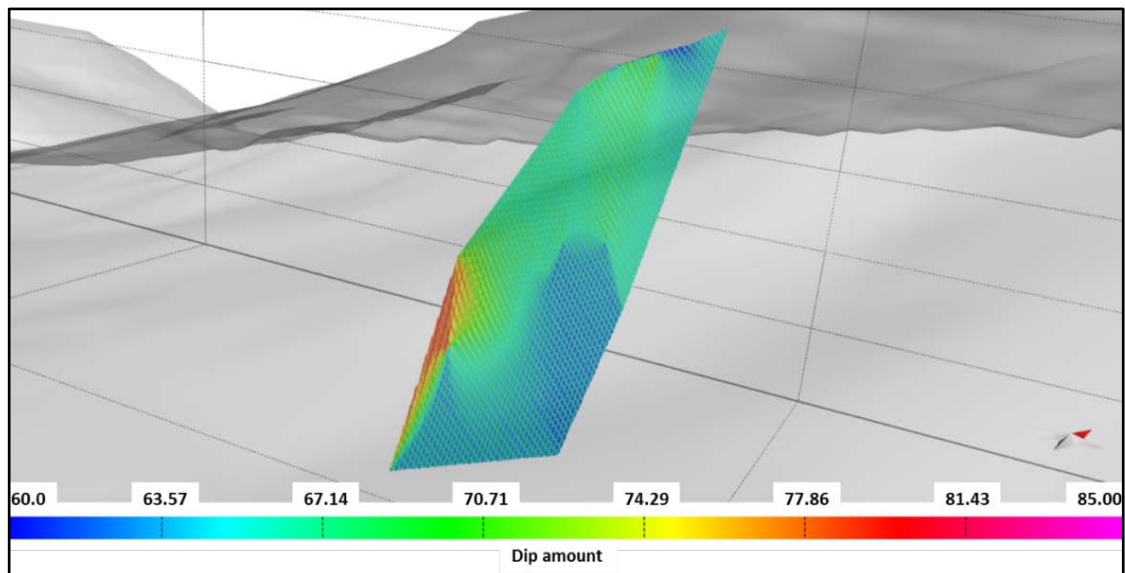
**Figure 4.36.** Colored dip amount map of KK3 HW surface.

The mean Au grade of the vein is 3.484 g/t which is very close to the mean Au grade of KK1 vein 3.356 g/t. The highest and the lowest Au grades are 6.407 g/t and 0.082 g/t respectively. Scatter graph of thickness vs. gold grade has a correlation coefficient value of 0.007 (Figure 4.38b) which was calculated by removing the outlier point (10, 6.407) and p-value was found as 0.12 (p>0.01). The highest gold grade 6.407 g/t comes from the thickest part of the vein which is 10 m.

*KK4 vein* was modeled using 1 diamond cut and 2 RC drillhole data (Figure 4.39). The modeled geometry indicates that the vein continues at depth towards southwest. Modeled vein geometry shows no change in dip amount of the vein with depth. Median values of the HW and FW surfaces of the vein are 058.4°/60.5° and 056.8°/58.4° respectively. Mean outcrop orientation of the vein 042/68 shows that the outcrop orientation data is not representative of the orientation of subsurface geometry of the vein (Figure 4.40). Strike of the FW surface of the vein is rotating counterclockwise towards the southwestern tip of the vein which also results in a decrease in thickness of the vein towards this tip (Figure 4.41). The limited drilling around the vein focus on deeper parts of the vein and the deepest vein intersection is around 100 m below surface.
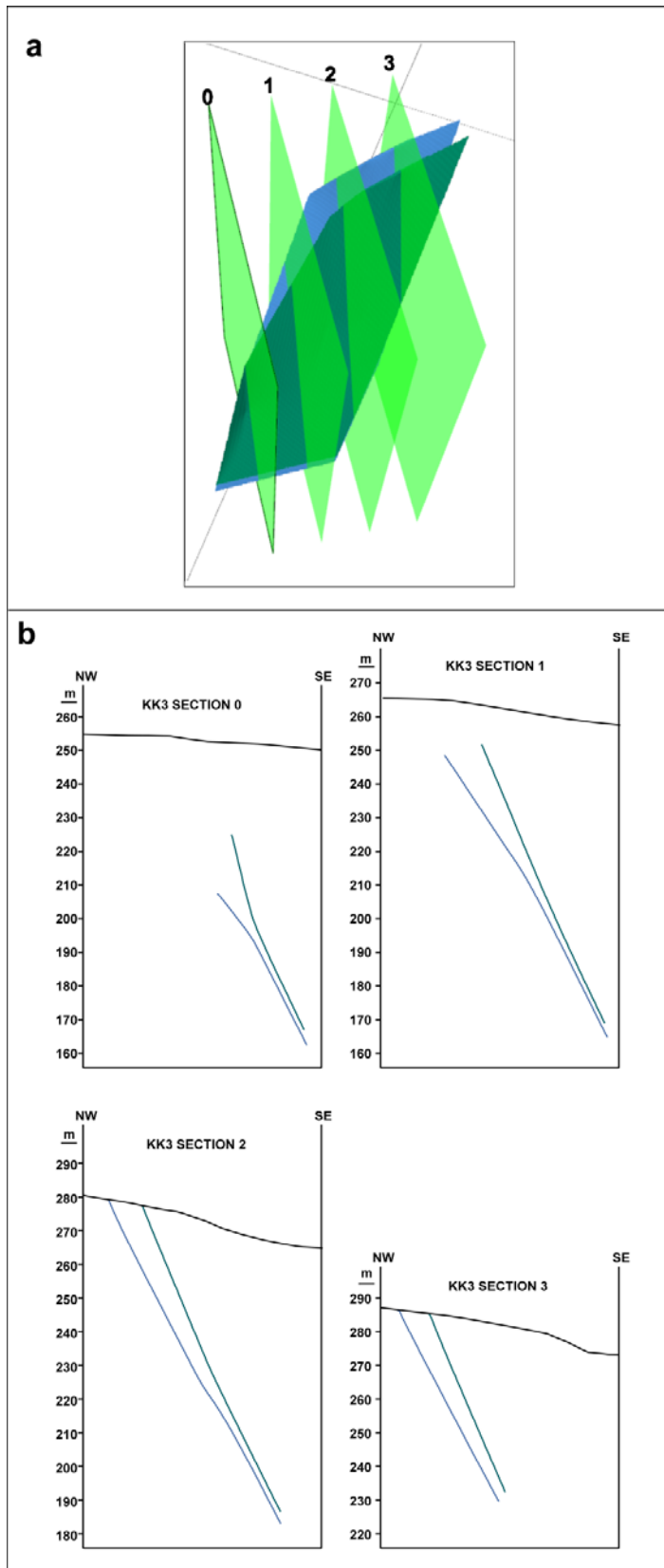
**Figure 4.37. (a)** Modeled KK3 vein with cross-section lines. **(b)** Vertical cross sections of KK3 vein.
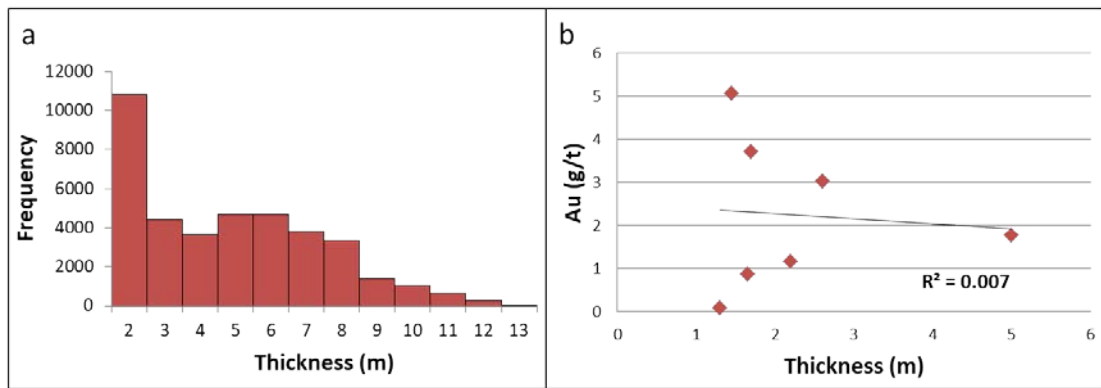
**Figure 4.38. (a)** Histogram of thickness data of KK3 vein. **(b)** Scatter graph of thickness vs. gold grades of KK3 vein.
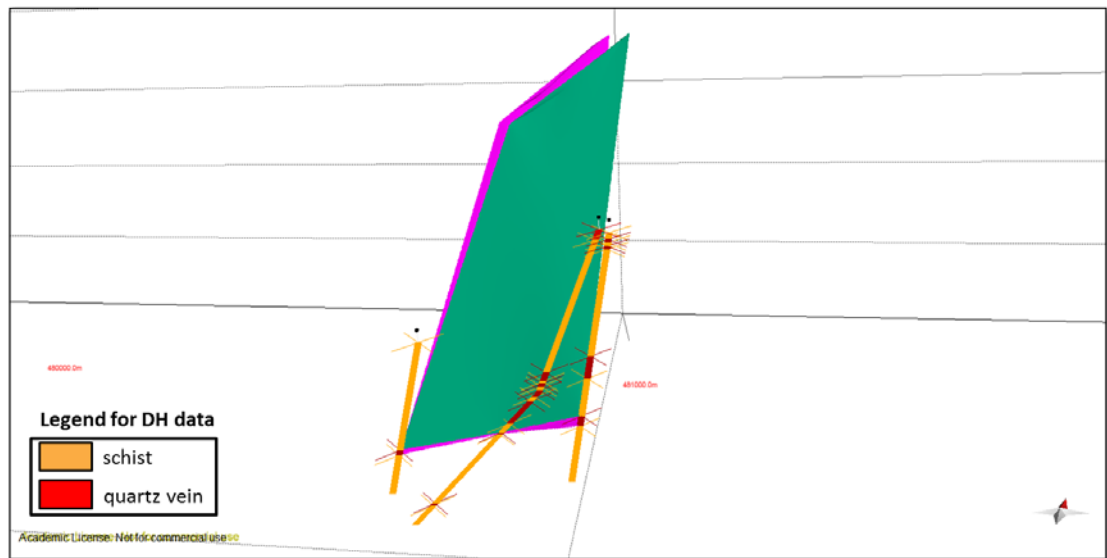


**Figure 4.39.** 3D view of modeled surfaces of KK4 vein with used drill holes.

Vertical cross sections created perpendicular to the constant vein strike (Figure 4.41) clearly indicate that the vein thickness gradually decreases as depth increases except at the northeastern tip of the vein where thickness is almost constant with depth because of the constant orientation of the vein surfaces at the subsurface. Mean thickness of the vein is 3.6 m (Figure 4.42a).

The mean Au grade of the vein is 0.866 ppm (g/t) with the highest and lowest grade results being 2.29 g/t and 0.175 g/t respectively. Scatter graph of

thickness vs. gold grade together has a correlation coefficient of 0.0042 (Figure 4.42b) and p-value was estimated as 0.96 (p>0.01).
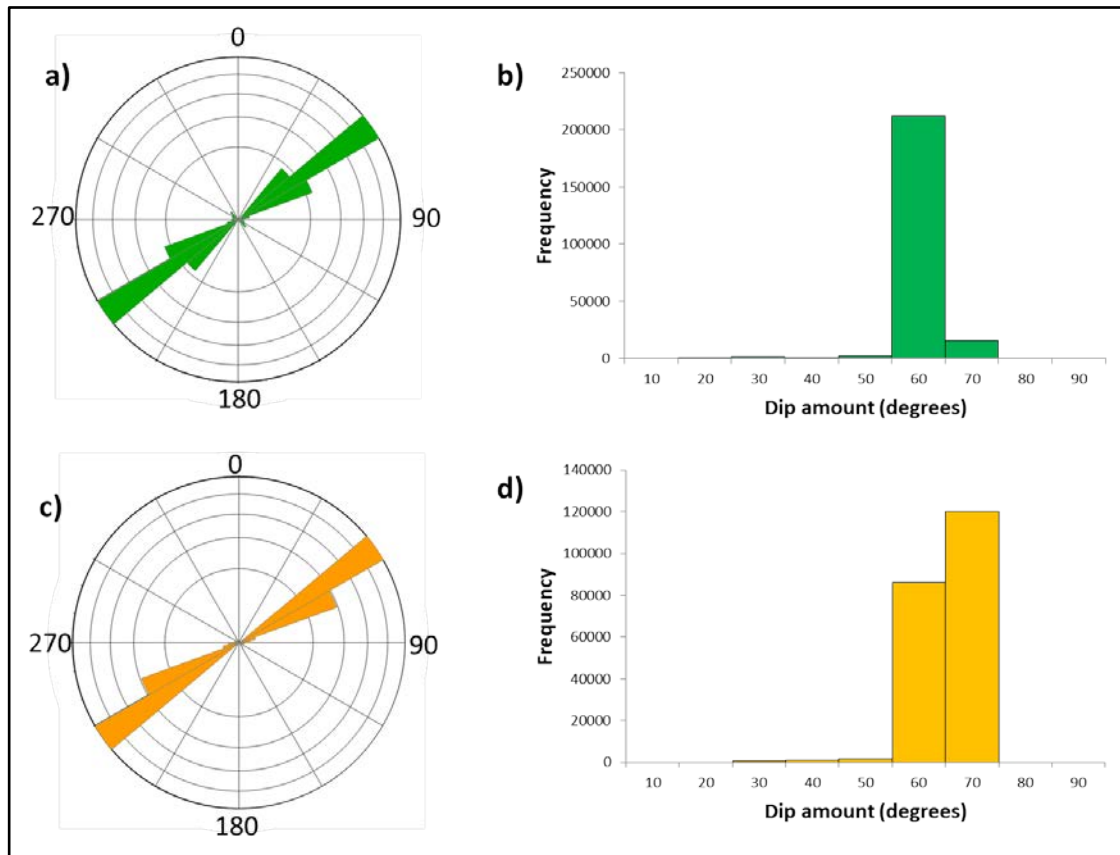


**Figure 4.40. (a)** Rose plot of strike data of modeled KK4 vein FW surface. (b) Histogram of dip amount data of modeled KK4 vein FW surface. (c) Rose plot of strike data of modeled KK4 vein HW surface. **(d)** Histogram of dip amount data of modeled KK4 vein HW surface.

*K1 vein* geometry was modeled using 5 diamond cut and 6 RC drillhole data (Figure 4.43). Due to insufficient drillhole data at the southwestern part of the vein only 140 m of the vein starting from its northeastern end could be modeled. There are some variations in the orientation of the vein along strike. The vein widens towards its northeastern end. Median values of the orientation of HW and FW surfaces of the vein are 049°/68.7° and 050.3°/64.7° respectively; quite different than the mean orientation of the vein outcrop (040°/75°). Rose diagrams of the strike values and histograms of the dip data of the vein surfaces are given in Figure 4.44. The deepest drill intersection is around 90 m below surface.
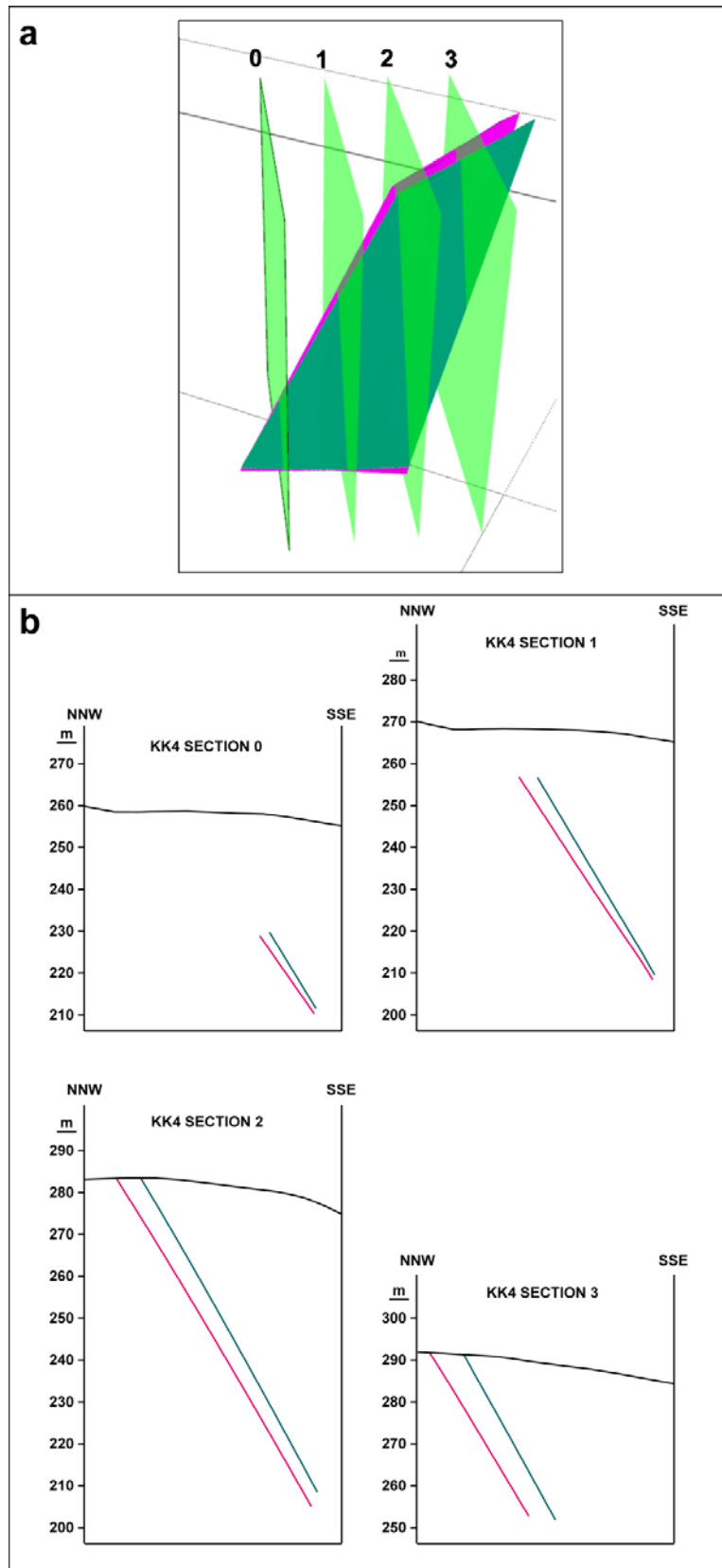
**Figure 4.41. (a)** Modeled KK4 vein with cross-section lines. **(b)** Vertical cross sections of KK4 vein.
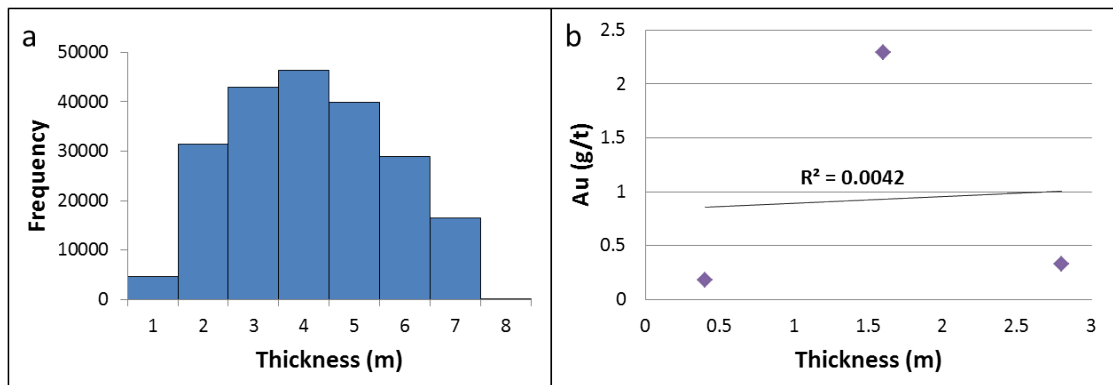
**Figure 4.42. (a)** Histogram of thickness data of KK4 vein. **(b)** Scatter graph of thickness vs. gold grades of KK4 vein.
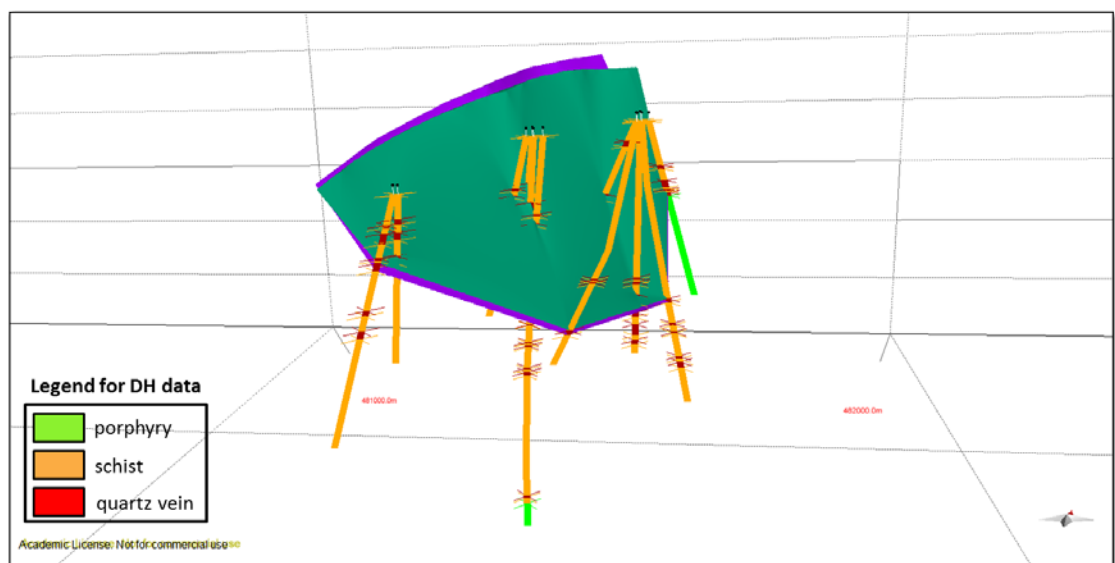


**Figure 4.43.** 3D view of modeled surfaces of K1 vein with used drill holes.

Vertical cross sections (Figure 4.45) indicate that there is a steady downwards decrease in the thickness of the vein. The vein bends along dip at around 264 m asl close to its southwestern tip and steepens there. Except the tips, the vein has so planar and smooth geometry that the dip of the vein is almost constant at each level. The vein bends again along dip close to its northeastern tip at around the level 230 m asl and flattens there. The mean thickness of the vein is 3.4 m (Figure 4.46).

The mean Au grade of the vein is calculated as 2.921 g/t. The highest and lowest grade results are as 27.075 g/t and 0.328 g/t respectively. The highest gold

101

grade value (27.075 g/t) comes from the location (around the level 228 m asl) just after the vein bends and gets thinner to 0.85 m (Figure 4.45b). Scatter graph of thickness vs. gold grade has a correlation coefficient of 0.1169 (Figure 4.47a) and p-value is 0.30 (p>0.01). When gold grades corresponding to bends are taken out, correlation coefficient is 0.2135 (Figure 4.47b)
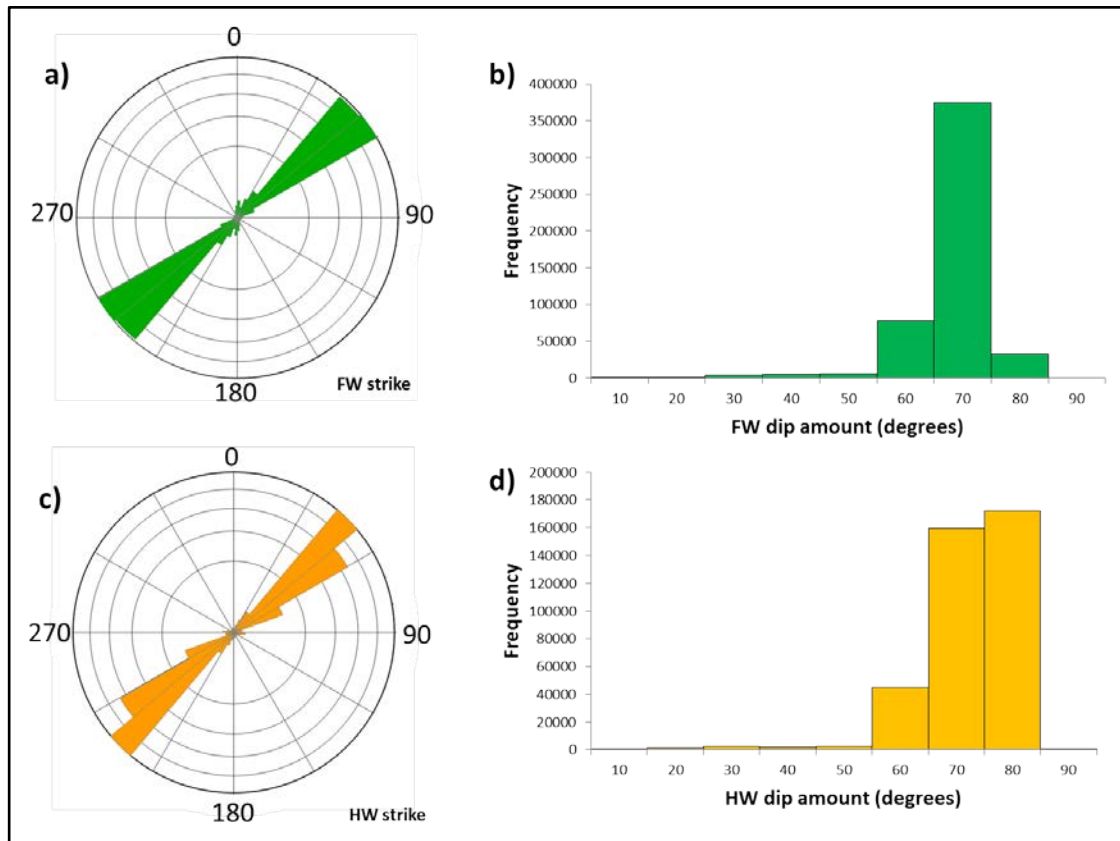


**Figure 4.44. (a)** Rose plot of strike data of modeled K1 vein FW surface. **(b)** Histogram of dip amount data of modeled K1 vein FW surface. **(c)** Rose plot of strike data of modeled K1 vein HW surface. **(d)** Histogram of dip amount data of modeled K1 vein HW surface.

*K3E vein*, the eastern part of the K3 vein hosted by porphyry, was modeled using 13 diamond cut drill holes (Figure 4.48). Vein surfaces have planar to curviplanar geometry and some undulations along strike and dip. Median values of the direction of HW and FW surfaces of the vein are 266.1°/72.4° and 264.9°/70.2° respectively. Mean orientation of the vein outcrop is 275°/71° and indicates that the outcrop is representative of dip amount of subsurface geometry of the vein although the strike of the vein varies in the subsurface (Figure 4.49).
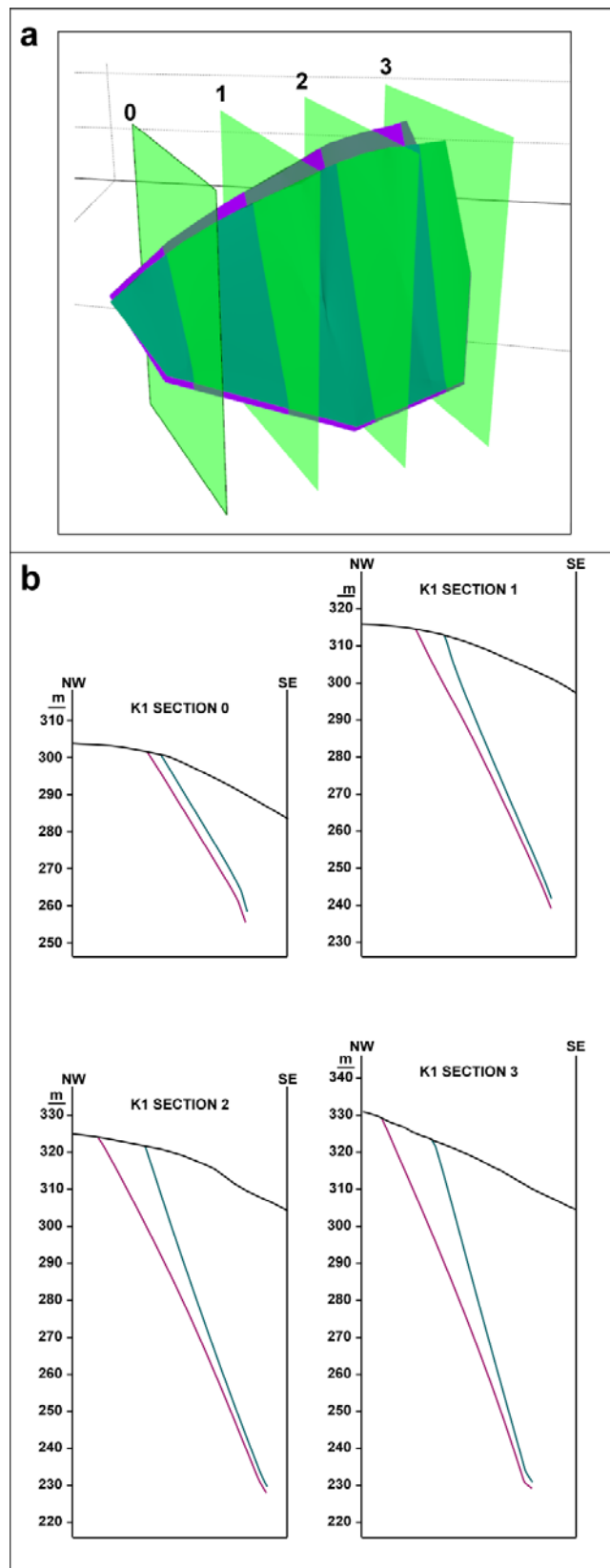
**Figure 4.45. (a)** Modeled K1 vein with cross-section lines. **(b)** Vertical cross sections of K1 vein.
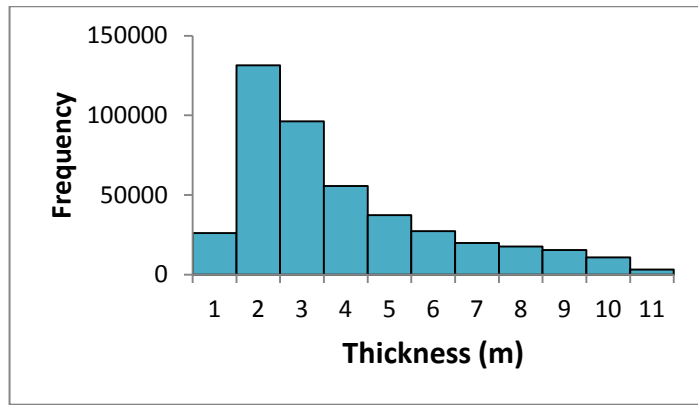
**Figure 4.46.** Histogram of thickness data of K1 vein.
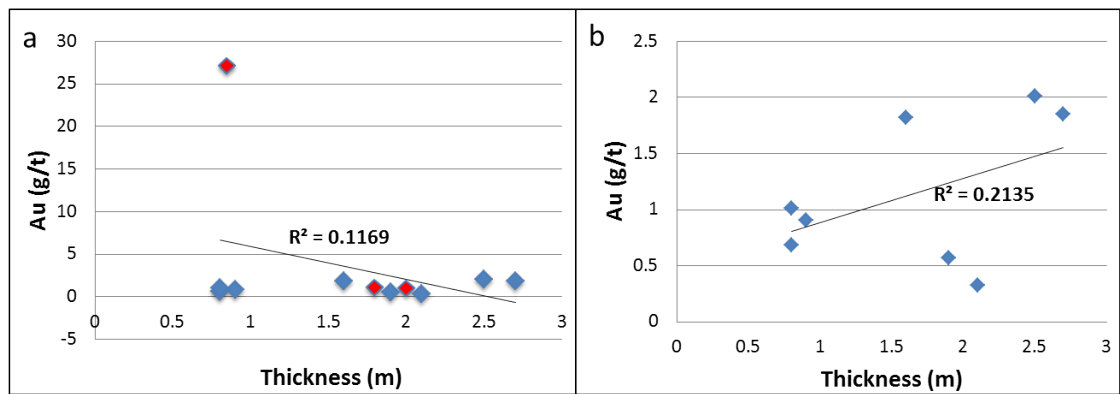


**Figure 4.47. (a)** Scatter graph of thickness vs. gold grades of K1 vein. Note that the points indicated by red color correspond to bend-related gold grades. **(b)** Scatter graph of thickness vs. gold grades of K1 vein when bend-related gold grades are taken out.
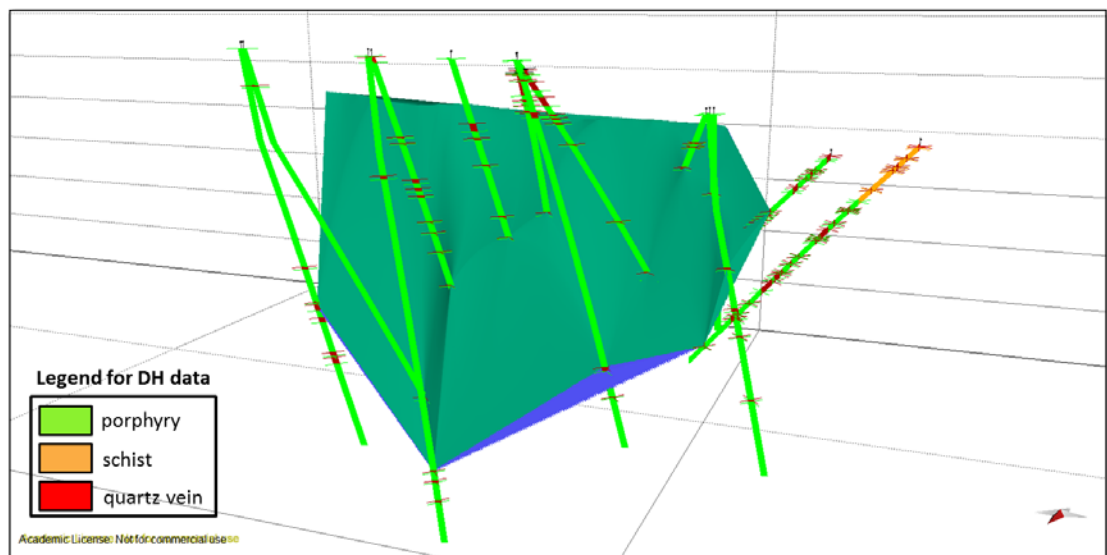


**Figure 4.48.** 3D view of modeled surfaces of K3E vein with used drillholes.

Cluster of dip amounts <40° at the FW and HW surface of the vein is artificial and related to interpolation between the outcrop point data in the shallower parts of the vein (Figure 4.50). The deepest drill intersection is around 215 m below surface (at the level 140 m asl).

According to the vertical cross sections (Figure 4.51), thickness of the vein steadily decreases with depth. At its eastern tip, the vein is smoothly planar and maintains a steep dip with depth (Figure 4.50). Except from its eastern tip, the vein has 3 bending locations. At its western tip, it bends at 325 m asl above where it shows a flared geometry. The highest gold grade result is obtained from this bending location. The vein has 2 more bending locations at the levels 255 m asl and 285 m asl, below where it gets thinner and steeper. The mean thickness of the vein is 2.5 m (Figure 4.52).
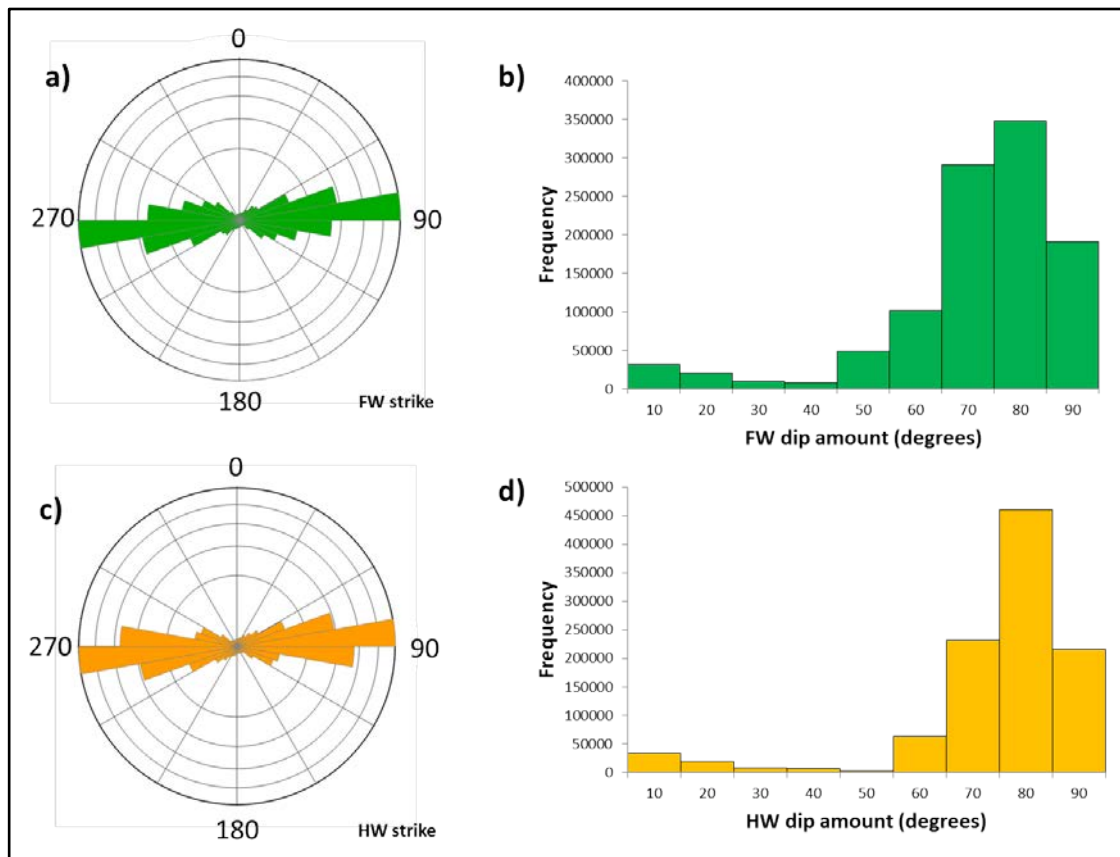


**Figure 4.49. (a)** Rose plot of strike data of modeled K3E vein FW surface. **(b)** Histogram of dip amount data of modeled K3E vein FW surface. **(c)** Rose plot of strike data of modeled K3E vein HW surface. **(d)** Histogram of dip amount data of modeled K3E vein HW surface.

The mean Au grade of the vein is 1.326 g/t, and the highest and lowest gold grade values are 7.13 g/t and 0.186 g/t respectively. Scatter graph of thickness vs. gold grade shows a correlation coefficient of 0.0126 (Figure 4.53a) and p-value was found as 0.72 (p>0.01). When bend related gold grades are taken out, correlation coefficient value rises to 0.1325 (Figure 4.53b).
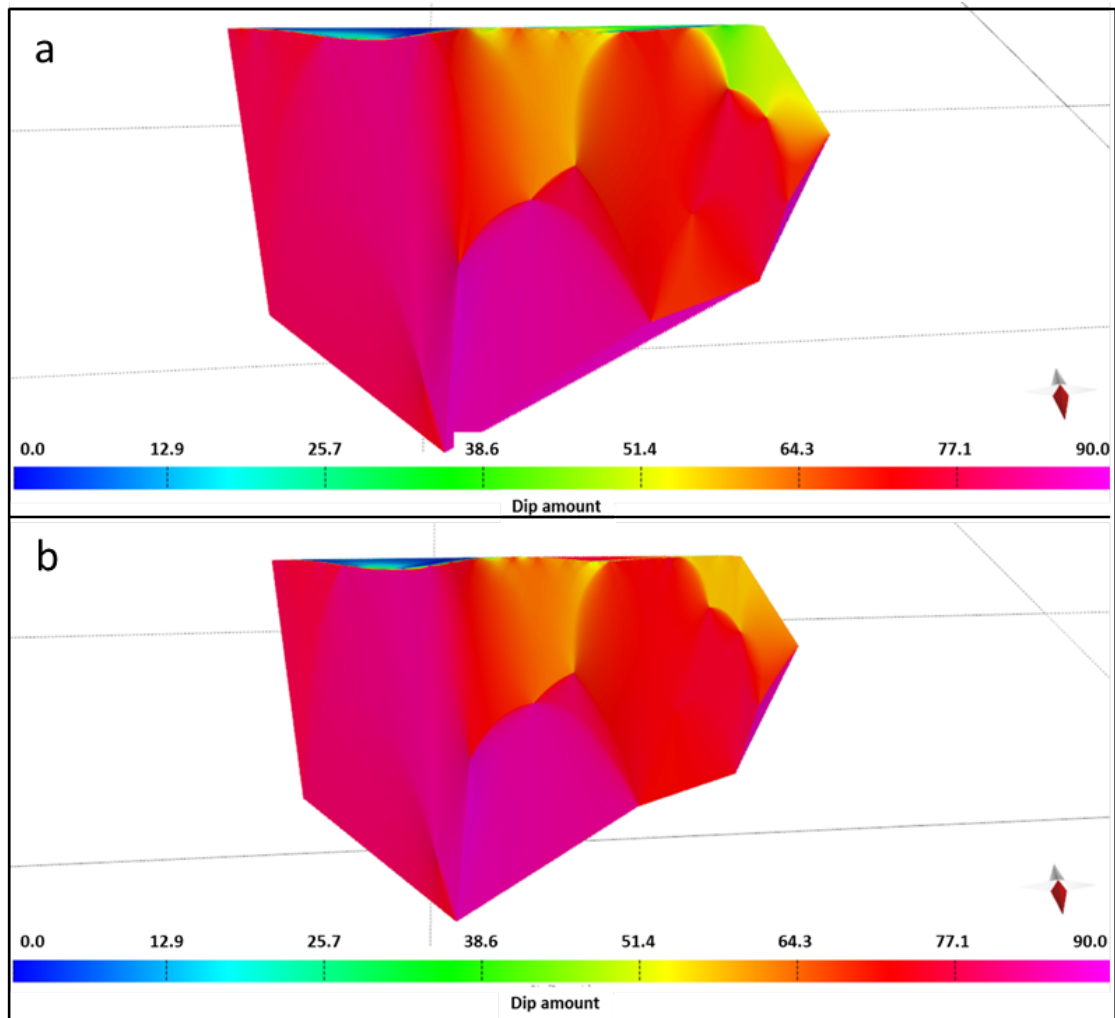


**Figure 4.50. (a)** Colored dip amount map of K3E FW surface. **(b)** Colored dip amount map of K3E HW surface.

*K3W vein*, the western part of the K3 vein hosted by schist, was modeled using 25 diamond cut and 8 RC drill holes (Figure 4.54). According to the modeled surfaces, the vein extends at depth along its strike towards northeast.
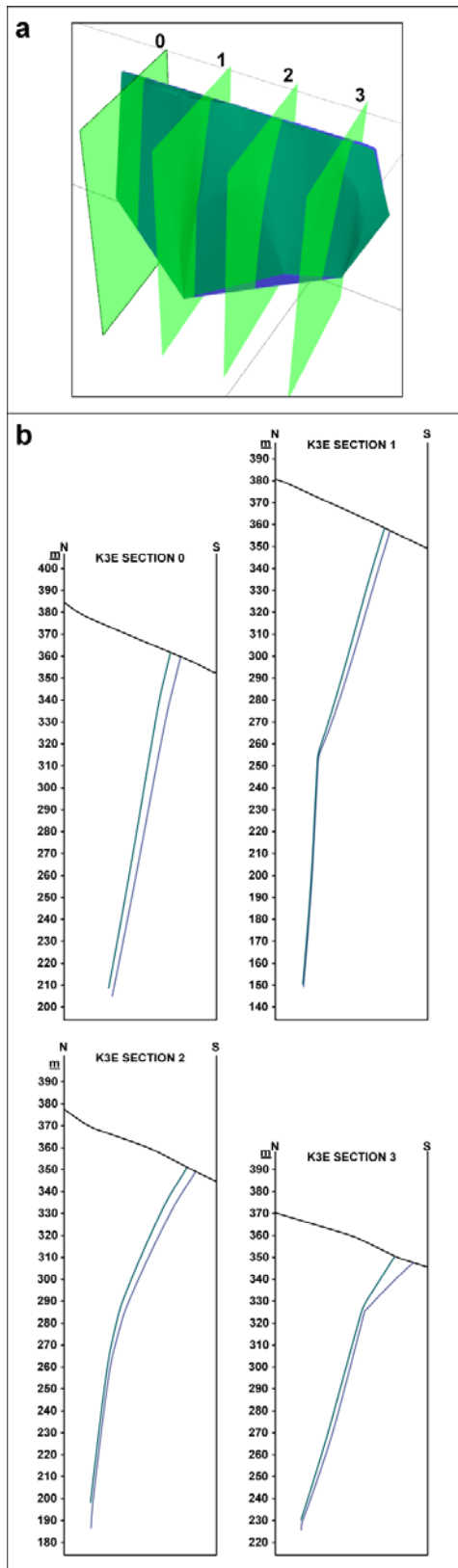
**Figure 4.51. (a)** Modeled K3E vein with cross-section lines. **(b)** Vertical cross sections of K3E vein.
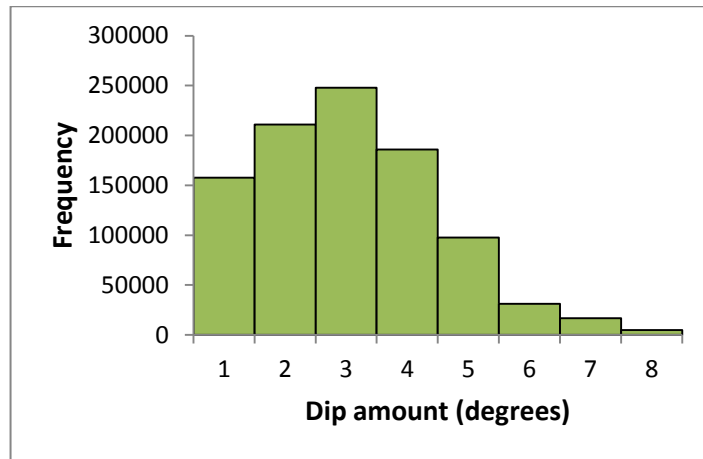
**Figure 4.52.** Histogram of thickness data of K3E vein.
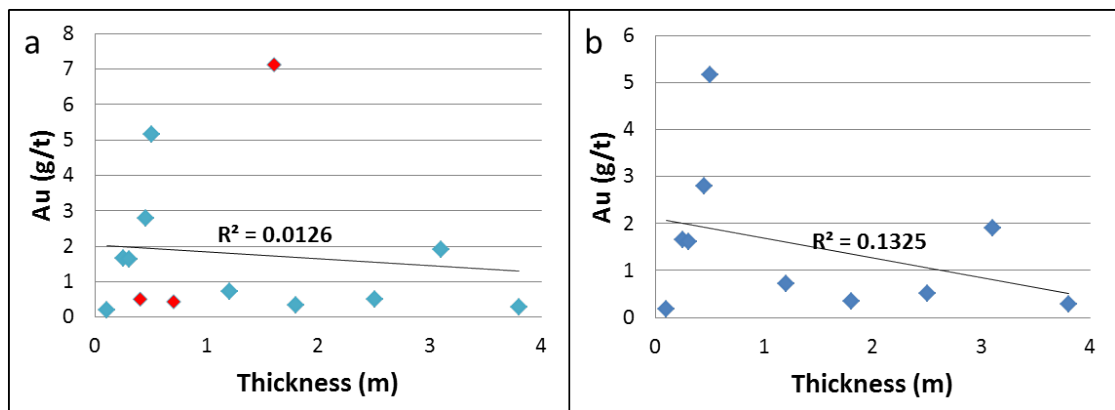


**Figure 4.53. (a)** Scatter graph of thickness vs. gold grades of K3E vein. Note that the points indicated by red color correspond to bend-related gold grades. **(b)** Scatter graph of thickness vs. gold grades of K3E vein when bend-related gold grades are taken out.

The modeled surfaces are rough and show curviplanar characteristics. Orientation of the vein undulates along strike and down dip. Median values of the orientation of HW and FW surfaces of the vein were calculated as 234.1°/66.4° and 232.3°/64.4° respectively. The mean orientation of the vein outcrop 237°/62° seems representative of the orientation of the subsurface geometry of the vein (Figure 4.55). Scattered strike values on the rose plots (Figure 4.55a-c) reflect the undulations on the vein surfaces. The cluster of dip values >80° and <50° shown on the histograms (Figure 4.55b-d) are the results of steep and gentle sections around the surface bends (Figure 4.56). The deepest drill intersection is around 140 m below surface (at the level 160 m asl).
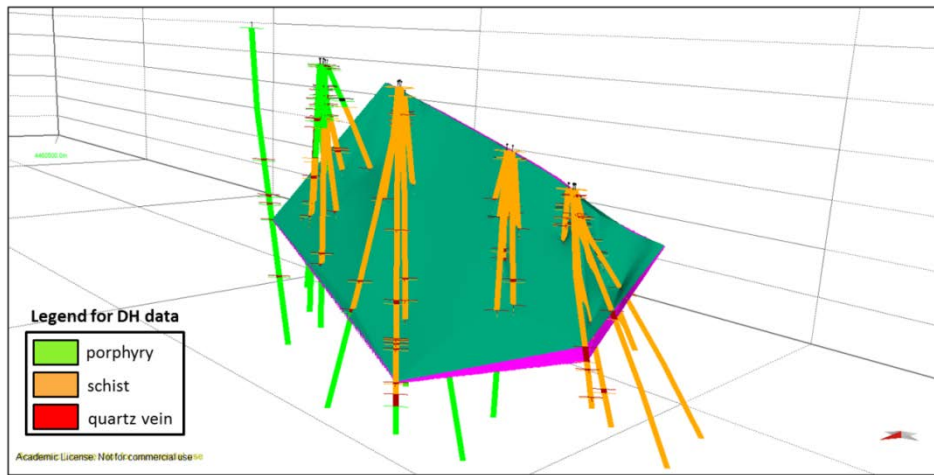
**Figure 4.54.** 3D view of modeled surfaces of K3W vein with used drill holes

12 vertical cross sections were created perpendicular to the K3W strike because the subsurface geometry of the vein is curviplanar and has many undulations. Vertical cross sections (Figure 4.57) indicate that the vein bends along dip at many locations. The mean thickness of the vein is 2.5 m (Figure 4.58).
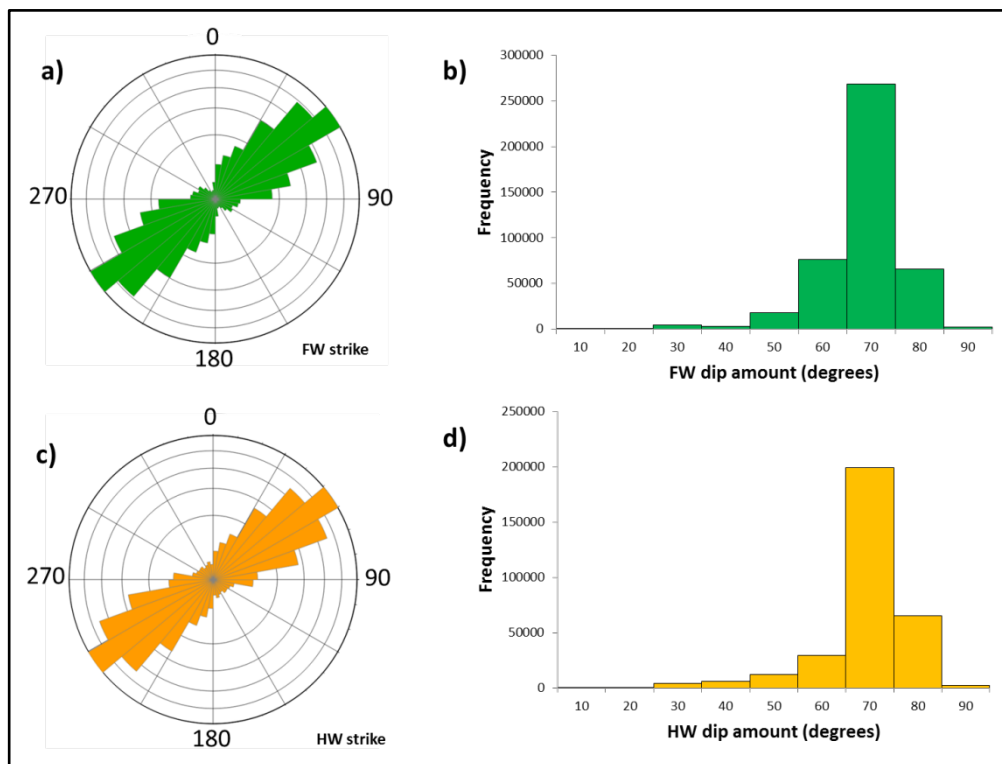


**Figure 4.55. (a)** Rose plot of strike data of modeled K3W vein FW surface. **(b)** Histogram of dip amount data of modeled K3W vein FW surface. **(c)** Rose plot of strike data of modeled K3W vein HW surface. **(d)** Histogram of dip amount data of modeled K3W vein HW surface.
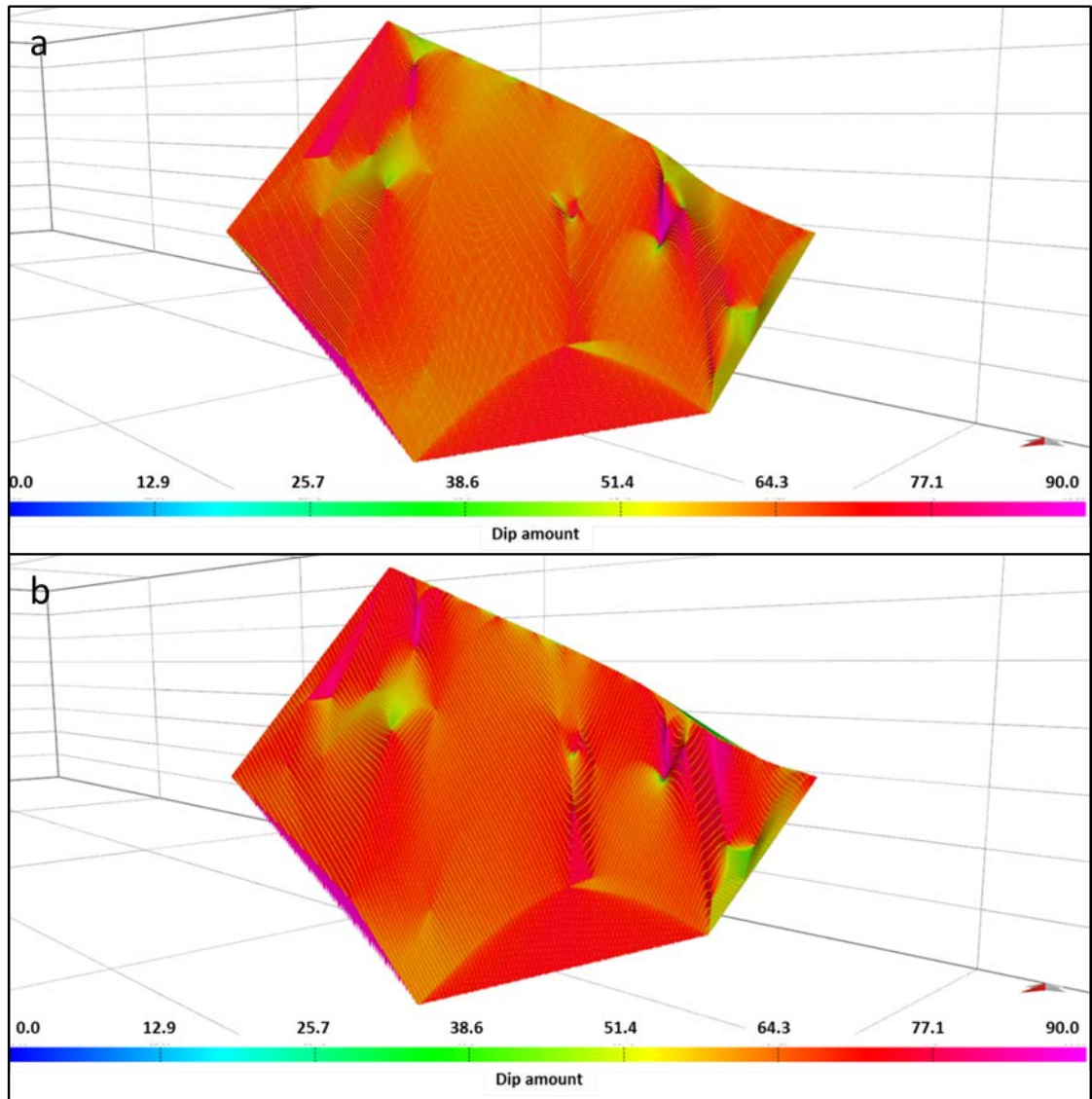
**Figure 4.56. (a)** Colored dip amount map of K3W FW surface. **(b)** Colored dip amount map of K3W HW surface.

The mean Au grade of the vein is 6.943 g/t, and the highest and lowest gold grade values are 79.85 g/t and 0.103 g/t respectively. Gold grades of K3W vein are higher compared to its eastern part K3E.

Scatter graph of thickness vs. gold grade has a correlation coefficient of 0.0032 (Figure 4.59a). In addition, p-value was calculated as 0.76 (p>0.01). When the bend associated gold grades are taken out, higher degree of correlation ($R^2$ of 0.0057) is found between thickness and gold grade (Figure 4.59b).
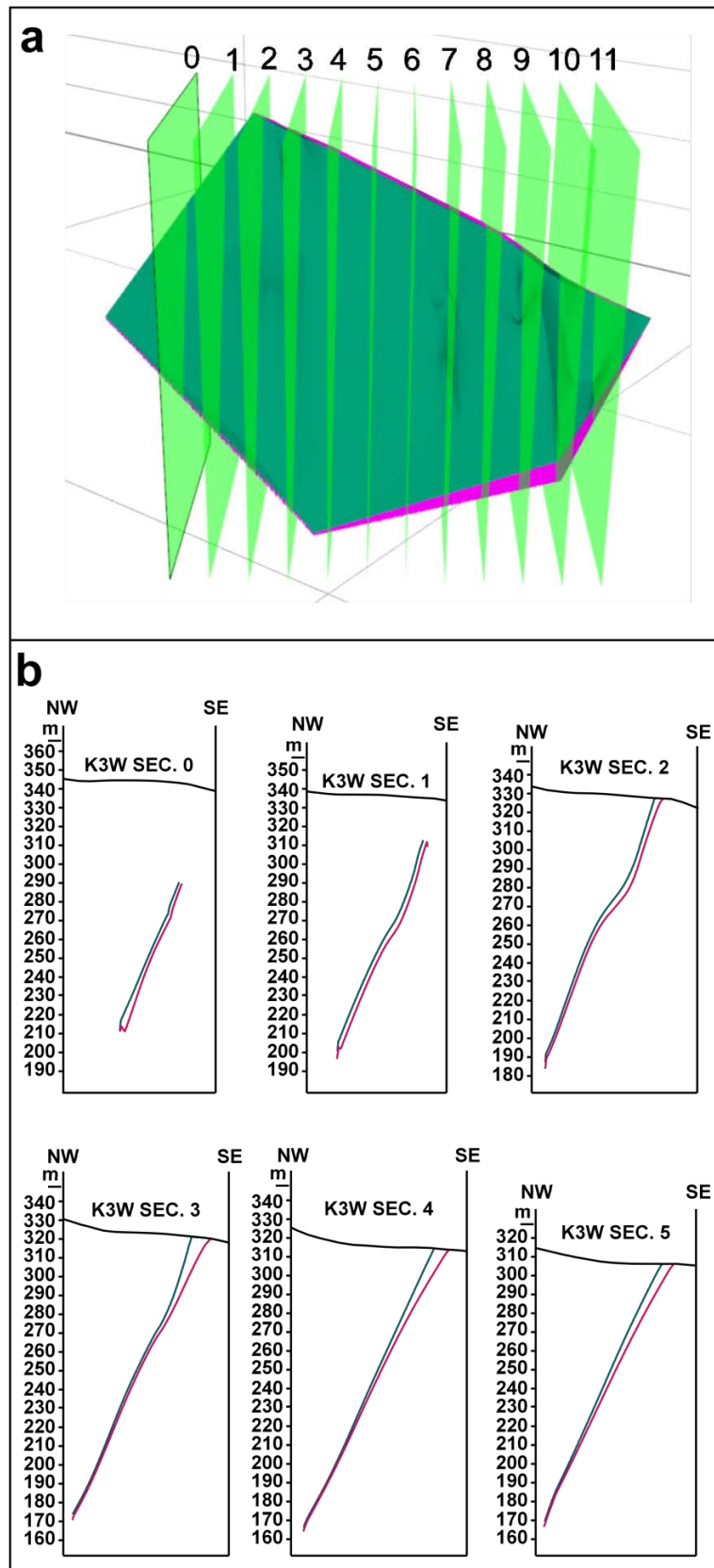
**Figure 4.57. (a)** Modeled K3W vein with cross-section lines. **(b)** Vertical cross sections of K3W vein.
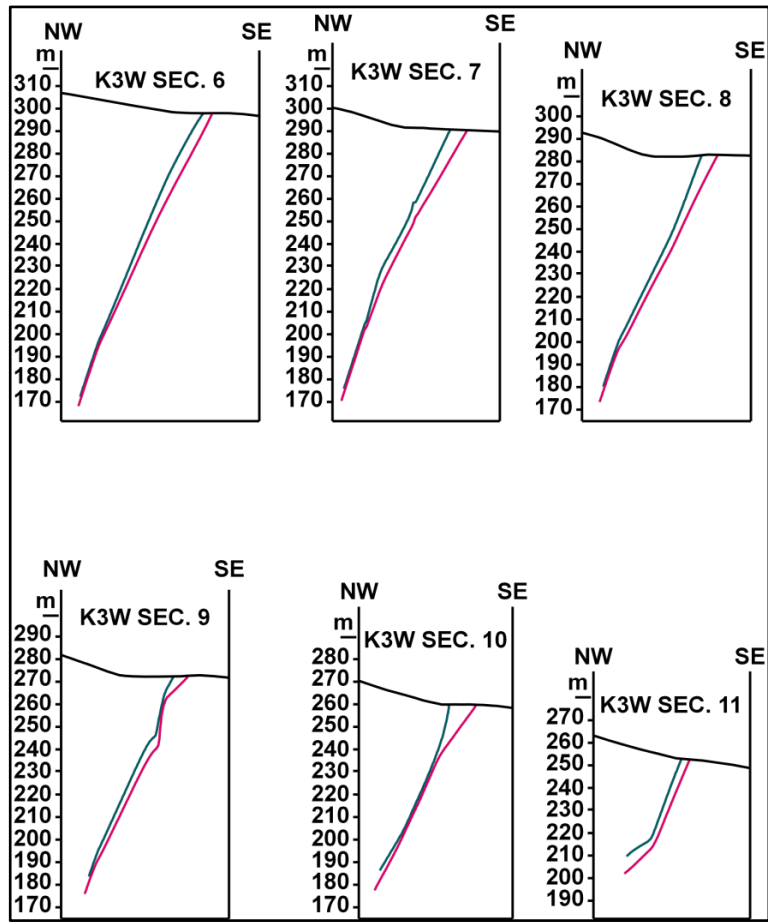
Figure 4.57b continued.
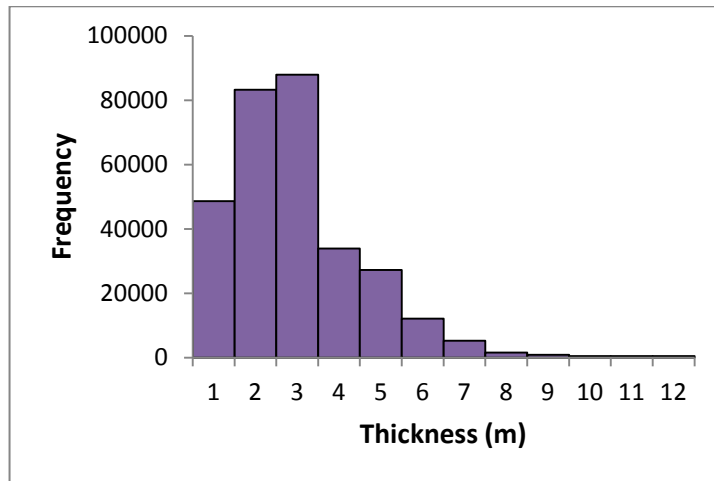


**Figure 4.58.** Histogram of thickness data of K3W vein.
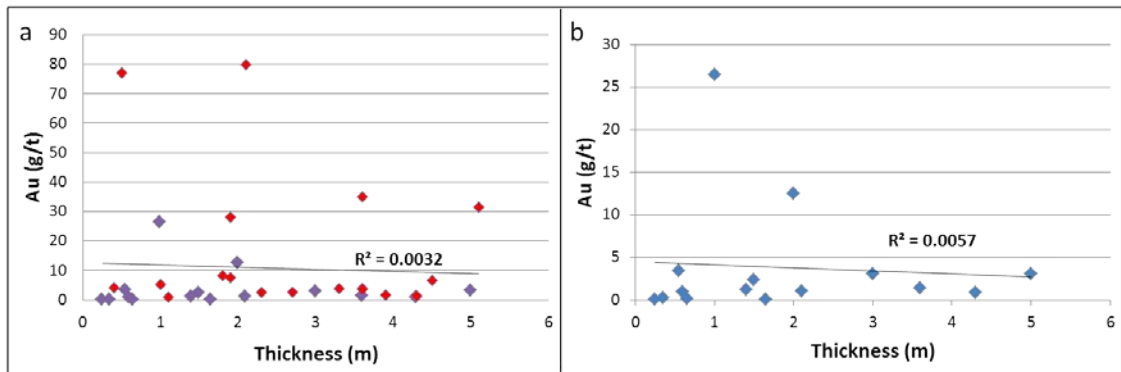
**Figure 4.59. (a)** Scatter graph of thickness vs. gold grades of K3W vein. Note that the points indicated by red color correspond to bend-related gold grades. **(b)** Scatter graph of thickness vs. gold grades of K3W vein when bend-related gold grades are taken out.

Number of drillholes used in modeling each vein and some descriptive statistical parameters (mean, median, no of data, standard deviation, and skewness) of the HW and FW surfaces of each vein are given in Table 4.2. Some descriptive statistical parameters (mean, median, no of data, standard deviation, and skewness) of thickness data together with mean, minimum and maximum gold grades for each vein are summarized in Table 4.3. Correlation coefficient values showing the degree of relationship between the thickness and gold grades, and p-values indicating whether this relationship is statistically significant or not calculated for each vein are also given in Table 4.3.

Descriptive statistical analysis was performed for 90 gold grades[*] in total coming from the modeled mineralized quartz veins. Median value was found *1.525 g/t* and the values above the median was considered as high gold grades. Thickness data from each vein and the gold grades were pooled and correlation coefficient value was also calculated for these whole data. $R^2$ was estimated as 0.005 (Figure 4.60), and the p-value was found as 0.51 (p>0.01).

[*] Gold grade: the concentration of gold (g/t) in the core/RC samples of the vein.

113

**Table 4.2.** Some descriptive statistical parameters of modeled surfaces of each vein.

| Vein | No of DH | Surface | n | Mean | | Standart deviation | | Median | | Skewness | |
|---|---|---|---|---|---|---|---|---|---|---|---|
| | | | | strike | dip | strike | dip | strike | dip | strike | dip |
| Karatepe | 9 | FW | 110847 | 91.9 | 55.9 | 26.3 | 8.5 | 85.8 | 56.3 | 5.3 | -3.9 |
| | | HW | 26048 | 92.7 | 55.8 | 25.1 | 10.9 | 85.8 | 57.3 | 4.2 | -3.1 |
| KK1 | 11 | FW | 7019 | 56.5 | 60.4 | 13.5 | 6.5 | 54.8 | 59.1 | 8.3 | -2.6 |
| | | HW | 6202 | 55 | 62.6 | 6.4 | 5.1 | 54.9 | 61.8 | 4.6 | -3.5 |
| KK2 | 8 | FW | 444923 | 65.7 | 51.8 | 11.8 | 4.6 | 66.3 | 52.1 | 0.6 | -0.9 |
| | | HW | 341583 | 67.5 | 53.2 | 16.4 | 8.6 | 65.8 | 55.8 | 7.6 | -2.4 |
| KK3 | 8 | FW | 45065 | 65.1 | 61.1 | 16.5 | 3.9 | 65.3 | 61.6 | 5.2 | -2.1 |
| | | HW | 52235 | 55.7 | 66.2 | 9 | 4.1 | 55.7 | 66.2 | 4.4 | -4.1 |
| KK4 | 3 | FW | 231999 | 56.6 | 57.5 | 7.9 | 3.8 | 56.8 | 58.3 | 5.5 | -5.9 |
| | | HW | 209578 | 58.3 | 59.9 | 5.2 | 3 | 58.4 | 60.5 | 7.6 | -7.4 |
| K1 | 11 | FW | 502776 | 52.9 | 63.6 | 22.8 | 6.8 | 50.3 | 64.7 | 5.8 | -3.5 |
| | | HW | 384859 | 52.9 | 67.5 | 19.8 | 7.6 | 49 | 68.7 | 6.8 | -2.9 |
| K3E | 13 | FW | 1048569 | 261.9 | 66.4 | 29 | 17 | 264.9 | 70.2 | -4.4 | -1.9 |
| | | HW | 1042016 | 261 | 69 | 29.6 | 16.6 | 266.1 | 72.4 | -4.6 | -2.5 |
| K3W | 33 | FW | 439652 | 225.9 | 63.3 | 31.9 | 8 | 232.3 | 64.4 | -2.8 | -1.7 |
| | | HW | 317971 | 227.8 | 64.5 | 31.3 | 8.9 | 234.1 | 66.4 | -2.7 | -2 |

**Table 4.3.** Some descriptive statistical parameters of thickness data and, minimum, maximum and mean gold values of each vein and correlation coefficient values and p-values for the relationship between thicknesses vs. gold grades for each vein.

| Vein | Thickness | | | | | Gold grade | | | $R^2$ | |
|---|---|---|---|---|---|---|---|---|---|---|
| | n | Mean | Std. Dev. | Median | Skewness | Min. | Max. | Mean | T.vs. Au | T.vs. Au$^2$ |
| Karatepe | 100821 | 5.11 | 1.36 | 5.04 | 0 | 0.133 | 1.021 | 0.458 | 0.003 | 0.003 |
| KK1 | 6039 | 2.42 | 1.31 | 2.17 | 0.45 | 0.043 | 8.68 | 3.356 | 0.0694 | |
| KK2 | 343352 | 5.39 | 1.81 | 5.72 | -0.44 | 0.365 | 3.556 | 2.081 | 0.0503 | 0.03 |
| KK3 | 38853 | 4.36 | 2.56 | 4.14 | 0.57 | 0.082 | 6.407 | 3.484 | 0.007 | 0.007 |
| KK4 | 210373 | 3.63 | 1.53 | 3.56 | 0.15 | 0.175 | 2.29 | 0.866 | 0.0042 | 0.0042 |
| K1 | 440659 | 4 | 2.3 | 2.57 | 1.17 | 0.328 | 27.075 | 2.921 | 0.1169 | 0.2135 |
| K3E | 953014 | 2.54 | 1.45 | 2.43 | 0.61 | 0.186 | 7.13 | 1.326 | 0.0126 | 0.1325 |
| K3W | 302223 | 2.48 | 1.57 | 2.18 | 1.49 | 0.103 | 79.85 | 6.943 | 0.0032 | 0.0057 |

[*] indicates $R^2$ values calculated when bend related gold grades are taken out.

Does boiling and associated gold precipitation occur at the bends where the thickness suddenly changes and the pressure drops rapidly? Accordingly, the sum of gold grades at the bends was compared to the sum of all gold grades. It was found that the *74.4%* of all gold grades coming from the modelled veins is located at the bends. When only the high gold grades were taken into account, it was found that ***77.7%*** of all high gold grades are located at the bends.
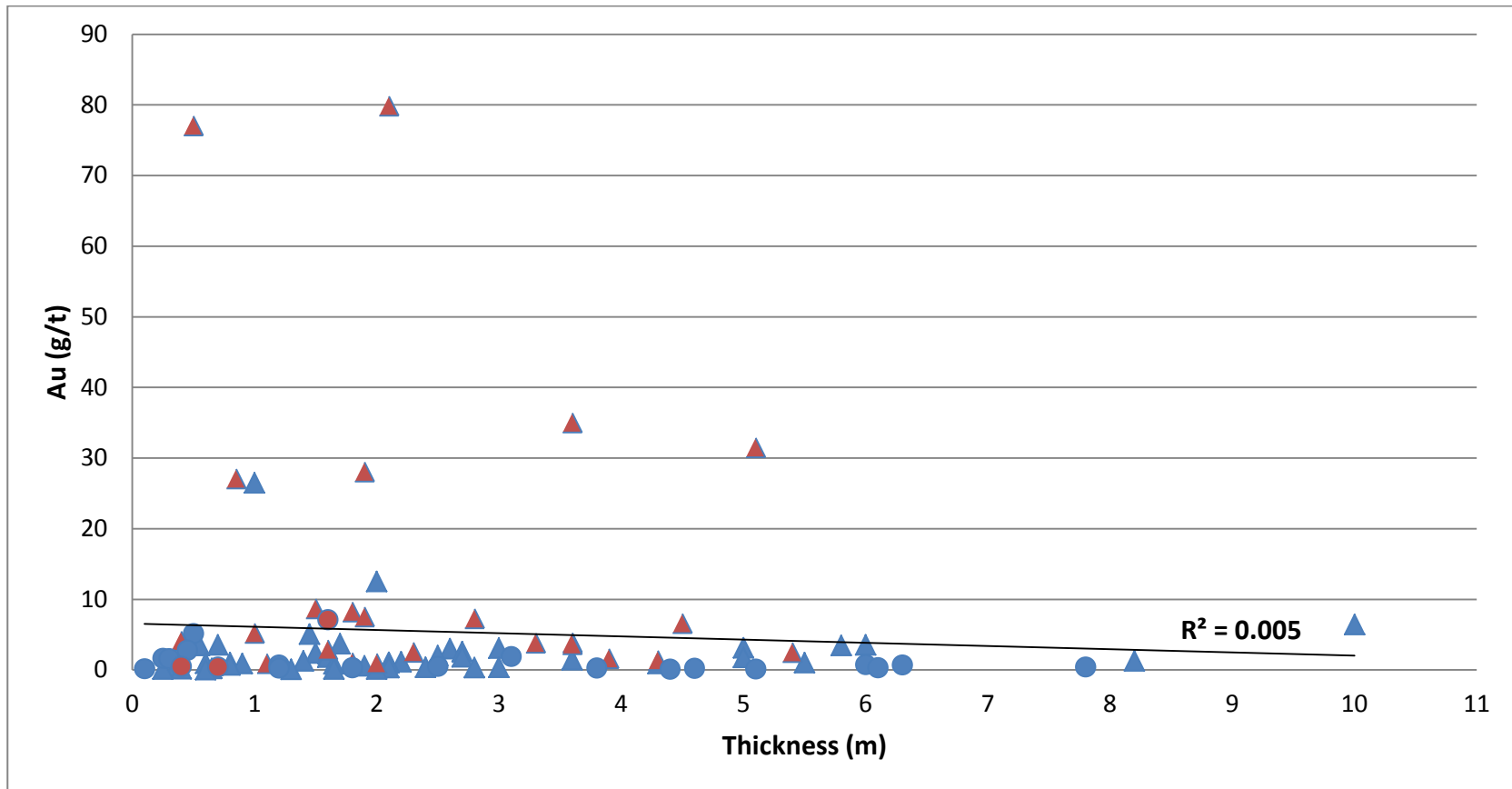
**Figure 4.60.** Scatter graph of thickness vs. gold grade data pooled from all of the modeled veins. Triangles represent the values coming from the schist hosted veins while circles represent those coming from the porphyry hosted veins. Red colored ones indicate bend-related values.

Descriptive statistical analysis was also performed for 28 bend-related gold grades. Median was calculated as *3.99 g/t* which is much higher compared to that of all gold grades. *78.6%* (22 out of 28) of the bends host high gold grades (>1.525 g/t). The two lowest bend-related gold grades (0.433 and 0.505 g/t) are hosted by porphyry while four of them correspond to the schist-hosted veins (Figure 4.61). In addition, 97.8% of the sum of bend related gold grades are located at the bends of schist hosted veins.
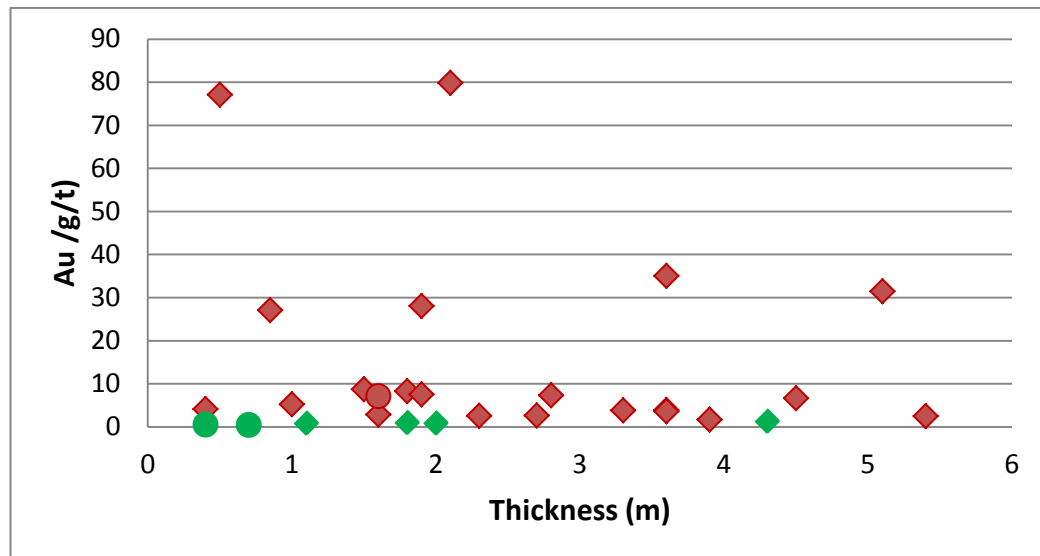


**Figure 4.61.** Scatter graph of bend-related thickness vs. gold grade data. Diamonds represent the values coming from the schist hosted veins while circles represent those coming from the porphyry hosted veins. Green colored ones indicate low gold grades (<1.525 g/t).

Percentage of the bends having high gold grade was also calculated for each vein. 100% of the bends in KK1 and KK2 veins have high gold grades, while 88.24% of the bends in K3W vein host high gold grades. This percentage is relatively lower in K1 and K3E veins as the percentage of the bends having high gold grades is 33.33.

A possible correlation between the host rock type and the gold grades were also examined. When the sum of all gold grades coming from the schist hosted veins (except the K2 vein which could not be modeled) was compared to the one coming from porphyry-hosted veins (except the Topyurt vein which could not be modeled), it was found that *94.4%* of the gold is located in the veins hosted by

schist. When just high gold grades are considered, it was found that **95.6%** of high gold grades are located in the veins hosted by schist.

62.5% of samples in the schist hosted veins (35 out of 56) contain high gold grade, while 30% of samples in the porphyry hosted veins (6 out of 20) correspond to high gold grade. 85.4% of the samples containing high gold grades (35 out of 41) come from the schist hosted veins.

## 4.4.2. Uncertainties in the models of vein subsurface geometries

Model uncertainties may have been resulted from the accuracy of the available drillhole data and the assumptions that have been made during modelling. As explained before, the top (HW) and bottom (FW) surfaces of the major mineralized quartz veins were modeled in 3D by interpolating the outcrop data points and drillhole data points.

The number and locations of drill holes around each vein was determined by the license holder company (Chesser Resources) based on the assay results of grab rock samples taken from the vein outcrops. Veins having higher gold grades were focused on by drilling more holes. For this reason, some veins have more sub-surface data points such as the K3W vein. Since these veins were modeled based on more data points, the curviplanar geometry of the vein surfaces may be due to more data points because the interpolation method used for modeling the surfaces is natural neighbor method which gives smooth surfaces except around the given data points. Logging errors (due to recording different depths for the loss of cores in diamond cut drill holes and difficulties in discriminating depths in reverse circulation holes) may have also caused the distortions from the real vein geometries. Sensitively (±0.1 cm) mapped outcrop outlines may not reflect the original outcrop geometries as some of the vein walls must have been lost to erosion. This also may have caused the distortions from the real geometries, although the curviplanar/rough vein geometries may not be model artifact.

During the selection of QV intersections to be matched to the vein outcrop, it was assumed that the attitude of the vein does not change in the subsurface.

Although this decision was justfied by the examination of textural and geochemical characteristics of the potential QV intervals, it would be wrong if the veins are breached more in dip at depth.

Model uncertainties due to the reasons listed above may have also affected the gold grade correlations i.e. all the high gold grades may be associated with bends, but few of the bends may not have been defined due to the insufficient drillholes.

## 4.5. Discussion and summary

Gold mineralization in the study area is associated with nine quartz veins: Karatepe, KK1, KK2, KK3, KK4, K1, K2, K3 (K3E and K3W) and Topyurt veins. The veins generally have a length of several tens to several hundreds of meters. Their outcrop widths vary between 0.8 and 13.6 m on the surface. The veins can be grouped into two general directions: E-W trending veins and NE-SW veins. E-W trending veins include Karatepe, K2 and K3E veins, while the others are NE-SW trending veins. The K3 vein is composed of two segments of different orientations hosted by two different host rocks perhaps due to the competency difference between the host rocks. Dip of the veins varies between 43.5° and 76.7°.

While Karatepe, K3E and Topyurt veins are hosted by porphyry, the others are hosted by schist. Host rock schist around the NE-SW trending KK1, KK2, KK3, KK4 and K1 veins does not change foliation adjacent to the veins and these veins have very sharp contacts with their host rock schist. In contrary, the schist changes its foliation orientation and is highly fractured and veined around E-W trending K2 vein and NE-SW trending K3W vein. The E-W trending Karatepe vein is associated with array of extensional veins in the wall rock that defines left-lateral kinematics. The NE-SW trending Topyurt vein components and its wall rock structures are consistent with a right-lateral en-echelon brittle shear zone.

In addition to major quartz veins, sheeted extension veins filled by well-developed macro crystalline mineralized quartz are located along the valley floor. Strike values of these extension veins together with the extension veins around

Karatepe and Topyurt veins were used to infer the kinematics of the vein-structure system during gold mineralization since all of them have the same hydrothermal infill. Extension veins around the Karatepe and Topyurt veins and the sheeted veins have similar kinematics consistent with horizontal component of the minimum principal stress direction determined as **N35°W**.

Vein surfaces modelled in 3D indicate that the thickness of the veins decreases with depth and that the veins generally have a flaring upwards geometry. The attitude of modeled vein surfaces is generally different from the attitude of vein outcrops since the veins change geometry with depth. Histograms of the subsurface dip data of modeled veins show that the predominant subsurface dip amount of each vein is close to their surface dip data. In addition, rose plots of the subsurface strike data indicate that the predominant subsurface strike of each vein is close to their surface strike data, although due to erosion along vein walls there are not many direct measurements of strike and dip from the surface. The mapped variable geometry along strike is mirrored at depth and most of the veins have multiple locations at depth where the dip changes (i.e. the veins have vertically segmented sections with differing dips). When compared, E-W trending veins have more geometric irregularities than NE-SW trending ones both along strike and dip. Lowest parts of the modelled veins do not have any evidence for the sheeted veins observed at the lowest level of the Kestanelik gold deposit. This shows that the sheeted mineralized extension veins are just confined to the valley section where they crop out or the boreholes do not go enough anywhere else to cut the sheeted veins.

Based on the mean gold grades calculated using the geochemistry data of modelled vein intersections, Karatepe vein has the lowest mean gold grade of 0.458 g/t, while K3W vein has the highest mean gold grade of 6.943 g/t. Indeed, all of the veins are Au rich except the Karatepe vein. According to the vertical cross sections, ***77.7%*** of high gold grades are located at where the veins bend along dip. This indicates that geometric irregularities in structures such as down-dip bends are more favorable locations for gold to precipitate than more planar sections of the

structures. In layered rocks, such dip segmentation has been observed as a result of the competency difference within different host rock (e.g. Schöpfer *et al*., 2006, 2007). However at this site the dip segmentation is independent of the host rock type. Segmentation in the dip direction may be caused by the growth and coalescence of small planar segments of the structures (whether faults of fractures) (*Cox, 2005*).

It was hypothesized that during upwards movement of fluid in the conduit, a thickness increase sudden in time in the conduit would lead to a drop in the fluid pressure which may cause boiling (the most dominant gold precipitation mechanism) and associated gold precipitation. The association between the true thickness of the vein and gold grade was therefore investigated. $R^2$ values of thickness vs. gold grade (varying between *0.0032 and 0.1169*) for all of the veins are so low that there is essentially no relationship between the thickness of the vein and gold grade. Moreover, p-values calculated for each vein vary between 0.12 and 0.96 all of which is higher than the α-value (decided as 0.01) indicating there is not statistically significant relationship between the thickness and the gold grade. When the thickness data and the gold grades coming from the all of the modeled veins were taken into the account, the correlation coefficient value and the p-value was estimated 0.05 and 0.51 (p>0.01) respectively demonstrating the lack of the relationship. When bend-related gold grades are taken out, calculated $R^2$ values increase (except KK2 vein) but are still low and still indicate no relationship between the thickness and gold grades. Lack of relationship between the thickness and gold grade is questionable for now.

Bend-related gold grades were also evaluated statistically, and it was calculated that *78.6%* (22 out of 28) of the bends correspond to high gold grades (>1.525 g/t).

When the gold grades in different host rocks were calculated, it was found that the schist-hosted veins (except the K2 vein) host the majority of gold mineralization (*94.4%*) and **95.6%** of high gold grades. In addition, 85.4% of the

samples containing high gold grades (35 out of 41) come from the schist hosted veins. *97.8%* of bend-related gold is also hosted by schist.

# Chapter 5: Vein Textures and Breccias

Studying the textures and breccias of low sulphidation veins is crucial as the vein infill records the repeated cycles of mineralization, sealing, brecciation and fluid flow. In this chapter, section 1 reviews quartz textures in epithermal veins. Section 2 reports the textures and breccias observed in Kestanelik outcrop and drill cores including petrographical analyses for three of the veins: Karatepe, KK1 and K3. Section 3 discusses the results and key findings under three sub-headings: (1) multiphase brecciation, fluid flow and associated mineralization, (2) rough paleodepth estimations and (3) relationship between the vein textures and the gold grades.

## 5.1. Quartz textures in epithermal veins: a background

Quartz is the most dominant gangue mineral precipitated throughout the life of all hydrothermal systems. Its characteristics, morphology, crystal structure therefore may help understand changing hydrothermal conditions during vein formation, consisting of those which favor gold precipitation (Dong *et al.*, 1995). The first study describing the vein quartz was conducted by Adams (1920), and then it became the base for subsequent studies on textures of vein quartz (Spurr, 1926; Shaub, 1934; Stillwell, 1950; Lovering, 1972; Boyle, 1979; Sander and Black, 1988; Saunders, 1990; Dowling and Morrison, 1990). Dong *et al.* (1995) carried out the most comprehensive study on textures of vein quartz and developed a classification of quartz textures by reviewing the literature and observing approximately 400 specimens and 150 thin sections from more than 20 adularia-sericite type (low-sulphidation) type Paleozoic epithermal gold deposits in north Queensland, Australia. They differentiated thirteen quartz textures which are massive, crustiform, colloform, moss, comb, zonal, mosaic, feathery, flamboyant, ghost sphere, pseudobladed, pseudoacicular, and saccharoidal. Apart from these textures, quartz can be subdivided into three based on the size of individual grains:

(macro)crystalline, microcrystalline and cryptocrystalline (Bates and Jackson, 1987). In addition, chalcedony is defined as cryptocrystalline quartz either with fibrous or granular habit (Phillips and Griffen, 1981).

*Massive* texture refers to quartz having more or less homogenous appearance which lacks banding, fractures and similar features (Dong *et al.*, 1995) (Figure 5.1). Other quartz textures can be described under three main classes based on their possible origins (Dong *et al.*, 1995): (1) primary growth textures are formed during crystal growth or the precipitation of amorphous silica; (2) recrystallization textures are produced by the recrystallization of chalcedony, or crystallization and subsequent recrystallization of amorphous silica to quartz; and (3) replacement textures are formed by the partial or complete pseudomorphs of other minerals by silica minerals.

Primary growth textures are crustiform, cockade (a subtype of crustiform texture), colloform, moss, comb and zonal textures (Figure 5.1).

*Crustiform* texture has successive narrow (up to a few centimeters), and subparallel bands of different color, mineral proportions and/or texture. Banding is generally developed symmetrically from both walls of a fissure. Crustiform bands form due to any change in fluid conditions which include cooling, mixing of two fluids, boiling and fluid-wall rock interaction (Buchanan, 1981).

*Cockade* is a subtype of crustiform texture surrounding isolated fragments of wall rocks or early vein materials in breccias. Dong *et al.* (1995) observed sharp contacts between fragments and banded materials and proposed hydrothermal brecciation as the mechanism for the formation of a cockade texture since it causes the deposition of silica minerals and other minerals around newly formed fragments.

A more recent study (Frenzel and Woodcock, 2014) reviews and discusses the six possible mechanisms for the formation of cockade breccia (cockade texture). They propose the rotation-accretion hypothesis as the most likely mechanism considering the evidence available from the literature (See the paper for the other

possible mechanisms). In the rotation-accretion mechanism; cockades occur as a result of repeated fracturing of a partially cemented breccia, commonly along the boundaries between each clast, and subsequent formation of partial layer of new cement. Repeated fracturing can occur due to the mechanical effects of moving fault walls and not the moving fluid alone, while the cementation forms mostly in interseismic periods (Frenzel and Woodcock, 2014).

*Colloform* texture describes chalcedonic grains in fine rhythmic bands, that have spherical, botryoidal, reniform and mammillary external surfaces. Under the microscope, colloform banded chalcedony has a microfibrous habit with sharp re-entrant angles between touching spheroids (Rogers, 1917; Dong *et al*., 1995).

*Moss:* In hand specimen, silica aggregates show heterogeneous turbid appearance. Under the microscope, spheres are diagnosed by the distribution of impurities within aggregates of silica minerals. Some spheres may also have internal concentric or radiating pattern (Adams, 1920; Dong *et al*., 1995).

Two processes were suggested for the formation colloform and moss textures. The first process, proposed by Rogers (1917) and Adams (1920), is based on the precipitation of silica gel in free space. The major factor controlling the process is surface tension in fluids, produced by near-surface intermolecular forces tending to reshape all nonspherical surfaces into spherical surfaces based on the minimum free energy configuration (Adamson, 1976). The second process is the segregation of impurities by crystallization from silica gel (Adams, 1920; Oehler, 1976) due to the slow rate of impurity diffusion compared with rate of crystal growth. Different appearances of colloform and moss textures may be due to difference in the formation of initial core: core on wall rock or early vein material result in colloform texture; while core suspended in silica gel cause moss texture.

*Comb* texture displays groups of parallel or subparallel quartz crystals oriented perpendicular to vein wall. Crystals generally show a uniform grain size and have euhedral terminations at their free ends (Adam, 1920; Boyle, 1979). The texture is produced by geometrical selection in which adjacent crystals compete for

space resulting in preferential growth where the orientation of maximum growth rate is perpendicular to the growth surface. This occurs when relatively slow changing conditions are provided in an open space (Dong *et al.*, 1995).

**Zonal** texture has alternating clear and milky zones within individual quartz crystals. Milky zones are rich in fluid or solid inclusions which are always parallel to crystal growth faces (Dong *et al.*, 1995). This texture is produced from the hydrothermal fluid which is slightly saturated with respect to quartz proposing slow to very mildly changing conditions during crystal growth (Fournier, 1985).
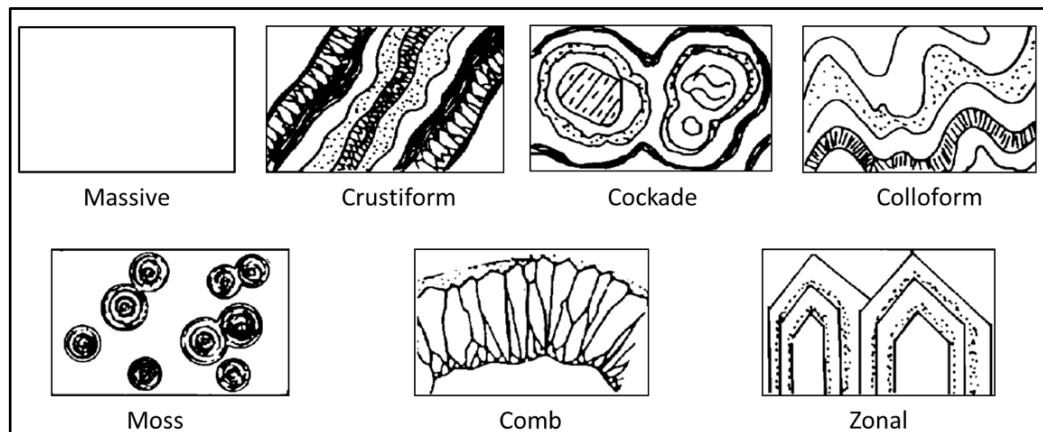


**Figure 5.1.** Primary growth textures of epithermal vein quartz (from Dong *et al.*, 1995).

Recrystallization textures consist of feathery, flamboyant, ghost-sphere and mosaic textures (Figure 5.2).

**Feathery:** In this texture, individual quartz crystals show feathery appearance under crossed polars with slight differences in extinction angles. The texture is generally formed on the margins of clear euhedral quartz crystals or as patches throughout quartz crystals (Adams, 1920; Dong *et al.*, 1995). Formation mechanism is similar to the epitaxial growth of quartz (Rimstidt and Cole, 1983): small crystals nucleate on the surface of an existing quartz crystal. Recrystallization of small crystals then occurs in approximate crystallographic continuity with the host quartz crystal.

**Flamboyant** texture displays radial or flamboyant extinction of individual quartz crystals with rounded crystal outlines (Adams, 1920; Sander and Black,

1988). Like feathery texture, it may form around the margins of the core of clear euhedral quartz crystals or throughout the crystal. The original components of the texture are fibrous chalcedony with rounded external surfaces, deposited from silica gel, either as the rims of early formed quartz crystals or wall rock, or as groups of spheres. Later, recrystallized materials follow the crystallographic direction of initial nuclei of each chalcedonic spheroid or that of large host crystal, crystalline or microcrystalline quartz crystals producing radiating extinction (Dong *et al.*, 1995).

*Ghost-sphere* texture generally forms within microcrystalline quartz as spheres defined by the distribution of impurities (Dong *et al.*, 1995). The texture is produced when by the recrystallization of amorphous silica or chalcedony with a moss texture provided that the original spherically distributed impurities are preserved in quartz crystals because of their low solubility (Dong *et al.*, 1995).

*Mosaic* texture has microcrystalline or crystalline quartz crystals with tightly packed highly irregular and interpenetrating grain boundaries. It is produced by the recrystallization of massive chalcedony or amorphous silica grains following the shape of the original small grains resulting in the formation of highly irregular and interpenetrating boundaries of the crystals (Lovering, 1972; Dong *et al.*, 1995).
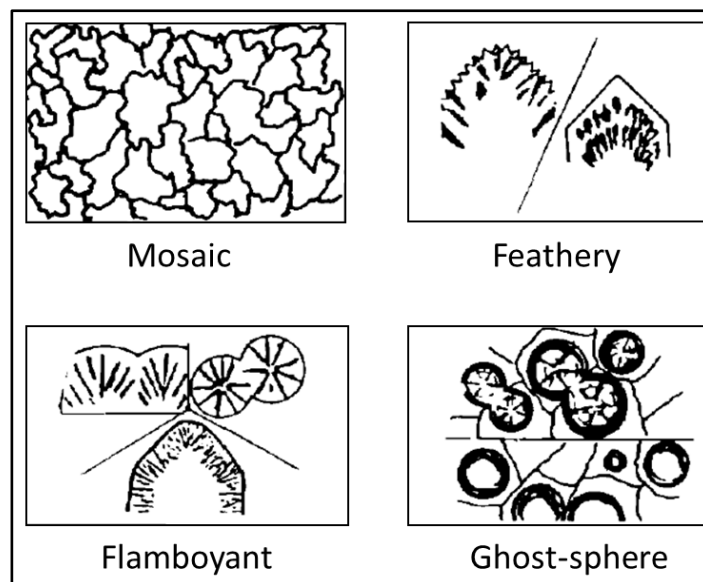


**Figure 5.2.** Recrystallization textures of epithermal vein quartz (from Dong *et al.*, 1995).

Replacement textures include pseudobladed, pseudoacicular and saccharoidal textures (Figure 5.3).

***Pseudobladed*** texture has bladed or platy quartz or chalcedony aggregates. Quartz generally replaces calcite (the most common soluble phase in epithermal veins). When replaced by quartz, microscopic inclusions in the original carbonate remain due to low solubility, defining original crystal outlines. Replacement generally proceeds along the lamellar partings of carbonate crystals rather than rhombic cleavage planes. The resulting parallel structures within pseudomorphs are diagnosed by different grain sizes, or degree of impurities. Three sub-types are based on blade aggregate morphology.

***Lattice bladed***: network of intersecting silica blades with polyhedral cavities is filled with comb quartz crystals partially. Under the microscope, each blade is composed of a series of parallel seams separated by quartz crystals symmetrically grown and perpendicular to the seams (Schrader, 1912; Morgan, 1925). The original bladed material is carbonate, and after total replacement, quartz crystals in every two adjacent layers merge into a seam with increasing grain size outward.

***Ghost bladed*** texture has randomly distributed blades within quartz aggregates and no cavities between them. In thin section, the blades and matrix have different grain size and shape. The original material is quartz intergrown with bladed carbonate, therefore after total replacement the bladed form is preserved by concentration of impurities (Dong *et al*., 1995).

***Parallel bladed*** texture has groups of parallel silica blades with different orientations (Adams, 1920; Dong *et al*., 1995). Each group has an overall granular, rectangular outline and is the product of replacement of massive granular calcite (Adams, 1920; Dong *et al*., 1995).

***Pseudoacicular*** texture has aggregates of silica minerals with adularia or its weathering products (sericite or kaolinite) and a radial acicular appearance. This forms as a result of calcite replacement by quartz and adularia along radial acicular structures of calcite crystals (Adams, 1920; Schrader, 1923; Dong *et al*., 1995).

*Saccharoidal* texture consists of loosely packed vitreous to milky fine grained quartz aggregates with a sugary appearance in hand specimen. In thin section, elongated subhedral crystals are found with a matrix of smaller anhedral grains. This texture is produced when quartz replaces massive granular carbonate along crystallographic defects rather than along lamellar partings (which forms parallel-bladed texture) (Lingdren, 1901; Adams, 1920; Lovering, 1972).
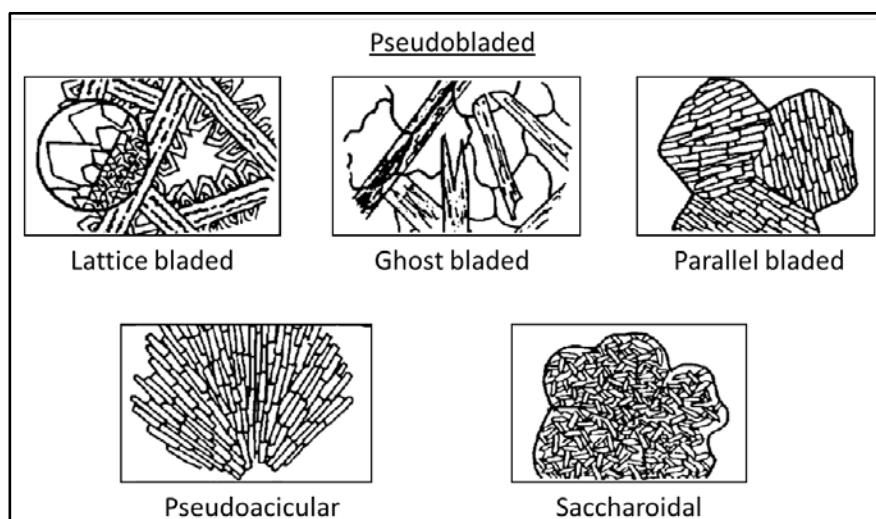


**Figure 5.3.** Replacement textures of epithermal vein quartz (from Dong *et al*., 1995).

## 5.2. Quartz textures and breccias in the Kestanelik veins

Epithermal gold mineralization in the study area associated with all nine major quartz veins plus sheeted quartz veins (Figure 5.4) were studied from outcrop and drill cores. KK3 and KK4 veins share same textural and breccia characteristics with the KK1 and KK2 veins respectively, so their textural and breccia characteristics are not given in the chapter. Quartz textures, their cross-cutting relationships and breccia types were recorded with characteristics such as clast type, cement type, roundness and sorting of clasts, and in situ estimation of clast/cement ratio.

Petrographical analyses were performed from samples of Karatepe, KK1 and K3 veins, which represent the gold mineralization in different parts of the study area. Samples were selected from: (1) locations where different quartz textures cross cut each other, potentially representing multiple episodes of mineralization to

determine the different episodes, (2) hanging wall and footwall margins of the veins to explore (micro)structural relationships between the textures that represent the earlier and latest phases of mineralization, (3) where the infill is complex and gold grade is high (for drill cores) to understand the possible textural controls on the gold precipitation (however sampling was only permitted by the license holder company at limited intervals), (4) different levels of the vein to examine any textural change in the vein infill type with depth.
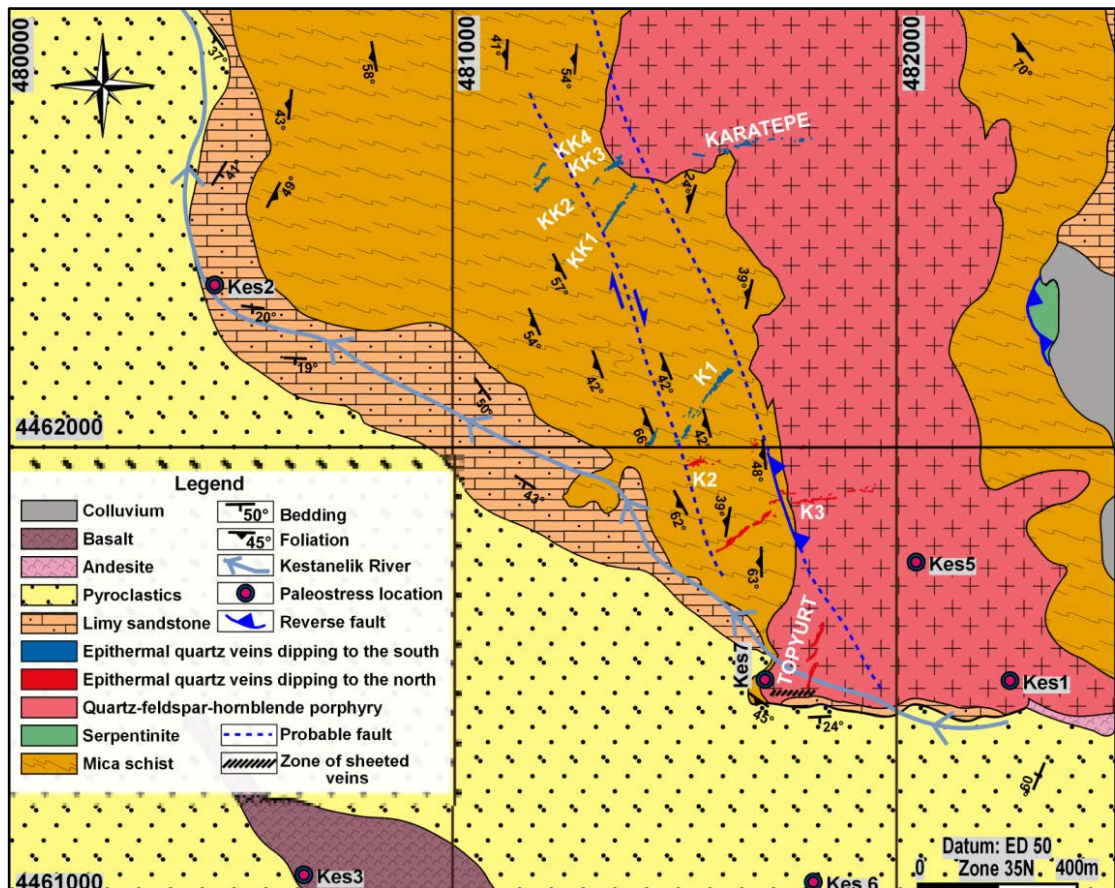


**Figure 5.4.** Geological map of the study area with the major epithermal quartz veins and sheeted quartz veins in the valley

### 5.2.1. Karatepe vein

Two different textures were differentiated: cockade chalcedony and crustiform chalcedony (Figure 5.5). *Six thin sections* were studied; three from a hand specimen taken from the vein outcrop and three from a drill core sample (Figure 5.6).
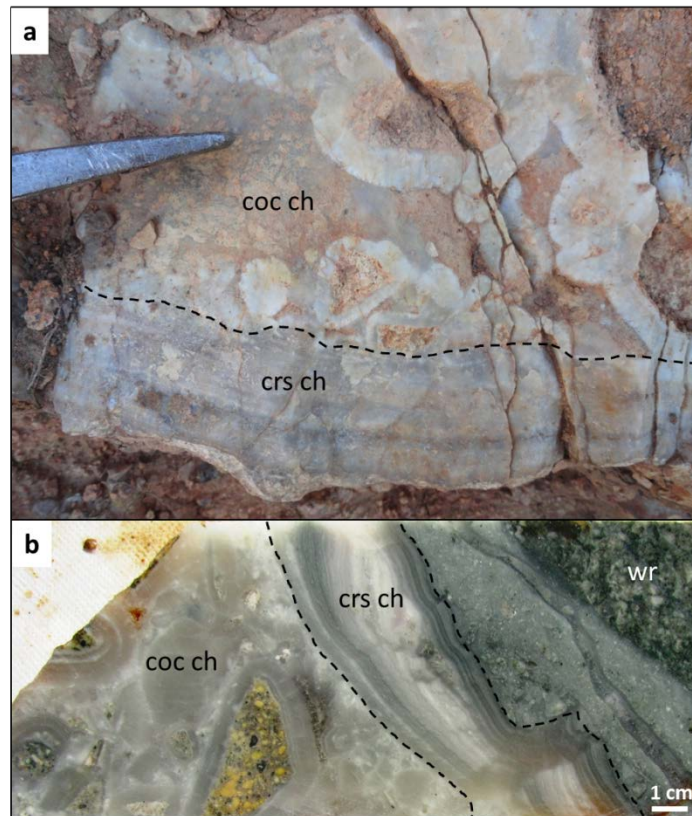
**Figure 5.5.** Quartz textures of Karatepe vein **(a)** in outcrop, and **(b)** in a drillcore of KED-16 at 124.2-124.4 m (coc ch: cockade chalcedony, crs ch: crustiform chalcedony, wr: wall rock).
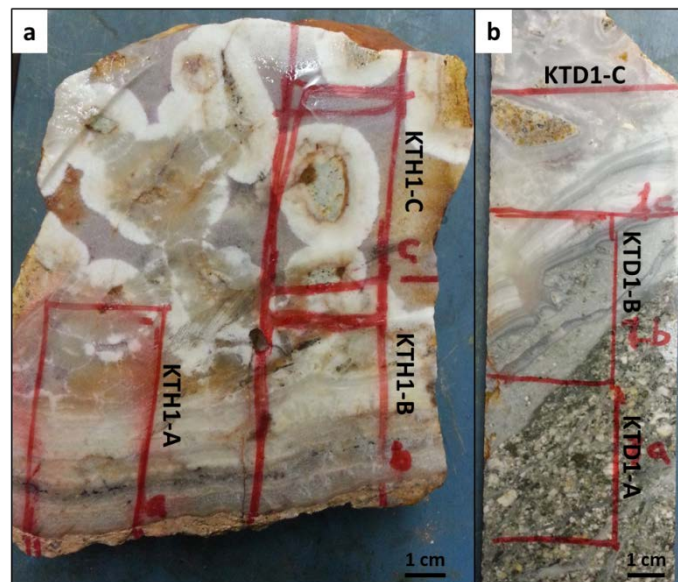


**Figure 5.6.** Thin section locations of **(a)** a hand specimen taken from the vein outcrop (398 m asl), **(b)** a drillcore sample taken from KED-16 at 124.1-124.3 m (237.7 m asl).

Crustiform chalcedony rims clasts of altered quartz-feldspar-hornblende (QFH) porphyry forming cockade texture (Figure 5.7). Crustiform chalcedony formed at the footwall margin of the vein cuts the phase 1 cockade chalcedony and fills microfractures in phase 1 cockade chalcedony (Figure 5.8). Crustiform chalcedony is therefore younger than the cockade chalcedony and the vein hosts two different phases of mineralization.
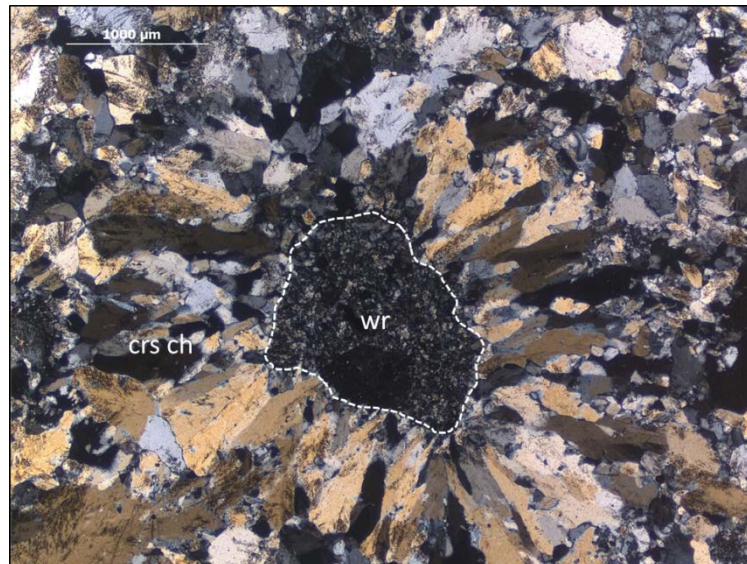


**Figure 5.7.** Crustiform chalcedony (crs ch) rimming a clast of altered wall rock QFH porphyry (wr) and forming the cockade texture (crossed polars image from KTH1-B).
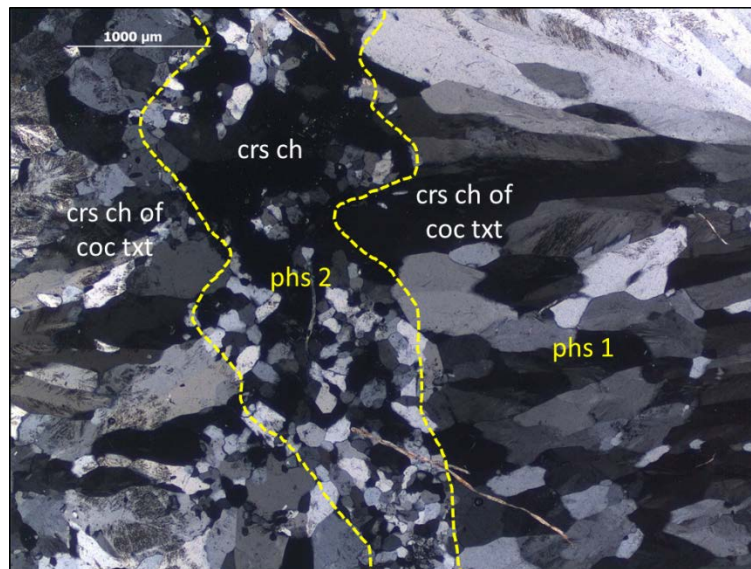


**Figure 5.8.** A veinlet of crustiform chalcedony (crs ch) cutting the phase 1 cockade chalcedony (coc txt: cockade texture) (crossed polars image from KTH1-A).

Cataclasite of feldspar (from the wall rock QFH porphyry) and phase 1 chalcedony (Figure 5.9) cemented by a later phase of chalcedony (phase 2) was observed by petrography of the thin section KTD1-A from the drill core sample taken from the footwall of the Karatepe vein-wall rock contact.
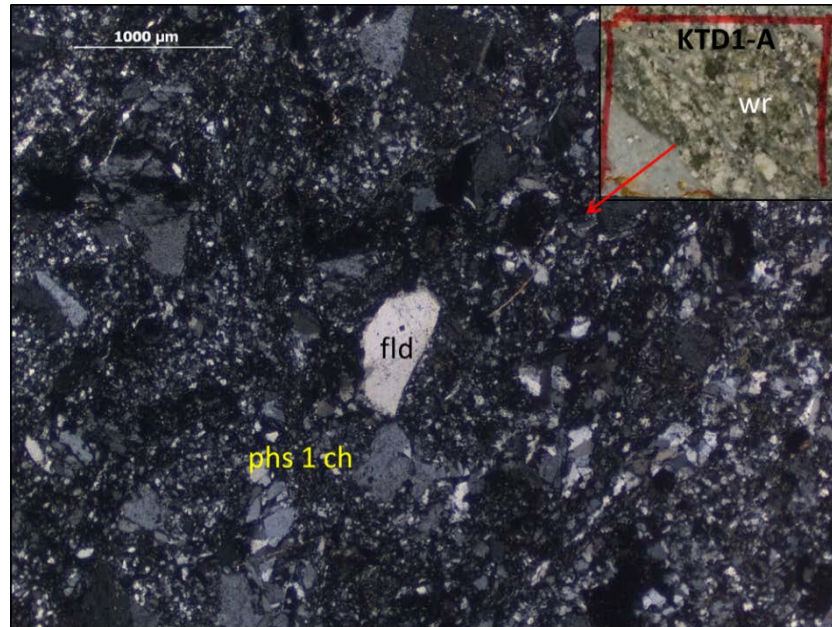


**Figure 5.9.** Cataclasite with fragments of feldspar (fld) (from the wall rock QFH porphyry (wr)) and phase 1 chalcedony (ch) (crossed polars image from KTD1-A).

Microcrystalline chalcedony (Figure 5.10) observed along the footwall of the vein-wall rock margin which was most likely formed due to rapid cooling as a result of the interaction between the hydrothermal fluid and wall rock.

In thin section KTD1-A, a comb quartz veinlet and thinner quartz veinlets traverse the clay-altered QFH porphyry (Figure 5.11a). Infill of the comb quartz veinlet has a granular texture and inequant fabric rather than a fibrous texture which shows that the opening of the fracture was more rapid than the growth of the quartz crystals (Figure 5.11b).

In thin section KTD1-B, chalcedony is filling a fracture created in phase 2 crustiform chalcedony and they are cutting each other (Figure 5.12) which indicate synchronous deposition.
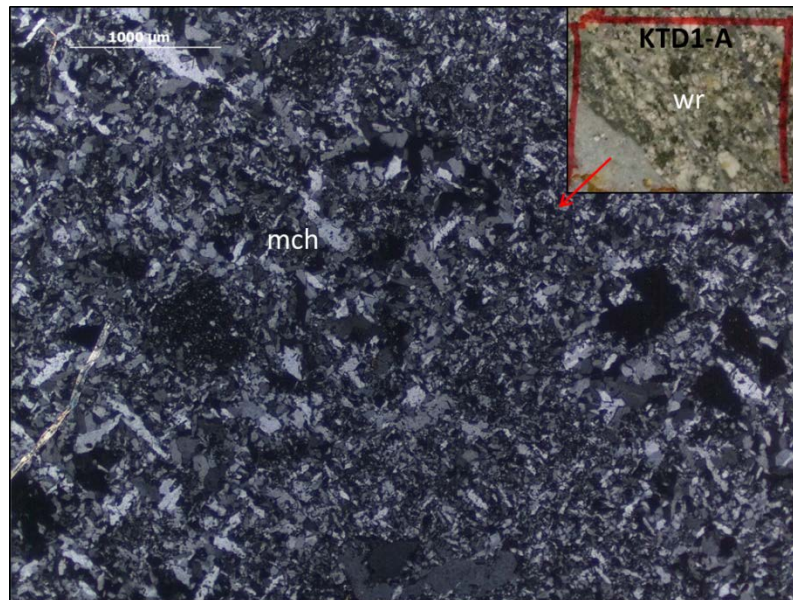
**Figure 5.10.** Microcrystalline chalcedony (mch) formed along the vein margin due to rapid cooling (wr: wall rock) (crossed polars image from KTD1-A).
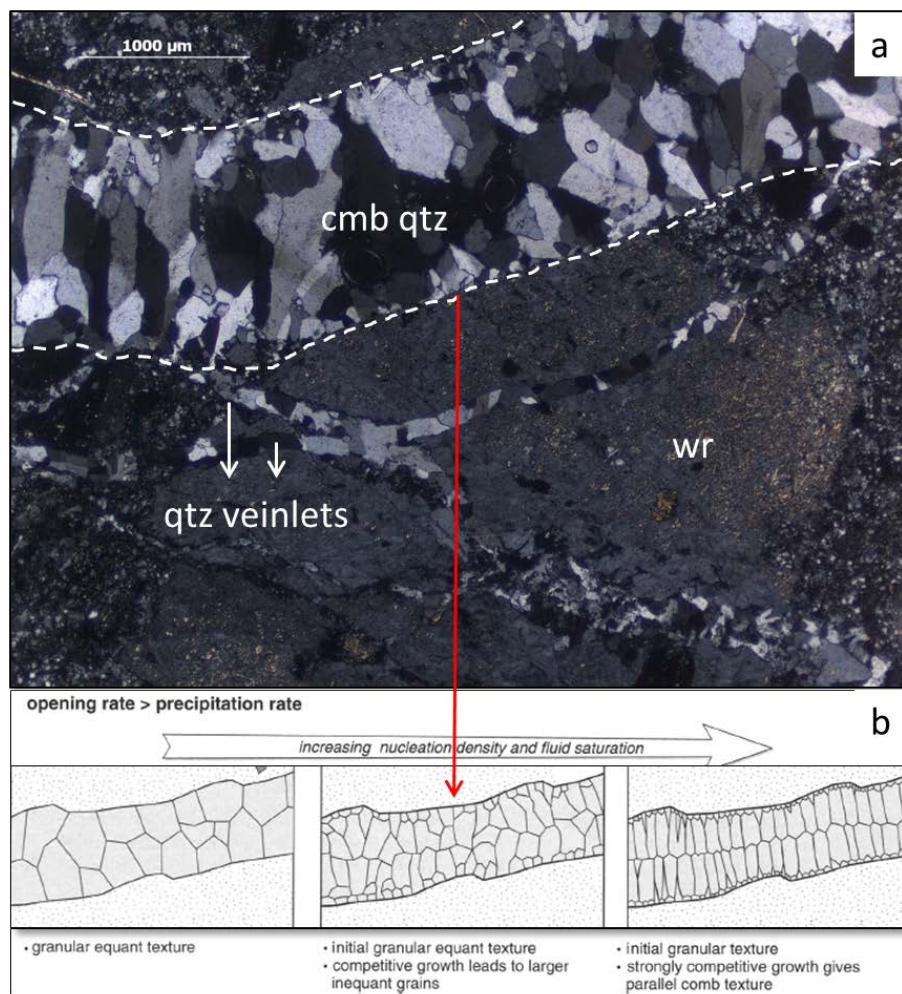
**Figure 5.11. (a)** A comb quartz (cmb qtz) veinlet and thinner quartz veinlets traversing the clay altered wall rock QFH porphyry (wr) (crossed polars image from KTD1-A). **(b)** Contrasting carbonate fabrics at varying fluid saturation levels when opening rate of the fracture > precipitation rate of the cement (taken from Woodcock *et al.*, 2007).
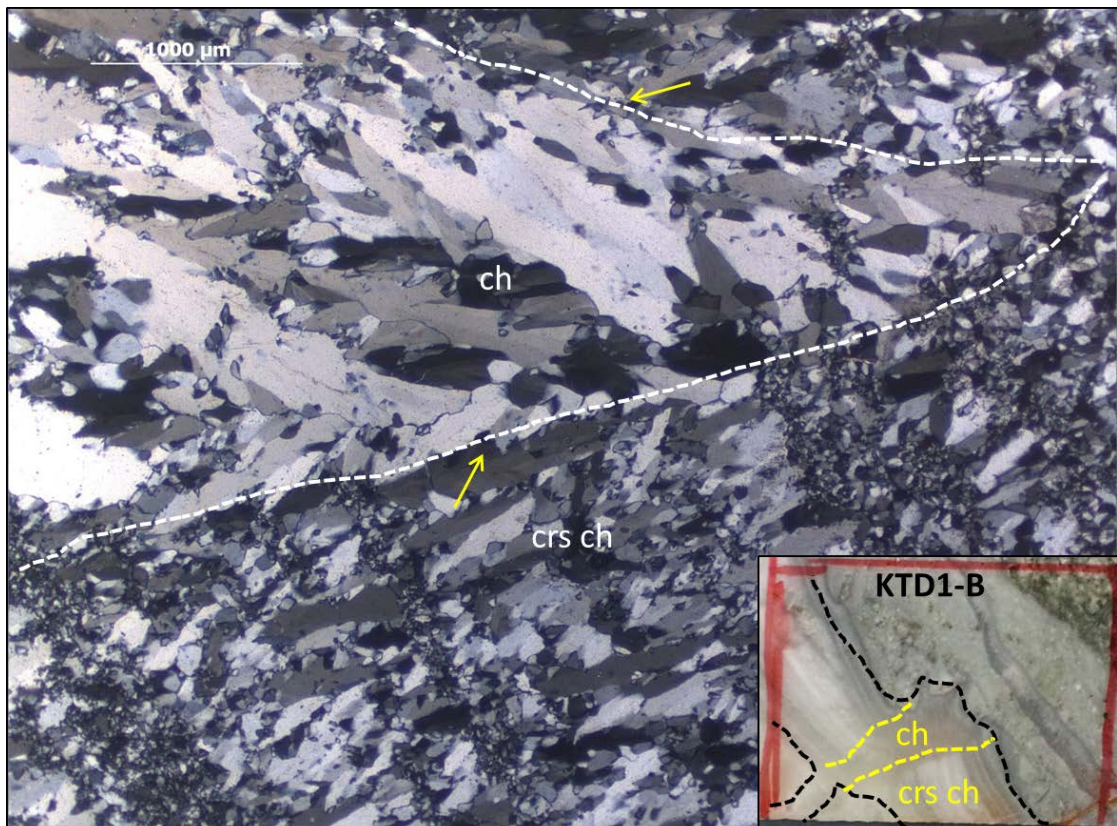


**Figure 5.12.** Synchronous deposition of chalcedony (ch) and crustiform chalcedony (crs ch) (crossed polars image from KTD1-B). Yellow arrows indicate some of the locations where the crustiform chalcedony overprints the chalcedony.

Wall rock clasts within the cockade breccia are sub-rounded to rounded and poorly sorted. Clasts show neither normal nor reverse grading in drill core samples from any depth (Figure 5.13). From drill cores cutting different levels of the vein core, it is evident that the cockade texture of the vein does not change with depth (Figure 5.14). However gold grades are variable with depth and vary between 0.082 and 1.37 g/t (Table 5.1).
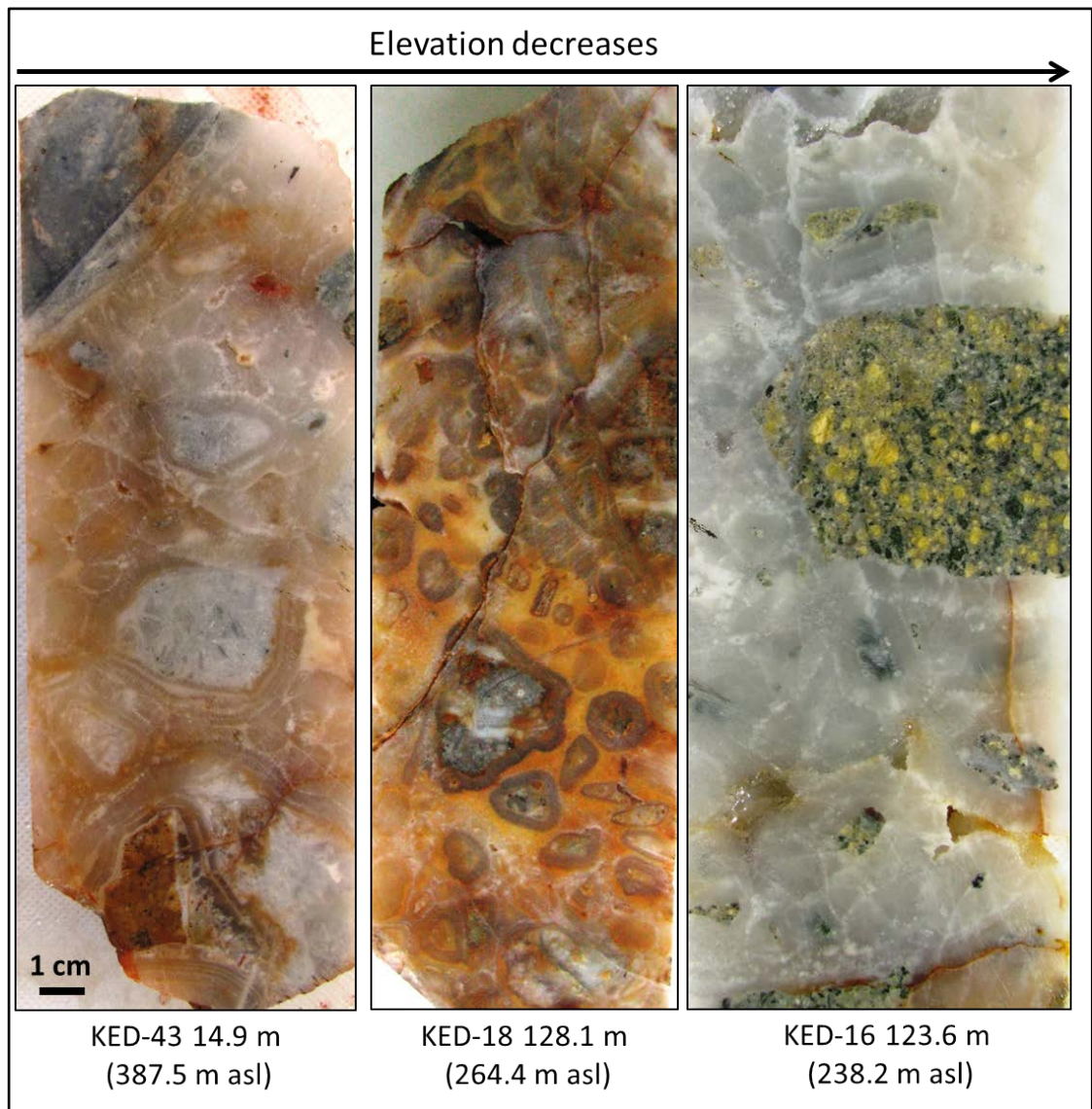
**Figure 5.13.** Cockade breccias at different levels of the Karatepe vein. Size of individual cockade breccias neither decreases nor increases as elevation decreases (Note that the scale is same for each photo).
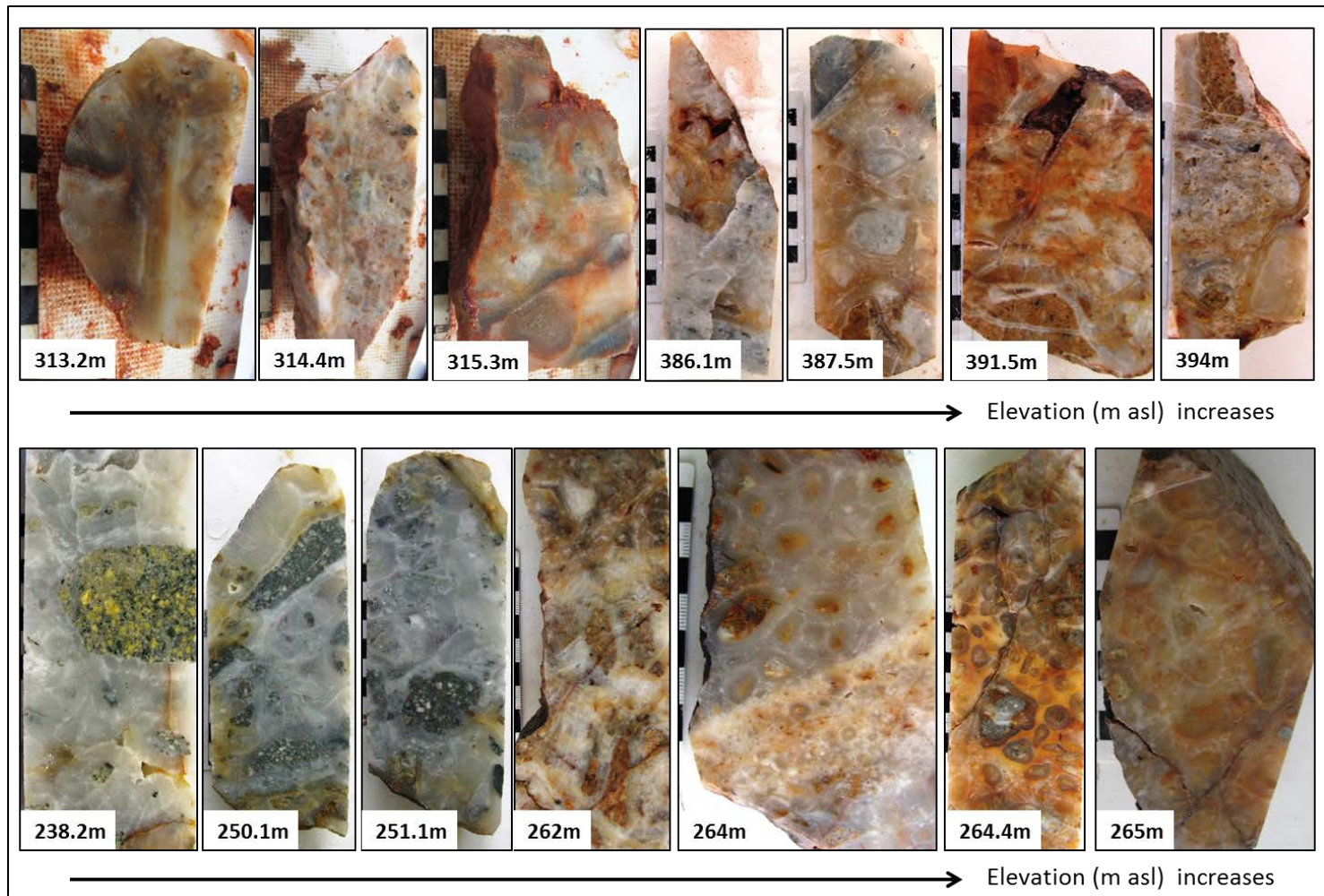
**Figure 5.14.** Cockade textured chalcedony of the Karatepe vein at different levels.

**Table 5.1.** Gold grades coming from the cockade textured chalcedony of the Karatepe vein at different vein levels.

| Drillhole ID | From (m) | Elevation (m asl) | Au (g/t) |
|---|---|---|---|
| KED-16 | 123.6 | 238.2 | 0.269 |
| KED-99 | 130.9 | 250.1 | 0.258 |
| KED-99 | 129.9 | 251.1 | 0.221 |
| KED-18 | 130.8 | 262 | 0.082 |
| KED-18 | 128.6 | 264 | 0.086 |
| KED-18 | 128.1 | 264.4 | 0.135 |
| KED-18 | 127.4 | 265 | 0.227 |
| KED-218 | 48.4 | 313.2 | 1.37 |
| KED-218 | 47.4 | 314.4 | 0.93 |
| KED-218 | 46.7 | 315.3 | 0.763 |
| KED-43 | 14.5 | 386.1 | 0.746 |
| KED-43 | 14.9 | 387.5 | 0.576 |
| KED-43 | 10.1 | 391.5 | 1.165 |
| KED-43 | 8.1 | 394 | 0.465 |

### 5.2.2. KK1 Vein

Outcrop textural observations of the 150m-long KK1 vein were made where intense weathering and vegetation allowed. Saccharoidal and pseudobladed quartz textures are commonly observed throughout the surface outcrop (Figure 5.15). Crackle (jigsaw-fit) breccias cemented by quartz-iron oxide in a network of veinlets were observed at some parts of the vein. Good- to well-sorted clasts are generally angular to sub-angular. In these cement-supported breccias, the cement is always less than 50% of the rock volume (Figure 5.15c).

Close to the KK1 vein margins, cement-supported breccias comprising host rock schist clasts, cemented by saccharoidal quartz were found (Figure 5.15d).

Poorly- to well-sorted clasts are angular to sub-angular, and the cement is over 50% of the rock volume. These breccias generally form semi-continuous domains on the exposed vein outcrops.
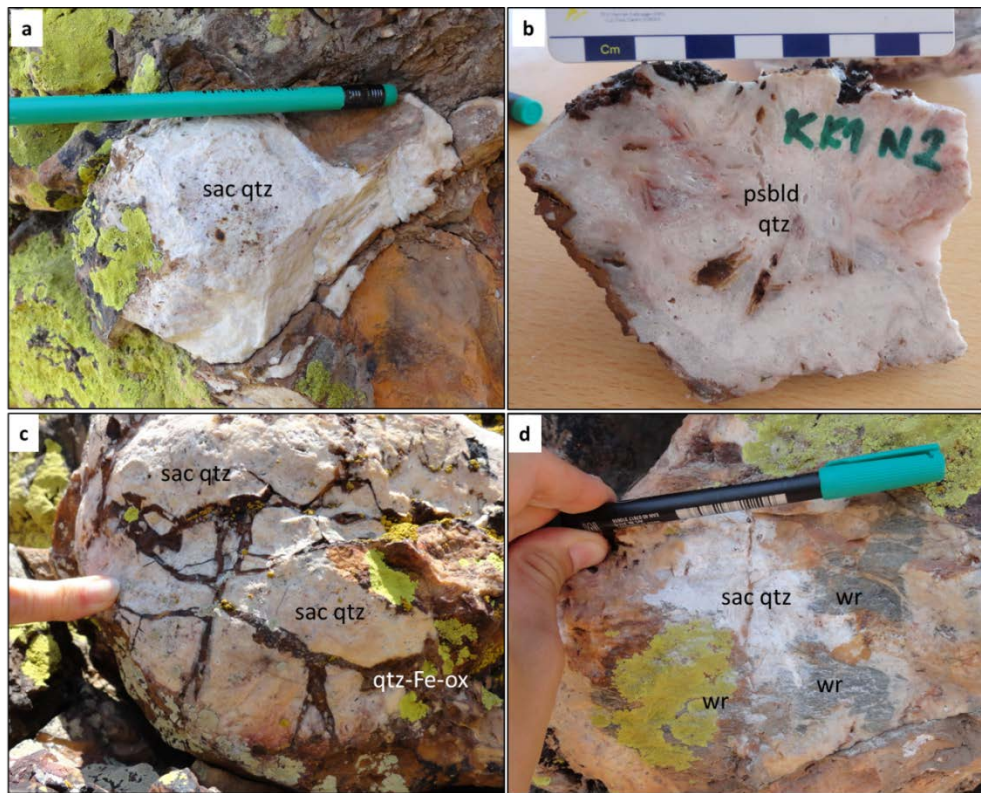


**Figure 5.15.(a)** Saccharoidal quartz (sac qtz) observed on the vein outcrop (318 m asl). **(b)** Pseudobladed quartz texture (psbld qtz) on an outcrop hand specimen. **(c)** Crackle breccia with clasts of saccharoidal quartz (sac qtz) separated by quartz-iron oxide (qtz-Fe-ox) cement (320 m asl). **(d)** Breccia with the clasts of wall rock schist (wr) plus a cement of saccharoidal quartz (sac qtz) at the HW margin of the KK1 vein (316 m asl).

Texture and breccia types do not vary throughout the KK1 vein apart from at the upper levels (330-340 m asl) where crackle to chaotic breccias frequently exist. These have sub-angular to angular, poorly sorted, mm to cm scale clasts of pre-existing vein infill saccharoidal quartz and pseudobladed quartz, cemented by quartz-iron oxide. The breccias are cement supported and have over 50% cement (Figure 5.16).

Texture and breccia characteristics of the KK1 vein were also examined in drillcores (Figure 5.17), although most of the drill holes cutting this vein are reverse circulation (RC) holes.

**Figure 5.16.** Crackle to chaotic breccias with the clasts of saccharoidal quartz (sac qtz) and pseudobladed quartz (psbld qtz) with a cement of quartz- iron oxide (Fe-ox) (334 m asl).

Saccharoidal vuggy quartz was the most common texture observed in drill cores (Figure 5.17a-b), while microcrystalline (Figure 5.17c) and pseudobladed quartz (Figure 5.17d) were also present. Breccia with clasts of wall rock plus a cement of microcrystalline quartz-iron oxide (Figure 5.17c), and crackle breccia with clasts of saccharoidal and pseudobladed quartz of earlier phase cemented by a later phase quartz-iron oxide (Figure 5.17d) were also observed.
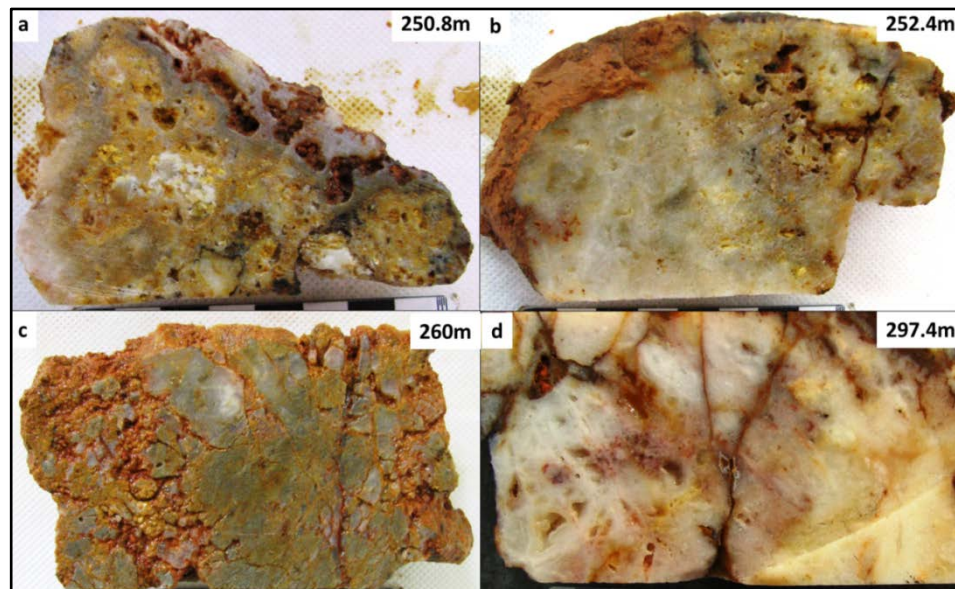


**Figure 5.17.** Textures and breccias of KK1 vein at different levels (see Table 5.2).

139

Relationship between KK1 vein textures and gold grades could be examined where gold assay data was available. Table 5.2 below gives the locations and textural descriptions of drill cores shown on Figure 5.17, and their gold grades.

**Table 5.2.** Locations, textural descriptions and gold grades of KK1 vein drill cores.

| Location on Figure 5.17 | Drillhole ID | Vein at (m) | From (m) | Elevation (m asl) | Description | Au (g/t) |
|---|---|---|---|---|---|---|
| a | KED-96 | 44-46.4 | 46 | 250.8 | Saccharoidal vuggy quartz and iron oxide(s) filling the vugs partially | 9.92 |
| b | KED-96 | 44-46.4 | 44.4 | 252.4 | Synchronous (?) saccharoidal and pseudobladed vuggy quartz and iron oxide(s) filling the vugs partially | 7.44 |
| c | KED-130 | 48.5-50 | 49 | 260 | crackle breccia with wall rock schist clasts and microcrystalline-quartz-iron oxide cement | 0.351 |
| d | KED-7 | 11.3-18 | 12.1 | 297.4 | crackle breccia with synchronous (?) pseudobladed and saccharoidal quartz clasts and quartz-iron oxide cement | 1.645 |

Petrographical analyses were conducted to examine the change in textures and breccias of KK1 vein with depth and along the surface from the margins to the core, and to differentiate different mineralization phases represented by different textures. Twenty thin sections in total were examined; 18 from hand specimens taken from different elevations of the vein outcrop (KK1H1-14) and 2 from two drill core samples (KK1D1 and KK1D2 from KED-7 12.5-12.7m and KED-7 13.1-13.2m respectively) (Figure 5.18 and Table 5.3).

**Table 5.3.** Locations of the thin section samples on the vein and their elevations and gold grades (nm: not measured)

| Sample ID | Location on the vein | Elevation (m asl) | Au (g/t) |
|-----------|----------------------|-------------------|----------|
| KK1H1 | FW | 335 | nm |
| KK1H2 | Core | 329 | nm |
| KK1H3 | HW | 327 | nm |
| KK1H4 | HW | 307 | nm |
| KK1H5 | Core | 309 | nm |
| KK1H6 | FW | 315 | nm |
| KK1H7 | FW | 320 | nm |
| KK1H8 | FW | 338 | nm |
| KK1H9 | Core | 312 | nm |
| KK1H10 | FW | 325 | nm |
| KK1H11 | FW | 322 | nm |
| KK1H12 | FW | 311 | nm |
| KK1H13 | FW | 331 | nm |
| KK1H14 | FW | 324 | nm |
| KK1D1 | Core | 299 | 0.628 |
| KK1D2 | Core | 298 | 0.628 |

4 different mineralization phases were revealed from the petrographic analyses. From oldest to the youngest, these phases are: (1) altered microcrystalline quartz (Figure 5.19), (2) altered saccharoidal quartz (Figure 5.20-23), (3) synchronous saccharoidal and bladed quartz (Figure 5.19-25) and (4) quartz goethite cementing all phases (Figure 5.23-25).
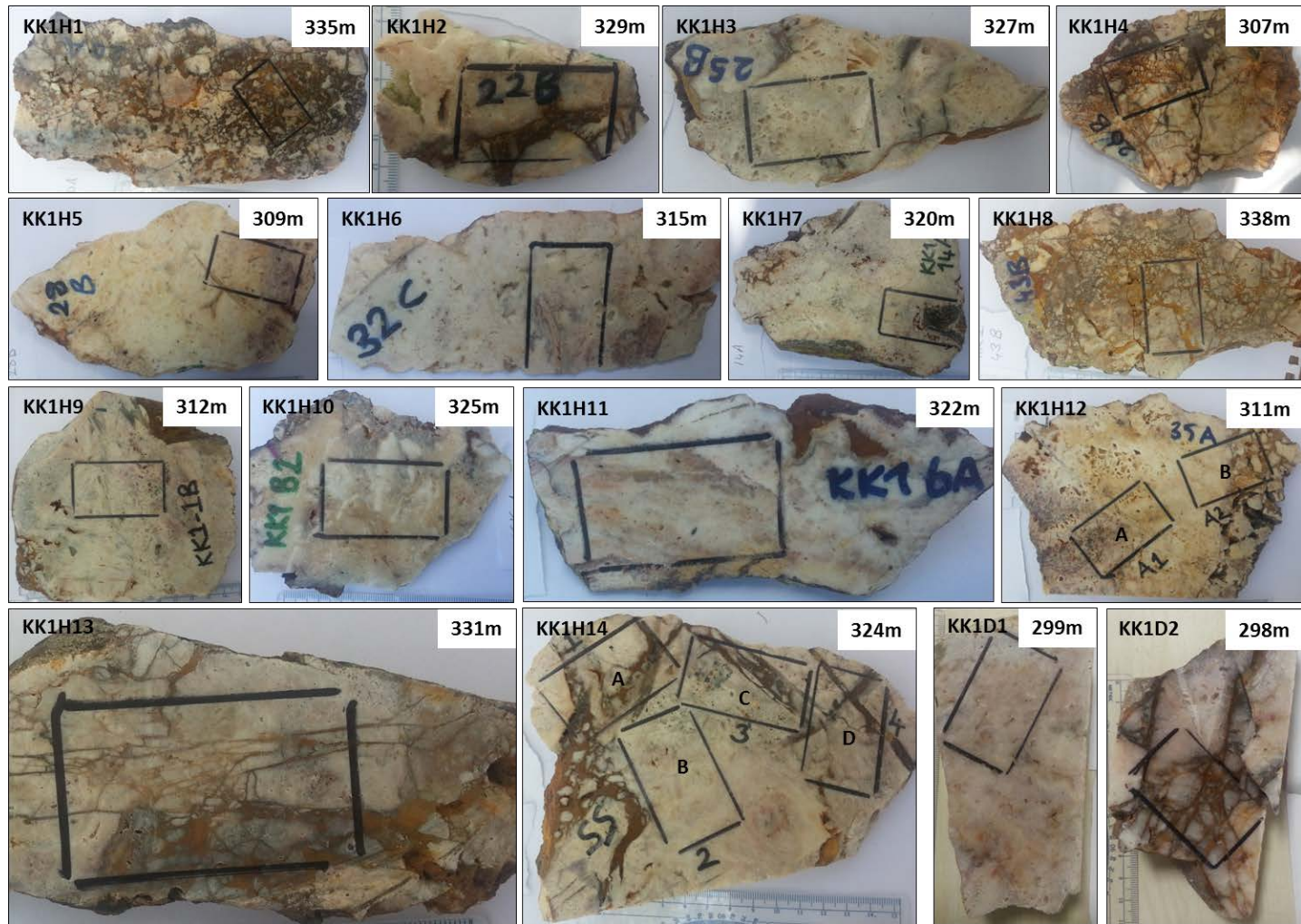
**Figure 5.18.** Thin section locations from the outcrop and drill core samples. The black rectangle on each picture has a width of 2.5 cm.
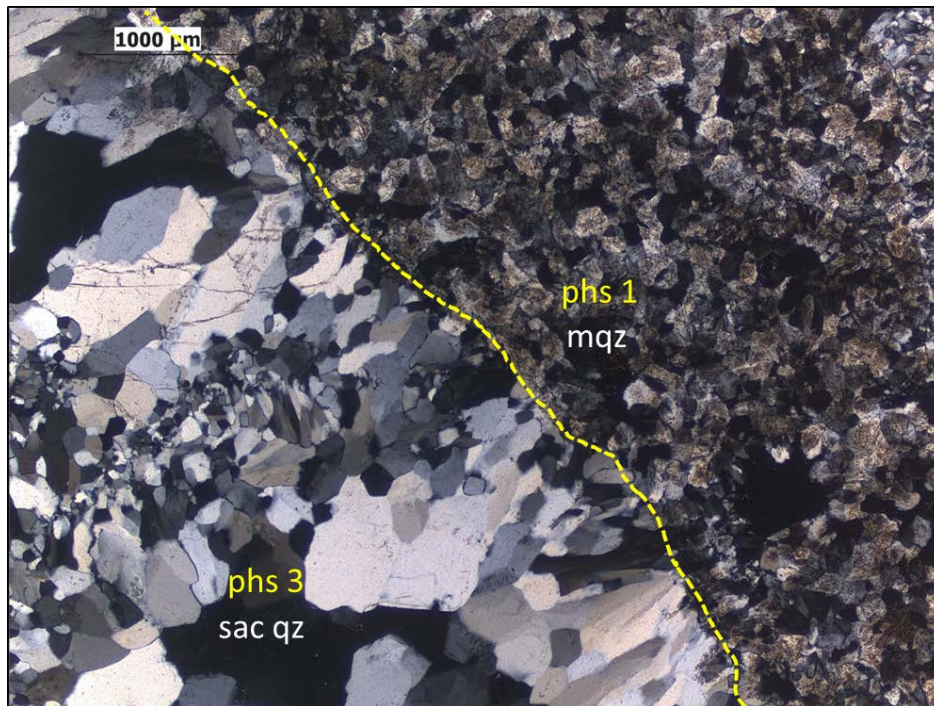
**Figure 5.19.** Altered microcrystalline quartz (mqz) (phase 1) cut by saccharoidal quartz (sac qtz) of phase 3 (crossed polars image from KK1H14-B).
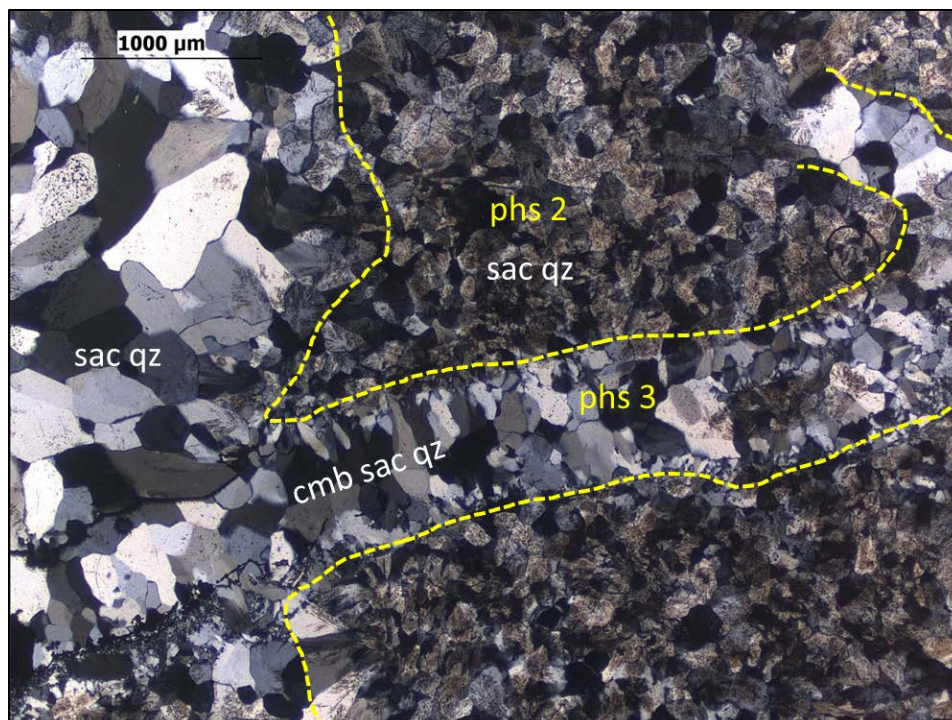


**Figure 5.20.** Saccharoidal quartz (sac qtz) of phase 3 forming a comb texture and cutting an earlier phase of altered saccharoidal quartz (cmb sac qtz: comb saccharoidal quartz) (crossed polars image from KK1H14-D).
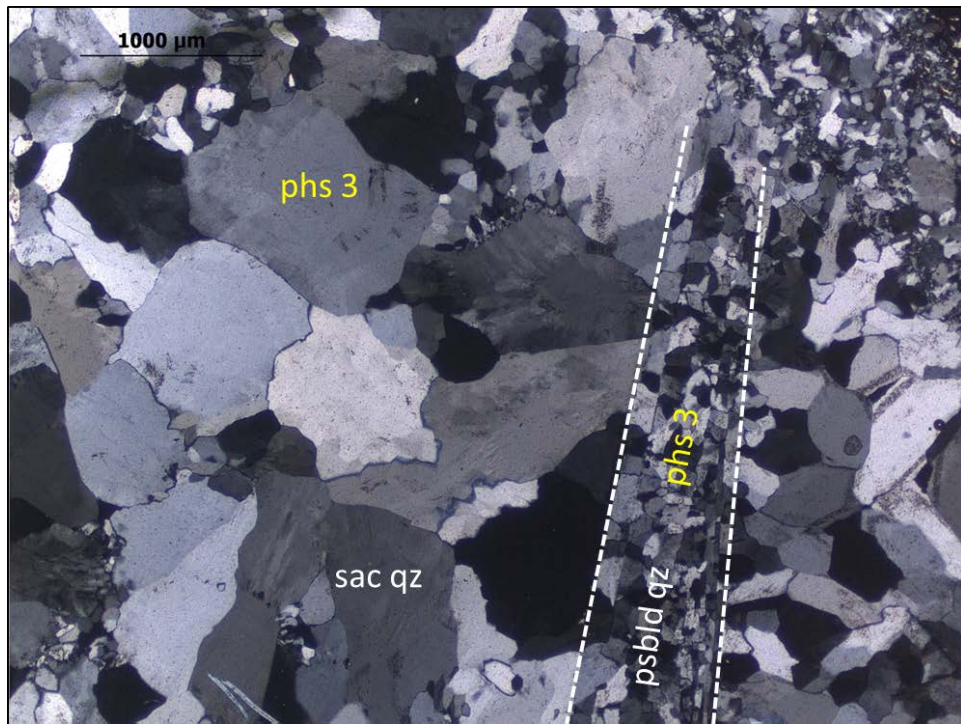
**Figure 5.21.** Saccharoidal quartz (sac qtz) replaced by bladed quartz (psbld qz) both of which are synchronous and phase 3 (crossed polars image from KK1H14-A).
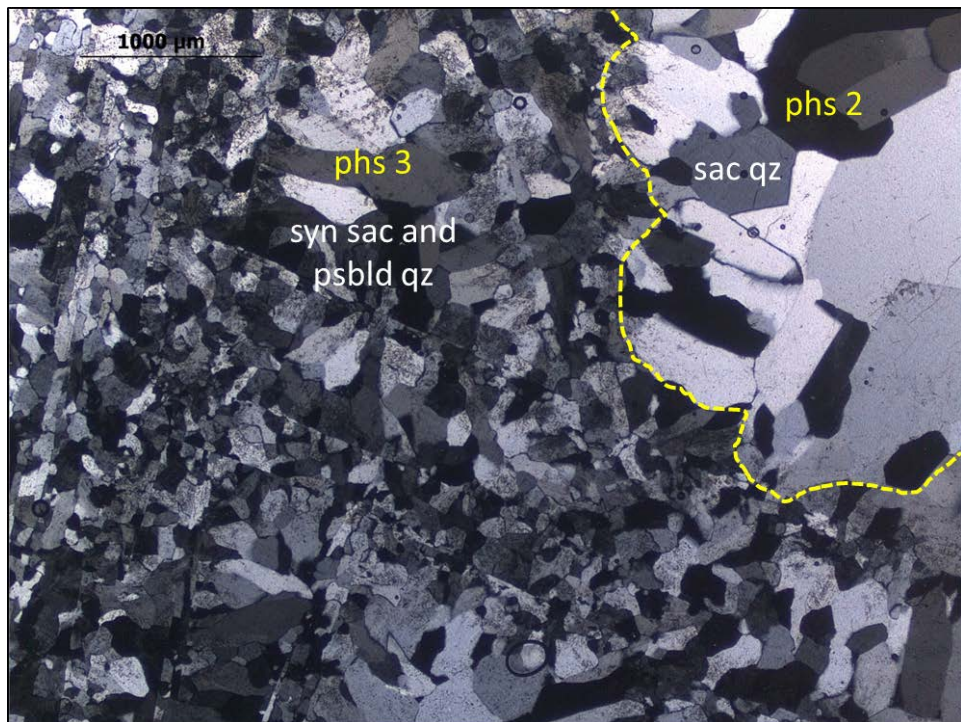


**Figure 5.22.** Synchronous saccharoidal (sac qtz) and pseudobladed quartz (psbld qz) (phase 3) cutting phase 2 saccharoidal quartz (crossed polars image from KK1H9).
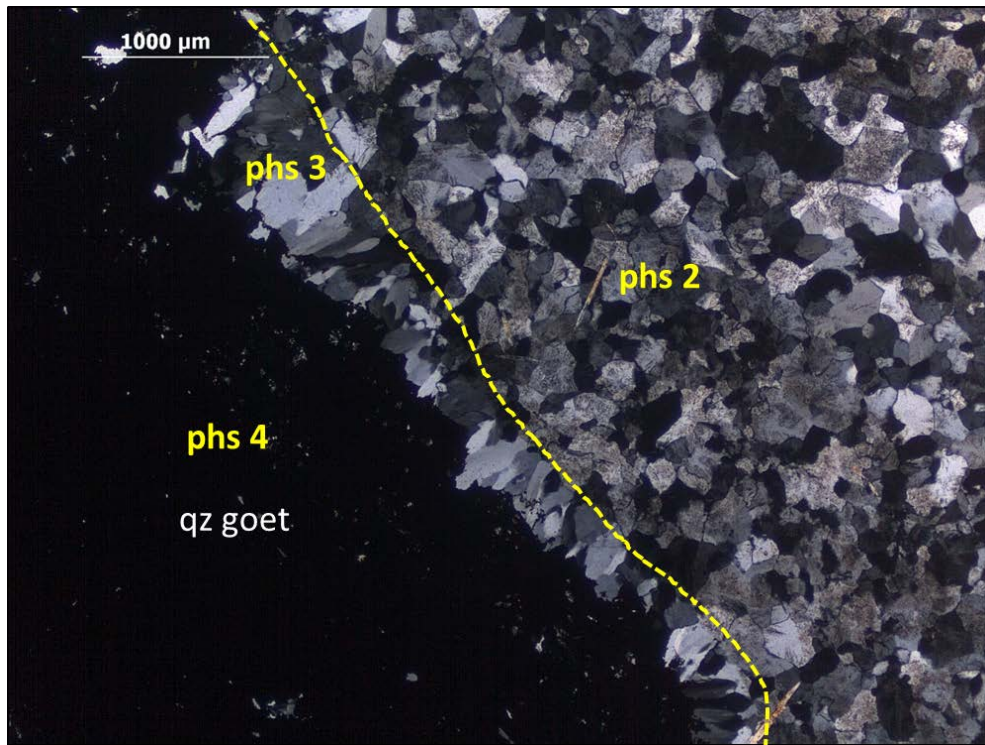
**Figure 5.23.** Quartz goethite (qz goet) (phase 4) cementing earlier phases phase 2 and 3 quartz (Crossed polars image from KK1H14-D).
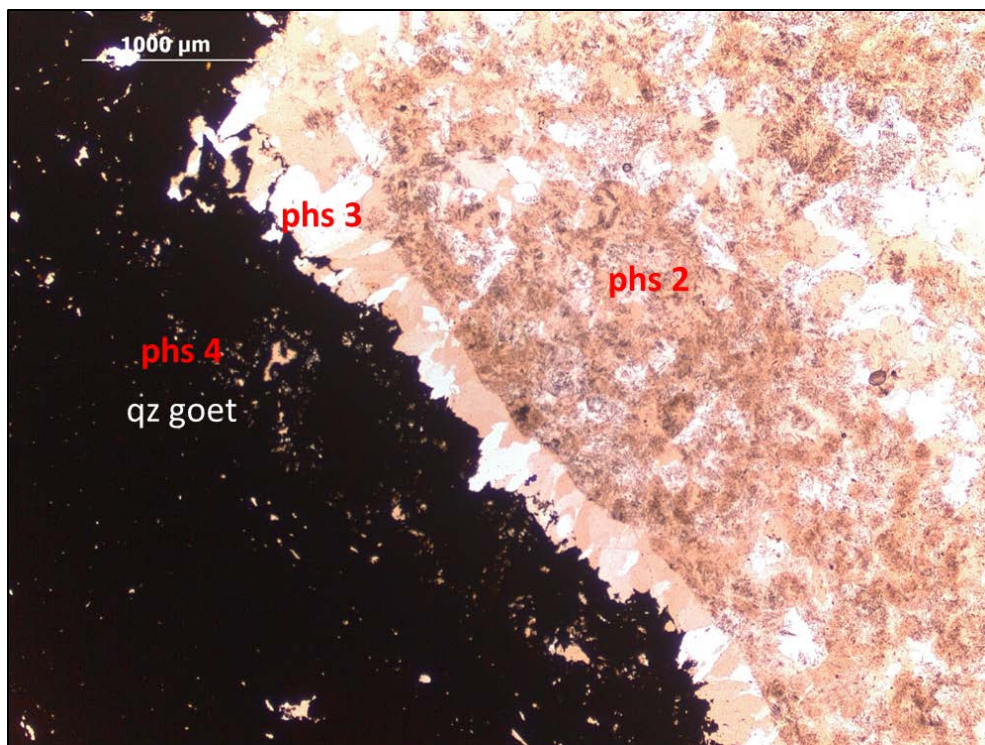


**Figure 5.24.** Quartz goethite (qz goet) (phase 4) cementing earlier phases phase 2 and 3 quartz (Plane polarized light image from KK1H14-D).

From both field and microscope observations the textures of KK1 vein do not vary with depth (from 340m asl to 250.8 m asl) (Figure 5.17-18). There is no specific level defined by the different mineralization phases, and all phases together can be seen at any levels of the vein (Figure 5.17-18). However, the youngest mineralization phase (phase 4) quartz goethite is more dominant at the margins of the vein and at the upper levels (330 m asl) of the vein (Figure 5.16, 5.18 and Table 5.3).
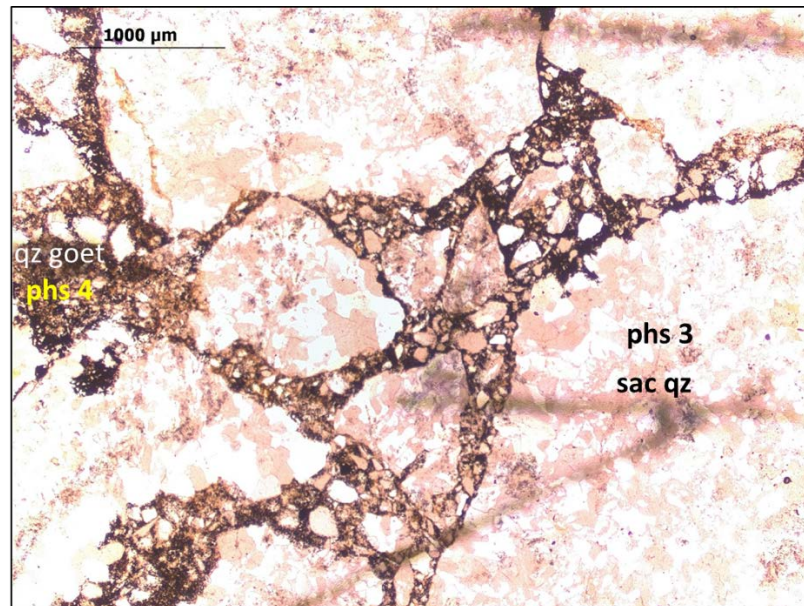


**Figure 5.25.** Hydrothermal mosaic breccia with angular to sub-rounded phase 3 saccharoidal quartz (sac qz) clasts cemented by phase 4 quartz goethite (qz goet) (Plane polarized light image from KK1D2).

In thin section KK1D2 from a drillcore sample close to the vein- hangingwall rock contact, hydrothermal breccia with jigsaw puzzle fit clasts was observed. This cement supported breccia has angular to sub-rounded poorly sorted clasts of phase 3 saccharoidal quartz cemented by phase 4 quartz goethite (Figure 5.25).

In thin section KK1H14-C made from a hand specimen taken from the vein outcrop, synchronous phase 3 saccharoidal and pseudobladed quartz crystals are invading through the wall rock mica schist clasts and silicifying them (Figure 5.26).

In thin section KK1H17, a comb saccharoidal quartz veinlet formed during phase 3 mineralization event is cutting a foliation-parallel silicified schist clast

(Figure 5.27) indicating that the foliation parallel hydrothermal silicification is older than the phase 3 silicification event.
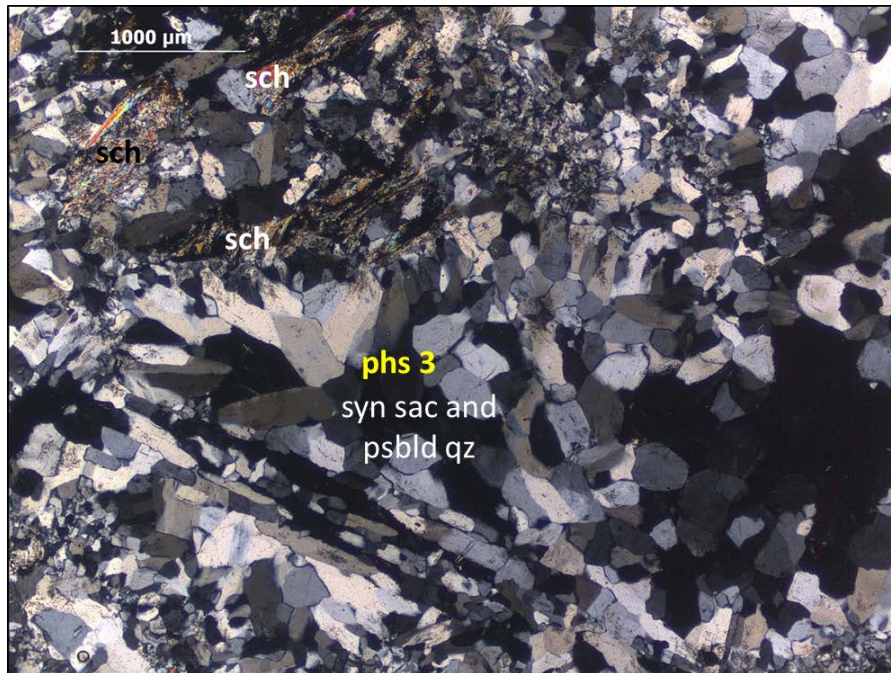


**Figure 5.26.** Synchronous saccharoidal and pseudobladed quartz (psbld qz, phase 3) replacing mica schist (sch) (Crossed polars image from KK1H14-C).
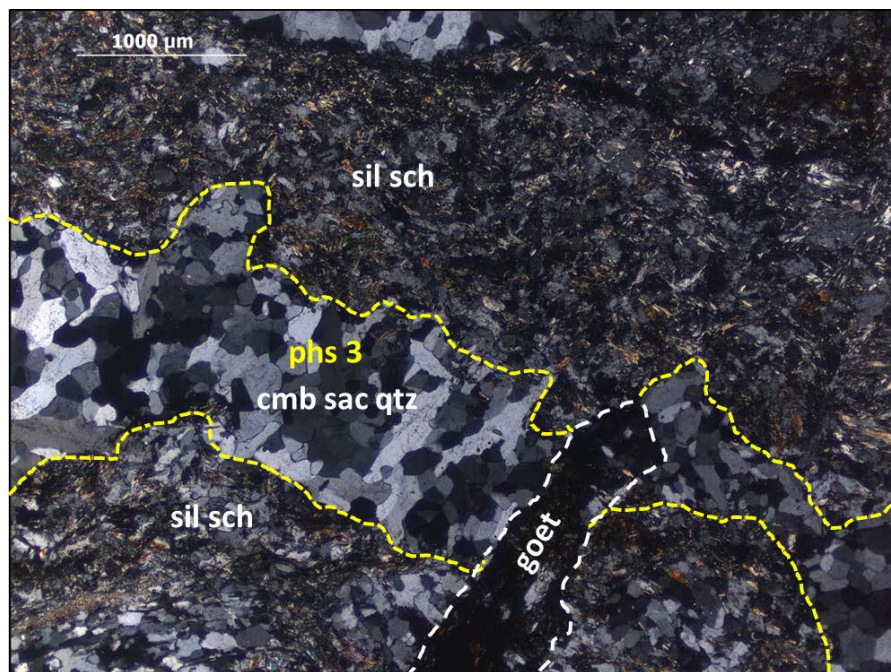


**Figure 5.27.** Comb form of phase 3 saccharoidal quartz (cmb sac qtz) cutting foliation-parallel silicified schist (sil sch) (Crossed polars image from KK1H7).

### 5.2.3. KK2 Vein

KK2 vein has an intermittent outcrop which extends for 185 m, and 24 m elevation difference exists between the tips of the vein outcrop. The most prominent textural feature of the vein outcrop is ubiquitous pseudobladed quartz generally in the form of lattice bladed texture (Figure 5.28a). Although saccharoidal quartz is also common throughout the vein surface (Figure 5.28b), lattice bladed texture predominates over it.
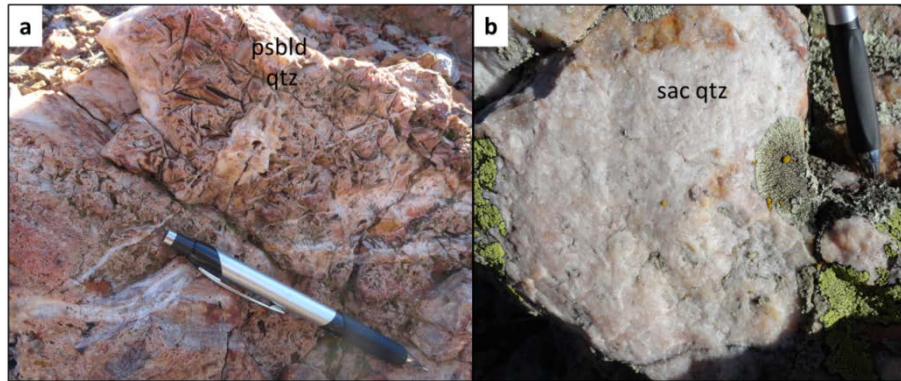


**Figure 5.28.(a)** Pseudobladed quartz (psbld qtz) in the form of lattice bladed texture observed on the vein outcrop (338 m asl). **(b)** Saccharoidal quartz (sac qtz) texture on the vein outcrop (336 m asl).



**Figure 5.29.** Cement supported breccias with clasts of earlier brecciated vein infill containing wall rock schist clasts (wr) surrounded by saccharoidal (sac qtz) and pseudobladed quartz (psbld qz) cemented by quartz-iron oxide close to the HW margin of the KK2 vein (338 m asl).

Adjacent to the margins of the vein, poorly sorted, sub-angular to sub-rounded wall rock schist clasts are surrounded by either pseudobladed or saccharoidal quartz, and form the clasts of cement supported breccias cemented by quartz-iron oxide (Figure 5.29). These breccias having the clasts of brecciated vein infill have cement ratio which is less than 50% of the rock volume.

In the core of the vein, crackle (jigsaw-fit) breccias with clasts of either saccharoidal or probably synchronous saccharoidal and pseudobladed quartz are cemented by quartz-iron oxide. Poorly- to well-sorted clasts are angular to sub-angular, and the cement is less than ~20 % of the rock volume (Figure 5.30).
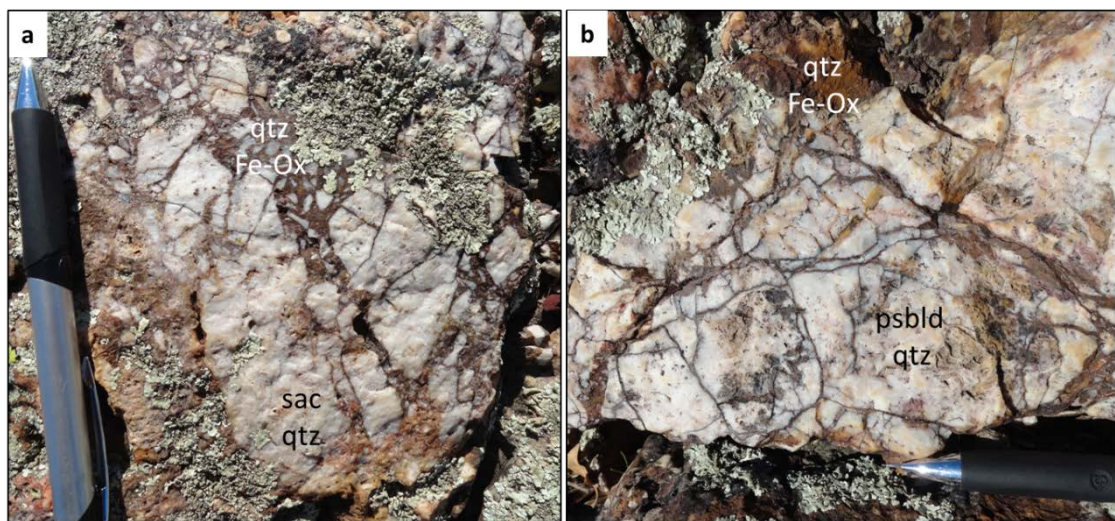


**Figure 5.30.(a)** Crackle breccia with clasts of saccharoidal quartz (sac qtz) and quartz-iron oxide (qtz-Fe-Ox) cement (334 m asl). **(b)** Crackle breccia with clasts of synchronous(?) saccharoidal (sac qtz) and pseudobladed quartz (psbld qtz) cemented by quartz-iron oxide (qtz Fe-Ox) (332 m asl).

Chaotic breccias, comprising previous poorly sorted clasts, angular to sub-angular vein phase clasts of either saccharoidal (Figure 5.30a) or pseudobladed quartz (Figure 5.30b), cemented by quartz-iron oxide were also observed both in the centre and close to the margins of the vein. In these cement supported breccias, cement ratio is always less than 50% (Figure 5.31).

**Figure 5.31.** Chaotic breccias characterized by clasts of saccharoidal (sac qtz) and pseudobladed quartz (psbld qtz) plus a cement of quartz-iron oxide (qtz-Fe-Ox) (339 m asl).

Vein textures and breccias were also studied in the drill cores given in Figure 5.32 and Table 5.4. Observed quartz textures are saccharoidal and pseudobladed matching the surface observations (Figure 5.32). Breccias are also similar to the surface observations, and have clasts of previous vein phases cemented by synchronous silicification and quartz-iron oxide deposition which also replaces the crystals of earlier phase lattice bladed quartz partially and forming the ghost bladed texture.

Macroscopic examination of textures and breccias of the KK2 vein (from 350m asl to 272.4 m asl) has defined 3 phases (at least) of brecciation and subsequent mineralization. From oldest to the youngest, these phases are associated with:

(1) Cryptocrystalline quartz,

(2) Probably synchronous pseudobladed (generally in lattice bladed form) and saccharoidal quartz,

(3) Synchronous crystalline quartz-iron oxide.
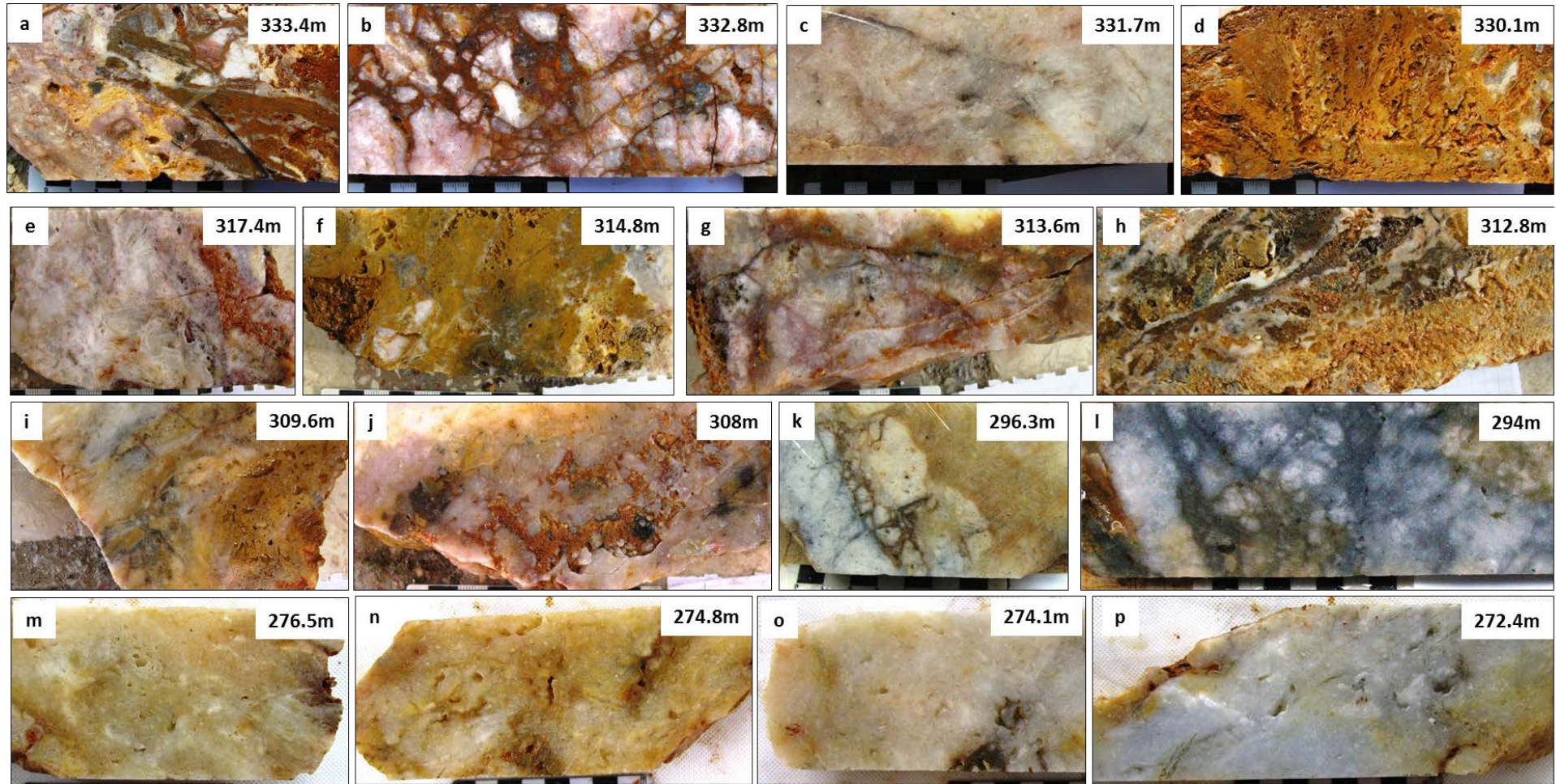
**Figure 5.32.** Textures and breccias of KK2 vein in drill cores at different levels (see Table 5.4 for their descriptions and details).

**Table 5.4**. Locations and textural descriptions of drill cores of KK2 vein and their gold grades.

| Location on Figure 5.32 | Drillhole ID | Vein at (m) | From (m) | Elevation (m asl) | Description | Au (g/t) |
|---|---|---|---|---|---|---|
| a | KED-1 | 10-14 | 10.9 | 333.4 | Crackle breccia with ghost bladed quartz-iron oxide cementing clasts of earlier breccia of synchronous(?) saccharoidal and lattice bladed quartz cementing white cryptocrystalline quartz | 2.69 |
| b | KED-1 | 10-14 | 11.6 | 332.8 | Crackle breccia with quartz-iron oxide cementing the clasts of earlier breccia of saccharoidal quartz cementing white cryptocrystalline quartz | 1.65 |
| c | KED-1 | 10-14 | 12.7 | 331.7 | Synchronous saccharoidal and lattice bladed quartz with possible sulphide clouds | 3.12 |
| d | KED-1 | 10-14 | 13.6 | 330.1 | Ghost bladed quartz-iron oxide replacing synchronous(?) lattice bladed and saccharoidal quartz | 2.49 |
| e | KED-9 | 5.5-16.9 | 7.8 | 317.4 | Synchronous saccharoidal and pseudobladed quartz breccia cemented by crystalline quartz-iron oxide | 0.173 |
| f | KED-9 | 5.5-16.9 | 9.8 | 314.8 | Ghost bladed quartz-iron oxide cementing and replacing synchronous(?) lattice bladed and saccharoidal quartz | 1.125 |
| g | KED-9 | 5.5-16.9 | 10.7 | 313.6 | Synchronous saccharoidal and pseudobladed quartz crackle breccia cemented by quartz-iron oxide | 1.59 |
| h | KED-9 | 5.5-16.9 | 11.3 | 312.8 | Ghost bladed quartz-iron oxide cementing and replacing synchronous(?) lattice bladed and saccharoidal quartz | 1.59 |
| i | KED-9 | 5.5-16.9 | 13.7 | 309.6 | Quartz-iron oxide cementing and replacing the saccharoidal quartz | 0.865 |
| j | KED-9 | 5.5-16.9 | 14.9 | 308 | Mosaic breccia with clasts of saccharoidal quartz and schist cemented by crystalline quartz-iron oxide | 0.713 |

Table 5.4 continued.

| | | | | | | |
|---|---|---|---|---|---|---|
| k | KED-2 | 46.2-49.2 | 46.9 | 296.3 | Crackle breccia of synchronous(?), biotite bearing(?) from the wall rock schist saccharoidal and pseudobladed quartz with quartz-iron oxide cement | 6.36 |
| l | KED-2 | 46.2-49.2 | 49.2 | 294 | Crackle to mosaic breccia with clasts of saccharoidal quartz cemented by gray sulphide bearing(?) microcrystalline quartz | 2.23 |
| m | KED-110 | 75.1-84.8 | 78.3 | 276.5 | Saccharoidal vuggy quartz with quartz-iron oxide partially filling the vugs | 0.091 |
| n | KED-110 | 75.1-84.8 | 80.3 | 274.8 | Saccharoidal vuggy quartz partially filled by quartz-iron oxide in vugs | 0.131 |
| o | KED-110 | 75.1-84.8 | 81.1 | 274.1 | Synchronous saccharoidal and lattice bladed vuggy quartz with sulphide clouds(?) partially filled by quartz-iron oxide especially in vugs | 0.039 |
| P | KED-110 | 75.1-84.8 | 83.2 | 272.4 | Saccharoidal vuggy quartz with sulphide clouds(?) and quartz-iron oxide filling the vugs partially | 0.012 |

## 5.2.4. K1 Vein

NE-SW trending K1 vein extends intermittently over 240 m, with 35 m elevation difference between the tips of the vein outcrop. Limited observations were made from the steep vein outcrops since access to the vein is very dangerous (Figure 5.33), and excess vegetation and weathering obscures the vein surface.

At the surface, saccharoidal quartz cements a cement supported breccia with angular wall rock schist clasts close to the HW margin (Figure 5.34a). In addition, probably synchronous saccharoidal and pseudobladed quartz (lattice bladed?) are found throughout the vein outcrop (Figure 5.34b).



**Figure 5.33.** A view from the K1 vein outcrop located on a steep slope.

Texture and breccia characteristics of the vein were also examined in drill cores (Figure 5.35 and Table 5.5). Saccharoidal and pseudobladed quartz textures are common matching the vein outcrop. Breccias are characterized by the clasts of synchronously brecciated earlier vein phases and wall rock schist cemented by later silicification, sometimes with synchronous iron-oxide deposition (Figure 5.35).
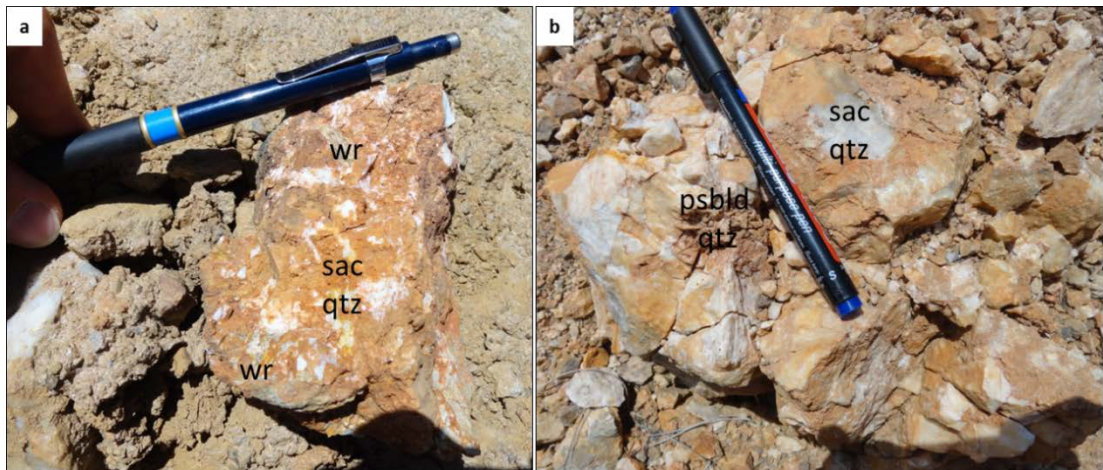
**Figure 5.34.** Textures and breccias observed on the surface of the K1 vein: **(a)** Cement supported breccia of wall rock schist cemented by saccharoidal quartz. **(b)** Probably synchronous saccharoidal and pseudobladed quartz (284 m asl).
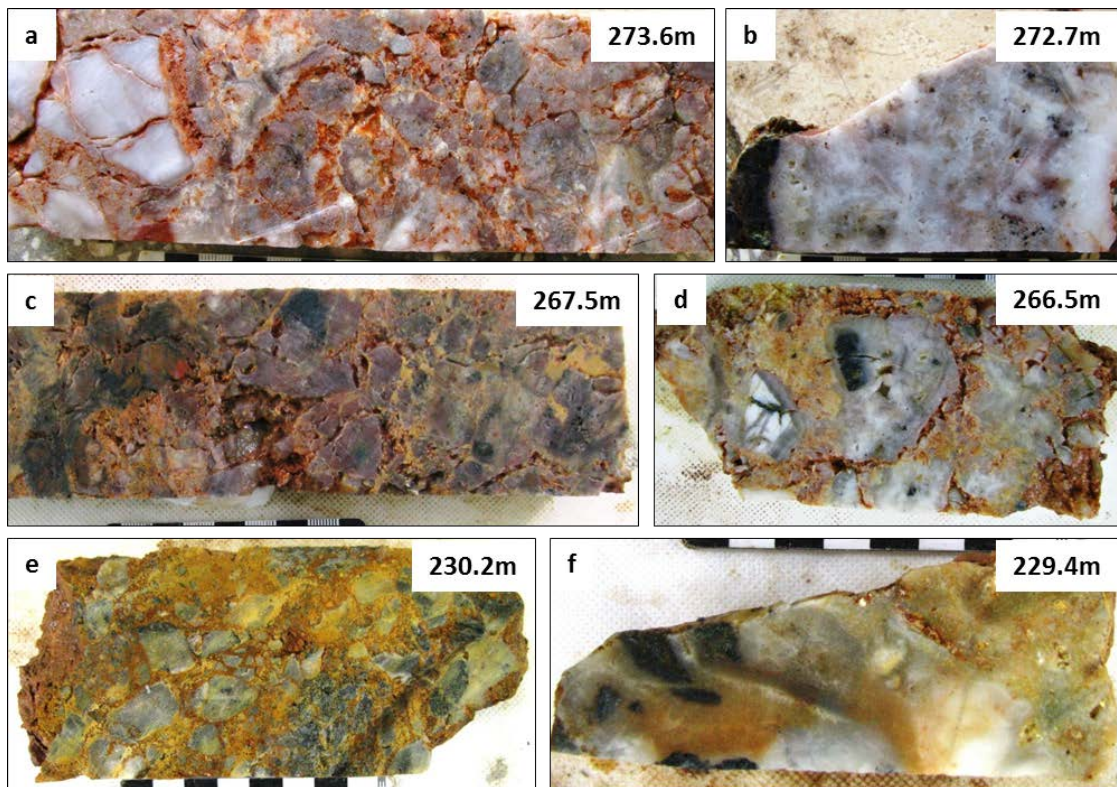


**Figure 5.35.** Textures and breccias of K1 vein in drill cores at different levels (see Table 5.5 for their descriptions and details).

Textures and breccias of the K1 vein (from 290 m asl to 229.4 m asl) define 3 phases (at least) of brecciation and subsequent fluid flow and mineralization. From oldest to the youngest, these phases are represented by:

(1) White cryptocrystalline quartz,

(2) Probably synchronous pseudobladed (generally lattice bladed) and saccharoidal (sometimes vuggy) quartz,

(3) Synchronous crystalline quartz-iron oxide.

## 5.2.5. K2 Vein

The E-W trending K2 vein has synchronous saccharoidal and less commonly lattice bladed quartz textures but no breccia (Figure 5.36).
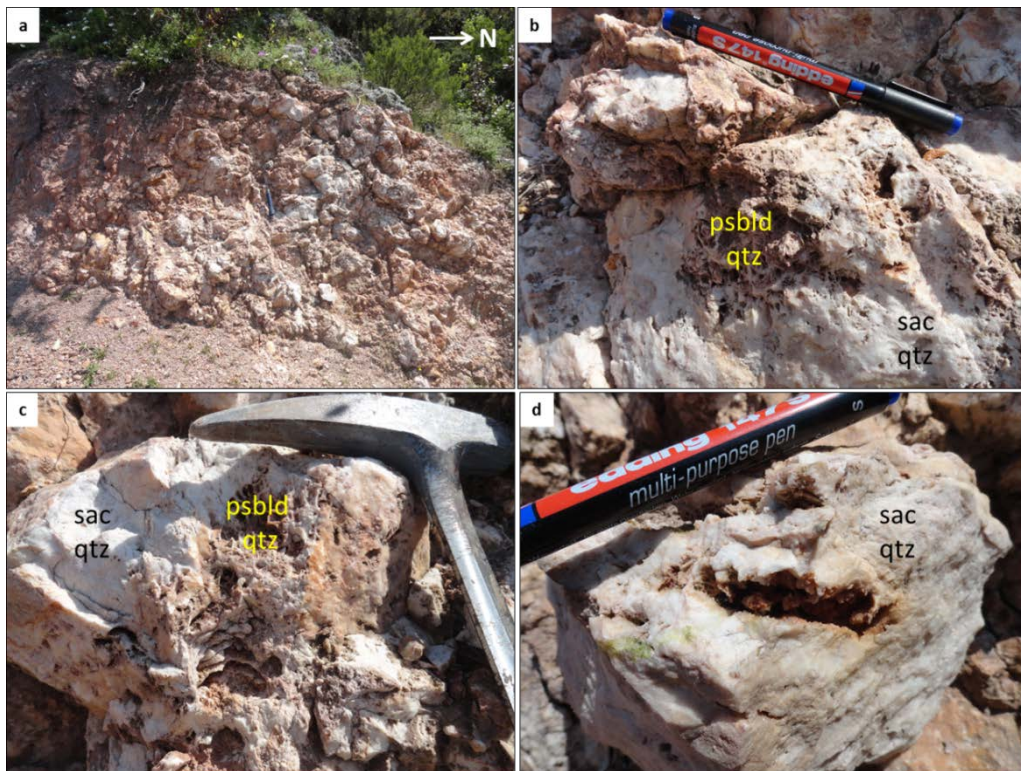


**Figure 5. 36. (a)** K2 vein outcrop. **(b)** and **(c)** Synchronous(?) saccharoidal vuggy and pseudobladed (lattice bladed) quartz. **(d)** Saccharoidal vuggy quartz (299 m asl).

In drill core samples (Figure 5.37), microcrystalline quartz and banded quartz are seen in addition to saccharoidal and lattice bladed quartz. Saccharoidal, lattice bladed and microcrystalline quartz textures are synchronous and sometimes form the bands of the banded texture. Table 5.6 gives the locations and textural descriptions of drill cores of the vein together with the related gold grades.

**Table 5.5.** Locations and textural descriptions of drill cores of K1 vein and their gold grades.

| Location on Figure 5.37 | Drillhole ID | Vein at (m) | From (m) | Elevation (m asl) | Description | Au (g/t) |
|---|---|---|---|---|---|---|
| a | KED-5 | 34.5-37.7 | 35.4 | 273.6 | Crackle to mosaic breccia of sulphide bearing (?) cryptocrystalline quartz plus a cement of quartz-iron oxide | 3.75 |
| b | KED-5 | 34.5-37.7 | 36.45 | 272.7 | Synchronous(?) lattice bladed and saccharoidal quartz with fragments of wall rock schist | 1.275 |
| c | KED-60 | 34.7-36 | 35 | 267.5 | Crackle to mosaic breccia with clasts of sulphide bearing (?) saccharoidal vuggy quartz cemented by quartz-iron oxide. Some fractures are stained and filled by clay minerals after brecciation | 0.782 |
| d | KED-60 | 34.7-36 | 36 | 266.5 | Mosaic to chaotic breccia with quartz-iron oxide cement cementing the clasts of earlier vein phases; phase 1 white cryptocrystalline quartz cementing the clasts of wall rock schist, and phase 2 saccharoidal vuggy quartz cementing the clasts of phase 1 and wall rock schist | 1.02 |
| e | KED-105 | 76.9-78.7 | 77.3 | 230.2 | Chaotic breccia with quartz-iron oxide cementing the clasts of wall rock schist and earlier phase saccharoidal quartz cementing schist clasts | 0.86 |
| f | KED-105 | 76.9-78.7 | 78.2 | 229.4 | Crackle to mosaic breccia with a cement of saccharoidal vuggy quartz including quartz-iron oxide and clay mineral(?) in some vugs, cementing the clasts of white cryptocrystalline quartz and wall rock schist | 0.504 |
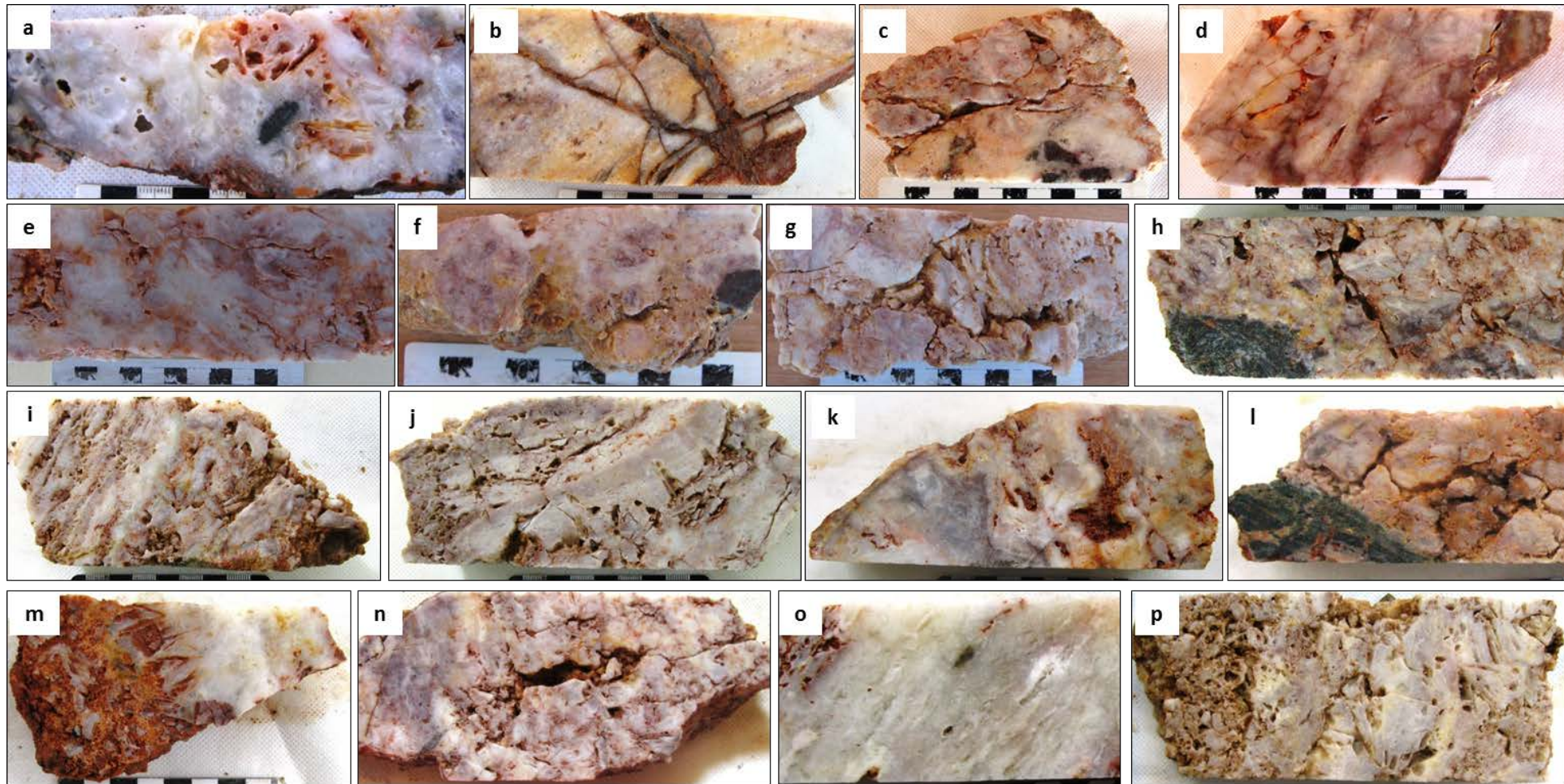
**Figure 5.37.** Textures and breccias of K2 vein in drill cores at different levels (see Table 5.6 for their descriptions and details).

**Table 5.6.** Locations and textural descriptions of drill cores of K2 vein and their gold grades. The table does not include elevation values, because the present elevation information for the drill cores is not reliable.

| Location on Figure 5.37 | Drillhole ID | Vein at (m) | From (m) | Description | Au (g/t) |
|---|---|---|---|---|---|
| a | KED-25 | 30.5-33.9 | 30.8 | Synchronous vuggy saccharoidal and lattice bladed quartz cementing the clasts and fragments of wall rock schist. Some vugs are partially filled by iron oxide mineral(s) | 0.867 |
| b | KED-25 | 30.5-33.9 | 32.6 | Crackle breccia with clasts of vuggy saccharoidal quartz cemented by quartz-iron oxide | 1.87 |
| c | KED-46 | 2-5.9 | 2.3 | Brecciated synchronous vuggy saccharoidal,lattice bladed and microcrystalline quartz cementing the clasts of wall rock schist. Brecciation post dates the mineralization and fractures are partially filled by iron oxide mineral(s) | 4.84 |
| d | KED-46 | 2-5.9 | 4.8 | Crackle to mosaic breccia with clasts of synchronous saccharoidal and microcrystalline quartz. There are some fractures and vugs postdating the mineralization which are partially stained and filled by iron oxide minerals | 8.98 |
| e | KED-47 | 2.5-5.5 | 3.2 | Brecciated synchronous vuggy saccharoidal and microcrystalline quartz. Brecciation post dates the mineralization, and fractures and vugs are stained and partially filled by iron oxide mineral(s) | 2.72 |
| f | KED-48 | 2.9-6.5 | 3.9 | Synchronous vuggy saccharoidal and microcrystalline quartz cementing a clast of wall rock schist. Some vugs are stained by iron oxide mineral(s) | 12.75 |
| g | KED-48 | 2.9-6.5 | 4.6 | Brecciated synchronous vuggy saccharoidal,lattice bladed and microcrystalline quartz. Brecciation post dates the mineralization and fractures and some vugs are stained by iron oxide mineral(s) | 5.13 |

Table 5.6 continued.

| | | | | | |
|---|---|---|---|---|---|
| h | KED-63 | 1.5-2.7 | 2 | Brecciated partly banded synchronous vuggy saccharoidal and microcrystalline quartz cementing a clast of wall rock schist. Brecciation post dates the mineralization, and fractures and vugs are stained and partially filled by iron oxide mineral(s) | 41 |
| i | KED-63 | 3.1-5.2 | 3.9 | Partly banded synchronous vuggy saccharoidal and microcrystalline quartz. Vugs are partially stained by iron oxide mineral(s) | 9.1 |
| j | KED-63 | 3.1-5.2 | 4.6 | Partly banded synchronous vuggy saccharoidal, lattice bladed and microcrystalline quartz. Vugs are partially stained by iron oxide mineral(s) | 31.4 |
| k | KED-65 | 5.5-8.5 | 6.7 | Synchronous vuggy saccharoidal and microcrystalline quartz. Vugs are stained and partially filled by iron oxide mineral(s) | 39 |
| l | KED-65 | 5.5-8.5 | 7.2 | Fractured partly banded synchronous and saccharoidal and microcrystalline quartz cementing a clast of wall rock schist. Fractures and some vugs are stained by iron oxide mineral(s) | 11.75 |
| m | KED-101 | 24.6-25.8 | 24.7 | Synchronous vuggy saccharoidal, lattice bladed and microcrystalline quartz. Some parts of saccharoidal quartz seem to be leached and partly filled by iron-oxide mineral(s) | 0.908 |
| n | KED-154 | 5.8-7.1 | 6.3 | Partly banded synchronous vuggy saccharoidal, lattice bladed and microcrsystalline quartz. Some vugs are partly stained by iron oxide mineral(s) | 11.95 |
| o | KED-158 | 3.9-5.4 | 5.1 | Partly banded synchronous vuggy saccharoidal and microcrystalline quartz cementing the fragments of wall rock schist. Some vugs are stained by iron oxide mineral(s) | 5.92 |
| P | KED-161 | 11.6-16 | 15.3 | Synchronous lattice bladed and vuggy saccharoidal quartz . Some vugs seem leached and stained by iron oxide mineral(s) | 5.39 |

Most remarkable feature of the K2 vein is brecciation postdating the mineralization which has allowed post-mineralization (supergene) oxidation process and leaching of some parts of the vein, especially saccharoidal quartz. This oxidation event not only caused the deposition of iron oxide mineral(s) along fractures and in vugs, but also caused supergene gold enrichment, evidenced by petrographic analysis of drill core sample (KED-4 21m). The sample contains cavities within the saccharoidal quartz and gold flakes are observed within them infilled by goethite (Figure 5.38).



**Figure 5.38.** Native gold flakes within cavities infilled by goethite (see yellow circles) using reflected light microscopy (taken from Kuşcu, 2013).

Two phases (at least) of brecciation and subsequent fluid flow and mineralization were determined from textures and breccias of the K2 vein. From oldest to the youngest, these phases are represented by:

(1) Probably synchronous vuggy saccharoidal, microcrystalline and lattice bladed quartz,
(2) Microcrystalline quartz iron-oxide.

### 5.2.6. K3 Vein

K3 vein outcrop has 2 segments extending over 510 m. Textural observations were made wherever intense weathering and vegetation allowed.

The vein is completely brecciated from the top (363 m asl) to the level 280 m asl by crackle to chaotic breccias with clasts showing different quartz textures from the previous vein phase(s) cemented by quartz-iron oxide. Clasts have occasionally banded crypto- to microcrystalline (Figure 5.39), lattice bladed (Figure 5.40a) and vuggy saccharoidal (Figure 5.40b) quartz textures. The breccia is clast to cement supported and has poorly sorted angular to subrounded clasts (Figure 5.39 and 5.40).
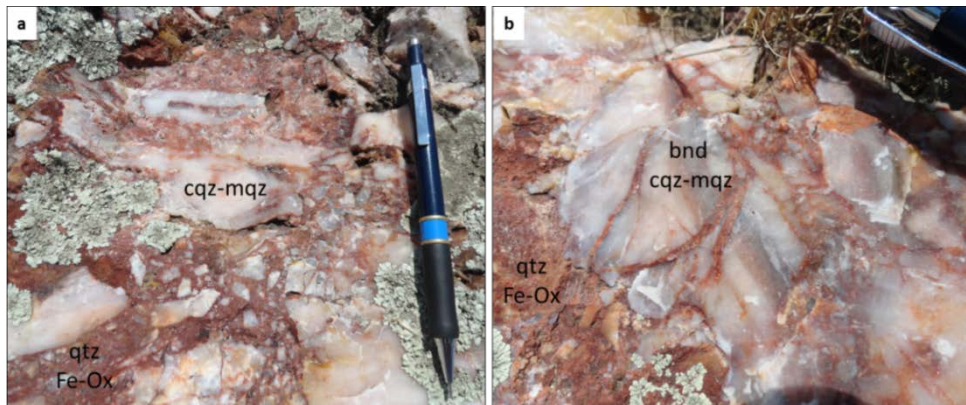


**Figure 5.39.(a)** Mosaic to chaotic breccia of crypto-to microcrystalline quartz with quartz-iron oxide cement. **(b)** Crackle breccia with banded crypto-to microcrystalline quartz (bnd cqz-mqz) clasts cemented by quartz-iron oxide (328 m asl).
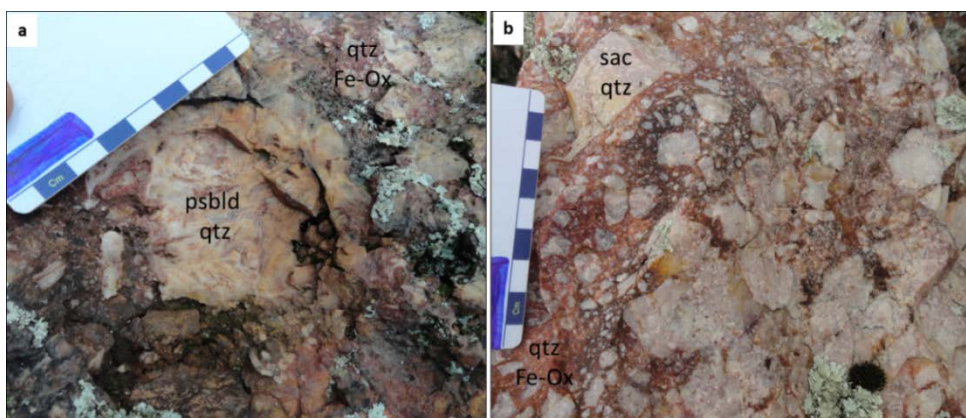


**Figure 5.40.** Crackle to chaotic breccias with clasts of **(a)** pseudobladed (psbld qtz) and **(b)** saccharoidal quartz (sac qtz) plus a cement of quartz-iron oxide (316 m asl).

Below 280m asl, these breccias may just exist at the footwall margin on the outcrop as ~10 cm-1 m thick bodies. At these parts, except the brecciated section at the FW margin, the vein is seen as a big body of intensely fractured and weathered quartz (Figure 5.41). Quartz textures observed here include vuggy saccharoidal (Figure 5.42a) and lattice bladed (Figure 5.42b).



**Figure 5.41.** A view of the fractured and weathered outcrop of the K3 vein (278 m asl).
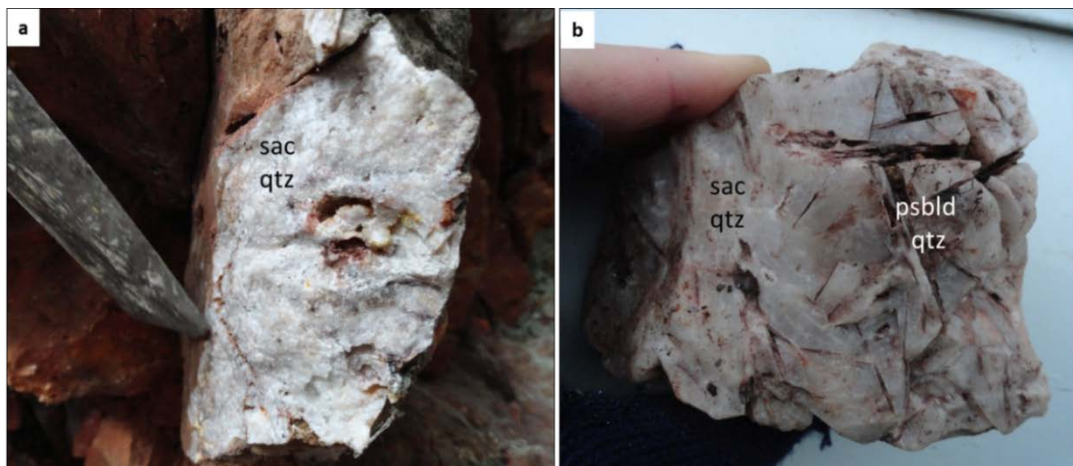


**Figure 5.42.** Textures observed on the surface of the K3 vein: **(a)** Vuggy saccharoidal quartz. **(b)** Probably synchronous saccharoidal and pseudobladed (lattice bladed) quartz.

Breccias were also observed in drillcores (Figure 5.43). Crackle to chaotic breccias include clasts from earlier vein phase(s) with saccharoidal, pseudobladed and occasionally banded crypto-to microcrystalline quartz textures (Figure 5.43).

Breccias with iron-oxide bearing quartz cement are syn-mineralization, whereas post-mineralization breccias lack cementation and contain fractures stained and/or partially filled by iron-oxide mineral(s).

A drillcore sample from KED-159 228.4m (Figure 5.43k) has a cement of black sulphide bearing (?) quartz instead of red iron oxide bearing quartz cement seen in other cores (e.g. Figure 5.43b). This may indicate that this sample (183.4m asl) comes from the unoxidized level where mixing related oxidation did not take place and sulphide was not oxidized to form an iron-oxide mineral.

Thirty-one thin sections of the K3 vein were studied in total; 20 from fourteen hand specimens taken from the different elevations of the vein outcrop (K3H1-14) and 11 from five drill core samples (Figure 5.44 and Table 5.8).

<u>2 mineralization phases</u> were defined and from oldest to the youngest, these are: (1) altered synchronous occasionally banded crypto-micro-crystalline (predominant)-saccharoidal and lattice bladed quartz (Figure 5.45-52), (2) occasionally banded crypto-microcrystalline quartz ± hematite and/or goethite (Figure 5.50-53).
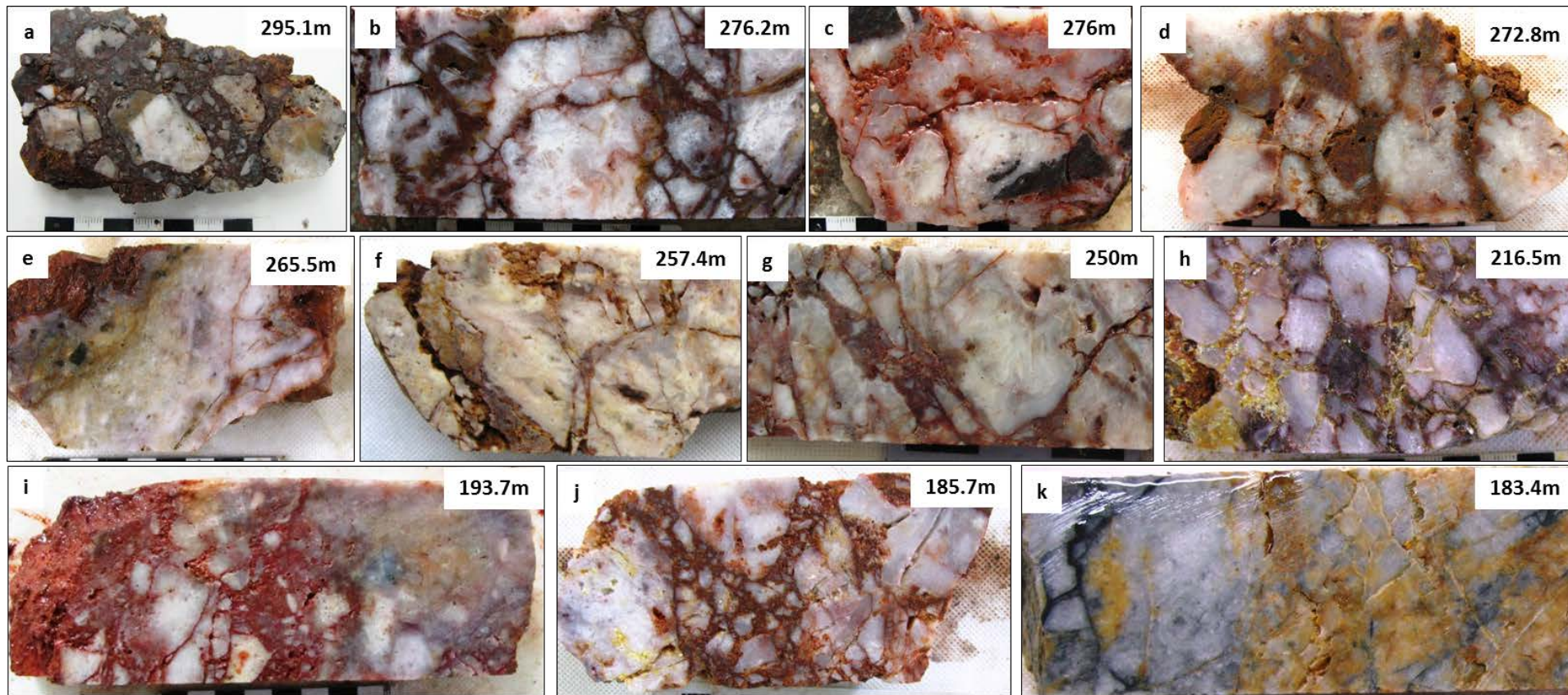
**Figure 5.43.** Textures and breccias of K3 vein in drill cores at different levels (see Table 5.7 for their descriptions and details).

**Table 5.7.** Locations and textural descriptions of drill cores of K3 vein and their gold grades

| Location on Figure 5.43 | Drillhole ID | Vein at (m) | From (m) | Elevation (m asl) | Description | Au (g/t) |
|---|---|---|---|---|---|---|
| a | KED-20 | 28.3-31.5 | 28.4 | 295.1 | Chaotic breccia with synchronous(?) crypto-microcrystalline and vuggy saccharoidal quartz clasts cemented by quartz-iron oxide cement. Some vugs are partly stained by iron-oxide minerals. | 3.3 |
| b | KED-14 | 69.5-74.5 | 70.5 | 276.2 | Crackle breccia with clasts of synchronous(?) lattice bladed and vuggy saccharoidal quartz cemented by quartz-iron oxide. Quartz-iron oxide replaces lattice bladed quartz at some places and form ghost bladed texture. | 2.36 |
| c | KED-14 | 69.5-74.5 | 70.8 | 276 | Brecciated synchronous(?) crypto-microcrystalline, vuggy saccharoidal and lattice bladed quartz cementing and partially silicifying wall rock schist clasts. Brecciation post dates the mineralization, and fractures and vugs are stained and partially filled by iron oxide mineral(s) | 1.23 |
| d | KED-141 | 71-73.6 | 72.7 | 272.8 | Brecciated vuggy saccharoidal quartz. Brecciation post dates the mineralization, and fractures and some vugs are stained and partially filled by iron oxide mineral(s) | 28.7 |
| e | KED-107 | 54-58.7 | 58.5 | 265.5 | Fractured synchronous(?) vuggy saccharoidal, crypto-microcrystalline and lattice bladed quartz cementing the clasts and fragments of wall rock schist. Fractures and some vugs are stained and partly filled by iron oxide mineral(s) | 2.12 |

Table 5.7 continued.

| | | | | | Brecciated synchronous(?) crypto-microcrystalline and vuggy saccharoidal quartz. Brecciation post dates the mineralization, and fractures and some vugs are partially filled by iron oxide mineral(s) | |
|---|---|---|---|---|---|---|
| f | KED-144 | 23.5-25 | 23.8 | 257.4 | Brecciated synchronous(?) crypto-microcrystalline and vuggy saccharoidal quartz. Brecciation post dates the mineralization, and fractures and some vugs are partially filled by iron oxide mineral(s) | 17.55 |
| g | KED-235 | 39.5-45 | 44 | 250 | Crackle to mosaic breccia of synchronous(?) vuggy saccharoidal, lattice bladed and partly banded crypto-microcrystalline quartz cemented by quartz-iron oxide | 2.97 |
| h | KED-97 | 63.6-67.9 | 65.4 | 216.5 | Crackle breccia of synchronous(?) crypto-microcrystalline and vuggy saccharoidal quartz plus a cement of quartz-iron oxide. Some fractures are stained by clay mineral(s) | 1.35 |
| i | KED-83 | 79.5-87.8 | 85.3 | 193.7 | Crackle to chaotic breccia of vuggy saccharoidal quartz with possible sulphide clouds(?) cemented by quartz-iron oxide | 0.885 |
| j | KED-72 | 92.3-101.3 | 93.5 | 185.7 | Crackle to mosaic breccia of synchronous(?) vuggy saccharoidal and microcrystalline quartz cemented by quartz-iron oxide. Some vugs are partially stained by iron oxide and clay mineral(s) | 1.335 |
| k | KED-159 | 227-229.4 | 228.4 | 183.4 | Fractured crackle breccia of crypto-microcrystalline quartz clasts cemented by sulphide bearing quartz. Fractures and some parts of the surface are stained by iron-oxide mineral(s) | 1.055 |

**Table 5.8.** Locations, elevations and gold grades of K3 vein thin section samples (nm: not measured).

| Sample ID | Location on the vein | Elevation (m asl) | Au (g/t) |
|---|---|---|---|
| K3H1 | HW | 280 | nm |
| K3H2 | Core | 280 | nm |
| K3H3 | Core | 280 | nm |
| K3H4 | Core | 280 | nm |
| K3H5 | Core | 280 | nm |
| K3H6 | Core | 280 | nm |
| K3H7 | Core | 280 | nm |
| K3H8 | Core | 280 | nm |
| K3H9 | Core | 280 | nm |
| K3H10 | FW | 280 | nm |
| K3H11 | Core | 310 | nm |
| K3H12 | Core | 300 | nm |
| K3H13 | Core | 295 | nm |
| K3H14 | FW | 290 | nm |
| K3D1 | HW-Core | 276.1 | 2.36 |
| K3D2 | Core | 275.6 | 1.23 |
| K3D3 | Core | 274.9 | 0.334 |
| K3D4 | Core | 237 | 4.47 |
| K3D5 | Core | 291.1 | 0.654 |
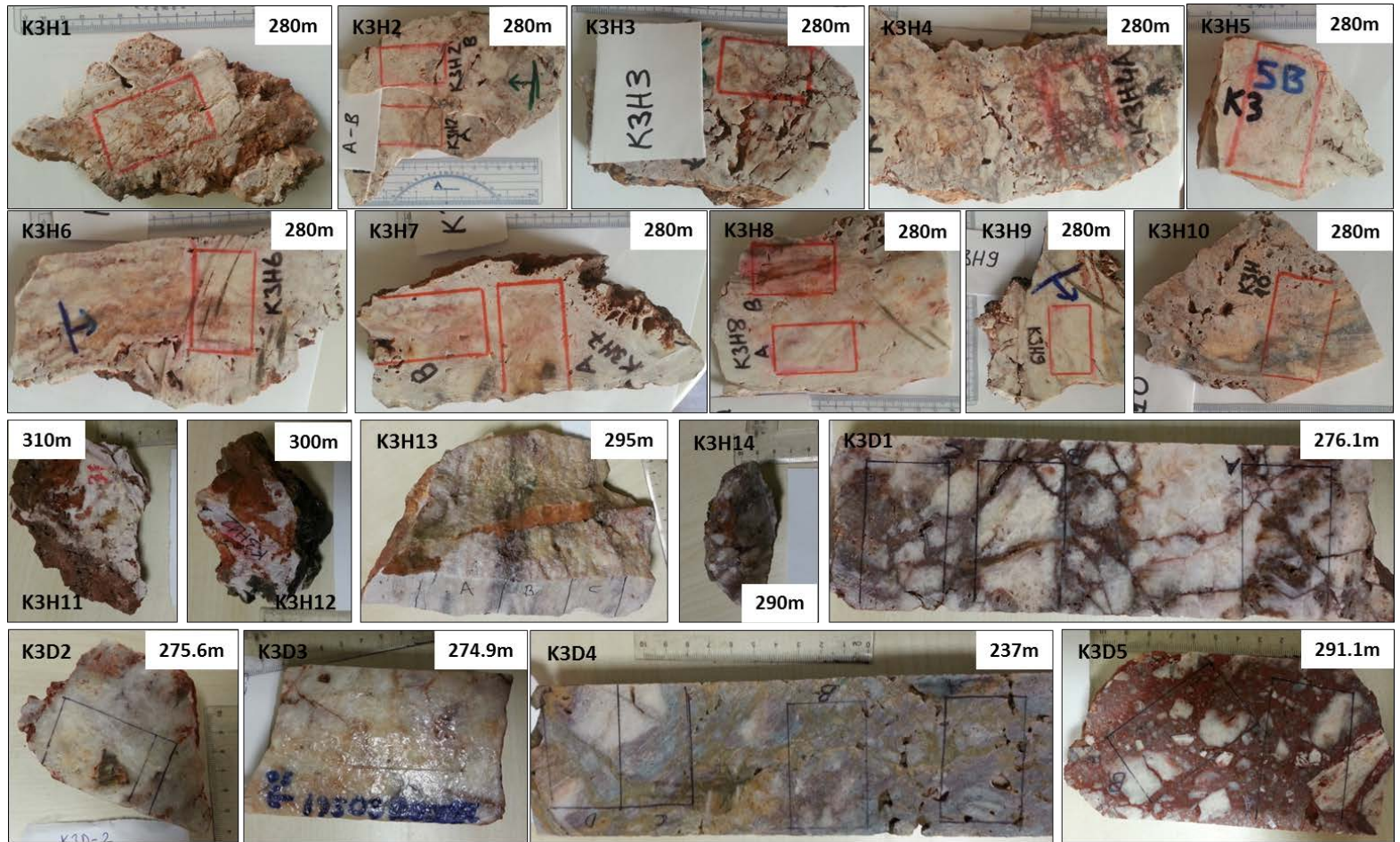
**Figure 5.44.** Thin section locations of samples taken from the K3 vein outcrop and drill cores. Note that the shorter side of rectangle seen in some pictures has a length of 2.5 cm.
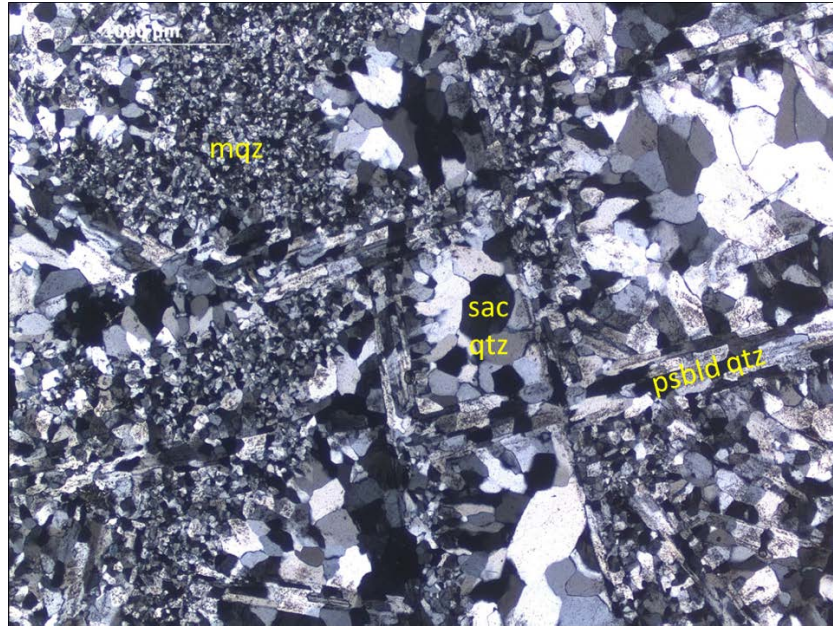
**Figure 5.45.** Altered synchronous microcrystalline (mqz) (predominant), saccharoidal (sac qtz) and lattice bladed quartz (psbld qtz.9 (phase 1) (crossed polars image from K3H5).
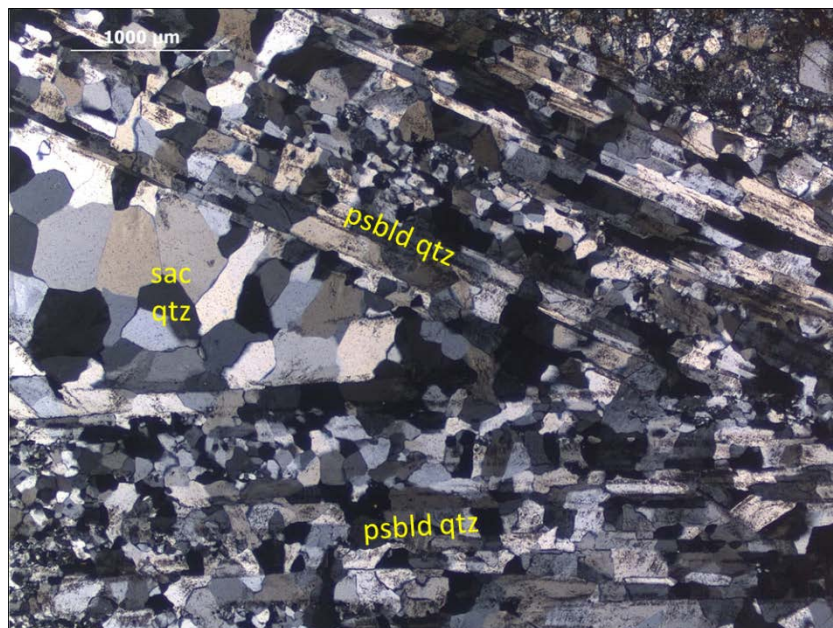


**Figure 5.46.** Altered synchronous interstitial saccharoidal (sac qtz) and lattice bladed quartz (psbld qtz) (phase 1) (crossed polars image from K3H2-A).

Close to the HW margin of the vein, altered synchronous micro-crystalline and parallel bladed quartz of phase 1 cement a clast of wall rock schist. In this

breccia, micro-crystalline quartz is also found in the foliation planes of schist indicating synchronous silicification of cement and foliation planes (Figure 5.47).

Crypto-micro-crystalline quartz and saccharoidal quartz of phase 1 sometimes show banded texture (Figure 5.48) irrespective of the level where they are found.

Crystals of saccharoidal quartz (phase 1) are zoned (Figure 5.49) at level 280m asl which points out deposition from relatively slow cooling hydrothermal solution.
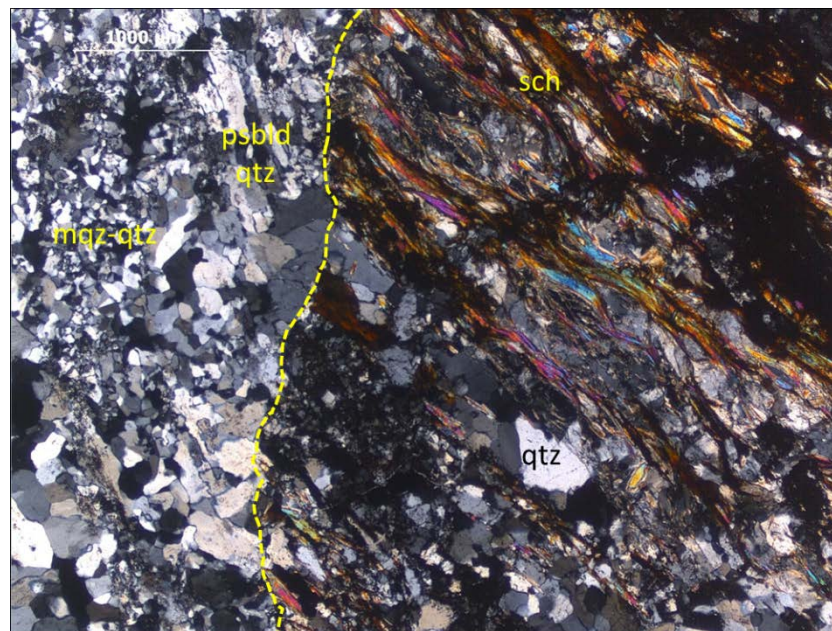


**Figure 5.47.** Altered synchronous micro-crystalline quartz (mqz) and parallel bladed quartz of phase 1 cementing a clast of wall rock schist (sch) and silicifying its foliation planes (qtz: crystalline quartz) (crossed polars image from K3D-2).

Phase 2 mineralization event is represented by somewhere banded crypto-microcrystalline quartz ± hematite and/or goethite (Figure 5.50) and seen as cementing the clasts of phase 1 quartz.

Crystal form of phase 2 quartz varies from crypto- to crystalline quartz (Figure 5.51) and where it is seen as cryptocrystalline form, it shows colloform banding (Figure 5.52).
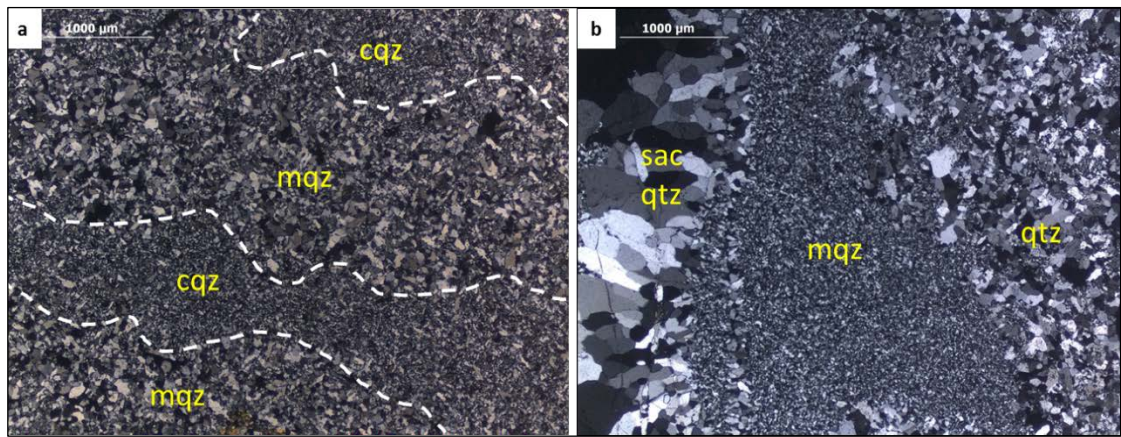
**Figure 5.48.(a)** Alternating bands of cryptocrystalline (cqz) and microcrystalline quartz (mqz) of phase 1 (crossed polars image from K3H8-A). **(b)** Banded saccharoidal (sac qtz), microcrystalline and crystalline quartz (qtz) of phase 1 (crossed polars image from K3H13-A).

At the lower levels of the vein (~230 m asl), microcrystalline quartz-hematite-goethite of phase 2 cements a clast of colloform banded quartz (phase 1?) (Figure 5.53).
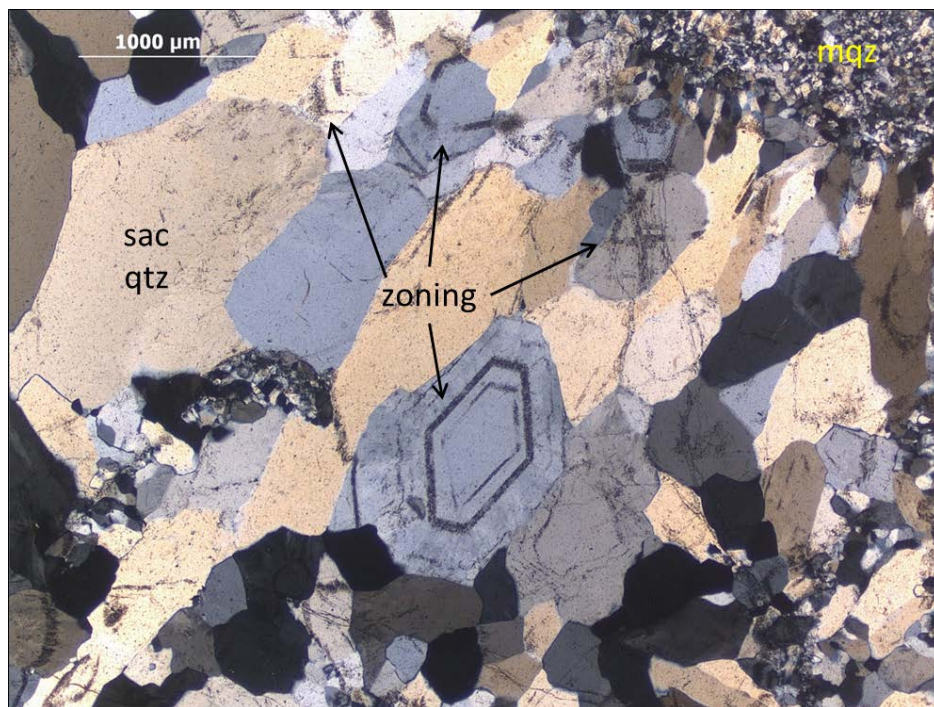


**Figure 5.49.** Zoned saccharoidal quartz (sac qtz) crystals (phase 1) (mqz: microcrystalline quartz) (crossed polars image from K3H2-B).

172
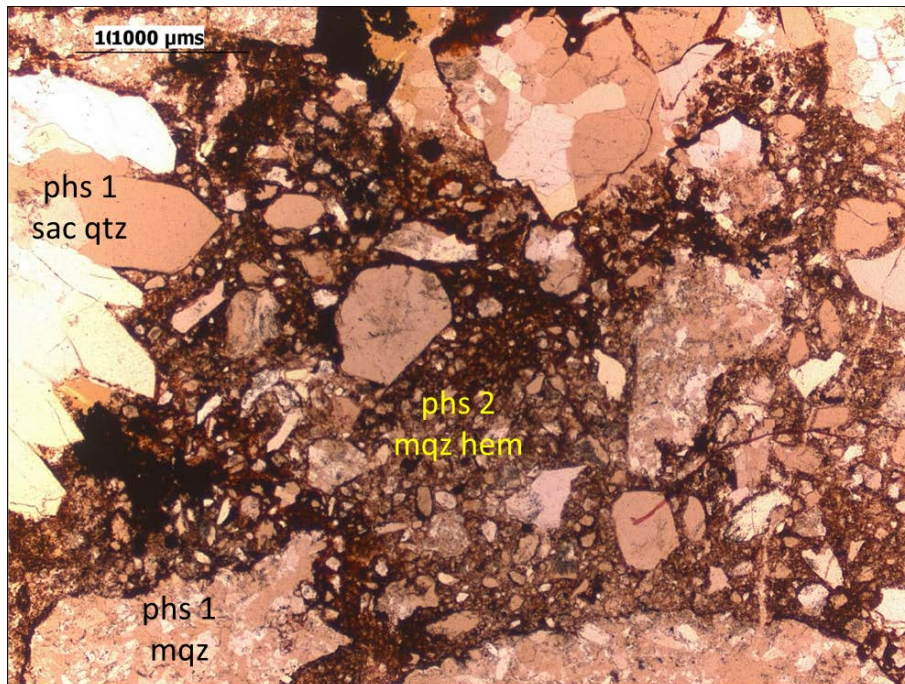
**Figure 5.50.** Cement supported breccia with clasts and grains of phase 1 saccharoidal (sac qz) and microcrystalline quartz (mqz) cemented by phase 2 microcrystalline quartz-hematite (mqz-hem) (Plane polarized light image from K3D5).
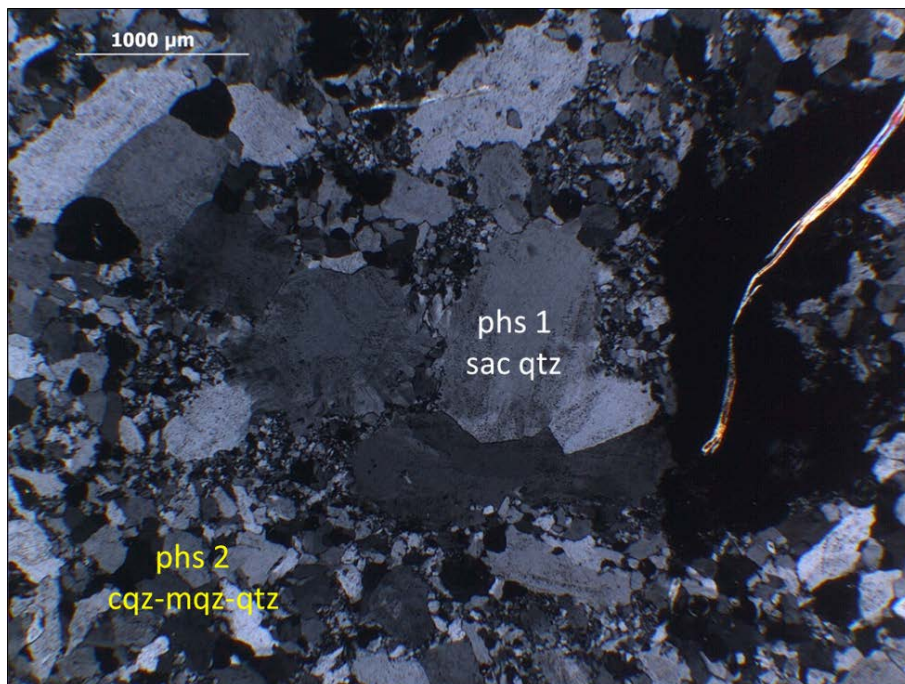


**Figure 5.51.** Crypto- to crystalline quartz (cqz-mqz-qtz) (phase 2) cementing and replacing a clast of zoned saccharoidal quartz (sac qtz) (phase 1) (crossed polars image from K3H3).
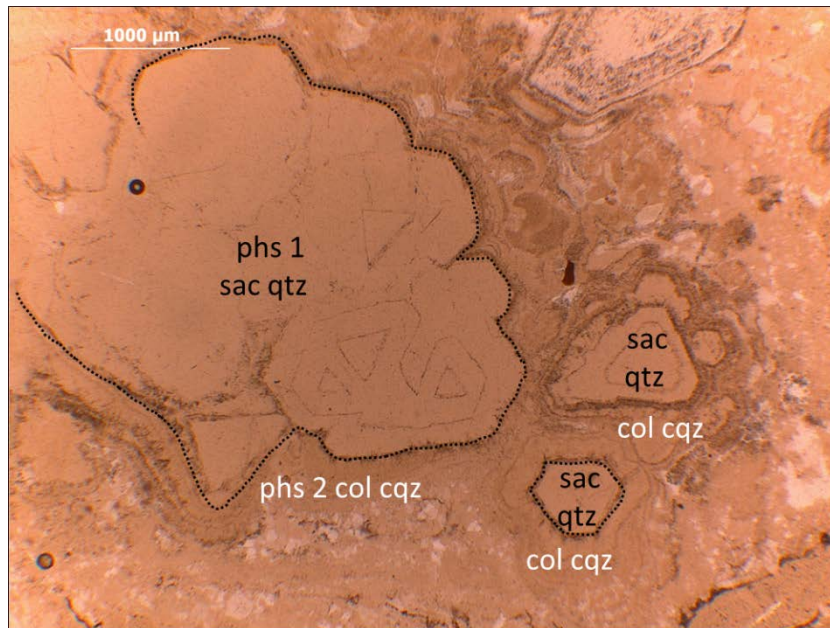
**Figure 5.52.** Colloform banded (col) cryptocrystalline qtz (cqz) (phase 2) lining euhedral saccharoidal quartz (sac qtz) crystals (phase 1) (Plane polarized light image from K3H3).
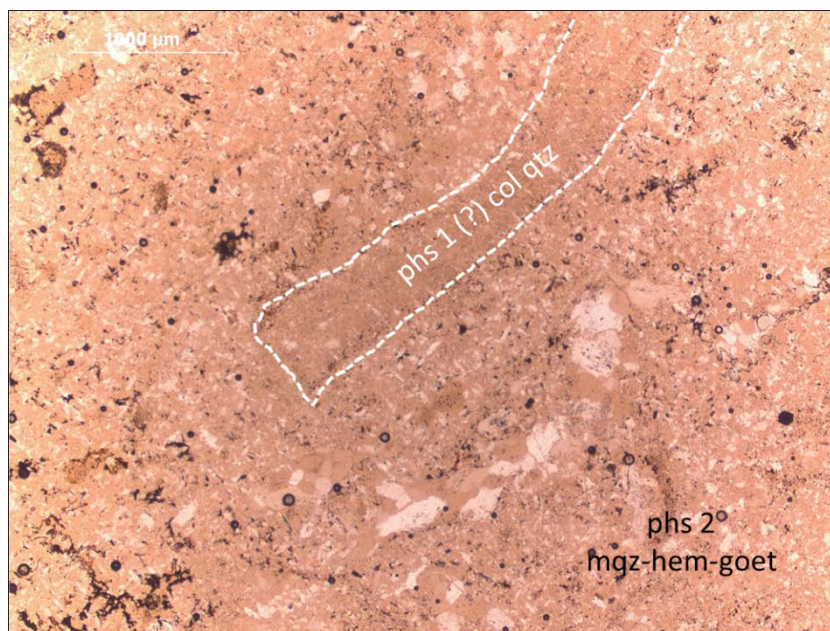


**Figure 5.53.** Microcrystalline quartz-hematite-goethite (mqz-hem-goet) of phase 2 cementing a clast of colloform banded quartz (col qtz) (phase 1?) (Plane polarized light image from K3D4).

Apart from the hypogene hematite and goethite deposited synchronously with the cement quartz (phase 2), supergene colloform hematite and goethite were also observed as rimming the post-mineral fractures (Figure 5.54).

174

At the vein footwall-wall rock contact, deformed clasts and grains of saccharoidal quartz belonging to the phase 1 have a cement of micro- to crystalline quartz-hematite of phase 2 (Figure 5.55).
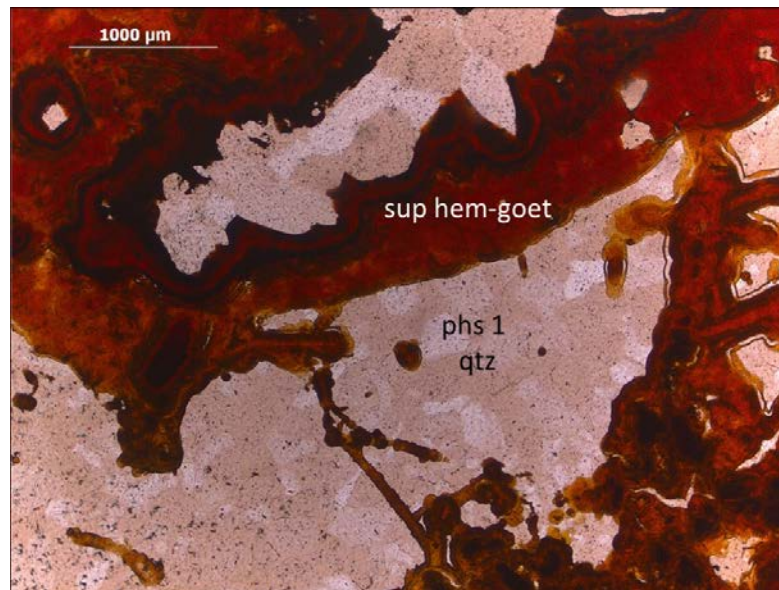


**Figure 5.54.** Colloform supergene hematite and goethite (sup hem-goet) rimming the fractures cutting the crystalline quartz (qtz) of phase 1 (Plane polarized light image from K3D1-A).
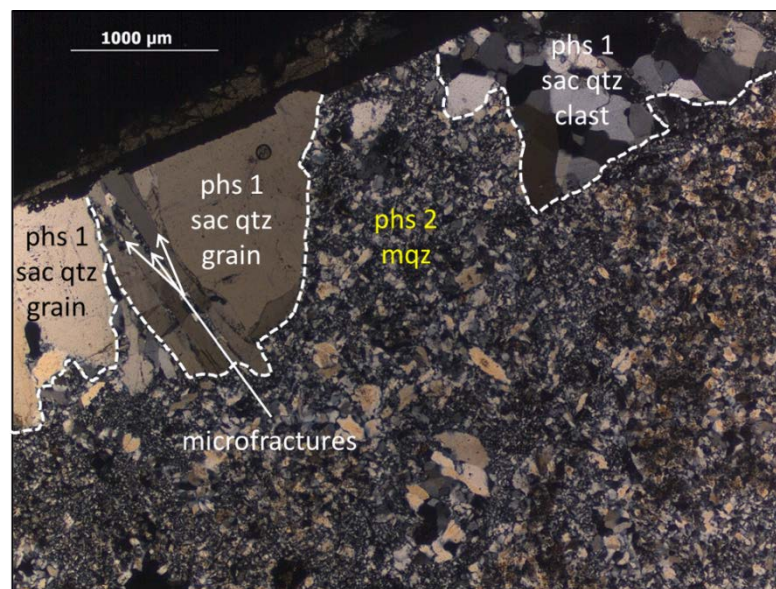


**Figure 5.55.** Deformed clasts and grains of phase 1 saccharoidal quartz (sac qtz) set in a microcrystalline quartz (mqz)(phase 2) cement (Note that the microcrystalline quartz replaces saccharoidal quartz fragments along the microfractures) (crossed polars image from K3H-13).

### 5.2.7. Topyurt vein system

Topyurt vein system has three sub-parallel NE-SW trending veins with a total exposed strike length of 154 m. Textural observations were only made of three veins where intense weathering and vegetation allowed. The veins could not be drilled as they are located in a protection area.

The veins are brecciated and the breccias are composed of the polymictic clasts of previous vein phases cemented by red iron-oxide bearing quartz. These breccias are cement supported and have poorly sorted angular to sub-rounded clasts (Figure 5.56a).

Three phases of mineralization were determined from the macroscopic observation of the vein system: (1) mostly cockade textured white partly vuggy microcrystalline quartz (Figure 5.56b-57b and 5.58a), (2) yellow to orange colored Fe-Ox bearing (?) microcrystalline quartz (Figure 5.57b and 5.58b) and (3) microcrystalline quartz- iron oxide cementing the previous phases (Figure 5.58).

Phase 1 partly vuggy microcrystalline quartz encloses the sub-angular to rounded clasts of wall rock QFH porphyry and forms cockade texture (Figure 5.56b). Some of the wall rock clasts especially the bigger ones are absent in the core of the cockade textured microcrystalline quartz (Figure 5.57a) due to removal of the clasts.
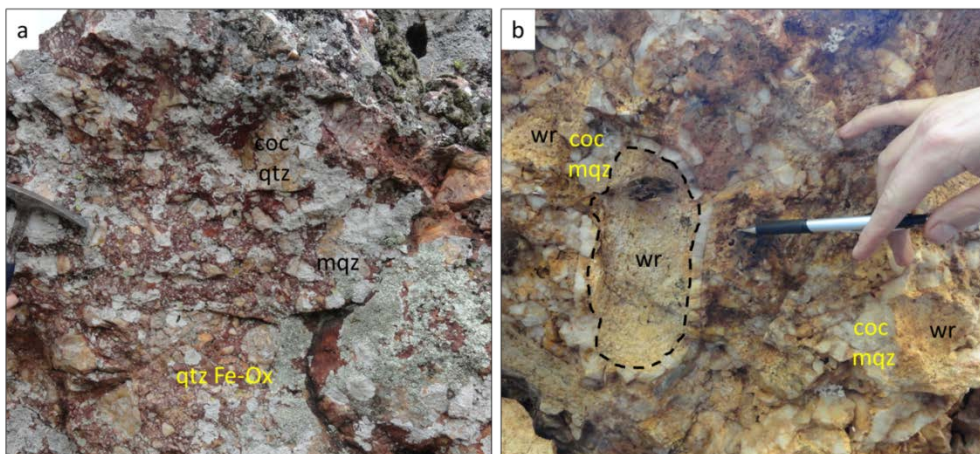


**Figure 5.56.(a)** Cement supported poorly sorted polymictic breccia with clasts of previous vein phases and a cement of quartz-iron oxide (281 m asl) (mqz: microcrystalline quartz, coc qtz: cockade quartz, Fe-Ox: iron oxide). **(b)** Cockade textured microcrystalline quartz (coc mqz) (phase 1) rimming the clasts of wall rock QFH porphyry (wr) (275 m asl).
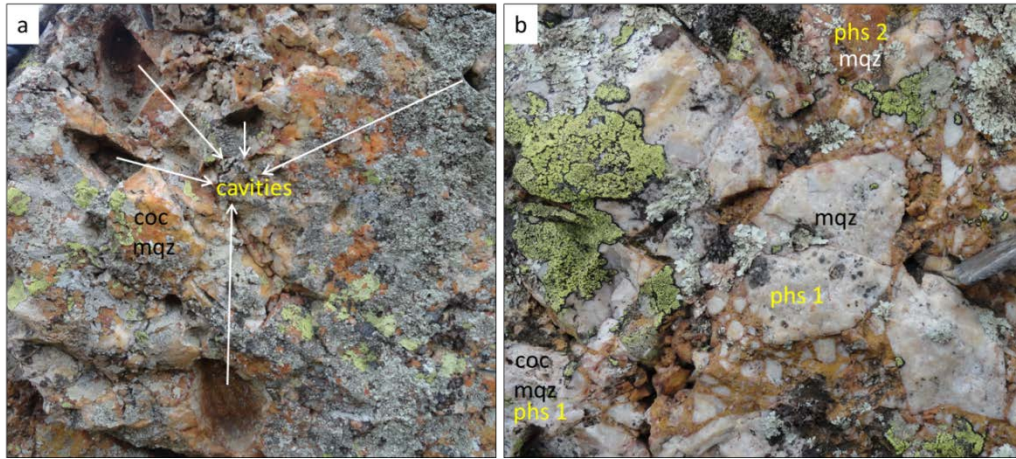
**Figure 5.57.(a)** Cavities in the cockade textured microcrystalline quartz (coc mqz) formed due to the removal of the clasts from the core (271 m asl). **(b)** Phase 2 yellow to orange colored Fe-Ox bearing(?) microcrystalline quartz (mqz) cementing the clasts of phase 1 mostly cockade textured white partly vuggy microcrystalline quartz (coc mqz) (273 m asl).

Phase 2 yellow to orange colored Fe-Ox bearing(?) microcrystalline quartz cements the clasts of phase 1 (Figure 5.57b) and found as clasts of cement supported breccia cemented by microcrystalline quartz-iron oxide (Figure 5.58b).
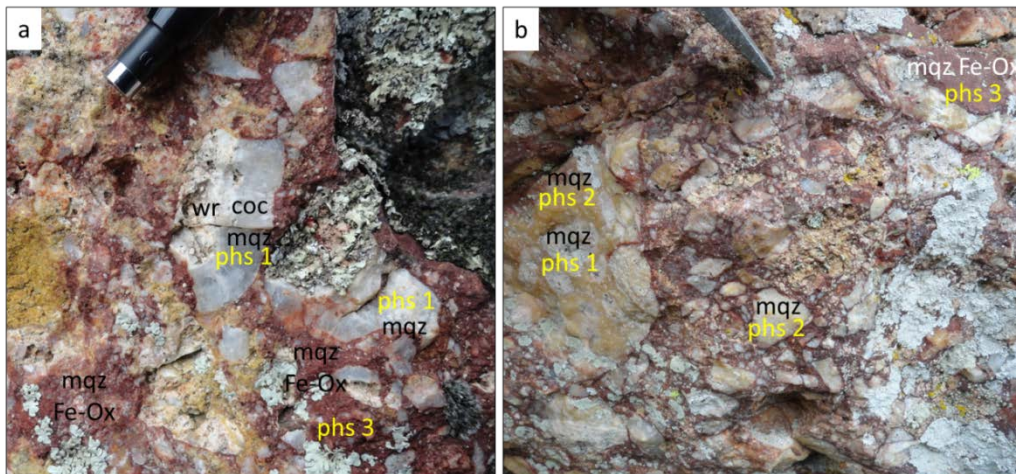


**Figure 5.58.(a)** Cement supported breccia of phase 1 silicification cemented by phase 3 microcrystalline quartz-iron oxide (mqz-Fe-Ox) (270 m asl) (coc mqz: cockade microcrystalline quartz). **(b)** Cement supported breccia of yellow to orange colored microcrystalline quartz (mqz) (phase 2) cemented by phase 3 microcrystalline quartz-iron oxide (268 m asl).

Youngest mineralization phase of the vein system, phase 3 is composed of microcrystalline quartz-iron oxide and cements the clasts of previous vein phases (Figure 5.58).

## 5.2.8. Sheeted quartz veins

Sheeted quartz vein textures were studied macroscopically from their outcrops. They are composed of well-developed crystalline quartz crystals which are oriented almost perpendicular to the vein walls and form comb texture (Figure 5.59).

Although most of them have a single phase of mineralization represented by comb textured crystalline quartz, some have a second phase composed of black silica at the core of the comb crystalline quartz (Figure 5.59b).

Up to 419 g/t gold grade has been reported from the samples taken from sheeted veins (personal communication, Cem Yüceer, 2013).



**Figure 5.59.(a)** A view from the sub-parallel sheeted quartz veins (264 m asl). **(b)** Closer view from the sheeted veins showing their comb textured crystalline quartz infill with a core of black silica.

## 5.3. Discussion and summary

### 5.3.1. Multiphase brecciation, fluid flow and associated mineralization

Examination of textures and breccias of Kestanelik veins reveal multiple episodes of brecciation and fluid flow and associated mineralization for the evolution of the veins. Observed chronology of the breccias and textures suggests at least two phases of mineralization in E-W trending veins such as Karatepe, K2 and K3 veins, but at least three phases of mineralization for NE-SW trending veins like KK1, KK2, KK3, KK4, K1, Topyurt veins. E-W trending veins have variable textural and breccia characteristics, while NE-SW trending ones share similar breccia properties.

The E-W trending Karatepe vein (Figure 5.4) has two phases of mineralization represented by older cockade chalcedony and younger crustiform chalcedony (Figure 5.5 and Figure 5.8). Cockade textured chalcedony has sub-rounded to rounded clasts of wall rock QFH porphyry which show neither normal nor reverse grading. The absence of any grading in the clasts of the cockade breccias of the Karatepe vein (Figure 5.13) may indicate that both shaking (where brecciation occurs due to seismic faulting and clasts are cemented during interseismic period) and fluidisation (where brecciation occurs due to hydraulic fracturing and subsequent fluid flow cements the clasts) may have played a role in the formation of the cockade breccias (c.f. Frenzel and Woodcock, 2014). These represent the first phase of fluid flow and formation of the Karatepe vein. Sub-rounded to rounded clasts (Figure 5.13 and 5.14) suggest that the crustiform chalcedony was deposited as rims around wall rock derived clasts (e.g. Figure 5.7) while they were being rotated in the hydrothermal solution. Just after the Karatepe structure was completely sealed, a second permeability creation event could have been caused by shearing along the vein footwall-wall rock contact. This is evident from the cataclasite of phase 1 chalcedony and feldspar (from the wall rock QFH porphyry) (Figure 5.9) observed during petrographic analyses. The newly created permeability caused the deposition of crustiform chalcedony between the phase 1 chalcedony and the footwall margin of the vein.

The E-W trending K2 vein (Figure 5.4) has at least 2 phases of mineralization represented by probably synchronous vuggy saccharoidal, microcrystalline and lattice bladed quartz (Figure 5.36b-c-d and 5.37), and microcrystalline quartz iron oxide from oldest to the youngest (Figure 5.37). Cement-supported breccias with the angular clasts of wall rock schist cemented by phase 1 quartz either close to the vein HW margin (Figure 5.37a-c-f-h) or in the vein core (Figure 5.37l) show that brecciation of wall rock schist triggered a fluid flow and resulted in cementation of the schist clasts with minor transport and milling during the phase 1 silicification. Crackle to mosaic breccias with angular phase 1 quartz clasts cemented by phase 2 quartz iron oxide observed close to the FW margin of the vein (Figure 5.37b-d) suggest that after the vein was clogged, brecciation of phase 1 quartz minerals occurred close to the FW margin of the vein resulting in deposition of phase 2 quartz-iron oxide as the cement of a newly formed breccia.

Two phases of brecciation and mineralization were picked up from the E-W trending K3 vein: (1) synchronous occasionally banded crypto-micro-crystalline (predominant)-saccharoidal and lattice bladed quartz (e.g. Figure 5.45) and (2) occasionally banded crypto-microcrystalline quartz ± hematite and/or goethite (e.g. Figure 5.50). Phase 1 mineralization cements the clasts of wall rock schist close to the HW margin of the vein (e.g. Figure 5.43c), and is continuous and fractured in the core of the vein (e.g. Figure 5.41 and 5.43f). Phase 1 clasts of crackle to chaotic breccias are cemented by phase 2 quartz-iron oxide close to the footwall margin of the vein (Figure 5.43i), in the vein core (Figure 5.43h) or close to the hangingwall margin of the vein (Figure 5.43b) up to 280 m asl. These suggest that a phase 1 mineralization lode which had been deposited by the first phase of hydrothermal fluid flow as a result of the brecciation of wall rocks was brecciated along the vein footwall-wall rock contact and its clasts were cemented by phase 2 quartz-iron oxide. Reactivation of the sealed K3 structure by the first phase of mineral deposition occurred by shearing along the FW of the vein-wall rock contact as evidenced by the deformed clasts and grains of saccharoidal quartz belonging to the first mineralization phase cemented by phase 2 micro-crystalline quartz-hematite

(Figure 5.55). In addition, silicification of foliation planes of the schist clast which is synchronous with the cement silica (phase 2) indicates fragmentation of wall rock during shearing as well (Figure 5.47). Observation of crackle to chaotic breccias of phase 1 quartz cemented by phase 2 quartz either close to the footwall margin or as complete infill of the K3 vein suggests the fluctuating power of hydrothermal brecciation due to the boiling event triggered after the rapid pressure drop by shearing.

At the upper levels of the vein (after the level 280m asl), crackle to chaotic breccias consist of poorly sorted angular to sub-rounded clasts of pre-existing vein infill showing different textural characteristics cemented by phase 2 mineralization (e.g. Figure 5.39 and 5.40). These breccias suggest the transportation of clasts after the brecciation of earlier vein infill to the upper levels of the vein where they are fixed by phase 2 quartz-iron oxides.

NE-SW trending veins have three different breccia types: (1) *Cement supported breccias with the clasts of wall rock:* These breccias have angular clasts of wall rock supported by later phases (phase 2 or 3) of quartz (Figure 5.15d and 5.34). They are found close to the either margin of the veins and some clasts have silicification synchronous with the cement silica (Figure 5.27). These breccias indicate rupturing along either the HW margin (e.g. Figure 5.15d) or FW margin (e.g. Figure 5.26) of the veins and derivation of wall rock in each brecciation phase. (2) *Crackle to mosaic breccias cemented by quartz-iron oxide(s)*: These breccias have jigsaw-fit angular clasts of previous vein phase and always cemented by the youngest phase in the vein(s) (e.g. Figure 5.15c and 5.25). Clasts may be composed of the quartz of previous vein phase (e.g. Figure 5.25 and 5.30a) and the breccia of earlier vein phases or wall rock cemented by previous vein phase (Figure 5.35d). These breccias suggest permeability enhancement by fluid-assisted hydrothermal brecciation as a result of a boiling event after the vein was sealed by the latest mineralization event. (3) *Chaotic breccias with the lodes of crackle breccias*: These are composed of polymictic clasts of host rock and/or pre-existing vein infill with different quartz textures. The cement is quartz-hematite or quartz-goethite, and the

clasts are sub-angular to angular and poorly- to well-sorted (e.g. Figure 5.16 and 5.31). These breccias are generally more frequent at the upper levels of the vein outcrops and indicate multiple brecciation of vein lode and transportation of the derived clasts to the upper levels of the vein where they are fixed by quartz-iron oxide(s).

**Table 5.9.** Table summarizing the textural association representing the different mineralizing phases of each vein

| Vein | Phase 1 | Phase 2 | Phase 3 | Phase 4 |
|---|---|---|---|---|
| *Karatepe* | coc ch | crs ch | | |
| *KK1* | cry qtz | sac qtz | syn sac+psbld qtz | cry qtz-goet |
| *KK2* | cry qtz | syn sac+psbld qtz | cry qtz-Fe-Ox | |
| *K1* | cry qtz | syn sac+psbld qtz | cry qtz-Fe-Ox | |
| *K2* | syn sac+psbld+cry qtz | cry qtz-Fe-Ox | | |
| *K3* | syn bnd+sac+psbld+cry qtz | cry bnd qtz-Fe-Ox | | |
| *Topyurt* | coc qtz | cry qtz | cry qtz-Fe-Ox | |

*Coc ch:* cockade chalcedony, *crs ch:* crustiform chalcedony, *cry qtz:* crystalline quartz, *sac qtz:* saccharoidal quartz, *syn sac+psbld qtz:* synchronous saccharoidal and pseudobladed quartz, *cry qtz-goet:* crystalline quartz-goethite, *cry qtz-Fe-Ox:* crystalline quartz-iron oxide, *syn sac+psbld+cry qtz:* synchronous saccharoidal, pseudobladed and crystalline quartz, *cry bnd qtz-Fe-Ox:* crystalline banded quartz-iron oxide, *coc qtz:* cockade quartz.

Each brecciation event seems to have triggered rapid boiling of hydrothermal fluids by sudden pressure release evident from the diagnostic boiling indicators: lattice bladed quartz replacing calcite (e.g. Figure 5.15b and 5.45) being the most dominant, as well as colloform (Figure 5.52 and 5.53) and crustiform (Figure 5.5) textures. Common occurrence of pseudobladed quartz and saccharoidal quartz observed in earlier stages of mineralization within the Kestanelik vein system shows that the hydrothermal fluid had high $CO_2$ content which was lost to the vapor phase and resulted in a pH increase and saturation of $CO_3$ leading to the deposition of bladed calcite and massive granular calcite which were then dissolved (evident from their porous appearance) by a decrease in temperature upon boiling and

pseudomorphed by quartz. In contrast, the youngest phase of the mineralization is associated with crystalline quartz indicating silica-saturated hydrothermal fluid. Change of textures from pseudomorphs of calcite to crystalline quartz suggests that the evolution of hydrothermal fluids from carbonate-saturated to silica-saturated. Hypogene iron oxides like hematite and goethite observed in the youngest phase of each vein (except Karatepe vein) which are synchronously deposited with the crystalline quartz (e.g. Figure 5.24 and 5.50) are indicative of oxidizing conditions suggesting the mixing of ascending hydrothermal fluids (depositing quartz) with oxidized meteoric groundwater.

Apart from the hypogene hematite and goethite deposited synchronously with the cement quartz, supergene hematite and goethite were also observed in some veins as rimming the post-mineral fractures (e.g. Figure 5.54) and filling some vugs which may have been deposited as a result of the infiltration of meteoric water into the post-mineral fractures. (e.g. Figure 5.38). Since boiling related textures and both hypogene and supergene hematite and goethite are associated with gold; boiling, mixing (hypogene oxidation) and supergene enrichment (supergene oxidation) can be suggested as gold precipitation mechanisms in the Kestanelik veins.

## 5.3.2. Rough paleodepth estimations

In LS epithermal systems, the most dominant mineral precipitation mechanism is boiling. Ore and gangue minerals dissolved in the hydrothermal fluid ascend along structural conduits and rapid pressure drops causes boiling of the fluid. Change in fluid chemistry due to the boiling cause first the base metals, then the ore and gangue minerals and finally the silica sinter to deposit in a well-recognized temporal and vertical sequence (Buchanan, 1981; Hedenquist *et al.*, 2000). The average vertical interval of LS ore mineralization zones is typically about 300 m, and the boundary between the upper precious metals and lower base metals is accepted as the level of boiling (Buchanan, 1981).

Within the precious metal ore interval, gold ore is commonly associated with the major gangue minerals; quartz (as the most dominant), calcite and adularia (both indicating near-neutral pH conditions) and hydrothermal sericite. In the precious metal ore horizon, the quartz gangue is typically very fine grained and commonly has banded and crustified textures (Buchanan, 1981; White and Hedenquist 1995; Hedenquist *et al.*, 2000). Factors controlling the deposition of the dominant gangue phase quartz are decreases in fluid temperature, pressure and salinity. These changes in fluid affect the morphology, crystal structure and chemical composition of silica and result in the formation of different quartz textures (Hayba *et al.*, 1985; Corbett and Leach, 1997; Dong *et al.*, 1995). The different textures of gangue quartz forming in LS epithermal deposits and their relation to possible hydrothermal conditions were explained in detail at the beginning of the chapter.

Above the precious metal ore horizon, precious metal values drop rapidly. The quartz vein filling extends above the top of the precious metal ore zone, but the width of it gradually decreases and the quartz is deposited as agate or chalcedony above the ore shoot because of the relatively cooler conditions. Toward the vein tops, volume of quartz and agate (or chalcedony) diminishes and calcite becomes more common (Buchanan, 1981).

At the surface of the system, rapid cooling of the fluid results in silica super-saturation and formation of silica sinters, the most distinctive paleosurface feature of LS deposits. They form finely laminated terraces of amorphous silica (White *et al.*, 1989; White and Hedenquist, 1995; Corbett and Leach, 1997; Hedenquist *et al.*, 2000). Silica sinter defines the position of the paleosurface and, most importantly, it points out the location of the principal upflow channel of boiling fluid (Hedenquist *et al.*, 2000).

Figure 5.60 is a conceptual model showing the vertical zonation of vein textures, metals and alteration zones with respect to a boiling level in a single epithermal vein.  According to the model, quartz textures can be used to calculate

the paleodepth of the system and more importantly to point out the level of precious metal zone.

Multiple stages of brecciation, fluid flow and mineralization in the Kestanelik vein system show boiling of hydrothermal fluids at different elevations (due to the different pressure build ups after each sealing event) for different mineralizing episodes leading to the overprinting of quartz textures formed at each single mineralization event. In this case, rough boiling level estimation for the veins should be made separately for each phase, however this is not possible due to the brecciated nature of the most of the Kestanelik veins (except Karatepe veins and sheeted veins in the valley), which caused the movement of quartz texture(s) indicative of a definite level by the effect of transporting fluid. For the other veins, inference for paleodepth can be made based on the dominant quartz textures observed.

Absence of amorphous silica (silica sinter) in the Kestanelik vein system clearly shows that the system has been subjected to erosion (Figure 5.61).

In the northern portion of the system, Karatepe vein is completely filled by chalcedony which places it in the base of chalcedonic superzone (Figure 5.61).

In the northwestern part of the area, Karakovan vein system (KK1 and KK2 veins), has pseudobladed, saccharoidal and microcrystalline quartz textures. Of these, pseudobladed and saccharoidal quartz textures are the most dominant indicating the top of chalcedonic superzone (Figure 5.61).
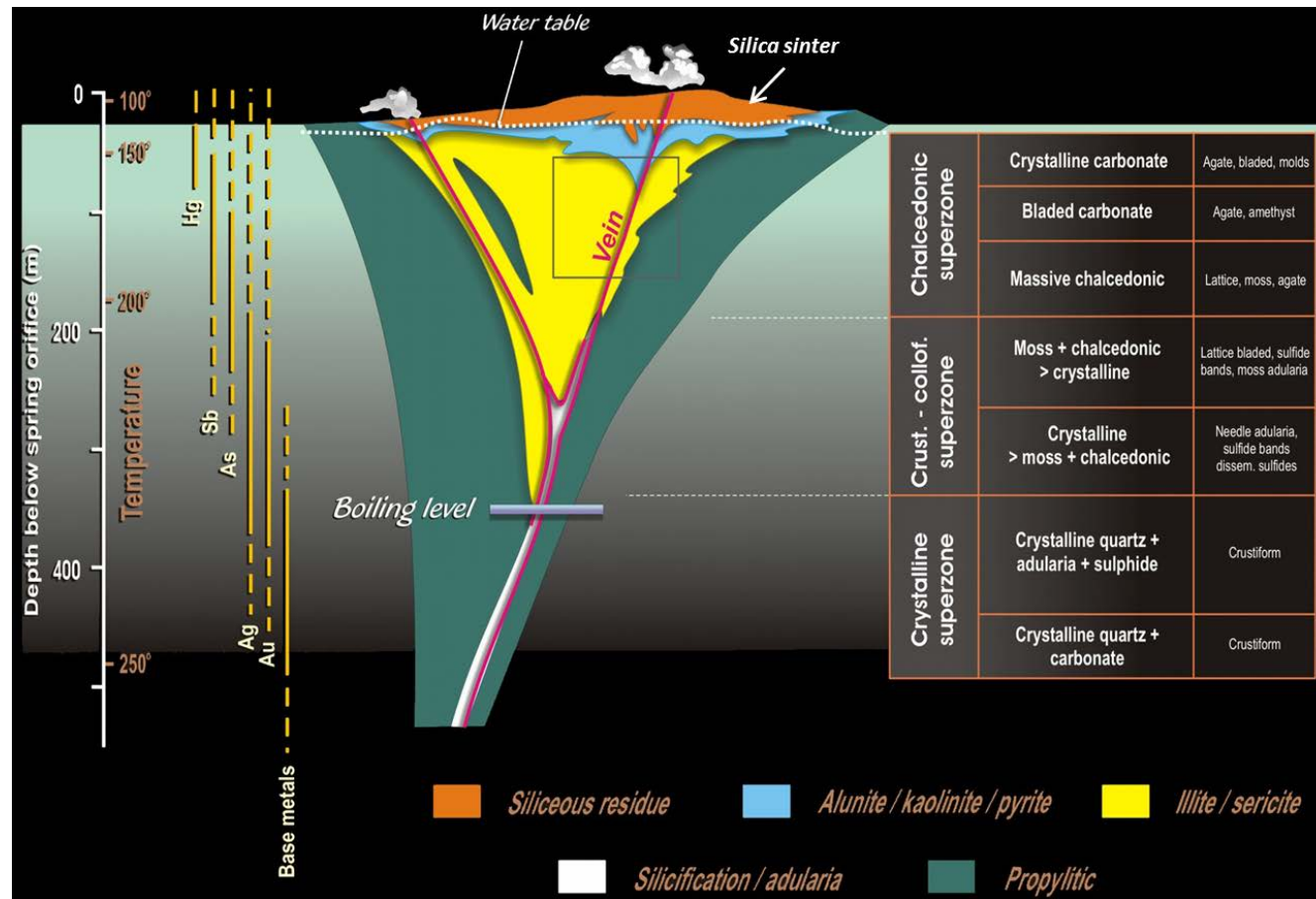
**Figure 5.60.** Vertical zonation of vein textures, metals and alteration zones with respect to a boiling level in a single epithermal vein (Modified from Buchanan, 1981; Morrison *et al*., 1990; Corbett and Leach, 1997).

In the mid part of the deposit (K1, K2 and K3 veins), in addition to the textures observed in the Karakovan vein system, banded quartz textures are observed. Relatively common occurrence of crystalline quartz with respect to the replacement textures (saccharoidal and pseudobladed) and the presence of banded texture suggest these veins represent the mid to top of crustiform-colloform superzone. In addition, observation of zoned crystals in saccharoidal quartz shows deposition from hotter fluids and confirms relatively deeper level of formation compared to the saccharoidal quartz observed in the Karakovan vein system (Figure 5.61).

In the southern part of the system, sheeted veins have well developed comb textured quartz crystals (requiring deposition in relatively slow changing conditions in an open space) which point out the top of crystalline superzone (Figure 5.61).

To sum up, level of erosion and the paleodepth in the Kestanelik vein system increases from the north to the south by a shift of dominant quartz textures from chalcedonic superzone to crystalline superzone.

### 5.3.3. Relationships between the vein textures and the gold grades

Kestanelik veins generally have complex multiple quartz textures due to the multiple phases of brecciation and mineralization. In order to examine the correlation between gold grades and quartz textures, and the effect of hypogene and supergene oxidation on the gold grades; textures and iron oxides observed both on the surface and in drill cores were grouped, and gold grades associated with each group were evaluated. Table 5.10 below gives the quartz texture and iron oxide content of each group and presents some descriptive statistical parameters of group-related gold grades.
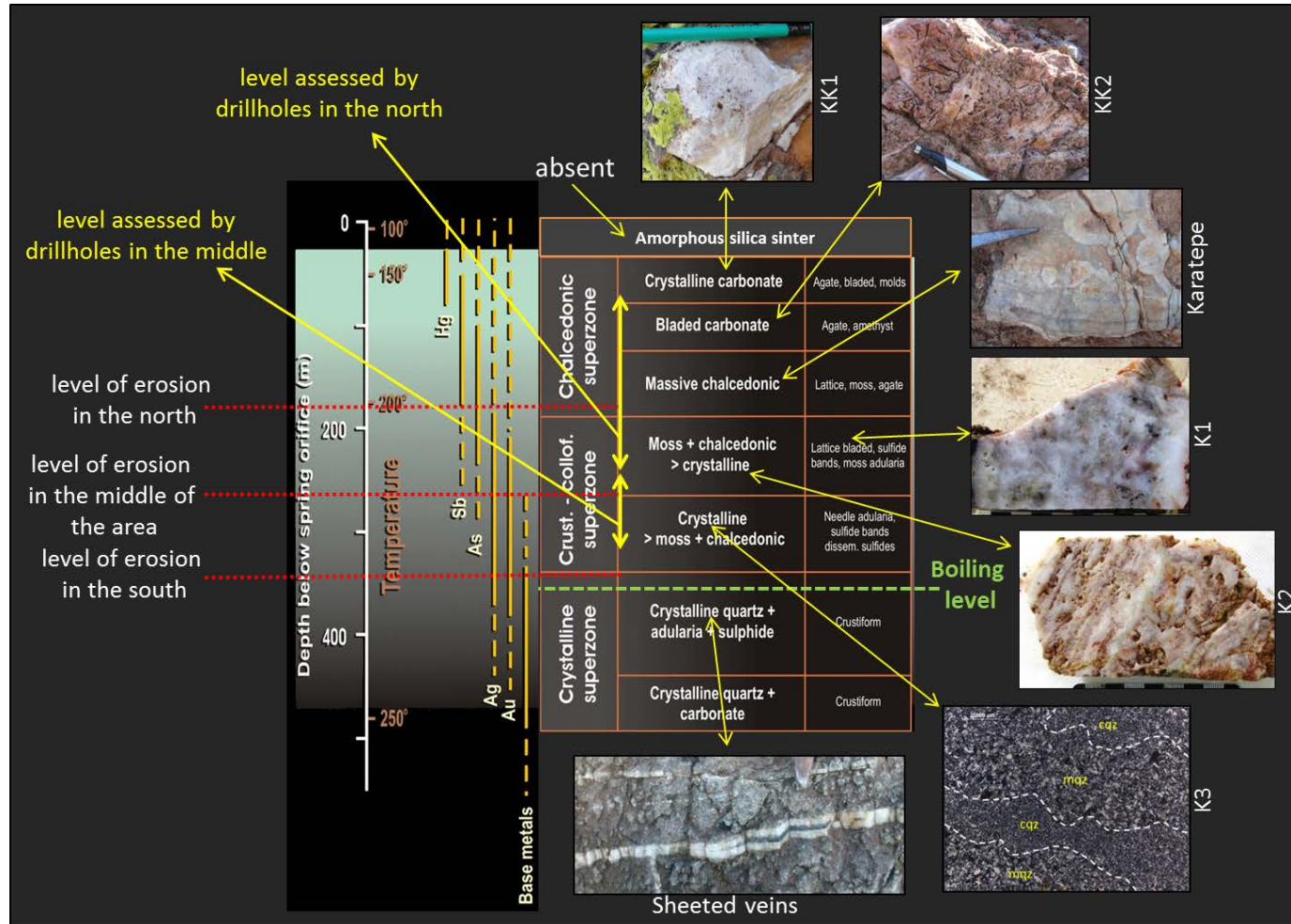
**Figure 5.61.** A schematic figure illustrating the vertical zonation of quartz textures in the Kestanelik vein system and indicating the level of erosion in different parts of the area.

**Table 5.10.** Texture, iron oxide content and descriptive statistical parameters of gold grades related to groups

| Group no | Content | No of data | Gold grade (g/t) | | | |
|---|---|---|---|---|---|---|
| | | | Min | Max | Mean | Median |
| 1 | coc ch | 14 | 0.082 | 1.37 | *0.52* | 0.367 |
| 2 | sac+psbld | 3 | 0.628 | 3.12 | *1.67* | 1.275 |
| 3 | sac+psbld+sec Fe-Ox | 5 | 0.867 | 28.7 | *10.46* | 7.44 |
| 4 | sac+psbld+qtz-Fe-Ox | 17 | 0.012 | 6.36 | *1.28* | 0.865 |
| 5 | sac+psbld+qtz+qtz-Fe-Ox | 3 | 1.335 | 2.69 | *1.79* | 1.35 |
| 6 | sac+psbld+qtz+sec Fe-Ox | 15 | 0.504 | 39 | *7.38* | 3.3 |
| 7 | sac+psbld+bnd+qtz+sec Fe-Ox | 6 | 2.97 | 41 | *17.5* | 11.85 |

Coc ch: cockade chalcedony, sac: saccharoidal quartz, psbld: pseudobladed quartz, cbnd: banded quartz, qtz: crystalline quartz, qtz-Fe-Ox: synchronous quartz-iron oxide (hypogene), sec Fe-Ox: secondary Fe-Ox (supergene).

- Cockade chalcedony (*Group 1*) has the lowest mean gold grade (0.52 g/t) which may be related to the deposition of chalcedony at the shallow level of the epithermal system far above the boiling zone where the gold is generally poor.

- Replacement quartz textures pseudobladed and saccharoidal quartz (*Group 2*) are associated with a mean gold grade of 1.67 g/t. Although the zone of crystalline and bladed carbonate is generally formed close to the surface and is poor in gold, the quartz dissolving and replacing them may have caused the increase in gold grade.

- Where secondary iron oxides are associated with replacement textures (*Group 3*) the mean gold grade is 10.46 g/t which suggests that supergene oxidation caused the enrichment of gold.

- Association of synchronous quartz and iron oxide with the replacement textures (*Group 4*) has a mean gold grade of 1.28 g/t which may indicate the lower efficiency of hypogene oxidation on the gold precipitation compared to that of supergene oxidation.

- *Group 5* is the same as *group 4* but with the presence of crystalline quartz, and has a mean gold grade of 1.79 g/t. This increase above group 4 may be due to the deposition of crystalline quartz within the boiling zone.

- Where replacement textures are found with crystalline quartz and secondary iron oxides (*Group 6*) the mean of the gold grades is 7.38 g/t. This is higher than group 5, confirming the effect of secondary oxidation in the enrichment of gold deposition.

- Mean gold grade from the *Group 7* samples, where banded texture is the most prominent texture, is the highest (**17.5 g/t**). It may be said that the banded texture has the most profound effect on the gold grades, which may be linked to its strong relationship with the boiling and associated deposition of gold.

# Chapter 6: Discussion

## 6.1. Evolution of the Kestanelik site

The study area Kestanelik gold deposit is located within the Biga Peninsula, NW Turkey where the Paleozoic metamorphic and ophiolitic basement rocks are cut by Eocene-Miocene aged plutons and covered by Cenozoic volcanic and sedimentary units (Figure 3.2). The gold mineralization in the area is associated with quartz veins hosted by Paleozoic mica schist and Lutetian (43.34±0.85 Ma) QFH porphyry (Figure 3.6). From mapping during this thesis, the oldest unit covering the veins is Priabonian limy sandstone, and the youngest host rock to the veins is porphyry with an assumed age of 43.34±0.85 Ma (see chapter 3). The age of the mineralization is therefore proposed as Late Lutetian-Early Priabonian (Late Eocene); however a more precise age may be supplied by dating mineralized veins. Although, the commonly dated mineral in LS epithermal veins is adularia (e.g. Sanematsu *et al.*, 2005), this has interestingly not been observed in the Kestanelik. The absence or minor occurrence of adularia at Kestanelik can be attributed to the calc-alkaline host rock because adularia rarely occurs when there is not enough potassium in the wall rock (Corbett and Leach, 1997). However, age of the mineralization could be determined by (U+Th)/He dating of hypogene hematite in the veins (e.g. Wernicke and Lippolt, 1997). Although the host rock porphyry was thought to be the heat source for the epithermal system by Chesser geologists, this is not possible because the coarse grain size of the porphyry (Figure 3.15) shows that it was emplaced at a greater depth and then uplifted and eroded before mineralization. For this reason, there must have been a younger intrusion below the mineralized quartz vein system to provide the heat source. Based on the timing of the mineralization (Late Eocene), the heat source most likely has a genetic link with the Cenozoic calc-alkaline magmatism prevailing in the Biga Peninsula (see chapter 3.2.2). This also suggests that Late Eocene metallogenesis in the Biga Peninsula is related to the Tethyan Metallogenic Belt (Yiğit, 2012). In addition, the areas close to the Cenozoic plutons can be regarded as potential areas for discovering genetically

related hydrothermal deposits like porphyry gold, high sulphidation (HS) and low sulphidation (LS). Presence of genetically and spatially associated epithermal deposits such as Kartaldag HS and Madendag LS deposits in the Biga Peninsula (Ünal-İmer *et al.*, 2013) suggests that the Kestanelik epithermal system may also be genetically and spatially associated with any other potential hydrothermal deposit(s).

Chesser geologists had classified the mineralization as LS epithermal. This has been confirmed during this PhD study because bladed quartz and hydrothermal breccia (Figure 3.32) were observed during the field and petrographical studies of the vein textures and breccias, however these should be supplemented by fluid inclusion data such as salinity and homogenization temperature to confirm low salinity and low temperatures (see chapter 2). Examination of the textures and breccias also aided in understanding (1) potential gold precipitation mechanisms in the veins and (2) paleodepth and level of erosion in the vein system (see chapter 5.3). The common occurrence of bladed and saccharoidal quartz shows that boiling is very likely to be the dominant mineral precipitation mechanism. In addition, hypogene hematite and goethite synchronous with the crystalline quartz (e.g. Figure 5.24 and 5.50) are indicative of oxidizing conditions suggesting the mixing of ascending hydrothermal fluids with oxidized meteoric groundwater. Apart from the hypogene hematite and goethite, supergene hematite and goethite were observed in some veins as rimming the post-mineral fractures (e.g. Figure 5.54) and filling some vugs which may have been deposited as a result of the infiltration of meteoric water into the post-mineral fractures. (e.g. Figure 5.38). Since boiling related textures and both hypogene and supergene hematite and goethite are associated with gold (there is gold in the hematite-goethite and in saccharoidal, bladed and banded quartz, see chapter 5.3.3); boiling, mixing (hypogene oxidation) and supergene enrichment (supergene oxidation) can be suggested as gold precipitation mechanisms in the Kestanelik veins.

Because silica sinter, the most diagnostic paleosurface indicator of LS epithermal systems, is missing in the area, the epithermal vein system has been

subjected to erosion. A general change of quartz textures from chalcedonic superzone (Karatepe vein in the north) through to textures from crystalline superzone (sheeted veins in the south) proposes that paleodepth and level of erosion in the Kestanelik vein system increases from the north to the south (see chapter 5.3.2) as lower levels of the system are exposed in the river valley. Because the veins are older than the tilted late Eocene limy sandstone, they must have also been tilted by at least as much as the bedding dip (29 degrees to the south). Untilting the veins by the bedding dip has the result of bringing the deeper parts of the vein system closer to the surface in the southern part of the system.  As the system has not completely been exposed to erosion, most of the gold potential must have been still preserved at deeper parts.

Gold mineralization in the study area is associated with nine major quartz veins: Karatepe, KK1, KK2, KK3, KK4, K1, K2, K3 (K3E and K3W) and Topyurt veins (Figure 3.6). The veins generally have a length of several tens to several hundreds of meters and their outcrop widths vary between 0.8 and 13.6 m on the surface. Wall rock veins, and the sheeted veins located along the valley floor also localize mineralization. The veins can be grouped into two general directions: E-W trending veins and NE-SW veins. E-W trending veins include Karatepe, K2 and K3E veins, while the others comprise NE-SW trending veins. While Karatepe, K3E and Topyurt veins are hosted by porphyry, the others are hosted by schist. The K3 vein is composed of two segments of different orientations hosted by two different host rocks (see chapter 4). This may be related to the refraction of the fracture hosting the vein during propagation due to the rheological contrast between the porphyry and the schist (e.g. Schöpfer *et al.*, 2007). Alternatively, K3W segment may have been offset by a probable dextral post-mineral fault. Constraining the presence of a fault would require drilling through the area between the two different segments, or clearing of the outcrop between the two veins (drilling would be less difficult).

Most of the veins are localized within the schist; therefore it is possible that the schist is more favorable host rock for the veins. This could be because the schist was more brittle at the time of veining compared to the porphyry. The high clay

(argillic) alteration the porphyry could increase ductility and reduce the brittleness potential (e.g. Davatzes and Hickman, 2005). The alteration of the porphyry seems to be related to LS epithermal fluid circulation as illite and rarely smectite are observed. This suggests that some veins may have been formed later than the other ones after the porphyry was altered enough to have a ductility potential. It would be interesting to use numerical simulations such as those in Moir *et al.* (2010) to constrain the behavior of the vein structures in different host rock lithologies. If a link can be shown between the host rock mechanics and the geometry and density of veining this could aid in predictions on vein-scale structures at similar deposits.

Host rock schist around the NE-SW trending KK1, KK2, KK3, KK4 and K1 veins does not change the orientation of foliation adjacent to the veins and these veins have very sharp contacts with the schist. In contrary, around E-W trending K2 vein and NE-SW trending K3W vein the schist changes its foliation orientation and is highly fractured and veined. Porphyry around the eastern segment of the K3 vein (K3E) is highly fractured and brecciated (see chapter 4). The porphyry around the E-W trending Karatepe vein and NE-SW trending Topyurt vein components is deformed by wall rock veins which have well-developed macro-crystalline quartz (Figure 4.12 and 4.13) and therefore can be defined as extensional veins.

The Karatepe vein and the array of extensional veins in the wall rock (Figure 4.12) define left-lateral kinematics while the Topyurt vein components and its wall rock structures (Figure 4.13) are consistent with a right-lateral en-echelon brittle shear zone. Sheeted extensional mineralized veins along the river valley have hydrothermal macro-crystalline quartz (Figure 4.10) similar to the ones around the Topyurt and Karatepe veins (Figure 4.12 and 4.13). The consistent textures and orientations of the extensional wall rock veins and sheeted veins suggest that all these veins are related to same hydrothermal mineralization event. Strikes of all these veins (Figure 4.19 and 6.1c) suggest that the direction of the horizontal component of the minimum principal stress ($\sigma_3$) was **N35°W.**

Combination of detailed structural and textural data from the field and in drill cores has led to the understanding of the origin of the fractures hosting the epithermal veins and the kinematics of the vein system. Cataclasite at the margin of the Karatepe vein (Figure 5.9) contains asymmetric shear indicators, suggesting that the structure hosting the vein is a fault. Hydrothermal quartz forming the Karatepe vein (Figure 5.5) and filling the comb fractures around it (Figure 4.13) shows that these structures are formed within the same deformation event. Furthermore, comb textured extension fractures around the Karatepe vein are proximal to the vein margin, and most of them curve towards the vein (Figure 4.12). These suggest that they are extensional fractures adjacent to the zone of Karatepe fault that formed after slip on the irregular Karatepe fault plane. It is assumed that that the minor principal stress is perpendicular to the extensional veins and their intersection with the Karatepe fault plane is parallel to intermediate principal stress. Thus the principal stress orientations $\sigma_1$, $\sigma_2$ and $\sigma_3$ can be determined from the vein geometries based on Anderson's theory of faulting, by plotting the plane of the Karatepe vein (fault) and the mean plane of the adjacent extensional veins. As a result, the orientations of $\sigma_1$, $\sigma_2$ and $\sigma_3$ are obtained as **034°/02°, 124°/59° and 304°/31°** respectively (Figure 6.1a-b). The orientation of the $\sigma_3$ here is consistent with the direction of the horizontal component of the minimum principal stress ($\sigma_3$) **N35°W** obtained by plotting the strikes of the all extension veins in the area.

The inferred directions of the principal stresses indicate almost NE-SW oriented compression and that the E-W trending Karatepe, K3 and K2 veins can be characterized as left lateral strike-slip faults, while NE-SW trending KK1, KK2, KK3, KK4 and K1 veins are extensional (Mode I) fractures (Figure 6.1d-e). In addition, the NE-SW trending Topyurt vein and associated N-S trending zone of wall rock veins correspond to a right lateral en-echelon brittle shear zone (Figure 6.1d-e). Although kinematic indicators could not be found for the fault-hosted veins, sheared cataclasite, tectonic breccia and intensely deformed characteristics of the wall rocks demonstrate that they are developed as a result of shearing. In addition, lack of any

shear indicators and wall rock deformation in the KK1, KK2, KK3, KK4 and K1 veins prove extensional fracturing (Mode I opening).

Horizontal σ1 and near vertical σ2 (Figure 6.1a) indicate transcurrent tectonics. This transcurrent tectonics is consistent with the NE-SW oriented horizontal compressional regime determined by paleostress analyses of the faults in the Kestanelik valley which cut the porphyry, limy sandstone and pyroclastics (Figure 3.30). As the age of the mineralization is proposed as Late Eocene, the kinematics of the site is most likely related to the collision and the further convergence after the closure of the northern branch of the Neo-Tethys Ocean (Late Cretaceous-Early Eocene: Şengör and Yılmaz 1981; Okay and Tüysüz, 1999; Sherlock *et al.* 1999; Önen and Hall 2000; Kaymakcı *et al.* 2007, 2009) (Figure 3.2). However, linking the local stress field of the site directly to the regional tectonics (i.e. the direction of the regional compression) require further kinematic studies. The attitudes of the post-mineral limy sandstone and pyroclastics suggest progressive tilting has affected the original attitude of the veins. "Un-tilting" the inferred stress axes during vein emplacement by the mean dip of the limestone bedding (110°/29°) results in orientations of $\sigma_1$, $\sigma_2$ and $\sigma_3$ of **038°/29°, 152°/40° and 289°/39°** respectively. However, these results are not reliable because (1) bedding attitude measurements are not consistent as there may be unmapped faults which tilt different blocks in the post mineral units and (2) progressive tilting may have affected the block of mineralized veins before the formation of the unconformity. More detailed structural field studies may be conducted in the south of the mineralized area to get more detailed info about the tilting. In addition, Late Miocene aged vertical axis rotations (15°-20° cw) in the Biga Peninsula (Kaymakcı *et al.*, 2007) must also be considered for reconstructing the paleo-stresses responsible for the geothermal system, but the amount of rotations are not reliable because there are large error ranges in the measurements due to the difficulties in differentiating the true vertical axis rotations from the secular variation in the magnetic field (Kaymakcı *et al.*, 2007; Nuretdin Kaymakcı, personal communication,

2017). Further detailed structural field and paleomagnetic studies are required to get more precise information about the vertical axis rotations in the Biga Peninsula.

Vein surfaces modelled in 3D indicate that the thickness of the veins decreases with depth and that the veins generally have a flaring upwards geometry (see chapter 4.4.1). This geometry may be caused by the decreasing confining pressures as the veins come closer to the surface. The mean attitude of modeled vein surfaces is generally different from the mean attitude of vein outcrops since the veins change geometry with depth. However, histograms of the subsurface dip data of modeled veins show that the modal subsurface dip amount of each vein is close to their surface dip data. Rose plots of the subsurface strike data indicate that the modal subsurface strike of each vein is close to their surface strike data (see chapter 4.4.1); although due to erosion along vein walls there are not many direct measurements of strike and dip from the surface. The mapped variable geometry along strike is mirrored at depth and most of the veins have multiple locations at depth where the dip changes (i.e. the veins have vertically segmented sections with differing dips). In layered rocks such dip segmentation has been observed as a result of the competency difference within different host rocks (e.g. Schöpfer *et al.* 2006, 2007). However in the Kestanelik, the dip segmentation is independent of the host rock type. Segmentation in the dip direction may be formed by growth and coalescence of isolated small planar segments of the structures (whether faults or fractures) (Cox, 2005). Observation of the sheeted veins at the lowest level of the deposit raises the question "Are the major veins fed by the sheeted veins?" However, the lowest parts of the modelled veins do not show any evidence for the sheeted veins – i.e. there is no evidence for multiple, thin veins in any of the lowest drillhole intersections. Either the sheeted veins are just confined to the valley section where they crop out, or the boreholes do not go deep enough anywhere else to cut the sheeted veins.

There is no correlation between the true vein thickness and the gold grade ($R^2$=0.005 and p-value=0.51>$\alpha$=0.01) suggesting that gradual thickness increases do not cause boiling and associated gold precipitation. However, boiling may have

occurred in relatively thicker areas, but the gold saturation may have been delayed (Hedenquist *et al.*, 2000). **~ 79%** of the bends correspond to high gold grade suggesting that these specific structural sites are favourable locations for gold precipitation compared to the more smooth and planar sections of the structures. In addition, sudden changes in thickness of the veins at the bends are more likely to cause boiling and subsequent gold precipitation by causing rapid pressure drop rather than the gradual thickness increases along the conduit. Presence of **85.4%** of samples containing high gold within the schist hosted veins which is higher than the percentage of bends (~79%) having high gold grade (see chapter 4.4.1) implies that the host rock geology has a greater effect than bends on the localization of the gold precipitation. This may be because the porphyry is cut by fewer veins; however the different mechanics of deformation in different host rocks may not be the only reason here and be co-founded by the chemistry of the solution, fluid-rock reaction and different ratios of fluid mixing etc. (e.g. Zhu *et al.*, 2011; Gammons and Williams-Jones, 1997). For now, implication of this result is yet to be explored by more work on the geochemical, stable isotope, fluid inclusion analyses of veins and wall rocks.

## 6.2. Vein scale permeability enhancement mechanisms

Examination of textures and breccias of the Kestanelik veins reveal multiple episodes of brecciation, fluid flow and associated mineralization implying that the veins were reactivated and opened up, after they were completely sealed and permeability was lost. As outlined in Chapter 1, the principal aim of this thesis was to explore vein-scale permeability enhancement mechanisms. Examination of the geology, dimensions, textures and breccias of the well-exposed Kestanelik epithermal vein system suggests three permeability enhancement mechanisms that could potentially have been active in the Kestanelik epithermal gold deposit:

1. coseismic rupturing
2. hydraulic fracturing
3. transient local stress variation

The three mechanisms are outlined in this section and their implications are discussed in section 6.3.1.
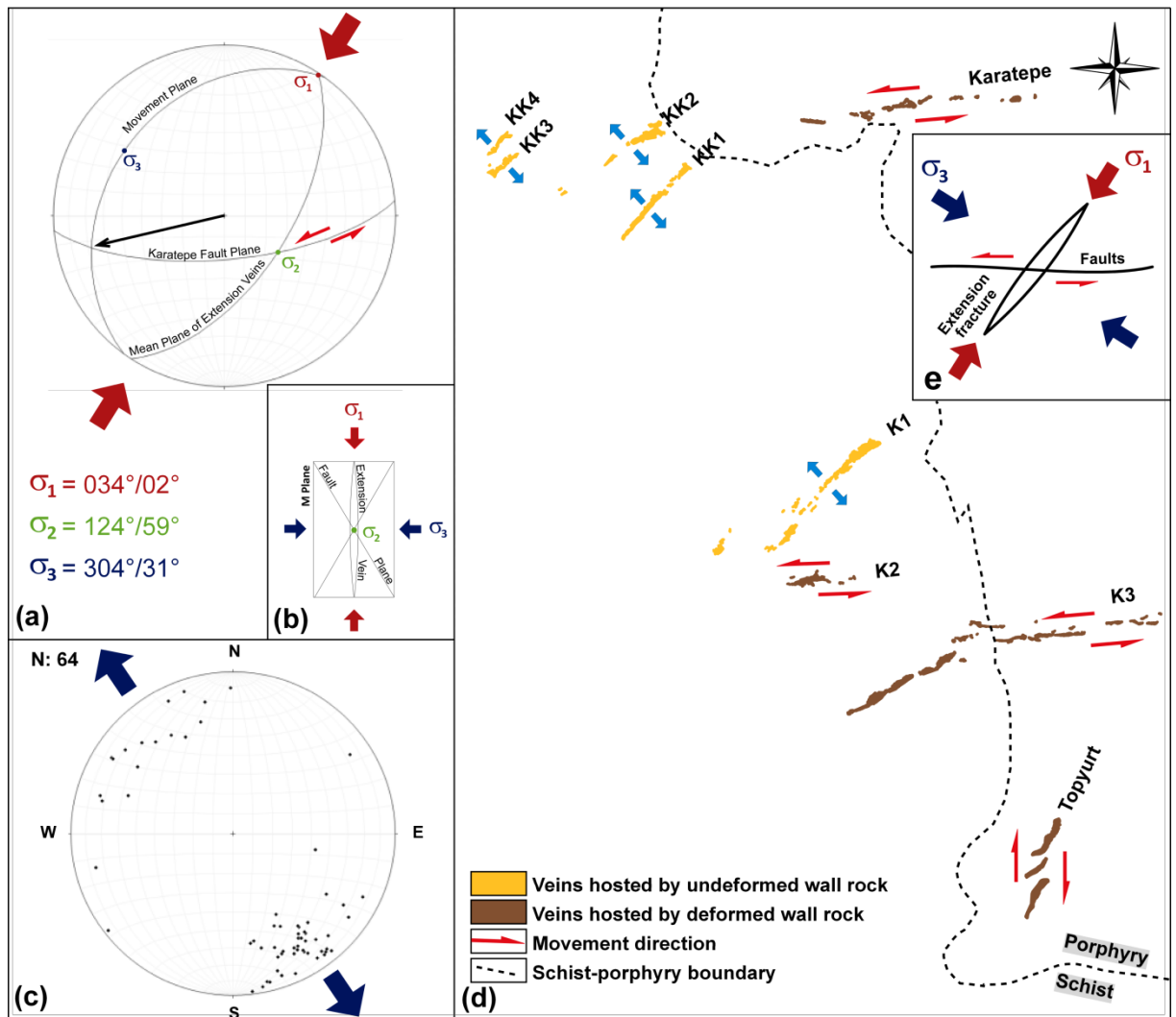


**Figure 6.1. (a)** Determination of principal stress orientations based on Anderson's theory of faulting by plotting the plane representing the mean orientation of the Karatepe vein and the mean plane of the adjacent extensional veins on an equal area stereonet based on assumptions: (1) Minor principal stress ($\sigma_3$) is perpendicular to the extensional veins (2) Their intersection with the fault plane is parallel to intermediate principal stress ($\sigma_2$). **(b)** A hypothethic diagram showing the relationship between the principle stress directions and opening of the veins and movement along the fault plane (M plane is the movement plane). **(c)** Poles to the all extensional veins in the Kestanelik deposit plotted on an equal-area stereonet with the arrows indicating the opening direction for the veins. **(d)** A sketch model showing the kinematics of the major quartz veins at Kestanelik based on the determined principal stress directions. **(e)** A hypothethical model showing the opening of the structures hosting the Kestanelik major quartz veins.

### 6.2.1. Coseismic rupturing

In the first mechanism, coseismic rupturing generates permeable pathways, which are clogged progressively by interseismic hydrothermal sealing. Sibson (1987) suggested that episodic fault rupture causes coseismic dilation at the rupture zones and an associated fluid pressure drop. The coseismic fluid pressure drop drives boiling, which is evidenced by the common occurrence of pseudo-bladed and saccharoidal quartz in Kestanelik veins. Quartz-iron-oxide cement within the breccias shows that ascending boiling fluid may have been mixed with descending oxidized surface meteoric water at the shallower parts of the system (Figure 6.2). Rapid closure of permeability by hydrothermal precipitation would clog pathways and result in local pressure build-up. Salinity and homogenization temperature data and type of inclusions by fluid inclusion analyses (e.g. Roedder and Bodnar, 1980) along with the O- and H- stable isotope analyses of fluid inclusions (e.g. Hedenquist and Lowenstern, 1994) could be used to further constrain boiling and mixing events.

Kestanelik was likely to have been an earthquake prone region because of the tectonic activity caused by the further convergence at the time of mineralisation (Late Eocene) after the closure of the northern branch of the Neo-Tethys Ocean (Late Cretaceous-Early Eocene: Şengör and Yılmaz, 1981; Okay and Tüysüz, 1999; Sherlock *et al.* 1999; Önen and Hall, 2000; Kaymakcı *et al.* 2007, 2009). In addition, it is well known that geothermal regions are dynamic, and that pressure transfer due to hydrothermal flow and mineralisation can induce seismicity (e.g. Hill, 1977; Waite and Smith, 2002).

Shear indicators such as cataclasite (Figure 5.9) and tectonic breccia (Figure 5.55) cemented by a later phase of silicification are observed at the footwall of the vein-wall rock contacts of the Kestanelik fault-hosted veins (Karatepe and K3W veins). These and the presence of angular wall rock clasts at the margins of extensional (Mode I) fractures (e.g. Figure 5.15d and 5.29) suggest rupturing along the fault planes and extensional fractures (Figure 6.2). Although none of the fault rock textures that have been observed are definitely diagnostic of dynamic rupture, it is not possible to exclude dynamic slip (Cowan, 1999; Rowe and Griffith, 2015).

The inequigranular infill of a comb quartz veinlet at the wall rock of the Karatepe vein (Figure 5.11) shows that the opening of the fracture was more rapid than the growing of the quartz crystals. This texture is more consistent with the brittle fracturing and dilation occurring during co-seismic or post-seismic aftershock phases of an earthquake, than with progressive silicification to seal the fracture during the passive interseismic phase (Woodcock *et al.* 2007). In addition, the absence of any grading in the clasts of the cockade breccias of the Karatepe vein (representing the first phase of fluid flow and formation of the Karatepe vein, Figure 5.13 and 5.14) may indicate that both shaking (where brecciation occurs due to seismic faulting and clasts are cemented during interseismic period) and fluidisation (where brecciation occurs due to hydraulic fracturing and subsequent fluid flow cements the clasts) may have played a role in the formation of the cockade breccias (c.f. Frenzel and Woodcock, 2014).
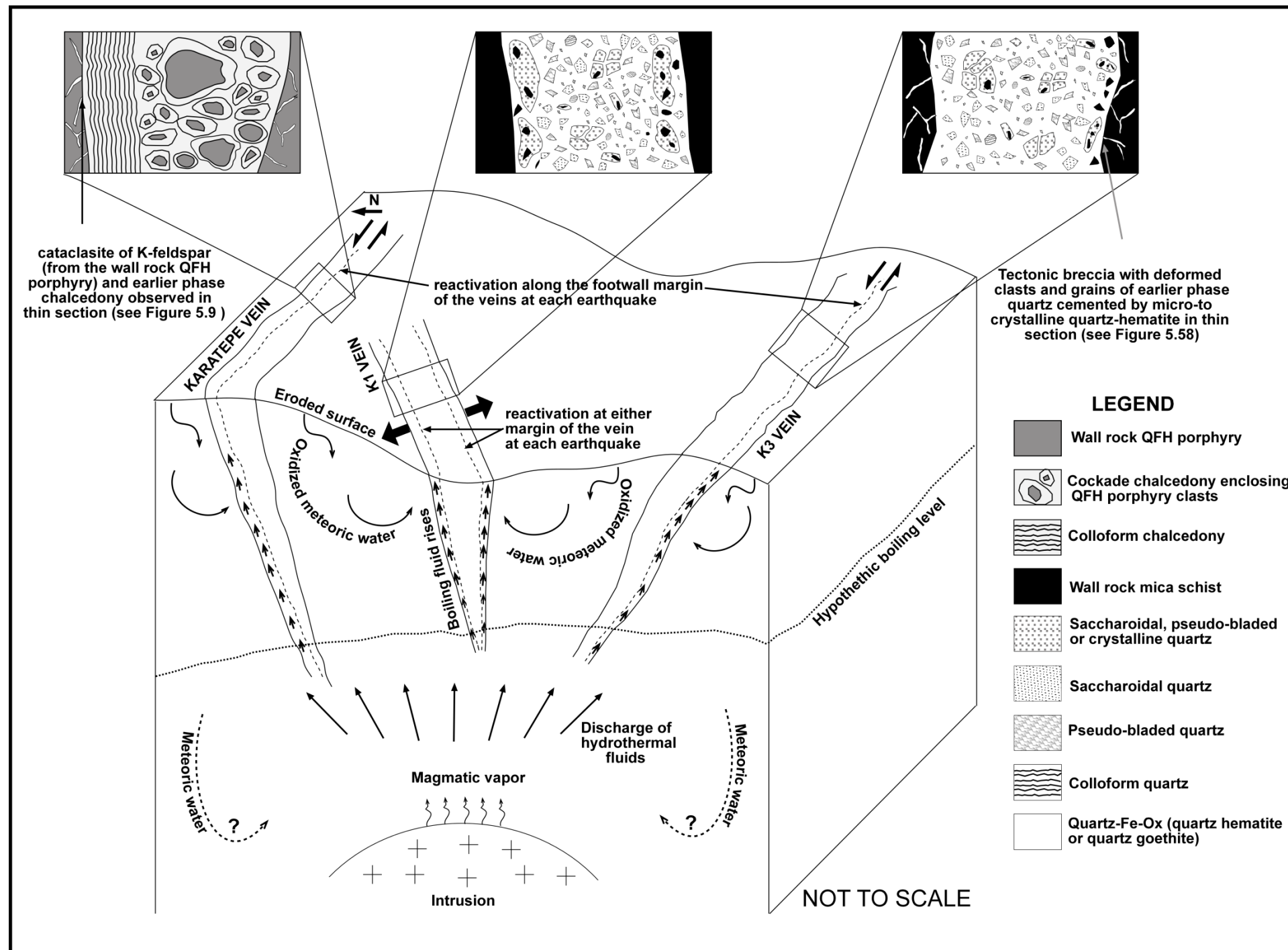
**Figure 6.2.** A schematic model showing repeated reactivation and opening of clogged veins and associated fluid flow, mineralisation and resulting vein textures at Kestanelik in the environment of geothermal activity with a shallow, sub-volcanic intrusion. When an earthquake occurs, E-W trending veins reactivate and open along their footwall-wall rock contacts while NE-SW trending veins reactivate and open along either margin and therefore permeable pathways are generated. Coseismic rupture and dilation results in rapid fluid pressure drop and drives boiling of hydrothermal fluids. Boiling fluid rises along the newly created permeable pathways and may mix with descending oxidized surface meteoric water at the shallower parts of the system. Shear indicators such as cataclasite and tectonic breccia of wall rock and pre-existing vein infill cemented by a later phase of silicification observed at the footwall of the vein-wall rock contacts of the two of the fault hosted veins (Karatepe and K3 veins), and the presence of angular wall rock clasts at the margins of extensional (Mode I) fractures form as a result of rupturing along the fault planes and extensional fractures. Chaotic breccias with polymictic clasts of pre-existing vein infill and wall rock with lodes of crackle breccia of pre-existing vein infill cemented by quartz-hematite or quartz-goethite form by multiple brecciation and sealing due to the repeated reactivation and opening. (Note that K3 vein represents the fault hosted veins (except Karatepe vein), while K1 vein represents the extensional (Mode I) fracture hosted veins of the Kestanelik.

### 6.2.2. Hydraulic fracturing

Rapid hydrothermal sealing of the pathways by mineral deposition could cause an increase in hydrothermal fluid pressure. Increase in fluid pressure promotes extensional-shear failure of the vein walls at depth, which are subsequently propagated upwards into the shallowest part of the crust. Provided that the pore fluid factor increases at rates higher than the increase in stress difference (Cox, 2005), when the hydrothermal fluid pressure exceeds the combined minimum principal stress ($\sigma_3$) and the tensile strength of the cap rock (T), then hydraulic fracturing occurs (Phillips, 1972). This triggers boiling due to pressure release and creates permeable structural conduits for the input of fluids, and results in formation of jigsaw puzzle textured hydrothermal crackle breccias (Hedenquist and Henley, 1985) without significant rotation of the fragments (Jebrak, 1997). The cements have to be very rapidly deposited or the clasts would settle out causing grading and/or rotation. Crackle breccias at Kestanelik form a network of veinlets with fragments of the early quartz infill without significant rotation cemented by later quartz or quartz iron-oxide (e.g. Figure 5.15c). These textures indicate dilatant fracturing with a negligible shear component (Micklethwaite, 2009) and suggest hydraulic fracturing occurred at the main vein conduits.

### 6.2.3. Transient local stress variation

Kestanelik site is associated with some mafic dykes only observed in drill cores and not exposed on the surface. In the drill core, dyke has the clasts of hydrothermally altered QFH porphyry, and the breccia of the dyke is cemented by hydrothermal quartz. Based on these textural observations, dykes intruded coeval with the epithermal quartz veins in the area (Figure 3.15c). Coeval dyke intrusion has important effects on the transient disruption of local stress causing transient kinematic variation and triggering earthquakes (e.g. Fukuyama *et al.* 2001; Toda *et al.* 2002; Waite and Smith, 2002; Micklethwaite, 2009). Additionally, geophysical studies indicate that geothermal systems are significantly dynamic owing to the

interactions between magmatic activity and faulting (e.g. Hill *et al.*, 1993; Dreger *et al.*, 2000) and therefore may explain the transient local stress variation.

Transient local stress variation might enhance permeability along the corrugated strike of the Kestanelik structures by facilitating slip on misoriented surfaces and influencing the kinematics of the structures. Secondly, locations where the dip changes (vein bends) in the Kestanelik structures have potential to enhance permeability since they lead to stress concentrations and localize intense deformation compared to the smooth and planar segments (Cox, 2005) during the earthquakes. It is important to note that permeability and fluid flow will be intermittent in both cases.

## 6.3. Implications of the study

### 6.3.1. Structural control, deformation, permeability enhancement and fluid flow in epithermal gold deposits – a contribution to the knowledge

Strike slip faults and extension (Mode I) fractures hosting the mineralized veins in the Kestanelik epithermal gold deposit indicate structurally controlled fluid flow in the epithermal systems (e.g. Buchanan, 1981; Hedenquist *et al.*, 2000; Cox *et al*. 2001; Cox, 2005). Additionally, extension veins around the Karatepe fault and the Topyurt en-echelon fractures host the epithermal mineralization showing that the array of extension veins that developed in the damage zone adjacent to the faults (e.g. Caine *et al.*, 1996; Cox, 2005) and in the en-echelon brittle shear zone surrounding the en-echelon veins may also localize the mineralization.

There are two models for the initiation of the vein sets and the first mineralization event that clogged the structures: **(1)** Faults and fractures exist before the development of a hydrothermal system and a reservoir. Heated fluid rises along these pre-existing structures and adiabatic boiling (Wilkinson, 2001; Simpson *et al.*, 2015) occurs when the pressure of the rising fluid gets equal to the lithostatic pressure. Boiling causes the precipitation of the minerals from the hydrothermal solution. **(2)** Faults and fractures form after the development of the

hydrothermal reservoir. Their formation may be initiated either by the decreased effective stress within the rocks above the hydrothermal pressurised reservoir, or by hydraulic fracturing due to the development of overpressured hydrothermal fluids. Both mechanisms trigger boiling of the fluids by the drop in confining pressure.

Multiple episodes of mineralization in the major Kestanelik veins indicate repeated reactivation of the clogged pathways. Coseismic rupturing is suggested as the primary permeability enhancement mechanism in the Kestanelik. It has been suggested in the literature that multiphase mineralization is related to repeated permeability development and fluid flow induced by seismicity (Sibson *et al*., 1975; Buchanan, 1981; Hedenquist and Henley, 1985; Sibson, 1987, White and Hedenquist, 1990, Hedenquist *et al*., 2000; Micklethwaite and Cox, 2004, 2006). All of these studies have focused on mechanical and geometrical aspects of fault-fracture systems hosting the epithermal deposits. However, this study investigates the repeated rupturing events by focusing on the textures and breccias of the vein infill (e.g. Tarasesewicz *et al*., 2005). According to the studies of vein textures and breccias in the Kestanelik deposit, it is proposed that after the veins were completely sealed, repeated reactivation occurs along the vein footwall-wall rock contact in the fault-hosted veins, and along the either margin in the extensional fractures. These observations point to a hypothesis for the structural and textural evolution of the fault- and extension fracture hosted veins as a result of repeated reactivation by earthquake rupturing during epithermal gold mineralization, which has not previously been proposed in the literature. According to this hypothesis; during an earthquake event reactivation of the sealed fault occurs along the vein footwall-wall rock contact and causes brecciation of both previous vein infill and wall rock (which may have silicification as veinlets or between bedding/foliation planed etc. due to the infiltration of the hydrothermal solution during the previous fluid flow and mineralization). Permeability generated by slip and associated brecciation causes a decrease in pressure and triggers vigorous boiling of hydrothermal solutions. Boiling initiates a hydrothermal eruption and most likely

masks the consequences of seismic slip (slickenlines, tectonic breccias etc.) by hydrothermal brecciation. This subsequent hydrothermal brecciation may cause: (a) partial brecciation of the vein lode (a part of previous vein lode is preserved along the vein hangingwall-wall rock contact) and the wall rock adjacent to the footwall of the vein-causing patchy flow, or (b) complete brecciation of the lode, and partial brecciation of the wall rock adjacent to the vein hangingwall and footwall. Subsequently, the ascending fluid causes the cementation of the wall rock and the previous vein lode clasts (Figure 6.3). The same processes occur in the extension fracture-hosted veins without any shearing event, after the reactivation occurs along the either margin of the vein. Cement supported chaotic breccias found at the upper levels of the most of the veins have clasts displaying various textures representing different depths of formation. These clasts must have been mechanically transported upward by the hydraulic action of the boiled hydrothermal fluid due to pressure release by coseismic rupturing or hydraulic fracturing.

**Figure 6.3.** Hypothetical model for the structural and textural evolution of fault-hosted veins by repeated reactivation along the vein FW-wall rock contact and associated boiling and hydrothermal brecciation. In (a), partial brecciation of the lode and the wall rock adjacent to the vein FW occurs, while in (b) complete brecciation of the lode and the partial brecciation of the wall rock adjacent to the vein FW and HW occurs (see the text for detailed explanation).Thick lodes (up to ~13 m) of fault hosted veins at Kestanelik suggest that earthquake events on faults not only result in shear but also significant opening implying remarkably large transient permeability increases.

Observed chronology of the vein textures and breccias suggests two phases of mineralization in E-W trending fault-hosted veins, but at least three phases of mineralization for NE-SW trending extensional (Mode I opening) veins at Kestanelik. It may not mean that all veins were affected-reactivated-opened at once when an earthquake was generated. However, it is more likely that an earthquake may have affected only one or two veins (or more), but not all at once, and that the location of the main boiling shifted through time. Paleoseismic studies show that repeated earthquakes reoccupy a narrow zone, and that individual paleoseismic zones are reused by different earthquakes (e.g. Gomez *et al.*, 2003). Similarly, observations of repeated spring reactivation (Burnside *et al.*, 2013) and mineralization distribution (Hammond and Evans, 2003) show that only a small part of an individual fault system is active at any one time. Alternatively, transient kinematic variation which may have been caused by coeval dyke intrusion at Kestanelik could have caused a change in fluid flow pathways by promoting rupturing on different veins at each earthquake event. Rupturing on different veins also causes the usage of different reservoirs of hydrothermal fluids, different ratios of fluid-wall rock interaction, and/or the mixing of hydrothermal fluid and meteoric water in different ratios. In either case, the full implications of the different number of mineralization events are yet to be explored. Stable isotopes (0, H and C) and fluid inclusion analyses can be used to investigate the varying fluid sources, mixing of them and different ratios of fluid-wall rock interaction (e.g. Urquhart, 2011) in infills of different veins and in different generations of fill in a single vein.

Although the fault hosted veins in Kestanelik have more than one phase of mineralization, damage zone structures only host one episode of mineralization. Three different explanations may be proposed for this case: **(1)** Damage zone structures developed only in the latest rupture event and thus hosted only one phase of mineralization. **(2)** The structures developed in the first rupture event and hosted the associated fluid flow and mineralization and the sealed damage zone structures deactivated during the following rupture events (as in Figure 6.3). The lack of reactivation of the damage zone structures may be due to the rotation of the

stress field optimum for reactivating these structures by transient stress variation, or to a strong, mechanical contrast at the boundary of these veins being a more effective location for future slip. In either case, some damage zone structures must have been sealed after the main fault hosted veins were present, because some of the damage zone veins curve towards the main vein. This curvature is most likely due to the competency difference between the altered host rock and vein quartz. **(3)** Damage zone structures could also have developed later as an effect of having the mechanical discontinuity in the wall rock caused by the filled major vein.

To sum up, damage zone structures adjacent to the main fault seem to only host one phase of mineralization and seal after the main fault is completely sealed. It has been suggested that more protracted fluid flow occur through damage zone structures compared to the main fault which is sealed rapidly (Micklethwaite and Cox, 2004, 2006; Sheldon and Micklethwaite, 2007). However, there is no evidence from the textures in the wall rock veins that is the case. Future work on the detailed geochemical, petrographical and stable isotope analyses from the different episodes of main veins and wall rock veins would be necessary to understand the temporal relationship within and between the main veins and wall rock veins.

## 6.3.2. Implications for gold exploration (prospect evaluation) in epithermal gold deposits

In the exploration for epithermal gold deposits, basically it is common practice to:

- Map the geology of the area, identify the areas of alteration by photo-geological maps, PIMA (portable infrared mineral analyser) analyses and consult remote sensing techniques such as thematic mapping, and geophysical techniques such as magnetic surveys and electrical methods in order to vector potential mineralized zones and to plan for drilling and sampling,

- Then, collect samples from rock, soil and drainage sediments for geochemical analyses to focus on the areas of geochemical anomalies for further drilling and detailed sampling programs.

In summary, in mineral exploration sector, much more focus is given to the geochemical aspects of the prospect areas (e.g. Buchanan, 1981; Corbett and Leach, 1997; Hedenquist *et al.*, 2000) than structural controls (Stenhouse and Cox, 2015). However, the results of this thesis have some important implications related to the structural and textural features of the prospect areas for the practice of gold exploration which are not routinely done in this sector.

➢ Mapping and understanding the geology of a known hydrothermal (e.g. porphyry, high sulphidation, low sulphidation) deposit, even without any geochronological data from the mineralization, may lead to a better understanding of the timing of mineralization, constrain a metallogenic age of the region, and help to discover other related potential hydrothermal deposits in the region.

➢ Mapping and study of the principal veins and wall rock veins alongside collection of structural data are powerful tools to unravel the kinematics of the vein system. Correlation of the kinematics of the mineralized or high-grade vein system along with timing of the mineralization may help to discover the areas or targets by defining the favourable orientation for structures to the mineralization.

➢ As repeated boiling and associated hydrothermal brecciation mask the effects of shearing and result in multiple overprinting of textures, key features such as the shear textures may be missed if only macroscopic observation is made from the outcrop or drill cores; therefore petrographic investigation of vein material and delineating the ore-vein textures addressing multiple boiling and silicification phases (especially close to the vein margins) is strongly advised.

➢ The understanding of textures showing clogging and subsequent boiling of the hydrothermal systems in correlation with structural ease or enhancement of fluid flow along the conduits may contribute to the target assessment in epithermal systems as the gold precipitation is

strongly enhanced by boiling (e.g. Hedenquist *et al.*, 2000) and oxidation in low sulphidation epithermal gold deposits.

➢ Mapping and petrographical analysis of the ore-vein textures both on the outcrops and in drillcores together with the geochemical analysis of gold assay data not only helps to understand the likely gold deposition mechanism(s) but also the potential gold distribution within the deposits.

➢ Mapping specific structural positions such as bends (which may be caused by vertical or horizontal connectivity of the isolated vein segments) could permit the key locations of high gold grade to be identified faster, and to focus further drilling and assays.

## 6.3.3. Implications for 3D orebody modelling

3D modelling of an orebody in the subsurface and subsequent evaluation of the size and extent of the orebody should serve as the basis of (1) further mineral exploration program and (2) resource estimation of the mineral deposit. In the mineral exploration industry, 3D orebody models are generally created automatically by geological modelling software upon selecting the geostatistical interpolation method (Stenhouse *et al.*, 2014). The modelling can be a difficult task owing to the complex nature of the orebodies, and wrong interpretations may cause large costs. For this reason, it is crucial to develop accurate models. In order to minimize the model uncertainties (such as the ones given in chapter 4.4.2) and make the interpretations better, recommendations on the basis of the experience gained during this PhD research are as follows:

✓ Mapping the geology of the deposit area together with post-mineral faults,

✓ Accurate mapping of vein outcrop using a highly sensitive Trimble GPS (±0.1cm),

- ✓ Collecting detailed structural data (attitude, thickness, infill type) from the major veins and vein associated structures,

- ✓ Examination of textures of major veins and wall rock veins from the surface,

- ✓ Adjusting the drillhole locations based on not only the assay results of vein rock samples, but also on the geometry of the vein surfaces i.e. the more complex vein outcrop geometry, more frequent drillhole locations,

- ✓ Adding structural data collection to the drill core logging (e.g. Stenhouse *et al.*, 2014),

- ✓ Adding textural data collection to the drillcore logging,

- ✓ Taking high resolution photos from the drillcores especially from QV intersections,

- ✓ Finally, selecting the most appropriate geostatistical interpolation method for the creation of the model based on the distribution of the data (i.e. grid data-kriging method, skewed data-natural neighbour method).

In this study, drillhole data was supplied by Chesser Resources. A flow chart illustrating the suggested model building methodology for future explorationists for the modelling of vein type epithermal gold deposits is given in Figure 6.4.
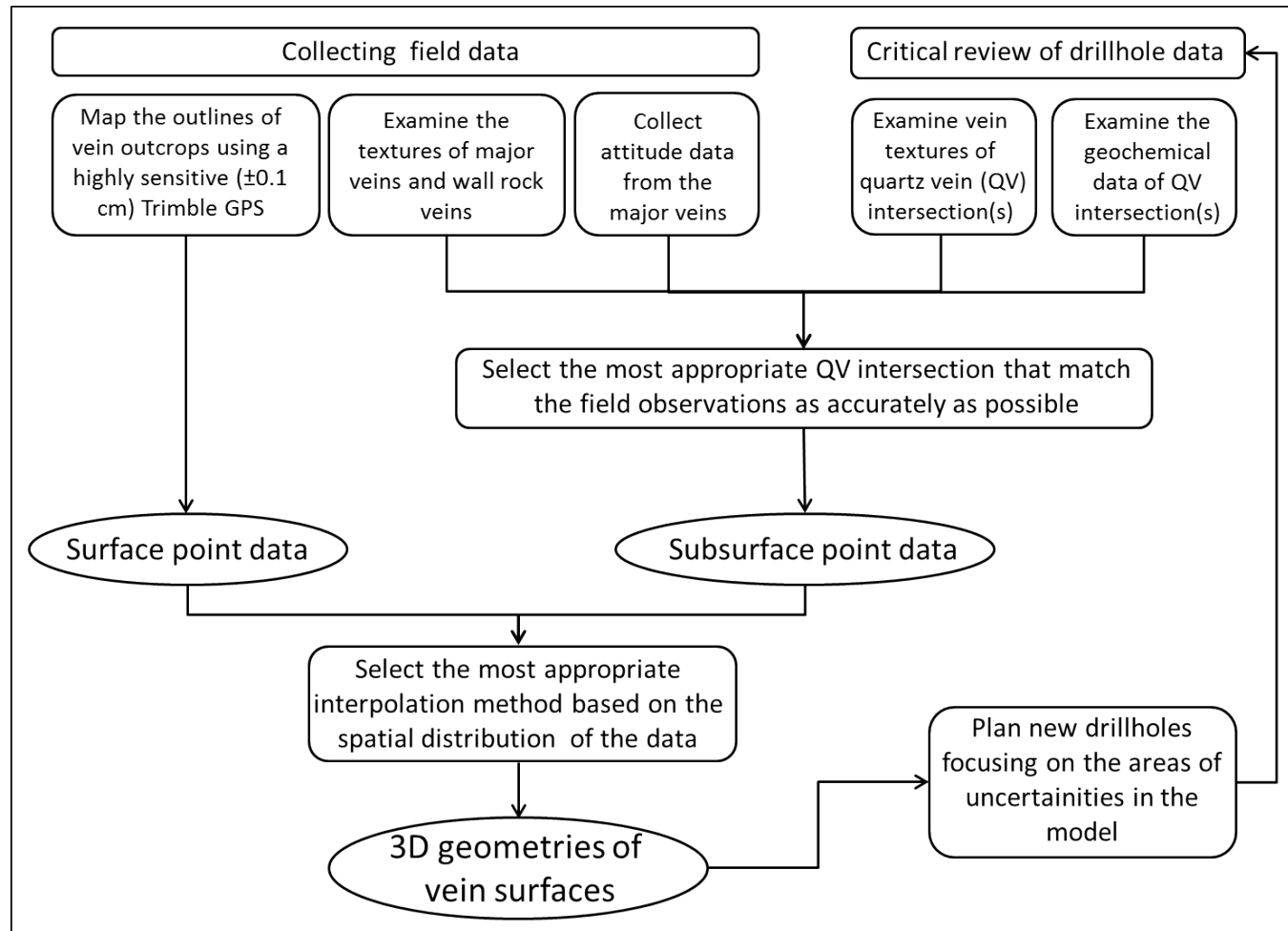
**Figure 6.4**. Flow chart illustrating the model building methodology, which could be applied at future exploration sites. Note that there is a feedback loop between developing an initial model, using this to plan a second campaign of drilling and revisiting the model.

# Chapter 7: Conclusions and Further Work

## 7.1. Conclusions of the study

The research presented in this thesis has (1) constrained the evolution of the Kestanelik vein-hosted LS epithermal gold deposit, (2) enhanced our understanding of permeability enhancement mechanisms in epithermal system, and (3) presented implications for gold exploration and a new workflow for 3D orebody modelling epithermal gold deposits.

Detailed geological mapping of the study area from surface exposures, drill pad exposures and drill core has revealed that:

i. The mineralization in Kestanelik is associated with major quartz veins, as well as sheeted quartz veins in the valley and, wall rock veins surrounding the major quartz veins.

ii. The veins are hosted by Lutetian quartz-feldspar-hornblende porphyry and Paleozoic mica schist, and the majority of the veins are hosted in the schist.

iii. The veins are enveloped by a hydrothermal argillic alteration halo dominated by illite and rarely smectite resulted from the circulation of epithermal fluids.

iv. The age of the mineralization, bracketed by cross cutting relations, is Late Lutetian-Early Priabonian.

v. The veins have a length of several tens to several hundreds of meters and their outcrop widths vary between 0.8 and 13.6 m on the surface. They trend either E-W or NE-SW, and have locally irregular strikes or dips.

vi. Host rock schist around the NE-SW trending veins does not change foliation adjacent to the veins and these veins have very sharp contacts with the schist. In contrary, around E-W trending K2 vein and NE-SW trending K3W vein the schist changes its foliation orientation and is highly fractured and veined. Porphyry around the eastern segment of the K3 vein (K3E) is highly fractured and brecciated. The porphyry around the E-W trending Karatepe

vein and NE-SW trending Topyurt vein components is deformed by extensional wall rock veins.

Kinematics and paleostress analysis have revealed that:

i. From their geometries and rare kinematic indicators, E-W trending veins are characterized as left lateral faults, whilst NE-SW trending veins are characterized as extensional (Mode I) fractures.

ii. The kinematics of the vein system is consistent with formation in a single local stress field. The inferred directions of the principal stresses indicate almost NE-SW oriented sub-horizontal compression. Majority of the faults in the area also seems to have a similar consistent stress field.

iii. Horizontal $\sigma 1$ and near vertical $\sigma 2$ indicate transcurrent tectonics.

Detailed structural and textural studies of quartz veins have revealed that:

i. The mineralization is low sulphidation epithermal type evident from pseudo-bladed quartz, colloform to crustiform quartz, comb to cockade vein textures and hydrothermal breccias.

ii. Boiling, mixing (hypogene oxidation) and supergene enrichment (supergene oxidation) are the likely mechanisms of gold deposition, because gold in the veins is associated with boiling related textures and both hypogene and supergene iron-oxides.

iii. Banded texture has the most profound effect on the high gold grades.

iv. The epithermal vein system has been subjected to erosion because silica sinter, indicative of the surface effusions of such hydrothermal deposits, is missing in the area. A general change of quartz textures from chalcedonic superzone in the north through to textures from crystalline superzone in the south shows that paleodepth and level of erosion in the Kestanelik vein system increases from the north to the south.

v. Most of the veins at their upper levels have cement supported chaotic breccias with clasts displaying various textures representing different depths of formation cemented by quartz-iron oxides. Multiple episodes of

215

brecciation, fluid flow and associated mineralization are recorded in the veins implying that the veins were reactivated and opened up multiple times after they were completely sealed and permeability was lost.

vi. Cataclasite and tectonic breccia of wall rocks and early quartz, hydrothermal crackle breccias, and cement supported chaotic breccias of pre-existing vein infill, all of which are cemented by late iron-oxide-bearing quartz indicate that coseismic rupturing and hydraulic fracturing are two major permeability enhancement mechanisms which would have caused repeated reactivation of clogged permeable pathways.

vii. Fault hosted veins are reactivated along their footwall contact with the host rocks, and extensional veins are opened along either margin.

viii. Transient local stress variation, caused by syn-mineral dyke intrusion, also has the potential to enhance permeability on mis-oriented surfaces and at locations where the dip changes on vein planes.

ix. Two phases of mineralization were determined from the E-W trending fault-hosted veins, while at least three were picked up from the NE-SW trending extensional (Mode I opening) ones which implies that an earthquake event does not affect all of the veins at once.

<u>3D modelling of the vein geometries in the subsurface together with some basic statistical analyses of vein geometries-related gold grades has revealed that:</u>

i. Thickness of the veins decreases with depth and that the veins generally have a flaring upwards geometry.

ii. The veins have multiple locations at depth where the dip changes (i.e. the veins have vertically segmented sections with differing dips).

iii. 78.6% of the bends host high gold grade showing these areas are more favorable structural locations for gold precipitation compared to the more smooth and planar sections of the veins.

iv. Presence of 85.4% of samples containing high gold within the schist hosted veins which is higher than the percentage of bends (~79%) having high gold

216

grade indicating that the host rock geology has a greater effect than bends on the localization of the gold precipitation.

**To sum up, the research presented in this thesis:**

1. has highlighted the permeability enhancement mechanisms in epithermal systems by detailed structural and textural evidences which also have been accepted by a peer-review journal (Gulyuz et al., 2017).
2. has developed a story for the geological and structural evolution of the Kestanelik gold deposit for the first time and linked it to the regional tectonics, magmatism and associated metallogeny.
3. has emphasized the importance of collecting detailed structural and textural data for gold exploration and developed a proposed workflow methodology for 3D orebody modelling for further exploration and resource estimation.

## 7.2. Further Work

The further work listed below need to be addressed to minimize the uncertainties discussed in Chapter 6 and to explore the full implications of the research.

➢ Hypogene hematite in the veins could be dated by (U+Th)/He dating to obtain a quantitative and more precise age of the epithermal mineralization at Kestanelik, as the age inferred is based on the cross-cutting relationship.

➢ Fluid inclusions of the vein quartz and/or calcite could be analysed to validate (1) the low sulphidation type of the epithermal mineralization and (2) boiling event both of which were determined from the diagnostic LS epithermal and boiling textures.

➢ Stable isotope (C,H,O) analyses of fluid inclusions in the hypogene vein minerals could be used to (1) further constrain the fluid mixing event, (2) to investigate the possible varying fluid sources in the epithermal system, and (3) to understand the different ratios of fluid-wall rock interaction.

- Detailed geochemical and petrographic analyses of hypogene vein minerals could be used together with the stable isotope analyses to understand the temporal relationship within and between the main veins and wall rock veins, because the different stages of mineralization determined from the textural relationships in the veins cannot be correlated with each other.

- Numerical simulations could be used to constrain the behaviour of the vein structures in different host rock lithologies at the surface and in the subsurface in order to understand the different orientations of the veins in different host rocks and the reason of along-dip bending in the subsurface.

- Detailed structural field and paleomagnetic studies could be conducted to get more precise information about the tilting at Kestanelik and vertical axis rotations in the Biga Peninsula in order to reconstruct the kinematics of the vein system during the mineralization, and link it to the regional tectonics.

# References

Adams, S.F. 1920. A microscopic study of vein quartz. *Economic Geology*, **15**, 623-664.

Adamson, A.W. 1976. *Physical chemistry of surfaces*. John Wiley and Sons, New York, 698.

Akay, E. & Erdoğan, B. 2004. Evolution of Neogene calc-alkaline to alkaline volcanism in the Aliaga- Foca region (Western Anatolia, Turkey). *Journal of Asian Earth* Science, **24**, 367–387.

Aldanmaz, E., Pearce, J.A., Thirlwall, M.F., & Mitchell, J.G. 2000. Petrogenetic evolution of late Cenozoic post-collision volcanism in Western Anatolia, Turkey. *Geothermal Research*, **102**, 67- 95.

Alıcı, P., Temel, A. & Gourgaud, A. 2002. Pb-Nd-Sr isotope and trace element geochemistry of Quaternary extension-related alkaline volcanism: a case study of Kula region (western Anatolia, Turkey). *Journal of Volcanology and Geothermal Research*, **115**, 487–510.

Allmendinger, R.W., Cardozo, N.C. & Fisher, D. 2013. *Structural Geology Algorithms: Vectors & Tensors*. Cambridge University Press, Cambridge, 289.

Altunkaynak, Ş., 2004. Eruptive history of post collisional bimodal volcanism in western Anatolia (Turkey): the Foça volcanic centre. *5 ISEMG, Thessaloniki, Greece, 14-20 April 2004, Proceedings*, **3**, 1263-1266.

Altunkaynak, Ş., 2007. Collision-driven slab break off magmatism in northwestern Anatolia, Turkey. *Journal of Geology*, **115**, 63-82.

Altunkaynak, S. & Dilek, Y. 2006. Timing and nature of postcollisional volcanism in western Anatolia and geodynamic implications. In: Dilek, Y. & Pavlides, S. (eds) Postcollisional tectonics and magmatism in the Mediterranean region and Asia. *Geological Society of America Special Paper*, **409**, 321–351.

Altunkaynak, Ş. & Genç, Ş.C. 2008. Petrogenesis and time-progressive evolution of the Cenozoic continental volcanism in the Biga Peninsula, NW Anatolia (Turkey). *Lithos*, **102**, 316–340.

Angelier, J. 1979. Determination of mean principal direction of stress for a given fault population. *Tectonophysics*, **56**, 17-26. 142

Angelier, J. 1984. Tectonic analysis of fault slip data sets. *Journal of Geophysical Research*, **89**, 5835-5848.

Angelier, J. 1989. From orientation to magnitudes in paleostress determinations using fault slip data. *Journal of Structural Geology*, **11**, 37-50.

Angelier, J. 1994. *Fault slip analysis and paleostress reconstruction*. In: P.L. Hancock (Editor), Continental deformation. Pergamon Press, Oxford, 53-101.

Armijo, R., Carey, E. & Cisternas, A. 1982. The inverse problem in microtectonics and the separation of tectonic phases. *Tectonophysics*, **82**, 145-160.

Aslaner, M. 1965. Etude geologique et petrographique de la region d' Edremit-Havran (Turquie). *MTA Bulletin,* 119.

Axen, G.J. 1992. Pore pressure, stress increase, and fault weakening in low-angle normal faulting. *Journal of Geophysical Research*, **97**, 8979– 8991.

Aydın, M., Demir, O., Özçelik, Y., Terzioğlu, N. & Satır, M. 1995. A geological revision of İnebolu, Devrekani, Ağlı and Küre areas: new observations in Paleo-Tethys - Neo-Tethys sedimentary successions. In: Erler, A., Ercan, T., Bingöl, E., Örçen, S. (Eds.), Geology of the Black Sea Region. *MTA Bulletin Special Publication,* 33–38.

Aygül, M., Topuz, G., Okay, A. I., Satır, M., & Meyer, H. P. 2012. The Kemer Metamorphic Complex (NW Turkey), a subducted continental margin of the Sakarya zone. *Turkish Journal of Earth Sciences*, **21**, 19–35.

Barton, P.B., Jr., & Skinner, B.J., 1979. Sulfide mineral stabilities, in Barnes, H.L., ed., *Geochemistry of Hydrothermal Ore Deposit*s, Wiley Interscience, New York, 278-403.

Bateman, A.M. 1950. *Economic Mineral Deposits.* John Wiley and Sons. Inc., New York, 916.

Bates, R.L. & Jackson, J.A. 1987. *Glossary of geology*. American Geological Institute, Alexandria, Virginia, 788.

Beccaletto, L., Bartolini, A.C., Martini, R., Hochuli, P.A. & Kozur, H. 2005. Biostratigraphic data from Çetmi Melange, northwest Turkey: palaeogeographic and tectonic implications. *Palaeogeography, Palaeoclimatology, Palaeoecology,* **221**, 215– 244.

Beccaletto, L., & Jenny, C. 2004. Geology and Correlation of the Ezine Zone: A Rhodope Fragment in NW Turkey? *Turkish Journal of Earth Sciences*, **13**, 145-176.

Bethke, P.M. 1984. Controls on base and precious metal mineralization in deeper epithermal environment. *U.S. Geological Survey open-file report 84-890*, 40.

Bilgin, İ. 1999. *Ezine (Canakkale) Ofiyolit ve Metamorfitlerinin Petrolojisi*. Institute of Natural and Applied Sciences, İstanbul University, İstanbul, PhD Thesis, 152 (in Turkish).

Bingöl, E., Akyürek, B., & Korkmazer, B. 1973. Biga Yarımadası'nın Jeolojisi ve Karakaya Formasyonu'nun bazı özellikleri, *MTA 50. Anniversary, Proceedings*, 71-77 (in Turkish).

Bingöl, E. 1974. Discussions on the metamorphic map of Turkey in a scale of 1:2,500,000 and geotectonic evolution of some metamorphic belts. *MTA Bulletin*, **83**, 119–131.

Bingöl, E., Delaloye,M. & Genç, S. 1994. Magmatism of northwestern Anatolia. *International Volcanological Congress*, IAVCEI 1994, Excursion Guide (A3).

Boyle, R.W. 1979. The geochemistry of gold and its deposits. *Canada Geological Survey Bulletin*, **280**, 584.

Brown, K.L. 1986. Gold deposition from geothermal discharges in New Zealand. *Economic Geology*, **81**, 979-988.

Buchanan, L.J. 1981. Precious metal deposits associated with volcanic environments in the southwest. *In*: Dickson, W.R. & Payne, W.D. (eds) *Relations of Tectonics to Ore Deposits in the Southern Cordillera.* Arizona Geological Society Digest, **14**, 237-262.

Burnside, N.M., Shipton, Z.K., Dockrill, B. & Ellam, R.M. 2013. Man-made versus natural $CO_2$ leakage: A 400 k.y. history of an analogue for engineered geological storage of $CO_2$. *Geology*, **41**, 471–474.

Byerlee, J. 1993. Model for episodic flow of high-pressure water in fault zones before earthquakes. *Geology*, 303-306.

Caine, J., Evans, J., & Forster, C. 1996. Fault zone architecture and permeability structure. *Geology*, **24**, 1025–1028.

Cardozo, N. & Allmendinger, R. W. 2013. Spherical projections with OSXStereonet: *Computers & Geosciences*, **51**, no. 0, 193-205.

Cavazza, W., Okay, A. I., & Zattin, M. 2009. Rapid early-middle exhumation of the Kazdağ Massif (Western Anatolia). *International Journal of Earth Science*, **98**, 1935–1947.

Cooke, D.R. & Simmons, S.F. 2000. Characteristics and genesis of epithermal gold deposits. *Society of Economic Geologists Review*s, **13**, 221-244.

Corbett, G.J., 2002. Structural controls to Porphyry Cu-Au and Epithermal Au-Ag deposits in Applied Structural Geology for Mineral Exploration. *Australian Institute of Geoscientists Bulletin,* **36**, 32-35.

Corbett, G.J., Leach, T.M. 1997. *Southwest Pacific Rim gold - copper systems: structure, alteration and mineralization*. Workshop manual, 185.

Cox, S., Knackstedt, M. & Braun, J. 2001. Principles of structural control on permeability and fluid flow in hydrothermal systems. *Reviews in Economic Geology*, **14**, 1-24.

Cox, S. 2005. Coupling between Deformation, Fluid Pressures, and Fluid Flow in Ore-Producing Hydrothermal Systems at Depth in the Crust. *Economic Geology*, **100**, 39-75.

Cowan, D.S. 1999. Do faults preserve a record of seismic slip? A field geologist's opinion. *Journal of Structural Geology*, **21**, 995-1001.

Curewitz, D. & Karson, J.A. 1997. Structural settings of hydrothermal outflow: Fracture permeability maintained by fault propagation and interaction. *Journal of Volcanology and Geothermal Research*, **79**, 149–168.

Davatzes, N. C., Eichhubl, P. & Aydin, A. 2005. Structural evolution of fault zones in sandstone by multiple deformation mechanisms: Moab fault, southeast Utah. *Geological Society of America Bulletin*, **117**, 135–148.

Davatzes, N.C. & Hickman, S.H. 2005. Controls on fault-hosted fluid flow; Preliminary results from the Coso geothermal field, CA*. Geothermal Research Council Transactions*, paper 144.

Delaloye, M. & Bingöl, E. 2000. Granitoids from western and northwestern Anatolia: geochemistry and modeling of geodynamic evolution. *International Geology Reviews*, **42**, 241-268.

Delvaux, D., Moeys, R., Stapel, G., Petit, C., Levi, K., Miroshenko, A., Ruzhıch, V., & Sankov, V. 1997. Paleostress reconstructions and geodynamics of the Baikal region, Central Asia, Part 2. Cenozoic rifting. *Tectonophysics*, **282**, 1–38.

Dilek, Y. & Altunkaynak, S. 2007. Cenozoic crustal evolution and mantle dynamics of post-collisional magmatism in western Anatolia. *International Geology Review*, **49**, 431–453.

Dilek, Y., Imamverdiyev, N., Altunkaynak, S., 2010. Geochemistry and tectonics of Cenozoic volcanism in the Lesser Caucasus (Azerbaijan) and the peri-Arabian region: collision-induced mantle dynamics and its magmatic fingerprint. *International Geology Review*, **52** , 536–578.

Dong, G., Morrison, G. & Jaireth, S. 1995. Quartz textures in epithermal veins, Queensland— classification, origin, and implication. *Economic Geology*, **90**, 1841–1856.

Dowling, K. & Morrison, G.W. 1990. Applications of quartz textures to the classification of gold deposits using North Queensland examples. *Economic Geology Monograph*, **6**, 342-355.

Dönmez M, Akçay A.E., Genç, C., Acar, Ş.  2005. Middle-Upper Eocene volcanism and marine ignimbrites of Biga Peninsula. *MTA Bulletin*, **131**, 49-61.

Dreger, D.S., Tkalcic, H. & Johnston, M. 2000. Dilational processes accompanying earthquakes in the Long Valley Caldera. *Science*, **288**, 122–125.

Ercan, T., Satir, M., Kreuzer, H., Türkecan, A., Günay, E., Çevikbas, A., Ateş, M. & Can, B. 1985. Batı Anadolu Senozoyik volkanitlerine ait yeni kimyasal, izotopik ve radyometrik verilerin yorumu. *Bulletin of the Geological Society of Turkey*, **28**, 121–136 (in Turkish).

Ercan, T., Satır, M., Steinitz, G., Dora, A., Sarıfakıoğlu, E., Adis, C., Walter, H.J. & Yıldırım, T., 1995. Biga Yarımadası ile Gökçeada Bozcaada ve Tavşalı adalarındaki (KB Anadolu) Tersiyer Volkanizmasının özellikleri: *MTA Bulletin*, 117, 55-86 (in Turkish).

Ercan, T., Satir, M., Steinitz, G., Dora, A., Sarifakioglu, E., Adis, C., Walter, H.J. & Yildirim, T. 1998. Features of Tertiary volcanism around the Sea of Marmara. *MTA Bulletin*, 120, 97–118.

Erkül, F., Helvacı, C. & Sözbilir, H. 2005. Stratigraphy and geochronology of the Early Miocene volcanic units in the Bigadiç, Borate Basin, western Turkey. *Turkish Journal of Earth Sciences*, **14**, 227–253.

Etchecopar, A., Vasseur, G. & Daigniers, M. 1981. An inverse problem in microtectonics for the determination of stress tensors from fault striation analysis. *Journal of Structural Geology*, **3**, 51-65.

Fournier, R.O. 1985. The behavior of silica in hydrothermal solution. *Reviews in Economic Geology*, **2**, 45-61.

Fournier, R.O. 1989. Geochemistry and dynamics of the Yellowstone National Park hydrothermal system. *Annual Review of Earth and Planetary Sciences*, **17**, 13–53.

Frenzel, M. & Woodcock, N.H. 2014. Cockade breccia: product of mineralisation along dilational faults. *Journal of Structural Geology*, **68**, 194-206.

Fry, N. 1999. Striated faults: visual appreciation of their constraint on possible paleostress tensors. *Journal of Structural Geology,* **21**, 7-21.

Fukuyama, E., Kubo, A., Kawai, H. & Nonomura, K. 2001. Seismic remote monitoring of stress field. *Earth, Planets and Space*, **53**, 1021–1026.

Gammons, C.H. & Williams-Jones A.E. 1997. Chemical mobility of gold in the porphyry-epithermal environment. *Economic Geology*, **92**, 45-59.

Genç, S.C., 1998. Evolution of the Bayramic Magmatic Complex, Northwestern Anatolia. *Journal of Volcanology and Geothermal Research*, **85**, 233-249.

Genç, S. C. & Yılmaz, Y. 1997. An example of postcollisional magmatim in northwestern Anatolia: the Kızderbent Volcanics (Armutlu Peninsula, Turkey). *Turkish Journal of Earth Sciences*, **6**, 33–42.

Giggenbach, W.F. & Stewart, M.K. 1982. Processes controlling the isotopic composition of steam and water discharges from steam vents and steam-heated pools in geothermal areas. *Geothermics,* **11**, 71-80.

Gomez, F., Meghraoui, M., Darkal, A. N., Hijazi, F., Mouty, M., Suleiman, Y., Sbeinati, R., Darawcheh, R., Al-Ghazzi, R., & Barazangi, M. 2003. Holocene faulting and earthquake recurrence along the Serghaya branch of the Dead Sea fault system in Syria and Lebanon. *Geophysical Journal International*, **153**, 658-674.

Gulyuz N., Shipton, Z.K., Kuscu, I., Lord, R.A., Kaymakci, N., Gulyuz, E. & Gladwell, D.R., 2017. Repeated reactivation of clogged permeable pathways in

epithermal gold deposits: Kestanelik epithermal vein system, NW Turkey. *Journal of the Geological Society* (accepted).

Gümüş, A. 1964. Contribution a l'etude geologique de secteur serpentrional de Kalabak köy-Eymür Köy region D'Edremit, Turqie, *MTA Bulletin*, **117**, 1-109.

Hammond, K.J. & Evans, J.P. 2003. Geochemistry, mineralization, structure, and permeability of a normal-fault zone, Casino mine, Alligator Ridge district, north central Nevada. *Journal of Structural Geology*, **25(5)**, 717-736.

Hardcastle, K. C. 1989. Possible paleostress tensor configurations derived from fault- slip data in eastern Vermont and western New Hampshire. Tectonics, 8, 265-284.

Harris, N.B.W., Kelley, S., & Okay, A.I. 1994. Post-collision magmatism and tectonics in northwest Anatolia. *Contributions to Mineralogy and Petrography*, **117**, 241-251.

Hayba, D.O., Bethke, P.M., Heald, P., & Foley, N.K., 1985. Geologic, mineralogic and geochemical characteristics of volcanic-hosted epithermal precious-metal deposits. *Reviews in Economic Geology*, **2**, 129-167.

Heald, P., Hayba, D.O., & Foley, N.K., 1987. Comparative anatomy of volcanic hosted epithermal deposits: Acid-sulfate and adularia-sericite types. *Economic Geology*, **82**, 1-26.

Hedenquist, J.W. 1990. The thermal and geochemical structure of Broadlands-Ohaaki geothermal system. *Geothermics*, **19**, 151-185.

Hedenquist, J.W., Arribas M. A. & Gonzalez-Urien, E. 2000. Exploration for epithermal gold deposits. *Reviews in Economic Geology*, **13**, 245-277.

Hedenquist, J.W. & Henley, R.W. 1985.  The importance of $CO_2$ on freezing point measurements of fluid inclusions: Evidence from active geothermal systems and implications for epithermal ore deposition. *Economic Geology*, **80**, 1379-1406.

Hedenquist, J.W. & Henley, R.W. 1985b. Hydrothermal eruptions in the Waiotapu geothermal system, New Zealand: their origin, associated breccias, and relation to precious metal mineralization. *Economic Geology*, **80**, 1640-1668.

Hedenquist, J.W. & Lowenstern, J.B. 1994. The role of magmas in the formation of hydrothermal ore deposits. *Nature*, **370**, 519-527.

Hedenquist, J.W., Matsuhisa, Y., Izawa, E., White, N.C., Giggenbach, W.F. & Aoki, M. 1994. Geology, geochemistry, and origin of high sulfidation cu-au mineralization in Nansatsu district, Japan. *Economic Geology*, **89**, 1-30.

Hedenquist, J.W. & Sillitoe, R.H. 2003. Linkages between volcanotectonic settings, ore-fluid compositions, and epithermal precious metal deposits. *Society of Economic Geologists Special Publication*, **10**, 315-343.

Henley, R.W. 1985. The geothermal framework of ephithermal deposits. *Reviews in Economic Geology*, **2**, 1-24.

Henley, R.W., & Ellis, A.J. 1983. Geothermal systems, ancient and modern. *Earth Science Reviews*, **19**, 1-50.

Henley, R.W., Truesdel, A.H., and Barton, P.B., Jr. 1984. Fluid-mineral equilibria in hydrothermal systems. *Reviews in Economic Geology*, **1**, 267.

Hill, D.P. 1977. A model for earthquake swarms. *Journal of Geophysical Research*, **82**, 1347–1352.

Hill, D.P., Reasenberg, P.A., Michael, A., Arabaz, W.J., Beroza, G., Brumbaugh, D., Brune, J.N., Castro, R., Davis, S., dePolo, D., Ellsworth, W.L., Gomberg, J., Harmsen, S., House, L., Jackson, S.M., Johnston, M.J.S., Jones, L., Keller, R., Malone, S., Munguia, L., Nava, S., Pechmann, J., Sanford, C.A., Simpson, R.W., Smith, R.B., Stark, M., Stickney, M., Vidal, A., Walter, S., Wong, V. & Zollweg, J. 1993. Seismicity remotely triggered by the Magnitude 7.3 Landers, California, Earthquake. *Science*, **260**, 1617–1623.

Hinsbergen, D.J.J., Kaymakcı, N., Spakman, W., Torsvik, T.H. & Amaru, M. 2010. Reconciling geological history with mantle structure in western Turkey. *Earth and Planetary Science Letters*, **297**, 674-686.

Hulin, C.D. 1929. Structural control of ore deposition. *Economic Geology*, **24**, 15-49.

Houston, M. 2013. *Report on the Exploration Potential and Geology of the Kestanelik Project*. Unpublished company report, 36.

Innocenti, F., Agostini, S., Di Vincenzo, G., Doglioni, C., Manetti, P., Savaşcın, M. Y. & Tonarini, S. 2005. Neogene and Quaternary volcanism in Western Anatolia: Magma sources and geodynamic evolution. *Marine Geology*, **221**, 397–421.

Jébrak, M. 1997. Hydrothermal breccias in vein-type ore deposits: a review of mechanisms, morphology and size distribution. *Ore Geology Reviews*, **12**, 111-134.

Kalafatçıoğlu, A. 1963. Ezine civarının ve Bozcaada'nın jeolojisi, kalker ve serpantinlerinin yaşı. *MTA Bulletin,* **60**, 61-70 (in Turkish).

Kaymakci, N., Aldanmaz, E., Langereis, C., Spell, T.L., Gurer, O.F. & Zanetti, K.A. 2007. Late Miocene transcurrent tectonics in NW Turkey: evidence from palaeomagnetism and $^{40}Ar–^{39}Ar$ dating of alkaline volcanic rocks. *Geological Magazine*, **144**, 379–392.

Kaymakci, N. Özcelik, Y. White, S.H. & Van Dijk, P.M. 2009. Tectono-stratigraphy of the Çankiri Basin: Late Cretaceous to Early Miocene evolution of the Neotethyan Suture Zone in Turkey. *In*: Van Hinsbergen, D.J.J., Edwards, M.A. & Govers, R. (eds) *Geodynamics of Collision and Collapse at the Africa-Arabia-Eurasia subduction zone*, Geological Society, London, Special Publications, **311**, 67-106.

Ketin, İ. 1966. Tectonic units of Anatolia (Asia Minor). *MTA Bulletin*, **66**, 23-34.

Köprübaşı, N. & Aldanmaz, E. 2004. Geochemical constraints on the petrogenesis of Cenozoic I-type granitoids in Northwest Anatolia, Turkey: Evidence

for magma generation by lithospheric delamination in a post-collisional setting. *International Geology Review*, **46**, 705–729.

Kuşcu, İ. 2013. *Mineralogy and petrography of twelve samples of an unknown origin from Chesser Resources, Turkey* (unpublished report), 14.

Lalou, C., Reyss, J.L., Brichet, E., Arnold, M., Thompson, G., Fouquet, Y. & Rona, P.A. 1993. New age data for Mid-Atlantic Ridge hydrothermal sites: TAG and Snakepit geochronology revisited. *Journal of Geophysical Research*, **98**, 9705-9713.

Le Pichon, X., & Angelier, J. 1979. The Hellenic arc and Trench system: a key to the neotectonic Evolution of the Eastern Mediterranean Area. *Tectonophysics*, **60**, 1-42.

Lindgren W. 1901. Metasomatic processes in fissure veins. *American Institute of Mining Engineers Transactions*, **30**, 578-692.

Lindgren, W. 1922. A suggestion for the terminology of certain mineral deposits. *Economic Geology*, **17**, 292-294

Lindgren W. 1933. *Mineral deposits*. Mc-Graw Hill, New York, 930.

Lockner, D.A. & Beeler, N.M. 2002. Rock failure and earthquakes. *International Handbook of Earthquake and Engineering Seismology,* **81**, 505-537.

Lovering T.G. 1972. Jasperoid in the United States- its characteristics, origin, and economic significance. *U.S. Geological Survey Professional Paper*, **710**, 164.

Lunn, R. J., Willson, J. P. Shipton, Z. K. & Moir, H. 2008. Simulating brittle fault growth from linkage of preexisting structures. *Journal of Geophysical Research*, **113,** B07403.

McKenzie, D.P. 1972. Active tectonics of the Mediterranean region. *Geophysical Journal International*, **30**, 109-185.

Mckenzie, D.P. 1978. Active Tectonics of the Alpine-Himalayan Belt: The Aegean Sea and Surroundings Regions (Tectonics of the Aegean Region). *Geophysical Journal International*, **55**, 217-254.

McLean, N. 2011. *43-101 Technical Report on the Kestanelik project, Çanakkale province, Turkey,* 68.

Meldrum, S. J. 2009. *Şahinli Epithermal Gold Project, Biga Peninsula, Turkey: Data Compilation and Review*. Unpublished Company Report, 12.

Meulenkamp, J.E., Wortel, W.J.R., Van Wamel, W.A., Spakman, W., & Hoogerduyn, S.E. 1988. On the Hellenic subduction zone and geodynamic evolution of Crete in the late middle Miocene. *Tectonophysics,* **146**, 203-215.

Micklethwaite, S. & Cox, S. 2004. Fault-segment rupture, aftershock-zone fluid flow, and mineralisation. *Geology*, **32**, 813-816.

Micklethwaite, S. & Cox, S. 2006. Progressive fault triggering and fluid flow in aftershock domains: Examples from mineralized Archean fault systems. *Earth and Planetary Science Letters*, **250**, 318-330.

Micklethwaite, S. 2009. Mechanisms of faulting and permeability enhancement during epithermal mineralisation: Cracow goldfield, Australia. *Journal of Structural Geology*, **31**, 288-300.

Micklethwaite, S., Sheldon H.A. & Baker, T. 2010. Active fault and shear processes and their implications for mineral deposit formation and discovery. *Journal of Structural Geology*, **32**, 151-165.

Moir, H., Lunn, R., Micklethwaite, S. & Shipton, Z. 2013. Distant off-fault damage and gold mineralization: the impact of rock heterogeneity. *Tectonophysics*, **608**, 461-467.

Moir, H., Lunn, R.J., Shipton, Z.K. & Kirkpatrick, J.D. 2010. Simulating Brittle Fault Evolution from Networks of Pre-existing Joints Within Crystalline Rock, *Journal of Structural Geology*, **32**, 1742-1753.

Morgan, P.G. 1925. The so-called "pseudomorphs" quartz of Tertiary gold-silver veins. *Economic Geology*, **20,** 203-207.

Morisson, G., Guoyi, D., & Jareith, S. 1990. *Textural Zoning in Epithermal Quartz Vein*. Amira Project Gold Research Group, James Cook University of North Queensland, 247.

Nemcok, M., Kovac, D. & Lisle, R.J., 1999. A stress inversion procedure for polyphase calcite twin and fault/slip data sets. *Journal of Structural Geology,* **21**, 597-611.

Oehler, J.H. 1976. Hydrothermal crystallization of silica gel. *Geological Society of America Bulletin*, **87**, 1143-1152.

Okay, A. I., Harris, N. B. W. & Kelley, S. P. 1998. Exhumatioin of blueschists along a Tethyan suture in northwest Turkey. *Tectonophysics*, **285**, 275–299.

Okay, A.I., Monod, O., & Monie, P., 2002. Triassic blueschists and eclogites from northwest Turkey: vestiges of the Paleo-Tethyan subduction. *Lithos*, **64**, 155-178.

Okay, A.I. & Satır, M. 2000. Upper Cretaceous eclogite facies metamorphic rocks from the Biga Peninsula, northwest Turkey. *Turkish Journal of Earth Sciences*, **9**, 47-56.

Okay, A. I., & Satır, M. 2000b. Coeval plutonism and metamorphism in a latest Oligocene metamorphic core complex in Northwest Turkey. *Geological Magazine*, **137**, 495–516.

Okay, A.I., & Satır, M. 2006. Geochronology of Eocene plutonism and metamorphism in northwest Turkey: evidence for a possible magmatic arc. *Geodinamica Acta*, **19**, 251-266.

Okay, A.I., Satır, M., Maluski, H., Siyako, M., Monie, P., Metzger, R. & Akyüz S. 1996. Paleo- and Neo-Tethyan events in northwest Turkey: geological and geochronological constraints. *In*: Yin, A. & Harrison, M. (ed.) *Tectonics of Asia*, Cambridge University Press, Cambridge, 420-441.

Okay, A.I., Siyako, M. & Bürkan, K.A. 1990. Geology and tectonic evolution of the Biga Peninsula (in Turkish). *Bulletin of the Turkish Association of Petroleum Geologists*, **2**, 83-121.

Okay, A.I., Siyako, M., & Burkan, K.A. 1991. Geology and tectonic evolution of the Biga Peninsula, northwest Turkey. *Bulletin of the Technical University of İstanbul*, **44**, 191-256.

Okay, A.I. & Tüysüz, O. 1999. Tethyan sutures of northern Turkey. In: Durand B., Jolivet, L., Horváthand F. & Séranne, M. (eds) *The Mediterranean Basins: Tertiary extension within the Alpine orogen*, Geological Society, London, Special Publications, **156**, 475-515.

Orife, T. & Lisle, R.J. 2003. Numerical processing of paleostress results. *Journal of Structural Geology*, **25**, 949-957.

Önen, A.P. & Hall, R. 2000. Subophiolite metamorphic rocks from NW Anatolia, Turkey. *Journal of Metamorphic Geology*, **18**, 483-495.

Özcan, E., Less, G., Okay, A.I., Báldi-Beke, M., Kollanyi, K. & Yılmaz, İ. Ö. 2010. Stratigraphy and larger foraminifera of the Eocene shallow-marine and olistostromal units of the southern part of the Th race Basin, NW Turkey. *Turkish Journal of Earth Sciences*, **19**, 27–77.

Phillips, W. J. 1972. Hydraulic fracturing and mineralisation: *Journal of the Geological Society of London*, **128**, 337– 359.

Philips, W.R. & Griffen, D.T. 1981. *Optical mineralogy: The nonopaque minerals*. W.H. Freeman and Company, San Francisco, 677.

Pirajno, F. 2009. *Hydrothermal processes and mineral systems*. Geological Survey of Western Australia, Springer, Dordrecht, London, 1250.

Ransome, F.I. 1907. The association of alunite with gold in the Goldfield district, Nevada. *Economic Geology*, **2**, 667-692.

Reyes, A.G. 1990. Petrologogy of Philippine geothermal system and the application of alteration mineralogy to their assessment. *Journal of Volcanology and Geothermal Research*, **43**, 279-309.

Richardson-Bunbury, J. M. 1996. The Kula volcanic field, western Turkey: the development of a holocene alkalibasalt province and the adjacent normal faulting graben. *Geological Magazine,* **133**, 275–83.

Rimstidt, J.D. & Cole, D.R. 1983. Geothermal mineralization I: The mechanism of formation of the Beowawe, Nevada, Siliceous sinter deposit. *American Journal of Science*, **283**, 861-875.

Robb, L. 2005. *Introduction to Ore-forming Processes*. Blackwell Publishing, Malden, 373.

Roedder, E. 1984. Fluid inclusions. *Reviews in Mineralogy*, **12**, 644.

Roedder, Edwin and Bodnar, R.J. 1980. Geologic pressure determinations from fluid inclusion studies. *Annual Review of Earth and Planetary Science*, **8**, 263-301.

Rogers, A.F. 1917. A review of amorphous minerals. *Journal of Geology*, **25**, 515-541.

Rowe, C. D. & Griffith, W. A. 2015. Do faults preserve a record of seismic slip: A second opinion. Invited Review, *Journal of Structural Geology*, **78**, 1-26.

Rowland, J.V. & Sibson, R.H. 2004. Structural controls on hydrothermal flow in a segmented rift system, Taupo Volcanic Zone, New Zealand. *Geofluids*, **4**, 259–283.

Sanchez-Alfaro, P., Reich, M., Driesner, T., Cembrano, J., Arancibia, G., Perez-Flores, P., Heinrich, C.A., Rowland, J., Tardani, D., Lange, D. & Campos, E. 2016. The optimal windows for seismically-enhanced gold precipitation in the epithermal environment. *Ore Geology Reviews*, **79**, 463-473.

Sander, M.V. & Black, J.E. 1988. Crystallization and recrystallization of growth-zoned vein quartz crystals from epithermal systems – implications for fluid inclusion studies. *Economic Geology*, **83**, 1052-1060.

Sanematsu, K. Duncan, R., İmai, A. & Watanabe, K. 2005. Geochronological Constraints Using 40Ar/39Ar Dating on the Mineralization of the Hishikari Epithermal Gold Deposit, Japan. *Resource Geology*, **55(3)**, 249-266.

Saunders, J.A. 1990. Colloidal transport of gold and silica in epithermal precious-metal systems: evidence from the Sleeper deposits, Nevada. *Geology*, **18**, 757-760.

Savaşcın, M. Y. & Oyman, T. 1998. Tectonomagmatic evolution of alkaline volcanics at the Kirka-Afyon-Isparta structural trend, SW Turkey. *Turkish Journal of Earth Sciences*, **7**, 201–214.

Schoen, R., White, D.E & Hemley, J.J. 1974. Argillisation by descending acid at Steamboat springs, Nevada. *Clays and Clay Minerals*, **22**, 1-22.

Schöpfer, M.P.J., Childs, C. & Walsh, J.J. 2006. Localisation of normal faults in multilayer sequences. *Journal of Structural Geology*, **28**, 816-833.

Schöpfer, M.P.J., Childs, C., Walsh, J.J., Manzocchi, T. & Koyi, H.A. 2007. Geometrical analysis of the refraction and segmentation of normal faults in periodically layered sequences. *Journal of Structural Geology*, **29**, 318-335.

Schrader, F.S. 1912. A reconnaissance of the Jarbidge, Contact, and Elk mountain mining districts, Elko County, Nevada. *U.S. Geological Survey Bulletin*, **497**, 62.

Schrader, F.S. 1923. The Jarbidge mining district, Nevada. *U.S. Geological Survey Bulletin*, **741**, 86.

Schuiling, R.D. 1959. Uber eine praherzynische faltunggspase im Kazdağ kristallin, *MTA Bulletin*, **53**, 89-93.

Seyitoğlu, G., Anderson, D., Nowell, G. & Scott, B. 1997. The evolution from Miocene potassic to Quaternary sodic magmatism in western Turkey: implications

for enrichment processes in the lithospheric mantle. *Journal of Volcanology and Geothermal Research*, **76**, 127–147.

Sfondrini, G. 1961. Surface geological report on Ar/TPO/I/538 and 537. *TPAO Research Group Report Number*, 1429, 9.

Shaub, B.M. 1934. The cause of bending in fissure veins. *American Mineralogist*, **19**, 393-402.

Sheldon, H.A. & Micklethwaite, S. 2007. Damage and permeability around faults: Implications for mineralization. *Geology*, **34**, 903–906.

Sherlock, S., Kelley, S., Inger, S., Harris, N. & Okay, A.I., 1999. $^{40}$Ar-$^{39}$Ar and Rb/Sr geochronology of high-pressure metamorphism and exhumation history of the Tavsanli Zone, NW Turkey. *Contributions to Mineralogy and Petrology*, **137**, 46-58.

Sibson, R. 1981*. A brief description of natural neighbour interpolation*. In V Barnett, editor, Interpreting Multivariate Data, Wiley, New York, USA, 21–36.

Sibson, R.H. 1987. Earthquake rupturing as a mineralizing agent in hydrothermal systems. *Geology*, **15**, 701–704.

Sibson R.H., Moore, J.McM., Rankin A.H. 1975. Seismic pumping- a hydrothermal fluid transport mechanism. *Geological Society of London*, **131**, 653-659.

Sillitoe, R.H. 1993. Giant and bonanza gold deposits in the epithermal environment, in Whiting, B.H., Mason, R., Hodgson, C.J., eds., Giant ore deposits. *Society of Economic Geologists Special Publications,* **12**, 125–156.

Sillitoe, R.H. 2010. Porphyry Copper Systems*. Economic Geology*, **105**, 3-41.

Sillitoe, R. H. & Hedenquist, J. W. 2003. *Linkages between volcanotectonic settings, ore-fluid compositions, and epithermal precious metal deposits*. Society of Economic Geologists, Special Publications, **10**.

Simmons, S.F. & Browne, P.R.I. 1990. Mineralogic, alteration and fluid inclusion studies of epithermal gold-bearing veins at the Mt. Muro prospect, Central

Kalimantan (Borneo), Indonesia: geology, geochemistry, origin, and exploration. *Journal of Geochemical Exploration*, **35**, 63-104.

Simmons, S.F. & Christenson, B.W. 1994. Origins of calcite in a boiling geothermal system. *American Journal of Science*, **294**, 361-400.

Simmons, S. F., White, N. C. & John, D. 2005. Geological characteristics of epithermal precious and base metal deposits: *Economic Geology 100th Anniversary Volume*, 485-522.

Simpson, M.P., Palinkas, S.S., Mauk, J.L. & Bodnar R.J. 2015. Fluid inclusion chemistry of adularia- sericite epithermal Au-Ag deposits of the southern Hauraki Goldfield, New Zealand. *Economic Geology*, **110(3)**, 763-786.

Siyako, M., Burkan, K., Okay, A.I. 1989. Biga ve Gelibolu yarımadalarının Tersiyer jeolojisi ve hidrokarbon olanakları. *Türkiye Petrol Jeologları Derneği Bülteni*, **1**, 183-199 (in Turkish).

Spurr, J. E. 1925. Ore magmas versus magmatic waters. *Engineering and Mining Journal*, **119**, 890.

Spurr J.E. 1926. Successive banding around rock fragments in veins. *Economic Geology*, **21**, 519-537.

Stenhouse, P. & Cox, S. 2015. Fluid pathways in low-displacement fault networks. *Tectonic Studies Group Annual Meeting Abstracts, Edinburgh, 2015.*

Stenhouse, P., Jones, O., Stokes, L., Langdon, R. & Brough, C. 2014. Structural controls on the geometry of the Tuzon gold deposit, Southern Liberia. *Tectonic Studies Group Annual Meeting Abstracts, Cardiff, 2014.*

Stillwell F.L. 1950. Origin of the Bendigo saddle reefs. *Economic Geology*, **45**, 697-701.

Sümengen, M. & Terlemez, İ. 1991. Stratigraphy of the Eocene sediments in the southwest Thrace. *MTA Bulletin*, **113**, 15-29.

Şengör, A. M. C., Görür, N. & Şaroğlu, F. 1985. Strike-slip deformation basin formation and sedimentation: Strike-slip faulting and related basin formation in

zones of tectonic escape: Turkey as a case study, in Biddle, K.T. and Christie- Blick, N., eds., Strike-slip faulting and basin formation. *Society of Economic Paleontologists and Mineralogist Special Publication*, **37**, 227-264.

Şengör, A.M.C. & Yılmaz, Y. 1981. Tethyan Evolution of Turkey: A Plate Tectonic Approach. *Tectonophysics*, **75**, 181-241.

Tarasewicz, J.P.T., Woodcock, N.H. & Dickson, J.A.D.2005. Carbonate dilation breccias: Examples from the damage zone to the Dent Fault, northwest England. *GSA Bulletin*, **117**, 736-745.

Taylor, S.W., O'Brien, S.J.& Swinden, H.S. 1979. Geology and mineral potential of the Avalon Zone and granitoid rocks of eastern Newfoundland. *New Foundland Department of Mines and Energy, Mineral Development Division Report*, **79 (3)**, 50.

Toda, S., Stein, R. S. & Sagiya, T. 2002. Evidence from the AD 2000 Izu islands earthquake swarm that stressing rate governs seismicity. *Nature*, **419**, 58–61.

Türkecan, A. & Yurtsever, A. 2002. *1:500 000 scale geological map of Turkey, İstanbul sheet.* General Directorate of Mineral Research and Exploration publications, Ankara.

Urquhart A.S.M. 2011. *Structural controls on $CO_2$ leakage and diagenesis in a natural long-term carbon sequestration analogue : Little Grand Wash fault, Utah.* The university of Texas at Austin, Texas, PhD thesis, 437.

Ünal-İmer, E., Gulec, N., Kuscu, I. & Fallick, A.E. 2013. Genetic investigation and comparison of Kartaldag and Madendag epithermal gold deposits in Canakkale, NW Turkey. *Ore Geology Reviews*, **53**, 204-222.

Waite, G.P. & Smith, R.B., 2002. Seismic evidence for fluid migration accompanying subsidence of the Yellowstone caldera. *Journal of Geophysical Research*, **107**, 2177.

Watson D.F. 1992. *Contouring: A Guide to the Analysis and Display of Spatial Data*. Pergamon Press, Oxford, UK.

Wernicke R.S. & Lippolt, H.J. 1997. Evidence of Mesozoic multiple hydrothermal activity in the basement at Nonnenmattweiher (southern Schwarzwald), Germany. *Mineralium Deposita*, **32**, 197-200.

White, D. E., Fournier, R. O., Muffler, L. J.P., & Truesdell, A. H. 1975. Physical results of research drilling in thermal areas of Yellowstone National Park, Wyoming: *U.S. Geological Survey Professional Paper,* **892**, 70.

White, N.C. & Hedenquist, J.W. 1990. Epithermal environments and styles of mineralisation: Variations and their causes, and guidelines for exploration. *Journal of Geochemical Exploration*, **36**, 445–474.

White, N.C. & Hedenquist, J.W. 1995. Epithermal gold deposits: Styles, characteristics and exploration. *Society of Economic Geologists Newsletter*, **23**, 9–13.

White, N.C., Wood, D.G. & Lee, M.C. 1989. Epithermal sinters of Paleozoic age in North Queensland, Australia. *Geology*, **17**, 718-722.

Wilkinson, J.J. 2001. Fluid inclusions in hydrothermal ore deposits. *Lithos*, **55**, 229-272.

Woodcock, N.H., Dickson, J.A.D. & Tarasewicz, J.P. 2007. Transient permeability and reseal hardening in fault zones: evidence from dilation breccia textures. *In*: Lonergan, L., Jolley, R.J.H., Rawnsley, K. & Sanderson, D.J. (eds) *Fractured Reservoirs*, Geological Society, London, Special Publications, **270**, 43–53.

Yılmaz, Y., Genç, S. C., Gürer, Ö. F. *et al*. 2000. When did the western Anatolian grabens begin to develop? In: Bozkurt, E., Winchester, J. A. & Piper, J. A. D. (eds) Tectonics and Magmatism in Turkey and the Surrounding Area. *Geological Society, London, Special Publication*, **173**, 353–384.

Yiğit, Ö. 2012. A prospective sector in the Tethyan Metallogenic Belt: Geology and geochronology of mineral deposits in the Biga Peninsula, NW Turkey. *Ore Geology Reviews*, **46**, 118-148.

Yücel-Öztürk, Y., Helvaci, C. & Satır, M. 2005. Genetic relations between skarn mineralization and petrogenesis of the Evciler Granitoid, Kazdağ, Çanakkale, Turkey and comparison with world skarn granitoids. *Turkish Journal of Earth Sciences*, **14**, 255–280.

Yüzer, E. & Gürkan, T. 2012. *Biga Yarımadası'nın Genel ve Ekonomik Jeolojisi*. MTA Publications, Ankara (in Turkish).

Žalohar, J. & Vrabec, M. 2007. Paleostress analysis of heterogeneous fault-slip data: the Gauss method. *Journal of Structural Geology*, **29**, 1798–1810.

Zhu, Y., And, F. & Tan, J. 2011. Geochemistry of hydrothermal gold deposits: A review. *Geoscience Frontiers*, **2**, 367-374.